Università degli studi di Trieste

Dipartimento di Fisica

Corso di Laurea Magistrale in Fisica

Curriculum Fisica della Materia Condensata

Tesi di Laurea Magistrale

Multimode homodyne detection applied to time-resolved Raman spectroscopy

Detezione omodina multimodo applicata alla spettroscopia Raman risolta in tempo

Laureando:
Giacomo Jarc

Relatore:
Prof. Daniele Fausti

Correlatore:
Filippo Glerean

ANNO ACCADEMICO 2018-2019

"Chi ha imparato ad ascoltare gli alberi
non brama di essere un albero.
Vuole essere quello che è."

Hermann Hesse

Contents

Introduction **1**

1 Detection of quantum light states **5**
1.1 The quantum state of a physical system 5
1.2 Phase-sensitive measurement of light: Balanced Homodyne Detection 7
1.2.1 Quantum noise sensitivity 10
1.3 Multimode quantum light states 13

2 Theoretical framework of photon-phonon interaction **17**
2.1 Classical formalism 17
2.1.1 Optical driving force 18
2.1.2 Pump-probe dynamics 20
Linear refractive modulation (LRM) 22
Impulsive stimulated Raman Scattering (ISRS) 24
2.2 Quantum model 27
2.2.1 Derivation of the interaction Hamiltonian 27
2.2.2 ISRS phonon excitation process 30
2.2.3 Pump-probe dynamics 33
Linear refractive modulation (LRM) 34
Impulsive Stimulated Raman Scattering (ISRS) 37

3 Experimental apparatus **43**
3.1 Time-resolved multimode homodyne set-up 43
Polarization selectivity 46
3.1.1 Multimode homodyne with multiple-shaped local oscillator 47
3.2 Ultrafast pulse-shaping 48
3.2.1 Two-dimensional Liquid Crystal Spatial Light Modulator (LC-SLM) 49
Pulse-shaper calibration 54
3.3 Detection system 57
3.3.1 Balanced detector and fast digitizer 57
Differential current integration 58

4 Measuring quantum fluctuations: set-up noise calibration **61**
4.1 Noise in unbalanced conditions 62
4.2 Characterizing the set-up noise: the "Beam Splitter Model" 63
Classical noise characterization 65
Shot-noise 66

4.2.1 Local oscillator low fluence regime . . . 67
Electronic noise . . . 68
Classical noise characterization . . . 69
Shot-noise test . . . 70
4.2.2 Local oscillator high fluence regime . . . 71
4.3 Defining quadrature units: vacuum noise calibration . . . 75
4.4 Correlation between successive pulses . . . 79

5 Mean value time-resolved measurements 81
5.1 Time-resolved experimental response . . . 82
5.2 Time-resolved measurements on α-quartz . . . 85
5.2.1 Parallel configuration . . . 88
5.2.2 Cross configuration . . . 91
5.2.3 Pump-probe polarization angle dependence . . . 94
5.2.4 Comparison with the model . . . 98
Parallel configuration . . . 100
Cross configuration . . . 101
Phonon cross-sections estimation . . . 103
Static birefringence estimation . . . 107
Pump-probe polarization angle dependence . . . 110
5.3 Beyond non-absorbing materials:
time-resolved homodyne on $CuGeO_3$ . . . 113

6 Towards statistical analysis 119
6.1 Single mode statistical measurements . . . 120
6.1.1 Variance data analysis . . . 120
6.1.2 Measurements on $CuGeO_3$ . . . 121
6.1.3 Measurements on α-quartz . . . 124
Parallel configuration . . . 124
Cross configuration . . . 125
6.2 Perspectives: measuring multimode quantum correlations . . . 128

Conclusions 133

Appendices 137

A Multimode homodyne current 139

B Potentiality of the set-up: multimode homodyne with shaped signal 141

Riassunto 143

Introduction

The development of femtosecond lasers has pushed forward the perspectives of standard vibrational spectroscopies, allowing the detection of the coherent motion of the atoms on time scales that are shorter than their oscillation periods.

The typical approach in this sense is the *pump-probe* one that consists in injecting in the system a large number of vibrational excitations (*phonons*) within a femtosecond time window and subsequently monitor the system optical response by mean of a second ultrafast pulse (*probe*) at a variable delay time. The modification of the probe spectral features as a function of the delay from the sudden excitation will carry information on the temporal dynamics of the excited vibrational mode and eventually on the photon-phonon coupling.

This coupling between optical and vibrational degrees of freedom is easier to understand in non-absorbing materials. In such materials there are no electronic transitions allowed within the probe bandwidth and the energy exchange in photon-phonon interaction is mediated by *Impulsive Stimulated Raman Scattering* (ISRS). ISRS is an intrinsic multimode process and occurs whenever an ultrashort pulse (i.e. with a frequency bandwidth greater than the phonon frequency Ω) propagates in a Raman-active medium. As a matter of fact, all optical modes in the pulse with an energy difference corresponding to $\hbar\Omega$ can resonantly interact and create (Stokes Raman process) or annihilate (Anti-Stokes Raman process) a phonon (Figure 1). Owing to its multimode nature, we hence expect ISRS to imprint on the transmitted pulse a correlation structure between all the phonon-coupled optical modes.

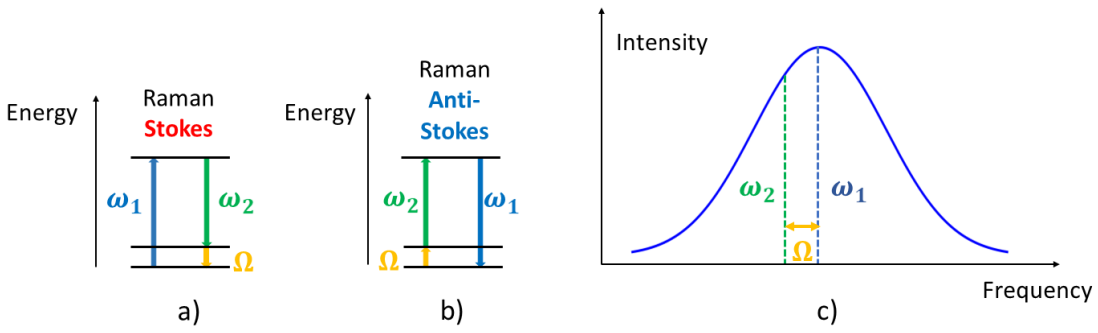

Figure 1: Schematic representation of Stokes (a) and Anti-Stokes (b) processes involving a pair of optical modes of frequencies ω_1 and ω_2 and a phonon of frequency Ω. The Raman interaction occurs between all the phonon-coupled frequencies within the pulse bandwidth.

In standard time-resolved Raman spectroscopy the coherent dynamics of the excited vibrational mode is addressed by measuring the intensity variation of

the probe pulse as a consequence of photon-phonon interaction. Even if this approach is useful to retrieve the excited vibrational frequencies, it does not allow to reconstruct the full structure of the probe electric field after its non-linear interaction. Indeed, all phase information is lost through the integration. Moreover, an integrated technique does not permit to unveil information hidden inside higher order momenta of photon number distribution, such as correlations introduced trough non-linear interactions.

In this thesis, we have set up an experiment that can go beyond the integrated approach. We have accomplished this purpose by mean of an interferometric technique named *Balanced Homodyne Detection* which has been coupled to the standard pump-probe set-up. The novelty of our approach resides in the fact that the homodyne detection of the probe has been performed in a multimode scheme. Thanks to this innovative possibility, we can selectively have access to amplitude and phase of each spectral component of the probe pulse and monitor their out-of-equilibrium dynamics.

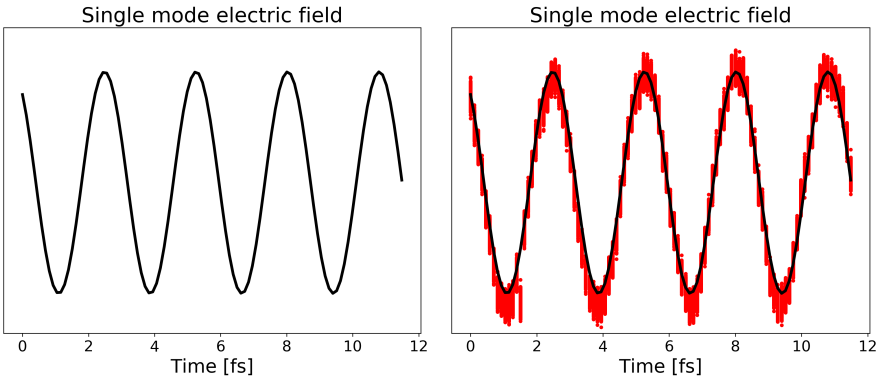

(a) (b)

Figure 2: Mean value (a) and statistical distribution (b) of a single mode electric field detected with our set-up. Shot-noise working conditions ensure the field fluctuations to be of purely quantum origin.

Furthermore, we have exploited the capability of our detection system of performing single pulse acquisition on equally prepared quantum systems to have access to the full statistics of each probe mode after the pump excitation (Figure 2). In this sense, *Balanced Homodyne Detection* has a powerful potentiality: it allows to maintain the external noise smaller than the intrinsic fluctuations of the number photons (shot-noise limit). Therefore, the field fluctuations detected with our set-up all pertain to the fundamental quantum nature of light. This possibility, together with the frequency resolution of our technique, opens the perspective of unveiling multimode quantum correlation imprinted on an optical pulse trough its non-linear interactions with a phononic system. The latter are indeed encoded in multimode higher-momenta distributions of the photon number.

The thesis is organized as follows:

- In Chapter 1 we provide the theoretical concepts on what "measuring quantum light systems" means and how homodyne detection can achieve this purpose. We will then focus on the application of the technique on multimode light states.

- Chapter 2 provides the theoretical framework needed to describe photon-phonon interaction. A classical and a fully quantum model will be presented and exploited to interpret the mean value outcomes of an homodyne measurement in time domain.

- Chapter 3 is dedicated to the description of the experimental set-up specifically developed in the *q4q* laboratory at Elettra Sincrotrone Trieste. It enables to perform shot-noise-limited measurements of amplitude and phase of each mode of a pulse.

- In Chapter 4 we present the complete characterization of our set-up noise, which is crucial to test the quantum noise sensitivity of the technique and eventually select suitable experimental conditions to ensure a shot-noise-limited detection.

- In Chapter 5 the mean value outcomes of time-resolved multimode homodyne are presented. The technique has been firstly tested on α-quartz, which represents a benchmark system to track the photon-phonon Raman coupling in transparent materials. In particular, we have exploited the information obtained both from phase and amplitude dynamics of each probe mode to characterize photon-phonon coupling effects and eventually estimate their cross-sections. The cross-sections have been calculated exploiting the quantum model presented in Chapter 2. We have then tested the technique on an absorptive system ($CuGeO_3$) where photon-phonon coupling allows high energy orbital transitions.

- In Chapter 6 we present the preliminary statistical measurements performed in shot-noise regime on α-quartz and $CuGeO_3$. The objective of the last part of the thesis is to see whether exists a pump-driven modification of the probe quantum statistics. In this sense, we have explored the statistics variation of a single probe mode and the modification of the joint statistics of phonon-coupled probe modes. We expect the latter to encode ISRS-driven quantum correlations.

Chapter 1

Detection of quantum light states

In quantum mechanics all the properties of a physical system are encoded in its quantum state [6]. Measuring the quantum state of a system means predicting the statistical distributions of the outcomes of all possible measurements that can be performed on it [10]. In this thesis we will focus on the detection of quantum light systems and in particular in the study of how they can be modified as a consequence of their interaction with a photo-excited material.

In this chapter we introduce the theoretical framework in which the detection of quantum light states is inserted. In particular, we will point out the necessity of having simultaneously access to amplitude and phase of an optical field in order to completely characterize its quantum state and show a phase-resolved technique (*Balanced Homodyne Detection*) able to accomplish this requirement. We will preliminary apply the technique to single mode states of the electromagnetic field and then move to multimode fields, that are the ones employed in the thesis. Looking at intrinsic multimode statistical properties of an optical field is particularly interesting, since we expect the latter, rather then the single mode ones, to encode the quantum correlations introduced between the field modes through the non-linear interaction with matter.

1.1 The quantum state of a physical system

In this section we present a brief introduction on what measuring a quantum state means. We will exploit the concepts provided in this section as a benchmark framework for introducing the detection of quantum light systems. In particular, we will see how performing measurements on equally prepared quantum systems allows to have access to deeper statistical information on the state itself. This is the one we are looking for with our spectroscopic approach.

"State means whatever information is required about a specific system, in addition to pysiscal laws, in order to predict its behaviour in future experiments" [10]. The state of a quantum object is commonly described by a normalized vector $|\psi\rangle$ belonging to a Hilbert-space $\mathcal{H}$. If we want to extract a piece of information about the system, we have just to compute the expectation value of the corresponding operator $\widehat{O}$ on the quantum state $|\psi\rangle$:

$$\langle \widehat{O} \rangle = \langle \psi | \widehat{O} | \psi \rangle \tag{1.1}$$

If the initial state and the Hamiltonian operator of the system are known, the

previous formalism provides a complete description of the system, of its time evolution and of the properties of its observables [13].

Nonetheless, there are physical circumstances in which we are not able to know $|\psi\rangle$. In this cases the system can be described in a statistical way, making the ensemble average over many identical systems equally prepared and introducing a new formalism: the **density matrix** one. In order to introduce this formalism, let us assume to have an ensemble of physical states equally prepared and to have statistical information about them, that is, to have a set of eigenstates $|\psi_n\rangle$ in which the system stays with probabilities p_n. In this case, the mean value of a physical observable $\widehat{O}$ becomes:

$$\langle \widehat{O} \rangle = \sum_n p_n \langle \psi_n | \widehat{O} | \psi_n \rangle \tag{1.2}$$

Therefore, the statistic state of a quantum system can be defined as a linear combination of the states $|\psi_n\rangle$ weighted on the corresponding probabilities p_n. All the previous information can be gathered in just one operator, called *density operator*, which is the weighted average over the projectors on the states $|\psi_n\rangle$:

$$\widehat{\rho} = \sum_n p_n |\psi_n\rangle\langle\psi_n| \tag{1.3}$$

In this statistical framework, the mean value of a physical observable can be expressed in terms of the density operator as follows:

$$\begin{aligned} \langle \widehat{O} \rangle &= \sum_n p_n \langle \psi_n | \widehat{O} | \psi_n \rangle \\ &\sum_m \sum_n p_n \langle \psi_n | \widehat{O} | \psi_m \rangle \langle \psi_m | \psi_n \rangle \\ &= Tr(\widehat{\rho}\widehat{O}) \end{aligned} \tag{1.4}$$

where $Tr(\widehat{\rho}\widehat{O})$ is the trace of $\widehat{\rho}\widehat{O}$, i.e. the sum of its diagonal matrix elements in any matrix representation.

The set of the matrix elements of the operator $\widehat{\rho}$ on whatever basis is called **density matrix** and plays the crucial role in the statistical description of a quantum state. As a matter of fact, the probability of any outcome of any measurement performed on a system can be extracted from the density matrix of that system [6]. In particular, the diagonal elements ρ_{nn} represent the probability of the system to be in the eigenstate $|\psi_n\rangle$, while the off-diagonal elements ρ_{mn} provide the coherence between the state $|\psi_n\rangle$ and $|\psi_m\rangle$. This means that ρ_{mn} is different from zero only if the system is in a coherent superposition of the eigenstates $|\psi_n\rangle$ and $|\psi_m\rangle$ [9].

Therefore, all the information needed to perform statistical previsions on a quantum system are encoded inside the density matrix. By its elements ρ_{ij} we are hence able to predict the statistical distributions of the outcomes of all possible measurements that can be performed on the system.

We stress that, while the state of a classical system can be determined by performing repeated measurements on it, the knowledge of a quantum state is not accessible, in general, when a single copy of the system itself is available. In fact, the act of measuring an observable of the system changes its state, making repeated measurements on it meaningless towards the determination of its initial

state [6]. Therefore, statistical previsions on a quantum system are only possible when an ensemble of identically prepared systems is available.

As proved in [10], in order to fully reconstruct the density matrix, it is necessary to measure a set, called *quorom*, of at least two non-commuting observables $\widehat{O}_i$.

The previous statement has a direct implication on the measurement of optical quantum state. Indeed, it implies that no complete statistical information on an optical field can be retrieved if we limit in measuring only its intensity. To have access to a meaningful statistics, a **phase-resolved** approach has to be implemented.

1.2 Phase-sensitive measurement of light: Balanced Homodyne Detection

In the previous section we have pointed out the necessity of having access to the statistics of at least two non-commuting observables in order to perform statistical previsions of any measurement on a quantum state. In the quantum optics framework, this requirement implies the necessity of having access to phase dynamics, which cannot be unveiled in standard intensity measurements. In this section we will present an interferometric technique, named *Balanced Homodyne Detection* (BHD), able to accomplish this requirement. We will preliminary study this approach in the case in which the optical state under investigation is a single electromagnetic field mode of the form[1][9]:

$$\widehat{E}_j(z,t) = i\sqrt{\frac{\omega_j}{2\epsilon_0 V}}\left[\widehat{a}_j e^{-i(\omega_j t - k_j z)} - \widehat{a}_j^\dagger e^{i(\omega_j t - k_j z)}\right] \tag{1.5}$$

where $\widehat{a}_j$ and $\widehat{a}_j^\dagger$ are the ladder operators of the quantum-harmonic oscillator satisfying the bosonic commutation relation:

$$[\widehat{a}_j^\dagger, \widehat{a}_k] = \delta_{jk} \tag{1.6}$$

The expression of the quantized electromagnetic field can be written in terms of the adimensional position and momentum of the quantum harmonic oscillator

$$\begin{aligned} \widehat{Q}_j &= \frac{1}{2}(\widehat{a}_j^\dagger + \widehat{a}_j) \\ \widehat{P}_j &= \frac{i}{2}(\widehat{a}_j^\dagger - \widehat{a}_j) \end{aligned} \tag{1.7}$$

as follows:

$$\widehat{E}_j(z,t) = \sqrt{\frac{\omega_j}{2\epsilon_0 V}}\left[\widehat{Q}_j \cos(\phi_j) + \widehat{P}_j \sin(\phi_j)\right] \tag{1.8}$$

where we have defined the phase ϕ_j as:

$$\phi_j \equiv \omega_j t - k_j z + \frac{\pi}{2}$$

[1]To simplify the notation in the present expression we have not considered the polarization index of the field, but only its mode index j.

If we now define the phase-dependent operator $\widehat{X}_{\phi_j}$ as:

$$\widehat{X}_{\phi_j} = \frac{1}{\sqrt{2}}\left(\hat{a}_j e^{-i\phi_j} + \hat{a}_j^\dagger e^{i\phi_j}\right) \tag{1.9}$$

the quantized electromagnetic field can be expressed as:

$$\widehat{E}_j(z,t) = \sqrt{\frac{\omega_j}{\epsilon_0 V}}\widehat{X}_{\phi_j} \tag{1.10}$$

$\widehat{X}_{\phi_j}$ is dubbed the *quadrature* operator, it is proportional to the quantized electric field and we will see that it is the detected observable in a *Balanced Homodyne* experiment, whose main features will be highlighted in the following.

Balanced Homodyne Detection (BHD) is a powerful method for measuring phase-sensitive properties of travelling optical fields that is used for the reconstruction of quantum light states [6]. In this framework, the quantum state is characterized through the repeated measurement of the optical field quadratures $\widehat{X}_{\phi_j}$ (Equation 1.9) for different phases $\phi_j \in [0, \pi]$ [8]. Quadratures at fixed phase ϕ_j are continuum-spectrum observables and constitute a *quorum* of observables, whose measurement hence provides a complete information about the quantum state of the electromagnetic field [7]. The schematic diagram employed in Balanced Homodyne Detection is depicted in Figure 1.1. The optical state under in-

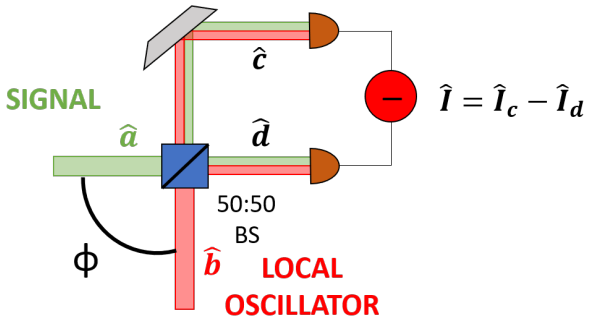

Figure 1.1: Schematic representation of balanced homodyne detector. The signal under investigation (in the mode state $\hat{a}$) is mixed in a 50:50 beam splitter with the local oscillator (in the mode state $\hat{b}$) whose relative phase ϕ can be controlled. The intensities of the output modes ($\hat{c}$ and $\hat{d}$) are detected by two photodiodes and the differential current $\hat{I}$ (homodyne current) is measured.

vestigation, named *signal*, is mixed with a strong classical reference state, named *local oscillator* (LO), by a 50:50 beam spitter (whence the attribute *balanced*). Since the signal beam (mode $\hat{a}$ in Figure 1.1) can be prepared in a unknown way, it can be conveniently described in a statistical way by mean of its density operator $\hat{\rho}$ (Equation 1.3). The local oscillator (mode $\hat{b}$ of Figure 1.1) is instead in a classical coherent state[2] $|z\rangle\langle z|$. Therefore, it satisfies:

$$\hat{b}|z\rangle = z|z\rangle \qquad z \in \mathbb{C} \tag{1.11}$$

[2]Coherent states are the eigenstates of the annihilation operator $\hat{a}$ of the harmonic oscillator. They are used in quantum optics to represent classical states, since the mean evolution of the canonical operators ($\hat{p}$ and $\hat{q}$) on those states is the same as the classical one.

The BS outputs in the mode states $\widehat{c}$ and $\widehat{d}$ are collected by two photodiodes and the differential photocurrent $\widehat{I}$ (*homodyne photocurrent*) is measured. The modes $\widehat{c}$ and $\widehat{d}$ are linked to the incoming modes $\widehat{a}$ and $\widehat{b}$ by mean of the balanced beam splitter, whose action is ruled by the unitary operator (see Section 1.2.1):

$$\widehat{U}_{BS} = \frac{1}{\sqrt{2}} \begin{pmatrix} 1 & 1 \\ -1 & 1 \end{pmatrix} \tag{1.12}$$

Therefore, as a consequence of the action of $\widehat{U}_{BS}$, we get:

$$\begin{cases} \widehat{a} & \longmapsto \widehat{c} = (\widehat{a} + \widehat{b})/\sqrt{2} \\ \widehat{b} & \longmapsto \widehat{d} = (\widehat{b} - \widehat{a})/\sqrt{2} \end{cases} \tag{1.13}$$

After the 50:50 BS, the two modes are detected by two identical photodiodes and the respective photocurrents ($\widehat{I}_c$ and $\widehat{I}_d$) are measured and subtracted. The currents $\widehat{I}_c$ and $\widehat{I}_d$ (Figure 1.1) are the measured values of the photon number observables $\widehat{n}_c = \widehat{c}^\dagger\widehat{c}$ and $\widehat{n}_d = \widehat{d}^\dagger\widehat{d}$. Therefore, the differential photocurrent $\widehat{I}$ reads:

$$\widehat{I} = \widehat{n}_c - \widehat{n}_d = \widehat{c}^\dagger\widehat{c} - \widehat{d}^\dagger\widehat{d} \tag{1.14}$$

which, exploiting the beam spitter transformation (Equation 1.13), becomes:

$$\widehat{I} = \widehat{a}^\dagger\widehat{b} + \widehat{b}^\dagger\widehat{a} \tag{1.15}$$

The phase-sensitivity of the technique is achieved by tuning the phase difference between the local oscillator and the signal, which can be controlled by changing the length of the LO optical path. This implies that the LO mode is subjected to the following phase shift:

$$\begin{cases} \widehat{b} & \longmapsto \widehat{b}e^{i\phi} \\ \widehat{b}^\dagger & \longmapsto \widehat{b}^\dagger e^{-i\phi} \end{cases} \tag{1.16}$$

and the homodyne current operator can be subsequently redefined as:

$$\widehat{I}_\phi = \widehat{a}^\dagger\widehat{b}e^{i\phi} + \widehat{b}^\dagger\widehat{a}e^{-i\phi} \tag{1.17}$$

Now, a natural question arises: how, by measuring the phase-resolved homodyne current $\widehat{I}_\phi$ can we obtain a value for the quadrature of the electric field? The answer comes from the fact that the expectation value of the homodyne current $\widehat{I_\phi}$ on the total LO-signal input state $\widehat{\rho} \otimes |z\rangle\langle z|$ is proportional to the expectation value of the field quadrature $\widehat{X_\phi}$ defined in Equation 1.10[3]

$$\begin{aligned} \langle \widehat{I}_\phi \rangle &= Tr\left[\widehat{\rho} \otimes |z\rangle\langle z|\widehat{I}_\phi\right] = Tr\left[\widehat{\rho} \otimes |z\rangle\langle z|(\widehat{a}^\dagger\widehat{b}e^{i\phi} + \widehat{b}^\dagger\widehat{a}e^{-i\phi})\right] \\ &= \sqrt{2}|z|\langle \widehat{X}_\phi \rangle \end{aligned} \tag{1.18}$$

By mean of balanced homodyne detection we can therefore measure the quadrature of the signal field and amplify it by mean of the local oscillator. Indeed, the detected homodyne current scales linearly with the LO amplitude $|z|$.

[3]In the following equation we will neglect the phase of the initial local oscillator coherent state, i.e. $z = |z|$ (Equation 1.11).

We underline that, in order to ensure the homodyne current to be a representative observable of the field quadrature at each phase, is not sufficient that their expectation values coincide. Indeed, all higher order momenta of the two observables must coincide. For the second order momentum we get the following expression [7]:

$$\begin{aligned}\langle \widehat{I}_\phi^2 \rangle &= \frac{1}{2|z|^2} Tr\left[\widehat{\rho} \otimes |z\rangle\langle z|(\widehat{a}^\dagger \widehat{b} e^{i\phi} + \widehat{b}^\dagger \widehat{a} e^{-i\phi})^2\right] \\ &= \langle \widehat{X}_\phi^2 \rangle + \langle \frac{\widehat{a}^\dagger \widehat{a}}{2|z|^2} \rangle\end{aligned} \tag{1.19}$$

which can be generalized to higher momenta [12] as follows:

$$\langle \widehat{I}_\phi^n \rangle = \langle \widehat{X}_\phi^{2n-2} (\widehat{X}_\phi^2 + \frac{\widehat{a}^\dagger \widehat{a}}{2|z|^2}) \rangle \tag{1.20}$$

We notice that the homodyne current higher momenta tend to the quadrature ones only if $|z|^2 >> \langle \widehat{a}^\dagger \widehat{a} \rangle$. Therefore, through BHD we can extract meaningful statistical information on the quantum signal field only if we mix it with a much more intense classical field (the local oscillator). This situation can be hence referred as a quantum regime of the interferometer, opposed to the classical one in which the signal field is in a large-amplitude coherent state $|\alpha\rangle$:

$$\widehat{a}|\alpha\rangle = \alpha|\alpha\rangle \qquad \alpha \in \mathbb{C} \tag{1.21}$$

In the latter case only mean value coincides and classical interference pattern can be retrieved. If the signal field is classical ($|z|^2 \sim \langle \widehat{a}^\dagger \widehat{a} \rangle = |\alpha|^2 >> 1$) we have indeed[4]:

$$\langle \widehat{X}_\phi \rangle = Tr[\widehat{X}_\phi |\alpha\rangle\langle\alpha|] = \langle \alpha | \frac{\widehat{a} e^{-i\phi} + \widehat{a}^\dagger e^{i\phi}}{\sqrt{2}} |\alpha\rangle = \sqrt{2}|\alpha| \cos(\phi) \tag{1.22}$$

which implies:

$$\langle \widehat{I}_\phi \rangle = 2|z||\alpha| \cos(\phi) \tag{1.23}$$

We will make use of this result in Chapter 2, where we will exploit the homodyne framework to retrieve mean value information on photon-phonon interaction.

Equations 1.20 and 1.19 show that a requirement for BHD to be sensitive on quantum fluctuations of the signal quadrature is to work with a local oscillator in a strong classical state. A natural question therefore arises: how can we filter out its inevitable classical noise and ensure a **quantum noise sensitiviy**? In the following section we will analyse this issue and prove that through balanced homodyne the quantum sensitivity is ensured.

1.2.1 Quantum noise sensitivity

The crucial element on which quantum noise sensitivity relies is the last **beam splitter** before the differential detection (Figure 1.1).

[4] In the equation we have neglected the phase of the signal coherent state, i.e. supposed $\alpha = |\alpha|$.

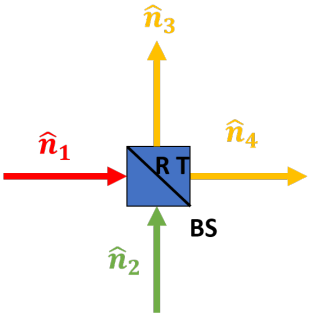

Figure 1.2: Representation of a lossless beam splitter. In a quantum formalism, $\hat{n}_2$ must always be present, even if the signal channel is blocked. In this case, $\hat{n}_2$ is described by the vacuum state $|0\rangle$.

A beam splitter is a dielectric medium able to split a beam into two with a defined proportion [19]. A representation of a lossless beam splitter is depicted in Figure 1.2, in which two beams, that we will indicate with their annihilation operators $\hat{a}_1$ and $\hat{a}_2$, imping on it and two other beams ($\hat{a}_3$ and $\hat{a}_4$) emerge from it. We can write the relation between the input and the output states as:

$$\begin{aligned} \hat{a}_3 &= R\hat{a}_1 + T\hat{a}_2 \\ \hat{a}_4 &= T\hat{a}_1 + R\hat{a}_2 \end{aligned} \tag{1.24}$$

where R and T represent the complex reflectivity and transmittance of the beam splitter: $R = |R|e^{i\phi_R}$, $T = |T|e^{i\phi_T}$. In order to ensure photon number conservation the following relations must hold between the BS parameters:

$$\begin{aligned} |R|^2 + |T|^2 &= 1 \\ RT^* + TR^* &= 0 \end{aligned} \tag{1.25}$$

As a consequence of Equation 1.24, the output photon number operators are related to input ones by the relations:

$$\begin{aligned} \hat{n}_3 &= \hat{a}_3^\dagger \hat{a}_3 \\ &= |R|^2 \hat{a}_1^\dagger \hat{a}_1 + R^* T \hat{a}_1^\dagger \hat{a}_2 + T^* R \hat{a}_2^\dagger \hat{a}_1 + |T|^2 \hat{a}_2^\dagger \hat{a}_2 \end{aligned} \tag{1.26}$$

$$\begin{aligned} \hat{n}_4 &= \hat{a}_4^\dagger \hat{a}_4 \\ &= |R|^2 \hat{a}_1^\dagger \hat{a}_1 + T^* R \hat{a}_1^\dagger \hat{a}_2 + R^* T \hat{a}_2^\dagger \hat{a}_1 + |R|^2 \hat{a}_2^\dagger \hat{a}_2 \end{aligned} \tag{1.27}$$

From the expressions of the number operators (Equation 1.26 and 1.27) we can retrieve for each output the mean number of photons and the related variance. The expressions for the mean photon number of the two outputs are:

$$\begin{aligned} \langle \hat{n}_3 \rangle &= |R|^2 \langle \hat{n}_1 \rangle + |T|^2 \langle \hat{n}_2 \rangle \\ \langle \hat{n}_4 \rangle &= |T|^2 \langle \hat{n}_1 \rangle + |R|^2 \langle \hat{n}_2 \rangle \end{aligned} \tag{1.28}$$

The same calculation can be done for the related variances. In order to simplify the notation, we will only consider the case in which $\hat{n}_2$ is in a vacuum state $|0\rangle$. In this situation, the expressions of the variances of the two output beams read:

$$\begin{aligned} \sigma_3^2 &= |R|^4 \sigma_1^2 + |T|^2 |R|^2 \langle \hat{n}_1 \rangle \\ \sigma_4^2 &= |T|^4 \sigma_1^2 + |T|^2 |R|^2 \langle \hat{n}_1 \rangle \end{aligned} \tag{1.29}$$

We can recognize that the variances of both channels have two contributions [19] (Figure 1.3):

- **Classical noise**: it is proportional to the input noise σ_1^2 of the only physical beam impinging on the BS and it is related to the intensity of the reflected/transmitted beam.
- **Quantum (partition) noise**: it is caused by the random division of the input photons in the two channels with probabilities $|R|^2$ and $|T|^2$. Therefore it pertains to the intrinsic quantum nature of the electromagnetic field.

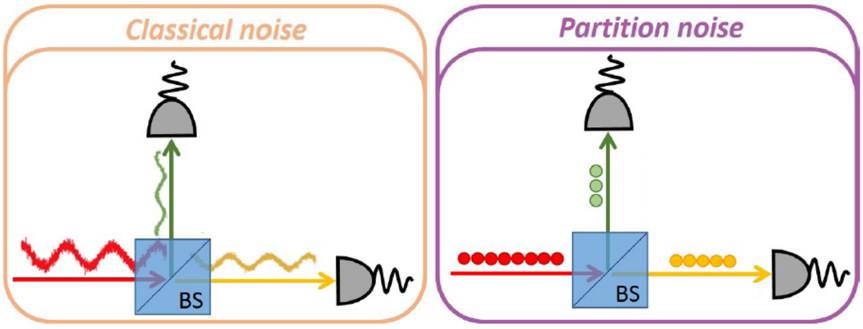

Figure 1.3: Classical vs Partition noise (Adapted from [19]).

Let us now exploit the beam splitter formalism to retrieve mean value and noise information on the homodyne current, which is the observable in our experiment (Figure 1.1). For the fluctuations, we will limit to the second order momentum (variance), thus neglecting the information encoded in higher order momenta. With the notation of Figure 1.2, mean value and variance of the homodyne current $\hat{n}_3 - \hat{n}_4$ can be expressed as follows:

$$\langle \hat{n}_{3-4} \rangle = \langle \hat{n}_3 - \hat{n}_4 \rangle = (|R|^2 - |T|^2)\langle \hat{n}_1 \rangle \tag{1.30}$$

$$\begin{aligned} \sigma_{3-4}^2 &= \left\langle (\hat{n}_3 - \hat{n}_4)^2 \right\rangle - \langle (\hat{n}_3 - \hat{n}_4) \rangle^2 \\ &= (|R|^2 - |T|^2)^2 \sigma_1^2 + 4|R|^2|T|^2\langle \hat{n}_1 \rangle \end{aligned} \tag{1.31}$$

From the previous equations we can immediately recognize that, by working in balanced conditions (i.e. by setting $|R|^2 = |T|^2 = 1/2$), the classical noise can be completely filtered out from the differential response. As a matter of fact, we get:

$$\sigma_{3-4}^2 = \langle \hat{n}_1 \rangle \tag{1.32}$$

which represents the minimum reachable noise level due to photon field quantization: the **shot-noise**. Although the mean of value of $\hat{n}_3$ and $\hat{n}_4$ are equal, single measurements are characterized by partition fluctuations (Figure 1.3(right)) scaling as $\langle \hat{n}_1 \rangle$.

In the homodyne framework (Figure 1.4(left)), where do these fluctuations come from? Since we have proved (Equation 1.20) that the differential current is a map of the signal at all the orders, they originate from the vacuum fluctuations of the signal encoded inside the partition noise of the local oscillator (Figure 1.4(right)). Vacuum noise is equal to 1/2 for every value of the phase ϕ and

hence provides a rescaling factor for signal fluctuations in the general cases in which the signal is not in a vacuum state. We will explore this issue in Section 4.3.

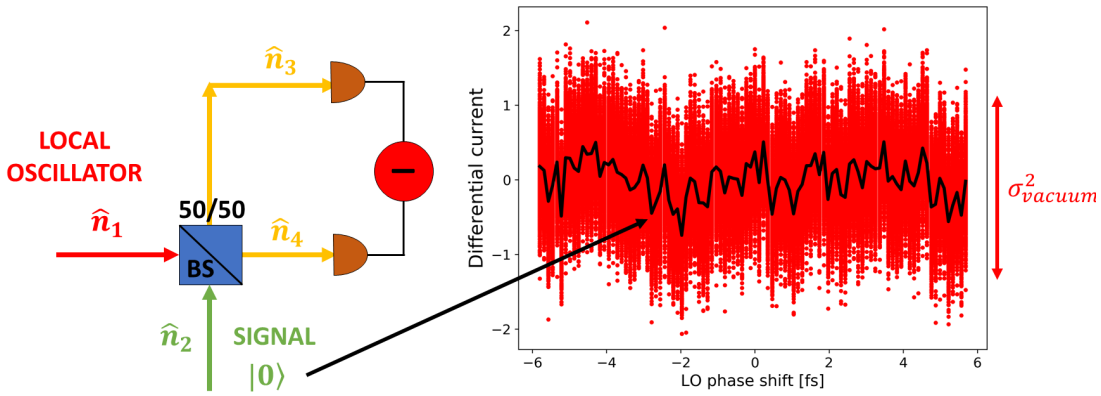

Figure 1.4: Homodyne trace of the vacuum signal state. Homodyne allows to map the signal vacuum fluctuations σ^2_{vacuum} onto the partition noise of the local oscillator.

1.3 Multimode quantum light states

The single mode description provided in the previous section has to be generalized when ultrashort laser pulses are used. Indeed, owing to the Heisenberg uncertainty principle, to a short pulse duration corresponds a broad spectrum of frequency modes of the radiation. In the following we will introduce multimode light states and show that we can generalize single mode homodyne formalism for their statistical description.

In Section 1.1, we have seen that all the information required to perform statistical previsions on a quantum state are encoded inside its density matrix. The density matrix dimension is determined by the number of elements of the Hilbert space basis on which the quantum state is represented.

The state space of a multimode field can be expressed as the tensor product of the Fock spaces of N harmonic oscillators [2], where N is the number of modes of the optical field. In terms of number states, the basis vector of this multimode space can be written as:

$$|n_1 : 1\rangle \otimes |n_2 : 2\rangle \otimes ...|n_N : N\rangle \equiv |n_1 : 1, n_2 : 2, ..., n_N : N\rangle \tag{1.33}$$

In the previous expression we have denoted the single mode state as $|n_l : l\rangle$ where n_l represents the number of photons in the l mode. If the multimode basis can be expressed as a factorized state (Equation 1.33), the density operator $\hat{\rho}$ of the multimode state reads:

$$\hat{\rho} = \widehat{\rho_1} \otimes \widehat{\rho_2} \otimes ... \otimes \widehat{\rho_N} \tag{1.34}$$

where:

$$\hat{\rho}_l = \sum_{n_l} p_l |n_l : l\rangle\langle n_l : l| \tag{1.35}$$

In this case the density matrix of the N-mode state is hence the product of the single mode density matrixes.

However, due to the possibility of performing superpositions between different modes, there is much more "space" in the multimode Hilbert space. For this reason, the factorized basis of Equation 1.33 is generally not a complete one. For example, a single photon can be shared between two different mode states (m and n), i.e. it can live in a multimode superposition of the form:

$$\frac{1}{\sqrt{2}}(|0:m\rangle + |1:n\rangle) \tag{1.36}$$

This state is called *entangled* if no change of the basis exists such that the state is mapped onto a factorized one (Equation 1.33). Entangle states are generated whenever an interaction between the modes is allowed [2], i.e. when dealing with interacting quantum systems. For example, the decay of an excited atomic state generates a continuous superposition of one-photon states, where an infinite number of modes share a single photon.

The description of a multimode interacting optical state can be significantly simplified in the case of *gaussian* light states, i.e. states in which the probability distribution of the field canonical variables $\widehat{P}$ and $\widehat{Q}$ (Equation 1.7) is gaussian. A gaussian state is completely characterized by second-order momenta[5] and can be completely described by mean of its covariance matrix $C_{ij}(\omega_i, \omega_j)(\phi_i, \phi_j)$ [1]:

$$C_{ij}(\omega_i,\omega_j)(\phi_i,\phi_j) = \begin{pmatrix} \sigma^2(\widehat{X}_1(\omega_1))(\phi_1) & \dots & \langle \widehat{X}_1(\omega_1)\widehat{X}_N(\omega_N)\rangle(\phi_1,\phi_N) \\ \vdots & \ddots & \vdots \\ \langle \widehat{X}_N(\omega_N)\widehat{X}_1(\omega_1)\rangle(\phi_N,\phi_1) & \dots & \sigma^2(\widehat{X}_N(\omega_N))(\phi_N) \end{pmatrix} \tag{1.37}$$

where $\widehat{X}_i(\omega_i)(\phi_i)$ is the single mode phase-dependent quadrature operator defined in Equation 1.9. The number of elements of the covariance matrix is $2N \times 2N$ and represent the dimension of the basis of a gaussian state with N modes. We underline that the factor 2 accounts for the fact that for each matrix element amplitude and phase have to be given.

The diagonal terms of the covariance matrix account for single mode fluctuations, while the off-diagonal ones encode correlations between modes of different frequency. Multimode quantum correlations are possible since quadratures belonging to different modes commute:

$$\left[\widehat{X}_i(\omega_i), \widehat{X}_j(\omega_j)\right] = 0 \tag{1.38}$$

and can be hence measured simultaneously [1].

We stress that in this framework we are considering multimode correlations up to second order, thus neglecting correlations involving more than two frequency components. Therefore, without loss of generality, we can consider only two modes inside the broadband pulse (with indexes i and j) and subsequently calculate the two-modes covariance matrix as follows:

$$C_{ij}(\omega_i,\omega_j)(\phi_i,\phi_j) = \begin{pmatrix} \sigma^2(\widehat{X}_i(\omega_i))(\phi_i) & \langle \widehat{X}_i(\omega_i)\widehat{X}_j(\omega_j)\rangle(\phi_i,\phi_j) \\ \langle \widehat{X}_j(\omega_j)\widehat{X}_i(\omega_i)\rangle(\phi_j,\phi_i) & \sigma^2(\widehat{X}_j(\omega_j))(\phi_j) \end{pmatrix} \tag{1.39}$$

The elements of the covariance matrix can be measured trough homodyne detection whose formalism has to be adapted in order to describe multimode

[5]For a gaussian state, momenta higher than the second order ones can always be expressed as a function of the second order ones.

interference. Supposing both the signal and the local oscillator to be in multimode states, the homodyne photocurrent operator reads:

$$\hat{I} = \sum_j \hat{a}_j^\dagger \hat{b}_j e^{i\phi_j} + \hat{b}_j^\dagger \hat{a}_j^\dagger e^{-i\phi_j} \tag{1.40}$$

In Appendix A we will prove that no contribution derives from mixed frequency terms, i.e. interference occurs only between modes of the same frequency. Consequently, the mean multimode current is (cfr Equation 1.18):

$$\langle \hat{I} \rangle = \sqrt{2} \sum_j |z_j| \langle \hat{X}_{\phi_j} \rangle \tag{1.41}$$

which, in the case of a signal in a classical coherent state, becomes:

$$\langle \hat{I} \rangle = 2 \sum_j |\alpha_j||z_j| \cos(\phi_j) \tag{1.42}$$

The multimode variance instead reads:

$$\sigma^2 \left[\hat{I} \right] = \sqrt{2}\sigma^2 \left[\sum_j \left(|z_j| \hat{X}_{\phi_j} \right) \right] \tag{1.43}$$

The previous equations have a fundamental consequence: if we are able to select a **single frequency** of the local oscillator (i.e. a mode $\hat{b}_j$) we can drive the the homodyne interference to select only the response of the corresponding mode of the signal field (Figure 1.5) and therefore reconstruct in a **frequency-resolved** scheme the mean quadratures of each signal mode and its phase-resolved statistics. These single mode fluctuations correspond to the diagonal terms of the covariance matrix (Equation 1.39).

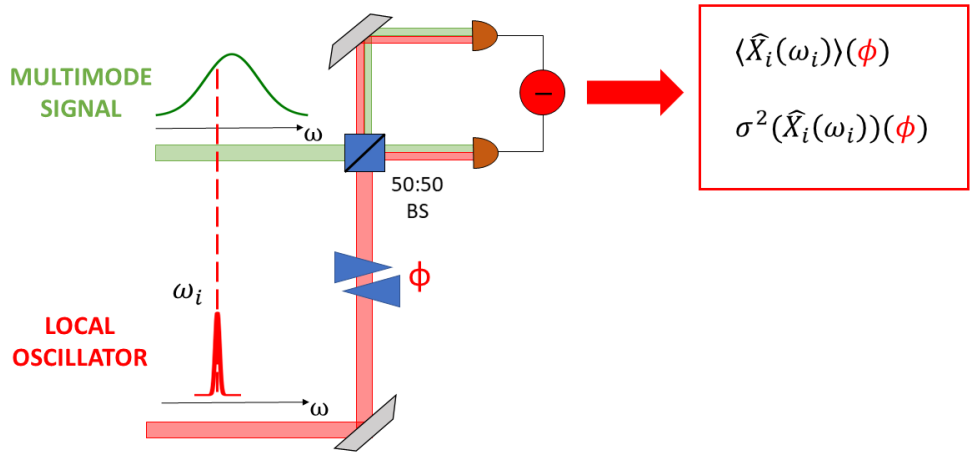

Figure 1.5: Multimode homodyne with a single frequency local oscillator. As a consequence of Equation 1.40, the selection of the local oscillator frequency drives the selection of the signal quadrature component at the same frequency and of its variance. The latter is linked to the diagonal terms of the covariance matrix of the multimode signal. We have neglected the dependence of the phase shift on the LO frequency by setting a frequency-independent phase delay ϕ.

Conversely, by working with a **multiple shaped** local oscillator (Figure 1.6) we can have access to the joint statistics of the corresponding signal modes ($\sigma^2(\widehat{X}_i(\omega_i) + \widehat{X}_j(\omega_j))$). This joint statistics encode instrinsic multimode effects, such as two-modes correlations, and can be exploited to reconstruct the off-diagonal terms of the covariance matrix through the following relation:

$$\langle \widehat{X}_i(\omega_i)\widehat{X}_j(\omega_j)\rangle(\phi) = \sigma^2(\widehat{X}_i(\omega_i) + \widehat{X}_j(\omega_j))(\phi) - \sigma^2(\widehat{X}_i(\omega_i))(\phi) - \sigma^2(\widehat{X}_j(\omega_j))(\phi) \tag{1.44}$$

In the previous equation $\sigma^2(\widehat{X}_i(\omega_i)$ and $\sigma^2(\widehat{X}_j(\omega_j)$ represent the phase-dependent single mode quadrature variance obtained through the homodyne measurement with a single LO frequency (Figure 1.5). Conversely, $\sigma^2(\widehat{X}_i(\omega_i) + \widehat{X}_j(\omega_j))(\phi)$ is the homodyne current variance measured in the case of a two mode-shaped local oscillator (Figure 1.6). In all the previous relations we have neglected the dependence of the phase shift on the frequency of the local oscillator. Indeed we have set a global frequency-independent phase delay ϕ.

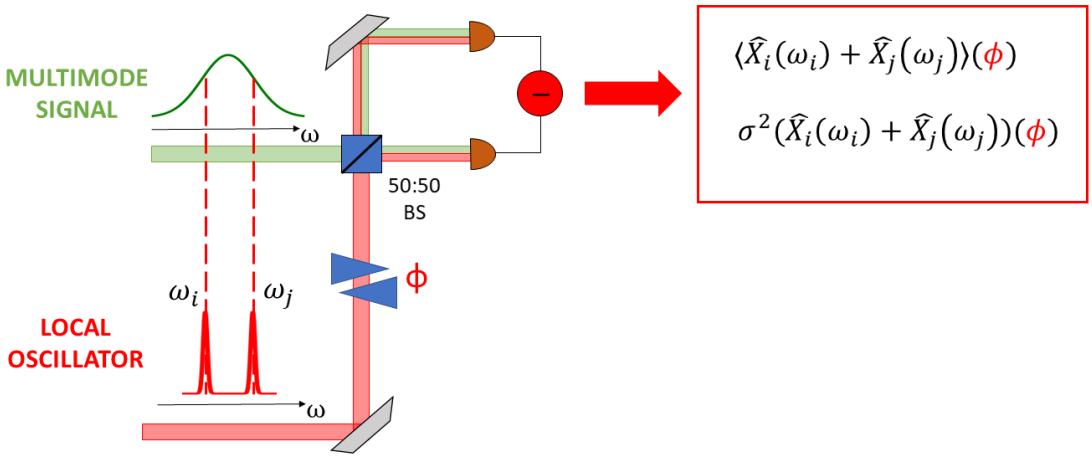

Figure 1.6: Multimode homodyne with a double frequency local oscillator. The sum of the corresponding quadrature components of the signal can be measured, as well as their joint statistics. Through Equation 1.44 the latter can be used to calculate the off-diagonal terms of the covariance matrix, related to two-modes quantum correlations. We have neglected the dependence of the phase shift on the LO frequency by setting a frequency-independent phase delay ϕ.

Chapter 2

Theoretical framework of photon-phonon interaction

In Chapter 1 we have provided the theoretical framework in which the detection of quantum light states is inserted. In particular, we have seen that through the innovative scheme of *multimode homodyne detection* we are able to address all the statistical information encoded in each mode of the optical state under investigation.

The purpose of the thesis goes beyond the description of optical states by themselves. It indeed focuses on how they couple to collective excitations in condensed matter systems, allowing to disclose information on their dynamics. In this thesis, we have addressed the coherent evolution of lattice vibrations in solids, which are commonly dubbed *coherent phonons*. The typical approach to track coherent phonon dynamics is the *pump-probe* one. With this approach, a first intense pulse (*pump*) excites collective nuclear vibrations in the sample lattice, which were initially in a thermal ground state. These nuclear modes will modulate the atomic structure and, consequently, its optical properties. These are observed employing another ultrashort pulse, the *probe*.

While in standard pump-probe spectroscopy the optical observable is the probe intensity, with multimode homodyne detection we are able to selectively address each probe mode response in both its phase and amplitude and eventually reconstruct the full emitted field resulting from photon-phonon interaction.

In this chapter we provide the theoretical framework in which photon-phonon interaction is inserted. We will start with a classical picture and then move to a more fundamental quantum formalism [4]. In this chapter we will focus only on mean value features of the probe pulse (amplitude and phase) imprinted through its interaction with the excited phonon.

2.1 Classical formalism

In this section we study the photon-phonon interaction in a classical picture. In this framework, the phonon modes are treated as classical harmonic oscillators driven by a force exerted by a multimode electromagnetic field. We will analyse in detail how an optical pulse can be coupled with the vibrational degrees of freedom and disclose information on their dynamics.

2.1.1 Optical driving force

Optical phenomena can be interpreted as the effect of the interaction between the electric field components of an electromagnetic radiation and the charged particles inside the target material. In visible and near-infrared range ($\sim 10^2$ THz) the interaction is dominated by the coupling of the electric field with electrons, since the frequencies involved are too high for the nuclei to follow adiabatically the optical field oscillations [5]. In this regime the driving electric field couples with the electrons inducing dipole moments whose amplitude varies according to the strength of the bond with the nuclei. This microscopic effect can be mapped into a macroscopic one, that is the onset of a time-dependent macroscopic polarization, that, for an electric field with λ' polarization, reads:

$$P_\lambda(\boldsymbol{x},t) = \epsilon_0 \sum_{\lambda\lambda'} \chi_{\lambda\lambda'} E_{\lambda'}(\boldsymbol{x},t) \tag{2.1}$$

Although it is the electrons that are set in motion by the visible or near-IR optical fields, their oscillatory motion contains information about the motion of nuclei. The reason for this is that the adiabatic-electronic potential depends on the nuclear coordinate [5]. Therefore, even if the optical pulse can be coupled only with the electronic degrees of freedom, it can be used to disclose information about the nuclei vibrational modes, since the latter will modulate the electronic polarizability $\epsilon_0\boldsymbol{\chi}$. In the presence of a single nuclear mode inducing a tiny atomic displacement and far from any electronic transitions, we can expand the electronic susceptibility in terms of the nuclear positions q_n:

$$\chi_{\lambda\lambda'}(q_n) \simeq \chi^{(0)}_{\lambda\lambda'} + \left(\frac{\delta\chi}{\delta q_n}\right)_{\lambda\lambda'}\Bigg|_{q_n=0} q_n \tag{2.2}$$

In this expansion, $\chi^{(0)}_{\lambda\lambda'}$ represents the static susceptibility in the absence of any nuclear mode excitation. This term rules all the static refractive effects of the sample, such as birefringence and polarization rotation. The term $(\delta\boldsymbol{\chi}/\delta q_n)|_{q_n=0}$ can be instead interpreted as the cross-section of the interaction process, since it represents the strength of the coupling between nuclear and electronic coordinates [5]. The presence of a nuclear mode excitation (phonon) therefore leads to the onset of a polarization that oscillates following the position of the nuclei. The energy required to establish this polarization is:

$$U(\boldsymbol{x},t) = -\boldsymbol{P}(\boldsymbol{x},t)\cdot\boldsymbol{E}(\boldsymbol{x},t) = -\epsilon_0 \sum_{\lambda\lambda'} \chi_{\lambda\lambda'} E_\lambda(\boldsymbol{x},t) E_{\lambda'}(\boldsymbol{x},t) \tag{2.3}$$

From this expression of the interaction energy we can subsequently evaluate the force exerted by the driving optical field $\boldsymbol{E}(\boldsymbol{x},t)$ along the n^{th} normal mode coordinate of the phonon:

$$F_n(\boldsymbol{x},t) = -\frac{dU_{phot-phon}(\boldsymbol{x},t)}{dq_n} = \epsilon_0 \sum_{\lambda\lambda'} \left(\frac{\delta\chi}{\delta q_n}\right)_{\lambda\lambda'}\Bigg|_{q_n=0} E_\lambda(\boldsymbol{x},t) E_{\lambda'}(\boldsymbol{x},t) \tag{2.4}$$

Let us start with a simplified situation in which the optical driving field $\boldsymbol{E}(\boldsymbol{x},t)$ is a superposition of only two frequency components ω_1 and ω_2 far from any electronic resonance but whose difference $\omega_v = \omega_2 - \omega_1$ can match a phonon

excitation mode Ω. We will model these two incoming fields as plane waves propagating along z direction of the form:

$$\boldsymbol{E}_i(z,t) = \boldsymbol{A}_i e^{-i\omega_i\left(t-\frac{n}{c}z\right)} = \boldsymbol{A}_i e^{-i\omega_i t'} \qquad i = 1,2 \tag{2.5}$$

where the spatial dependence on the propagation length z has been included inside the term $t' = t - nz/c$. Moreover, let us treat the phonon as a classical harmonic oscillator with proper frequency Ω initially at rest. The combined time-dependent action of these two electric fields will perturb the electron cloud whose oscillations will exert a force along the nuclear coordinates, thus exciting the nuclear mode. In this classical framework, the previous process is described as an harmonic oscillator driven by the force exerted by the combined action of the two electric fields ($F_n(t')$). The equation of motion describing this process is:

$$\frac{dq_n(t')}{dt'} + \Omega^2 q_n(t') = \frac{F_n(t')}{m} \tag{2.6}$$

and its solution for the phonon oscillation has an amplitude $q_n(\omega_v)$ that reads:

$$q_n(\omega_v) = \frac{1}{m}\epsilon_0 \sum_{\lambda\lambda'} \left(\frac{\delta\chi}{\delta q_n}\right)_{\lambda\lambda'}\Bigg|_{q_n=0} \frac{A_1^{\lambda} A_2^{\lambda'*}}{\omega_v^2 - \Omega^2} \tag{2.7}$$

The previous expression shows that the extent of the forced nuclear oscillations is proportional to the amplitude of the two applied fields, to the magnitude of the coupling between the nuclear coordinate and the electronic polarizability ($(\delta\boldsymbol{\chi}/\delta q_n)|_{q_n=0}$) and it is resonantly enhanced when $\omega_v = \omega_2 - \omega_1 = \Omega$, i.e. when the frequency difference between the two driving fields matches the phonon one[1].

Having in mind this picture, let us now move to the case of an excitation driven by a multimode field. This case represents our experimental situation, since we employ ultrashort laser pulses. We model this multimode electric field as a coherent sum of plane waves:

$$\boldsymbol{E}(z,t) = \sum_{\omega} \boldsymbol{E}_{\omega} e^{-i\omega\left(t-\frac{n}{c}z\right)} + c.c = \sum_{\omega} \boldsymbol{E}_{\omega} e^{-i\omega t'} + c.c \tag{2.8}$$

Here and in all the following calculations we will use phase-matching conditions, assuming that before the interaction all the frequencies inside the pulse have the same phase. In this case, the force exerted along the n^{th} nuclear mode coordinate is:

$$F_n(t') = \epsilon_0 \sum_{\lambda\lambda'} \left(\frac{\delta\chi}{\delta q_n}\right)_{\lambda\lambda'}\Bigg|_{q_n=0} \left(\sum_{\omega} E_{\omega}^{\lambda} e^{-i\omega t'} + c.c\right)\left(\sum_{\omega'} E_{\omega'}^{\lambda'} e^{-i\omega' t'} + c.c\right) \tag{2.9}$$

However, we have notice (Equation 2.7) that phonon oscillations are resonantly enhanced by modes inside the impinging pulse whose frequency difference equals Ω. Therefore we can safely limit the multimode sum to the fields of frequency ω and $\omega \pm \Omega$. With this assumption, the resulting time-dependent force along the n^{th} phonon mode coordinate turns out to be:

$$F_n(t') = 2\epsilon_0 \sum_{\lambda\lambda'} \left(\frac{\delta\chi}{\delta q_n}\right)_{\lambda\lambda'}\Bigg|_{q_n=0} \sum_{w} E_{\omega}^{\lambda}\left(E_{\omega+\Omega}^{\lambda'} + E_{\omega-\Omega}^{\lambda'}\right)\cos(\Omega t') \equiv f_n \cos(\Omega t') \tag{2.10}$$

[1] In the resonant case $\omega_v = \omega_2 - \omega_1 = \Omega$ the amplitude diverges only because we have not taken into account the finite time application of the force.

The driving force therefore oscillates at the same frequency of the considered phonon mode and has an amplitude that depends on the cross-section of the interaction process ($(\delta\chi/\delta q_n)_{\lambda\lambda'}|_{q_n=0}$) and on the amplitudes of the exciting optical fields, i.e. all the pairs differing in frequency by Ω.

2.1.2 Pump-probe dynamics

Until now we have shown that by mean of a multimode pulse we can excite a nuclear mode oscillation. Indeed, the electric fields inside the incoming pulse differing in frequency by the phonon one couples themselves originating a periodic force that set in motion the nuclei.

In this section we will model in a classical framework the pump-probe experiment. As shown in Figure 2.1, the pump-probe approach enables to map the phonon evolution into the spectral modification of a second pulse (*probe*) interacting with the sample at a variable delay from the excitation. These probe spectral changes are commonly detected by means of intensity measurements.

In the present thesis we adopt an innovative approach. Indeed, we monitor them through multimode homodyne detection. With this frequency-resolved interferometric technique we can retrieve amplitude and phase dynamics of each probe mode and subsequently reconstruct the phonon field.

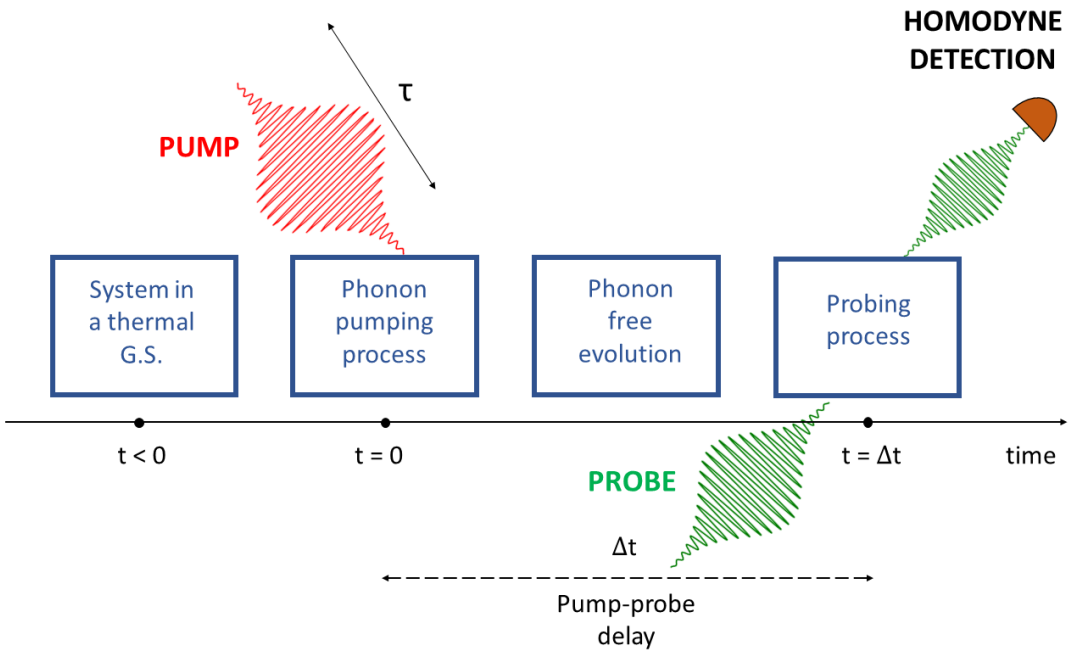

Figure 2.1: Schematic description of the pump-probe experiment. The pump induces a coherent vibrational excitation on the thermal phonon ground state. The latter is probed through homodyne detection at a variable delay Δt from the pump arrival.

Let us starting by modelling the pumping process and by retrieving the time evolution of the excited phonon position $q_n(t')$ resulting from the sudden interaction. In order to do this we solve the equation of motion of the driven harmonic oscillator (Equation 2.6) in the case of a sudden application of the force described

in 2.10 for a time τ. This interaction time τ is shorter than the phonon evolution period ($\sim$ 0.3 ps) and we set it comparable with the pump duration ($\sim$ 100 fs). Moreover, since we suppose that there are no excited nuclear modes before the pump interaction, we set the initial phonon amplitude to zero. By defining the amplitude of the pump force:

$$f_n^{pump} = 2\epsilon_0 \sum_{\lambda\lambda'} \left(\frac{\delta\chi}{\delta q_n}\right)_{\lambda\lambda'} \Bigg|_{q_n=0} \sum_w E_\omega^{\lambda\, pump} \left(E_{\omega+\Omega}^{\lambda'\, pump} + E_{\omega-\Omega}^{\lambda'\, pump}\right) \tag{2.11}$$

the solution of the equation of motion reads [15]:

$$q_n(t') = \frac{\tau f_n^{pump}}{2\Omega m} \sin(\Omega t') \tag{2.12}$$

As in [15] we set a sine function for the phonon position dynamics since the instant of the maximum cosine force (Equation 2.10) is the one when to the vibration is imparted the maximum momentum (Figure 2.2). This periodic lattice

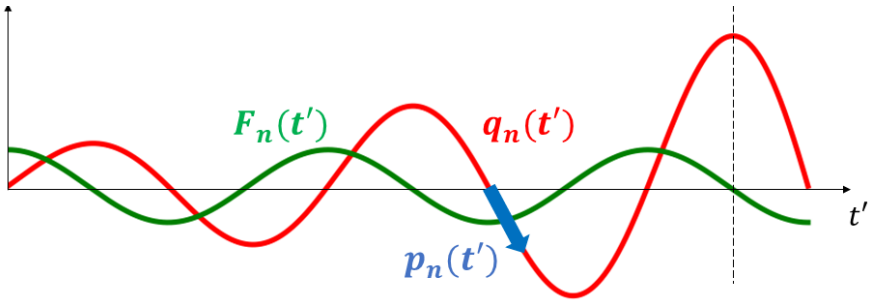

Figure 2.2: Time evolution of phonon position $q_n(t')$ resulting from the instantaneous application of the periodic force $F_n(t')$. As in [15] we set a sine function for the phonon position oscillations since the instant of the maximum driving force has to correspond with the maximum induced momentum $p_n(t')$.

deformation will consequently affect the electronic susceptibility, by making it oscillate in phase with the pump excited phonon:

$$\chi_{\lambda\lambda'}(t') = \chi_{\lambda\lambda'}^{(0)} + \left(\frac{\delta\chi}{\delta q_n}\right)_{\lambda\lambda'} \Bigg|_{q_n=0} \frac{\tau f_n^{pump}}{2\Omega m} \sin(\Omega t') \tag{2.13}$$

Starting from the previous equation, we can now express the force on the n^{th} mode as in 2.11 and, by using the notation $(\delta\chi/\delta q_n)_{\lambda\lambda'}\,|_{q_n=0} \equiv (\delta\chi/\delta q_n)^0_{\lambda\lambda'}$, we obtain:

$$\begin{aligned}\chi_{\lambda\lambda'}(t') =& \chi_{\lambda\lambda'}^{(0)} + \\ &+ \frac{\epsilon_0\tau}{\Omega m} \sum_{\mu\mu'} \left(\left(\frac{\delta\chi}{q_n}\right)^0_{\mu\mu'} \left(\frac{\delta\chi}{q_n}\right)^0_{\lambda\lambda'} \sum_w E_\omega^{\mu\, pump} \left(E_{\omega+\Omega}^{\mu'\, pump} + E_{\omega-\Omega}^{\mu'\, pump}\right) \right) \sin(\Omega t')\end{aligned} \tag{2.14}$$

The previous expression is crucial for the description of the spectral variations imprinted in the probe, since it rules the phonon-dependent optical properties. In particular, we underline that the nuclear mode-dependent dynamics is ruled by

the four rank non-linear susceptibility tensor $(\delta\chi/\delta q_n)^0_{\mu\mu'}(\delta\chi/\delta q_n)^0_{\lambda\lambda'}$, disclosing the fact that the phonon-dependent polarization response is non-linear.

In order to retrieve the spectral changes undergone by the probe pulse propagating in a media with a non-linear phonon-dependent susceptibility, let us start by the classical wave equation in a medium with no free charges:

$$\nabla^2\boldsymbol{E}(z,t) - \frac{1}{c^2}\frac{\partial^2\boldsymbol{E}(z,t)}{\partial t^2} = \frac{1}{c^2}\frac{\partial^2\left(\chi(q)\boldsymbol{E}(z,t)\right)}{\partial t^2} \tag{2.15}$$

Here, for simplicity, we have used the scalar formulation for $\chi(q)$ and considered a single nuclear mode, thus neglecting the n index:

$$\chi(q) \simeq \chi^{(0)} + \left(\frac{\delta\chi}{\delta q}\right)\Big|_{q=0} q \equiv \chi^{(0)} + \left(\frac{\delta\chi}{\delta q}\right)^0 q \tag{2.16}$$

We will show in the following that there are mainly two effects on the probe pulse propagating through the pumped sample: **Linear Refractive Modulation** (**LRM**) and **Impulsive Stimulated Raman Scattering** (**ISRS**) [4].

The first amounts to the modulation of the refractive index due to to the instantaneous position of the nuclei and does not involve an energy exchange among probe modes, while the latter produces a spectral shift among the phonon-coupled probe modes. We underline that these effects both results from a non-linear response in the electronic susceptibility. The term *linear* inside LMR is only used to clarify that in this process no probe frequency mixing occurs.

In the following we will separately study the two effects in a classical framework and, by mean of the homodyne formalism, we will retrieve in the two cases the amplitude and phase pump-probe dynamics for each probe frequency.

Linear refractive modulation (LRM)

Let us start by recalling the classical wave equation 2.15 describing the probe electric field propagating through the excited sample:

$$\nabla^2\boldsymbol{E}(t') - \frac{n^2}{c^2}\frac{\partial^2\boldsymbol{E}(t')}{\partial t^2} = \frac{1}{c^2}\left(\frac{\delta\chi}{\delta q}\right)^0\frac{\partial^2\left(q(t')\boldsymbol{E}(t')\right)}{\partial t^2} \tag{2.17}$$

Since the probe pulse impinges on the sample at a variable time Δt from the the pump excitation, we have to evaluate the nuclear displacement at $t' + \Delta t$:

$$\nabla^2\boldsymbol{E}(t') - \frac{n^2}{c^2}\frac{\partial^2\boldsymbol{E}(t')}{\partial t^2} = \frac{1}{c^2}\left(\frac{\delta\chi}{\delta q}\right)^0\frac{\partial^2\left(q(t'+\Delta t)\boldsymbol{E}(t')\right)}{\partial t^2} \tag{2.18}$$

If we now group all the terms containing the second time derivative of the probe field, we get a wave equation with a time-dependent index of refraction $\tilde{n}(\Delta t)$ that, if we consider $t' = 0$ as the pump excitation time, reads:

$$\tilde{n}(\Delta t) = \sqrt{n^2 + \left(\frac{\delta\chi}{\delta q}\right)^0 q(\Delta t)} \tag{2.19}$$

Since the modulation of the electronic susceptibility induced by the nuclear mode is small compared with the equilibrium one, we can Taylor expand the modulated refraction index $\tilde{n}(\Delta t)$ obtaining:

$$\tilde{n}(\Delta t) \simeq n\left(1 + \frac{1}{2n^2}\left(\frac{\delta\chi}{\delta q}\right)^0 q(\Delta t)\right) \tag{2.20}$$

Now the question is: how this periodic modulation of the sample refractive properties affects phase and amplitude of the electric fields of each probe mode?

In our experiment these observable are detected in a frequency-resolved scheme trough the measurement of the mean homodyne current. For this reason, let us recall the expression of the classical multimode homodyne current (Equation 1.42) that, under the hypothesis of a phase-matched local oscillator, reads:

$$I(\Delta t) = 2\sum_j |z_j||E_j(\Delta t)| \cos\left(\phi_j - \phi_j^T(\Delta t)\right) \tag{2.21}$$

Here we have denoted with $E_j(\Delta t)$ the j^{th} mode of the emitted probe field and with $\phi_j^T(\Delta)$ its phase. The modulation of the refraction index ruled by Equation 2.20 affects both the amplitude and the phase of the transmitted probe, in accordance with the following equations[2]:

$$\phi_j^T(\Delta t) = \tilde{n}(\Delta t)\frac{\omega_j}{c}z = n\frac{\omega_j}{c}z + \frac{\omega_j z}{2nc}\left(\frac{\delta\chi}{\delta q}\right)^0 q(\Delta t) \tag{2.22}$$

$$|E_j(\Delta t)| = |E_j^{inc}|\frac{2}{1+\tilde{n}(\Delta t)} \simeq |E_j^{inc}|\frac{1}{1+n}\left(1 - \frac{1}{2n(1+n)}\left(\frac{\delta\chi}{\delta q}\right)^0 q(\Delta t)\right) \tag{2.23}$$

These trends will subsequently cause a time-dependent variation of phase and amplitude of the field quadrature, that is the observable measured through homodyne. These detectable shifts induced by the phonon dynamics take the form:

$$\begin{aligned}\Delta\phi_j(\Delta t) &= \frac{\omega_j z}{2nc}\left(\frac{\delta\chi}{\delta q}\right)^0 q(\Delta t) \\ &= \frac{\omega_j z}{2nc}\left(\frac{\delta\chi}{\delta q}\right)^0 \frac{\tau f^{pump}}{2\Omega m}\sin(\Omega\Delta t)\end{aligned} \tag{2.24}$$

$$\begin{aligned}\Delta A_j(\Delta t) &= |z_j||E_j^{inc}|\frac{1}{n(1+n)}\left(\frac{\delta\chi}{\delta q}\right)^0 q(\Delta t) \\ &= |z_j||E_j^{inc}|\frac{1}{n(1+n)}\left(\frac{\delta\chi}{\delta q}\right)^0 \frac{\tau f^{pump}}{2\Omega m}\sin(\Omega\Delta t)\end{aligned} \tag{2.25}$$

In summary, the pump induces a time-dependent modulation of the refractive index of the sample in phase with the phonon oscillations. Therefore, as a function of the pump-probe delay Δt, the probe pulse will experience different refractive conditions. This results in an oscillation of the phase and amplitude of the transmitted probe field in phase with the nuclear displacement.

[2]For the amplitude of the transmitted electric field we have exploited the Fresnel equation in the case of normal incidence.

Furthermore, we note that the phase dynamics is only sensitive to the pump power through f^{pump} and it does not depend on the probe intensity. Conversely, the time-dependent amplitude shift is affected by both the pump and the probe power. In particular, it scales linearly with the amplitude of the incoming probe field.

Impulsive stimulated Raman Scattering (ISRS)

As previously stated, the refractive modulation is not the only spectral modification undergone by the probe pulse. We expect indeed that by changing the phase between the phonon and the force exerted by the probe pulse (ie. by controlling Δt) we can dynamically force or dump the atomic oscillations. In the former case the optical pulse will leave energy to the vibrational degrees of freedom, while in the latter it will gain energy from them. For this reason, we expect a time-dependent modification of the amplitude of the phonon-coupled optical modes. We will refer to this effect as *Impulsive Stimulated Raman* (ISRS). For modelling it, let us recall the wave equation 2.18 describing the emitted probe field $\boldsymbol{E}(t')$:

$$\nabla^2 \boldsymbol{E}(t') - \frac{n^2}{c^2}\frac{\partial^2 \boldsymbol{E}(t')}{\partial t^2} = \frac{1}{c^2}\left(\frac{\delta\chi}{\delta q}\right)^0 \frac{\partial^2 \left(q(t'+\Delta t)\boldsymbol{E}(t')\right)}{\partial t^2} \tag{2.26}$$

By changing the variable of the derivative from t to $t' = t - zn/c$ and by integrating the wave equation in the spatial domain with the boundary condition $\boldsymbol{E}(z = 0, t') = \boldsymbol{E}^{inc}(t')$ we get:

$$-2\frac{n}{c}\left(\frac{\partial \boldsymbol{E}(t')}{\partial t'} - \frac{\partial \boldsymbol{E}^{inc}(t')}{\partial t'}\right) = \frac{z}{c^2}\left(\frac{\delta\chi}{\delta q}\right)^0 \frac{\partial^2 \left(q(t'+\Delta t)\boldsymbol{E}(t')\right)}{\partial t'^2} \tag{2.27}$$

We can now integrate also in the t' variable. Assuming a that the polarizability modulation is much smaller then the equilibrium one, we can approximate $\boldsymbol{E}(t')$ with $\boldsymbol{E}^{inc}(t')$ in the r.h.s. of the Equation 2.27 and thus, after the integration, we obtain [15]:

$$\boldsymbol{E}(t') - \boldsymbol{E}^{inc}(t') = -\frac{z}{2nc}\left(\frac{\delta\chi}{\delta q}\right)^0 \frac{\partial\left(q(t'+\Delta t)\boldsymbol{E}^{inc}(t')\right)}{\partial t'} \tag{2.28}$$

Since we want to analyse the spectral modification of the probe pulse as a consequence of its sudden interaction with the excited phonon, it is useful to rewrite the fields inside Equation 2.28 in Fourier domain:

$$\boldsymbol{E}(\omega) = \int dt \boldsymbol{E}_\omega e^{i\omega t} \tag{2.29}$$

By substituting this Fourier expansion of the field inside 2.28 and recalling that nuclear displacement induced by the sudden interaction with the pump is ruled by Equation 2.12

$$q(t'+\Delta t) = \frac{\tau f^{pump}}{2\Omega m}\sin(\Omega(t'+\Delta t))$$

we get:

$$\boldsymbol{E}_\omega(\Delta t) - \boldsymbol{E}^{inc}_\omega = \frac{z}{4nc}\left(\frac{\delta\chi}{\delta q}\right)^0 \frac{\tau f^{pump}}{2\Omega m}\omega\left(\boldsymbol{E}^{inc}_{\omega+\Omega}e^{-i\Omega\Delta t} - \boldsymbol{E}^{inc}_{\omega-\Omega}e^{i\Omega\Delta t}\right) \tag{2.30}$$

Let us now link the expression of the emitted field with the homodyne current equation. In the hypothesis of a phase-matched local oscillator and since the propagation of the electric field is along z ($\boldsymbol{E}_\omega(z) \equiv E_\omega$), the current reads (Equation 1.42):

$$I(\Delta t) = 2\sum_j |z_j||E_j(\Delta t)|\cos(\phi_j - \phi_j^T(\Delta t)) \tag{2.31}$$

where we have denoted with ϕ_j^T the phase of the j^{th} emitted field mode ruled by the modulated refractive index $\tilde{n}$.

We want now to explore how the Raman process affects the amplitudes of the phonon-coupled modes and compare it with the LRM case. By labelling the frequencies inside the pulse as: $\omega_j = \omega_0 + j\delta, -J \leq j \leq +J$ and supposing that before the interaction the probe is in phase-matched state (i.e. $E_j^{inc} = |E_j^{inc}|$), the amplitude of the j^{th} emitted field mode up to first order in $(\delta\chi/\delta q)^0$ reads:

$$|E_j(\Delta t)| = \sqrt{|E_j^{inc}|^2 + \frac{z}{4nc}\left(\frac{\delta\chi}{\delta q}\right)^0 \frac{\tau f^{pump}\omega_j}{2\Omega m}|E_j^{inc}|\left(|E_{j+\frac{\Omega}{\delta}}^{inc}| - |E_{j-\frac{\Omega}{\delta}}^{inc}|\right)\cos(\Omega\Delta t)} \tag{2.32}$$

Since we expect the spectral amplitude variation to be much smaller than the incident one, we can Taylor expand the emitted amplitude, obtaining:

$$|E_j(\Delta t)| \simeq |E_j^{inc}| + \frac{z}{8nc}\left(\frac{\delta\chi}{\delta q}\right)^0 \frac{\tau f^{pump}\omega_j}{2\Omega m}\left(|E_{j+\frac{\Omega}{\delta}}^{inc}| - |E_{j-\frac{\Omega}{\delta}}^{inc}|\right)\cos(\Omega\Delta t) \tag{2.33}$$

From the previous equation we clearly notice that ISRS is an intrinsic multimode process resulting from the interaction between different photon modes of the incident pulse. In particular, considering a gaussian distribution of the incoming probe mode around ω_0, we note that by changing the delay between the force exerted by the pump and the probe (i.e. by controlling Δt) we have two different situations:

- $\boldsymbol{\Omega\Delta t = 0}$: the force induced by the probe is in phase with the one induced by the pump. Since the nuclear oscillations is $\pi/2$-shifted with respect to the pump force (Eqs. 2.10, 2.12), by choosing $\Omega\Delta t = 0$ the probe is exerting a force on the phonon in phase with its velocity. Exploiting Equation 2.33, we see that in this case the probe modes with frequency greater than the central one ω_0 are suppressed (since $|E_{j+\frac{\Omega}{\delta}}^{inc}| - |E_{j-\frac{\Omega}{\delta}}^{inc}| < 0$) while the ones with frequency smaller than ω_0 are enhanced (since $|E_{j+\frac{\Omega}{\delta}}^{inc}| - |E_{j-\frac{\Omega}{\delta}}^{inc}| > 0$).

  This means that in this case the probe-phonon interaction is a stimulated Stokes process, that result in a red-shift of the pulse.

- $\boldsymbol{\Omega\Delta t = \pi}$: the force induced by the pump is anti-phase with respect to the phonon velocity. Conversely, in this case the probe modes with frequency less than ω_0 are suppressed, while the others are enhanced. Therefore, the probe-phonon interaction is a stimulated Anti-Stokes process that result in a blue-shift of the incoming pulse.

In our experiment, this amplitude dynamics resulting from ISRS can be monitored by measuring the homodyne current for each probe mode. Indeed, the differential

amplitude induced by the Raman is:

$$\Delta A_j(\Delta t) = |z_j| \frac{z}{4nc} \left(\frac{\delta\chi}{\delta q}\right)^0 \frac{\tau f^{pump} \omega_j}{2\Omega m} \left(|E^{inc}_{j+\frac{\Omega}{\delta}}| - |E^{inc}_{j-\frac{\Omega}{\delta}}|\right) \cos(\Omega \Delta t) \qquad (2.34)$$

We note that the ISRS-driven amplitude shift is sensitive to the incident probe intensity. Indeed, it scales linearly with amplitude of the incoming probe field.

In Figure 2.3 we summarize the phase and amplitude features imprinted on the probe pulse in case of a Raman dominated interaction. We note that while the phase temporal dynamics is ruled by the nuclear oscillations, the amplitude follows the phonon momentum and exhibits the Raman features previously described.

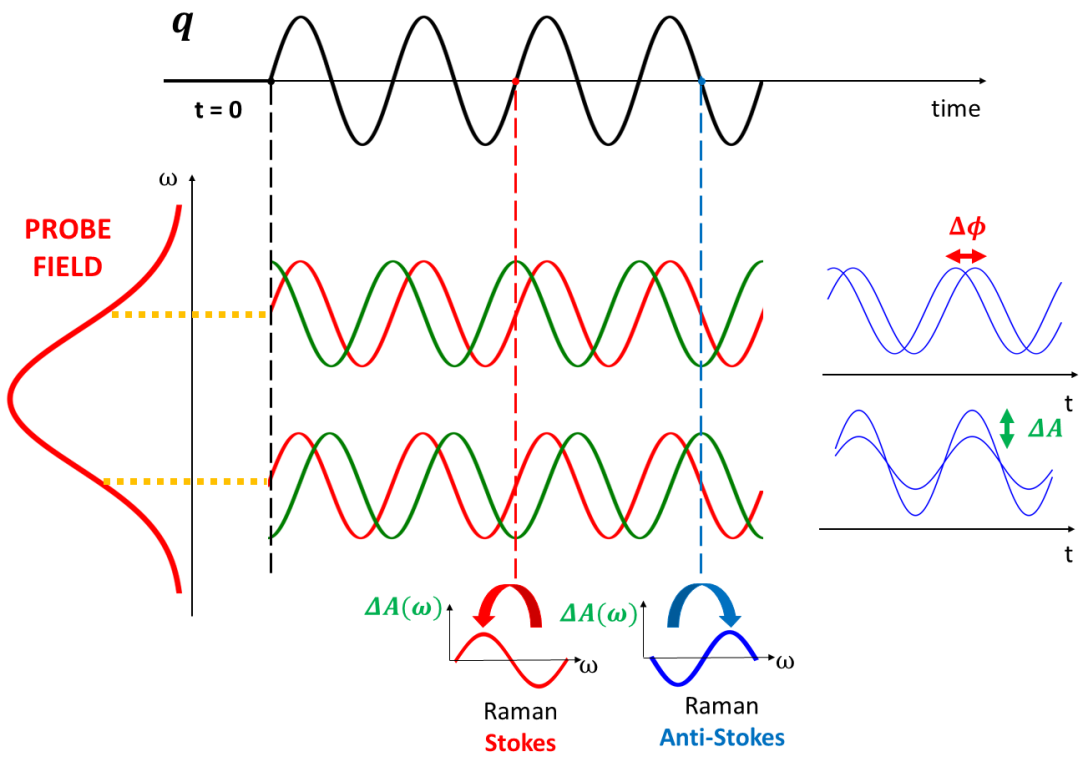

Figure 2.3: Schematic description of the temporal evolution of the probe spectral features in the case of ISRS probing process. In black we depict the phonon oscillations excited by the pump at $t = 0$, while in red and green the phase and amplitude shifts for two probe modes. ISRS causes a π-shift between the amplitude oscillations of modes with opposite frequency. This results in a time-dependent spectral shift among the probe modes that can be controlled through the pump-probe delay (red and blue dotted lines). Conversely, the phase shift follows the refractive modulation ruled by the phonon position q and in this limited energy range can be considered frequency-independent.

Finally, we underline that both LRM and ISRS are ruled by the four rank nonlinear susceptibility tensor $(\delta\chi/\delta q_n)^0_{\mu\mu'}$ $(\delta\chi/\delta q_n)^0_{\lambda\lambda'}$ (Equation 2.14) whose symmetry depends on the selected phonon and can be exploited to distinguish the two probing effects.

In particular, we expect ISRS not to change the polarization of the involved modes. Indeed, it is a stimulated process and the new photons are likely to be created in mode states initially occupied [21]. On the contrary, we expect LRM to be responsible for the polarization rotation of the probe modes. This indeed results from the anisotropy of the static electronic susceptibility.

2.2 Quantum model

In the previous section we have described the photon-phonon interaction in a classical picture, modelling both the optical and the vibrational degrees of freedom as classical harmonic oscillators. In this section we want to translate the classical language into a more fundamental quantum one.

The main reason of a fully quantum formalism of light-phonon interaction resides in the fact that it can be potentially applied also in more general situations where the classical model fails. This is the case of weak photon fields with quantum statistics. The model will permit us to go beyond the standard mean value approach, by opening the possibility of describing intrinsic quantum fluctuations imprinted on the probe pulse by the non-linear interaction and eventually multimode quantum correlations among the photon modes (Chapter 6). In this section we will preliminarly focus on mean value dynamics of the interacting photon field and retrieve from the quantum formalism the classical predictions.

In the previous section we have pointed out that the phonon-dependent optical response is determined by the modification of the electronic susceptibility ($(\delta\chi/\delta q)^0 q$) due to the lattice distortion (Equation 2.16). Therefore, the description of the probing process in a fully quantum formalism has to go through its quantization and through the contemporaney quantization of the optical field. In this section we achieve this purpose by treating both the optical and the elastic modes as quantum harmonic oscillators. Following the model presented in [4], we will translate the classical description of the photon-phonon interaction into a quantum formalism and derive the Hamiltonians describing LRM and ISRS. We will then exploit the homodyne formalism to retrieve the amplitude and phase mean dynamics of each optical mode induced by the separate action of the two Hamiltonians.

2.2.1 Derivation of the interaction Hamiltonian

The starting point for the quantum formulation is the photon-phonon interaction energy (Equation 2.3):

$$\begin{aligned} U(\boldsymbol{x},t) &= -\boldsymbol{P}(\boldsymbol{x},t)\cdot\boldsymbol{E}(\boldsymbol{x},t) \\ &= -\epsilon_0 \sum_{\lambda\lambda'} \chi_{\lambda\lambda'}(q_1,...,q_n) E_\lambda(\boldsymbol{x},t) E_{\lambda'}(\boldsymbol{x},t) \end{aligned} \tag{2.35}$$

Considering tiny nuclear displacements, the electronic susceptibility can be expanded as a function of the lattice normal mode coordinates q_n:

$$\begin{aligned}\chi_{\lambda\lambda'}(q_1,...,q_N) &\simeq \chi^{(0)}_{\lambda\lambda'} + \sum_{n=1}^{N}\left(\frac{\delta\chi}{\delta q_n}\right)_{\lambda\lambda'}\Bigg|_{q_n=0} q_n \\ &\equiv \chi^{0}_{\lambda\lambda'} + \sum_{n=1}^{N}\chi^{(1)}_{\lambda\lambda'}(n)\, q_n\end{aligned} \tag{2.36}$$

$\boldsymbol{\chi}^0$ is the static electronic susceptibility describing static refractive effects, such as birefringence and polarization rotation. $\boldsymbol{\chi}^{(1)}$ is instead the phonon modulated susceptibility whose components $\chi^{(1)}_{\lambda\lambda'}$ are assumed to be real and such that $\chi^{(1)}_{\lambda\lambda'} = \chi^{(1)}_{\lambda'\lambda}$. The fully quantum Hamiltonian ruling photon-phonon interaction is obtained by expressing the potential energy 2.35 in terms of the optical and elastic quantized fields.

The optical field is treated as a set of harmonic oscillators, each representing a radiation mode with a defined frequency $\omega_j = \omega_0 + j\delta, -J \leq j \leq +J$. Each optical mode is described through the operators $\widehat{a}^{\dagger}_{\lambda j}$ and $\widehat{a}_{\lambda j}$, representing respectively the creation and annihilation operators for the photons with frequency ω_j and polarization λ. They obey the bosonic commutation relation:

$$[\widehat{a}^{\dagger}_{\lambda j}, \widehat{a}_{\lambda' k}] = \delta_{\lambda\lambda'}\delta_{jk} \tag{2.37}$$

The λ-polarized quantized electric field can be subsequently written as a sum over all the single mode quantized fields and it reads:

$$\widehat{E}_{\lambda}(\boldsymbol{x},t) = i\sum_{j}\sqrt{\frac{\omega_j}{2V\epsilon_0}}\left(\widehat{a}_{\lambda j}e^{-i(\omega_j t - \boldsymbol{k}_j\cdot\boldsymbol{x})} - \widehat{a}^{\dagger}_{\lambda j}e^{i(\omega_j t - \boldsymbol{k}_j\cdot\boldsymbol{x})}\right) \tag{2.38}$$

In the expression of the quantized multimode electric field we have denoted with V the quantization volume and with $\boldsymbol{k}_j$ the propagation direction of the j^{th} mode component The elastic field describing the lattice distortion is analogously modelled as a set of harmonic oscillators, each representing a phonon mode. We denote with $\widehat{b}^{\dagger}_{\Omega_j,\boldsymbol{u}_n}$ and $\widehat{b}_{\Omega_j,\boldsymbol{u}_n}$ the creation and destruction operator of a phonon with frequency Ω_j propagating along the $\boldsymbol{u}_n$ normal mode coordinate. These two operators satisfy the bosonic commutation relation:

$$[\widehat{b}^{\dagger}_{\Omega_j,\boldsymbol{u}_n}, \widehat{b}_{\Omega_k,\boldsymbol{u}_m}] = \delta_{nm}\delta_{jk} \tag{2.39}$$

Therefore, the quantized canonical variables (position and momentum) corresponding to the n^{th} phonon are:

$$\begin{aligned}\widehat{q}_n(\boldsymbol{x},t) &= \frac{1}{\sqrt{2m_n\Omega_n V_s}}\left(\widehat{b}^{\dagger}_{\Omega_n}e^{i(\Omega_n t - \boldsymbol{u}_n\cdot\boldsymbol{x})} + \widehat{b}_{\Omega_n}e^{-i(\Omega_n t - \boldsymbol{u}_n\cdot\boldsymbol{x})}\right) \\ \widehat{p}_n(\boldsymbol{x},t) &= i\sqrt{\frac{m_n\Omega_n}{2V_s}}\left(\widehat{b}^{\dagger}_{\Omega_n}e^{i(\Omega_n t - \boldsymbol{u}_n\cdot\boldsymbol{x})} - \widehat{b}_{\Omega_n}e^{-i(\Omega_n t - \boldsymbol{u}_n\cdot\boldsymbol{x})}\right)\end{aligned} \tag{2.40}$$

In the previous equations we have denoted with V_s the sample volume, supposing that it is comparable with the correlation phonon volume.

The photon-phonon interaction Hamiltonian is derived by substituting the expression of the quantized optical and vibrational fields inside Equation 2.35 and by subsequently integrating over the sample volume:

$$\widehat{H}_{int} = -\epsilon_0 \int_{V_s} d\boldsymbol{x} \left(\chi^0_{\lambda\lambda'} + \sum_{n=1}^{N} \chi^{(1)}_{\lambda\lambda'}(n)\, \widehat{q}_n(\boldsymbol{x},t) \right) \widehat{E}_\lambda(\boldsymbol{x},t) \widehat{E}_{\lambda'}(\boldsymbol{x},t) \tag{2.41}$$

In order to simplify the Hamiltonian expression and point out its main features, let us exploit some approximations:

- We consider the interaction of a single nuclear mode with light, thus neglecting the summation over n inside the integral.
- We make use of the Rotating Wave Approximation, neglecting all the terms in the mixed products between optical and vibrational fields whose time-dependent exponents are such that $\omega_j - \omega_l \neq \Omega$.
- Since the nuclear mode wavelength is much longer than the optical one we can set the phonon wave vector $\boldsymbol{u}_n \simeq 0$ and treat the photon-phonon scattering as unidimensional. With this approximation, the wave vector of the emitted photon indeed coincides with the wave vector of the incident one.

Exploiting these approximations, we get a time-independent Hamiltonian [4] that can be split into two parts describing two different physical situations. $\widehat{H}_{ref}$ rules the *Linear Refractive Modulation*, while *Impulsive Stimulated Raman Scattering* is modelled through $\widehat{H}_{Raman}$.

$$\widehat{H}_{int} = \widehat{H}_{ref} + \widehat{H}_{Raman} \tag{2.42}$$

$$\widehat{H}_{Raman} = -\frac{\sqrt{V_s}}{2V\sqrt{2m\Omega}} \sum_{\lambda\lambda',j} \omega_j \chi^{(1)}_{\lambda\lambda'} \left[\left(\widehat{a}^\dagger_{\lambda j} \widehat{a}_{\lambda' j+\frac{\Omega}{\delta}} \right) \widehat{b}^\dagger_\Omega + \left(\widehat{a}_{\lambda j} \widehat{a}^\dagger_{\lambda' j+\frac{\Omega}{\delta}} \right) \widehat{b}_\Omega \right] \tag{2.43}$$

$$\widehat{H}_{ref} = -\frac{V_s}{2V} \sum_{\lambda\lambda',j} \omega_j \left(\chi^{(0)}_{\lambda\lambda'} + \widehat{q}_\Omega \chi^{(1)}_{\lambda\lambda'} \right) \left(\widehat{a}^\dagger_{\lambda j} \widehat{a}_{\lambda' j} + \widehat{a}_{\lambda j} \widehat{a}^\dagger_{\lambda' j} \right) \tag{2.44}$$

The previous expressions clarify all the main different features of the two photon-phonon interaction effects:

- $\widehat{H}_{Raman}$ involves the exchange of a quantum of elastic energy $\hbar\Omega$ between the pulse and the sample. Indeed, by the action of the Raman Hamiltonian photons with frequency ω_j are destroyed through $\widehat{a}_{\lambda j}$ and photons with frequency $\omega_j \pm \Omega$ are created through $\widehat{a}^\dagger_{\lambda j \pm \frac{\Omega}{\delta}}$, together with the absorption ($\widehat{b}_\Omega$) or emission ($\widehat{b}^\dagger_\Omega$) of a phonon. This results in a spectral weight shift inside the interacting optical pulse. The term containing $\widehat{b}^\dagger_\Omega$ inside $\widehat{H}_{Raman}$ rules the Stokes process, while the one containing $\widehat{b}_\Omega$ rules the Anti-Stokes process.
- $\widehat{H}_{Ref}$ does not describe an energy exchange between the pulse and the sample, since it does not couple optical modes of different frequency. $\widehat{H}_{Ref}$ acts indeed as a beam-splitter Hamiltonian, describing the photon redistribution between the two polarization λ and λ'. This is mediated by the static ($\boldsymbol{\chi}^{(0)}$) and by the phonon-dependent ($\boldsymbol{\chi}^{(1)}$) susceptibility. The latter is ruled by the phonon position operator $\widehat{q}_\Omega$.

In this quantum framework, we will now model the pump-probe experiment.

2.2.2 ISRS phonon excitation process

Let us start by describing the phonon excitation resulting from the interaction between the pump pulse and the sample. In the quantum language, the pump-driven excitation corresponds to the sudden application of $\widehat{H}_{Raman}$ on a phonon thermal ground state for a time τ much shorter than the phonon oscillation period. We stress that the phonon excitation is an ISRS process described by $\widehat{H}_{Raman}$. $\widehat{H}_{Raman}$ is indeed the part of the interacting Hamiltonian (Equation 2.42) ruling the energy exchange between vibrational and optical degrees of freedom.

Concerning the initial states, we model the pump state $|\alpha\rangle$ as a mode-locked coherent pulse consisting of linearly polarized photons with frequencies $\omega_j = \omega_0 + j\delta, -J \leq j \leq +J$:

$$|\alpha\rangle = \exp\left(\sum_{j,\lambda} \alpha_{\lambda j}\widehat{a}^{\dagger}_{\lambda j} - \alpha^{*}_{\lambda j}\widehat{a}_{\lambda j}\right)|0\rangle \qquad \widehat{a}_{\lambda j}|\alpha\rangle = \alpha_{\lambda j}|\alpha\rangle \tag{2.45}$$

Here $|0\rangle$ represents the multimode vacuum state and $\alpha_{\lambda j}$ the complex amplitude of the j^{th} mode. Moreover, we suppose that the $2J+1$ frequencies ω_j are gaussian distributed around the central frequency ω_0 with a separation δ depending on the laser repetition rate. Under these hypothesis we can write the j^{th} component of the multimode field as:

$$\alpha_{\lambda j} = \alpha_{\lambda} e^{-(j\delta)^2/2\sigma^2} e^{i\varphi_{\alpha}(j)} = |\alpha_{\lambda j}| e^{i\varphi_{\alpha}(j)} \tag{2.46}$$

Since the incoming pulse is mode-locked, the single mode phases satisfy $\varphi_{\alpha}(j) = j\varphi_{\alpha} + \varphi_0$[3]. As in the classical treatment we will suppose that the incoming pulse is phase-matched. This implies $\varphi_{\alpha} = 0$ and hence the j^{th} component of the impinging pulse reads:

$$\alpha_{\lambda j} = \alpha_{\lambda} e^{-(j\delta)^2/2\sigma^2} = |\alpha_{\lambda j}| \tag{2.47}$$

We want now to analyse what are the effects on the optical and vibrational degrees of freedom resulting from the sudden pump excitation. We will model this instantaneous interaction by mean of the evolution operator $\widehat{U}_{Raman}(\tau) = e^{-i\tau\widehat{H}_{Raman}}$. Under the action of $\widehat{U}_{Raman}$ a generic operator $\widehat{O}$ evolves in time following:

$$\widehat{O}(\tau) = \widehat{U}^{\dagger}_{Raman}(\tau)\,\widehat{O}\,\widehat{U}_{Raman}(\tau) \tag{2.48}$$

Since we are assuming that the phonon related non-linear susceptibility coefficients $\chi^{(1)}_{\lambda\lambda'}$ are small in absolute value [4], we can perform a perturbative expansions of $\widehat{O}(\tau)$ in the coupling parameter $\tau\boldsymbol{\chi}^{(1)}$. Therefore, up to second order in $\tau\boldsymbol{\chi}^{(1)}$ we obtain:

$$\widehat{O}(\tau) \simeq \widehat{O} + i\tau\left[\widehat{H}_{Raman}, \widehat{O}\right] - \frac{\tau^2}{2}\left[\widehat{H}_{Raman}, \left[\widehat{H}_{Raman}, \widehat{O}\right]\right] \tag{2.49}$$

Firstly, let us single out the effect of the ISRS-driven excitation on the vibrational degrees of freedom. By applying Equation 2.49 to the phononic operator $\widehat{b}_{\Omega}$, we

[3]Since φ_0 is a frequency-independent constant phase we will set it equal to 0.

get its perturbed expression up to a time τ:[4]

$$\hat{b}_\Omega(\tau) \simeq \hat{b}_\Omega + i\tau \frac{\sqrt{V_s}}{2V\sqrt{2m\Omega}}\hat{g} \quad ; \quad \hat{g} \equiv \sum_{\lambda\lambda',j} \omega_j \chi^{(1)}_{\lambda\lambda'} \hat{a}^\dagger_{\lambda j} \hat{a}_{\lambda' j+\frac{\Omega}{\delta}} \tag{2.50}$$

Since the photon-phonon system can be described as a factorized state $\hat{\rho}_0^{phon} \otimes |\alpha\rangle\langle\alpha|$ where $\hat{\rho}_0^{phon}$ is the density operator of the phonon thermal state, the mean value of $\hat{b}_\Omega(\tau)$ reads:

$$\begin{aligned} \langle \hat{b}_\Omega(\tau) \rangle &= Tr\left[\left(\hat{\rho}^{phon} \otimes |\alpha\rangle\langle\alpha|\right)\hat{b}_\Omega(\tau)\right] = \\ &= \langle \hat{b}_\Omega \rangle + i\tau \frac{\sqrt{V_s}}{2V\sqrt{2m\Omega}}\gamma \end{aligned} \tag{2.51}$$

where:

$$\gamma \equiv \langle \hat{g} \rangle = \sum_{\lambda\lambda',j} \omega_j \chi^{(1)}_{\lambda\lambda'} |\alpha_{\lambda,j}||\alpha_{\lambda',j+\frac{\Omega}{\delta}}| \tag{2.52}$$

From the previous calculation we can subsequently derive up to second order in $\tau\boldsymbol{\chi}^{(1)}$ the mean phonon position and momentum resulting from a Raman-driven excitation:

$$\langle \hat{q}_\Omega(\tau) \rangle = \frac{1}{\sqrt{2m\Omega V_s}}\left(\langle \hat{b}_\Omega(\tau) \rangle + \langle \hat{b}^\dagger_\Omega(\tau) \rangle\right) = \langle \hat{q}_\Omega(0) \rangle \tag{2.53}$$

$$\langle \hat{p}_\Omega(\tau) \rangle = i\frac{m\Omega}{\sqrt{2V_s}}\left(\langle \hat{b}^\dagger_\Omega(\tau) \rangle - \langle \hat{b}_\Omega(\tau) \rangle\right) = \langle \hat{p}_\Omega(0) \rangle + \frac{\tau}{2V}|\gamma| \tag{2.54}$$

Equation 2.54 shows that through ISRS the photon imparts to the phonon a momentum shift (Figure 2.4) proportional to the interaction time τ, to the photon-phonon coupling $\boldsymbol{\chi}^{(1)}$ and to the amplitude of the phonon-coupled optical modes. On the contrary, the mean phonon position shift ($\langle \hat{q}_\Omega(\tau) \rangle - \langle \hat{q}_\Omega(0) \rangle$) due to ISRS is null.

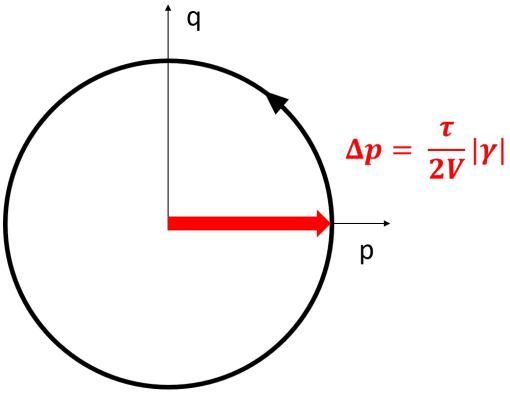

Figure 2.4: Representation of ISRS-driven excitation in phonon phase space. The photon imparts to the phonon a momentum displacement generating a phonon state with a non null mean momentum. The circular trajectory represents the free evolution of the phonon after the excitation. In absence of any dissipative effects, it is ruled by an harmonic oscillator Hamiltonian.

[4]This expression is correct up to 2^{nd} order since $[\hat{H}_{Raman}, [\hat{H}_{Raman}, \hat{b}_\Omega]] = 0$.

Moreover, exploiting Equation 2.50 we can evaluate up to second order in the coupling parameter $\tau\boldsymbol{\chi}^{(1)}$ the mean number of phonons excited by the optical pulse:

$$\langle\widehat{N}_\Omega(\tau)\rangle = \langle\widehat{b}^\dagger_\Omega(\tau)\,\widehat{b}_\Omega(\tau)\rangle = \langle\widehat{N}_\Omega(0)\rangle + \tau\frac{V_s|\gamma|}{2Vm\Omega}\langle\widehat{p}_\Omega(0)\rangle + \tau^2\frac{V_s}{8V^2m\Omega}\langle\widehat{g}^\dagger\widehat{g}\rangle \quad (2.55)$$

The previous equation clarifies how first order and second order photon-phonon coupling affects phonon population.

Indeed, only the phonon number variation linear in the coupling $\tau\boldsymbol{\chi}^{(1)}$ depends on the mean value properties of the initial vibrational state (i.e. the mean phonon momentum $\langle\widehat{p}_\Omega(0)\rangle$). This means that if the system is initially in a displaced phononic state, the description of its interaction with the optical modes can be limited to first order in the photon-phonon coupling $\tau\boldsymbol{\chi}^{(1)}$. Conversely, the second order contributions are the leading ones if the photon interacts with a vibrational thermal ground state (i.e. with $\langle\widehat{p}_\Omega(0)\rangle = \langle\widehat{q}_\Omega(0)\rangle = 0$).

The variations on the phononic degrees of freedom due to ISRS have their counterpart on the optical ones. The latter can be retrieved by applying Equation 2.49 to the operator $\widehat{a}_{\mu j}$, representing the j^{th} photon mode polarized along μ:

$$\begin{aligned}\widehat{a}_{\mu j}(\tau) &\simeq \widehat{a}_{\mu j} + i\tau\left[\widehat{H}_{Raman}, \widehat{a}_{\mu j}\right] - \frac{\tau^2}{2}\left[\widehat{H}_{Raman}, \left[\widehat{H}_{Raman}, \widehat{a}_{\mu j}\right]\right] \\ &\equiv \widehat{a}_{\mu j} + \widehat{a}^{(1)}_{\mu j}(\tau) + \widehat{a}^{(2)}_{\mu j}(\tau)\end{aligned} \quad (2.56)$$

Let us starting by calculating the first order corrections $\widehat{a}^{(1)}_{\mu j}(\tau)$. Since the involved optical frequencies (~ 400 THz) are larger then the vibrational ones (~ 10 THz) we can make use of the approximation $\omega_j + \Omega \sim \omega_j$ inside the commutator in 2.56, obtaining:

$$\widehat{a}^{(1)}_{\mu j}(\tau) = i\tau\frac{\sqrt{V_s}}{2V\sqrt{2m\Omega}}\sum_\lambda \chi^{(1)}_{\mu\lambda}\omega_j\left(\widehat{a}_{\lambda j+\frac{\Omega}{\delta}}\widehat{b}^\dagger_\Omega + \widehat{a}_{\lambda j-\frac{\Omega}{\delta}}\widehat{b}_\Omega\right) \quad (2.57)$$

The perturbation of $\widehat{a}^{(1)(\tau)}_{\mu j}$ due to ISRS is responsible for the spectral modification of the pulse, i.e. of phase and amplitude shifts of each optical mode. Their mean values can be retrieved from the expectation value of the homodyne current operator $\widehat{I}_{\mu,\phi_j}$, measured in a frequency-resolved scheme. Recalling Equation 1.17, under the hypothesis of a classical local oscillator in a phase-matched state, the latter reads:[5]

$$\widehat{I}_{\mu_j,\phi_j} = |z_{\mu j}|\left(\widehat{a}_{\mu j}e^{-i\phi_j} + \widehat{a}^\dagger_{\mu j}e^{i\phi_j}\right) \quad (2.58)$$

By substituting inside the previous equation the expression of the photonic operator derived in 2.57 and averaging on the factorized state $\widehat{\rho}^{phon}_0 \otimes |\alpha\rangle\langle\alpha|$, we get the correction to the frequency-resolved homodyne current up to first order in $\tau\boldsymbol{\chi}^{(1)}$:

$$\begin{aligned}\langle\widehat{I}^{(1)}_{\mu_j,\phi_j}(\tau)\rangle &= Tr\left[\left(\widehat{\rho}^{phon}_0 \otimes |\alpha\rangle\langle\alpha|\right)\widehat{I}^{(1)}_{\mu_j,\phi_j}(\tau)\right] \\ &= |z_{\mu j}|\frac{\omega_j\tau\sqrt{V_s}}{2V\sqrt{m\Omega}}\sum_\lambda \chi^{(1)}_{\mu\lambda}\left[|\alpha_{\lambda j+\frac{\Omega}{\delta}}|\langle\widehat{X}^{phon}_{\phi_j}(0)\rangle - |\alpha_{\lambda j-\frac{\Omega}{\delta}}|\langle\widehat{X}^{phon}_{-\phi_j}(0)\rangle\right]\end{aligned} \quad (2.59)$$

[5] In the experiment the detected probe and the local oscillator share the same polarization state μ.

In the previous expression we have denoted with $\widehat{X}^{phon}_{\phi_j}$ the quadrature of the phononic field which before the interaction (i.e. at $t = 0$) reads:

$$\begin{aligned}\widehat{X}^{phon}_{\phi_j}(0) &\equiv \frac{i}{\sqrt{2}}\left(\widehat{b}^{\dagger}_{\Omega}(0)e^{-i\phi_j} - \widehat{b}_{\Omega}(0)e^{i\phi_j}\right) \\ &= \cos(\phi_j)\frac{\sqrt{V_s}}{\sqrt{m\Omega}}\ \widehat{p}_{\Omega}(0) + \sin(\phi_j)\sqrt{m\Omega V_s}\ \widehat{q}_{\Omega}(0)\end{aligned} \tag{2.60}$$

Therefore, the ISRS-driven phonon excitation results in a variation of the homodyne response $\langle \widehat{I}^{(1)}_{\mu_j,\phi_j}(\tau)\rangle$ proportional to the phononic field quadrature. By substituting the expression of $\widehat{X}^{phon}_{\phi_j}(0)$ inside Equation 2.59 and adding to the homodyne current the equilibrium phonon-independent contribution, we get:

$$\begin{aligned}\langle \widehat{I}_{\mu_j,\phi_j}(\tau)\rangle =& |z_{\mu_j}||\alpha_{\mu_j}|\cos(\phi_j) + \\ &+ |z_{\mu_j}|\frac{\tau V_s \omega_j}{2V}\sum_{\lambda}\chi^{(1)}_{\mu\lambda}\Bigg(\cos(\phi_j)\left(|\alpha_{\lambda j+\frac{\Omega}{\delta}}| - |\alpha_{\lambda j-\frac{\Omega}{\delta}}|\right)\frac{\langle\widehat{p}_{\Omega}(0)\rangle}{m\Omega} + \\ &+ \sin(\phi_j)\left(|\alpha_{\lambda j+\frac{\Omega}{\delta}}| + |\alpha_{\lambda j-\frac{\Omega}{\delta}}|\right)\langle\widehat{q_{\Omega}}(0)\rangle\Bigg)\end{aligned} \tag{2.61}$$

This equation confirms that if the system is initially in a phonon thermal ground state $\widehat{\rho}^{phon}_0$(i.e. $\langle\widehat{q_{\Omega}}(0)\rangle = \langle\widehat{p_{\Omega}}(0)\rangle = 0$) no information on Raman interaction can be retrieved from the optical measurements if we limit at first order. This means that the pulse spectral modification due to ISRS interaction with a phonon thermal ground state is a second order effect and hence proportional to the square of the photon-phonon coupling $\left(\tau\boldsymbol{\chi}^{(1)}\right)^2$ (cfr Equation 2.55).

In our experiment we make use of the pump field to drive via ISRS a coherent[6] vibrational excitation with non-null mean momentum and position, and probe the displaced phononic state with another optical pulse (probe). As pointed out in Equation 2.61, the leading contribution to the probe optical response will be linear in its coupling with the excited phonon. Moreover, as we will explore in detail in Section 2.2.3, the pump excitation will drive an enhancement of the cross-section between the probe pulse and the coherent phonon.

2.2.3 Pump-probe dynamics

In the previous section we have formalized in a quantum framework the pump-driven phonon excitation. In the following, we will exploit the homodyne formalism to retrieve the spectral modification undergone by the probe pulse propagating through the pumped sample at a variable time Δt from the excitation. In particular, we will single out the two main probing effects: the *Linear Refractive Modulation* ruled by $\widehat{H}_{ref}$ and the *Impulsive Stimulated Raman Scattering* ruled by $\widehat{H}_{Raman}$.

To do this, we have to preliminary model the phonon temporal evolution after the the pump interaction. Neglecting any dissipative effects, the excited phonon

[6]We stress that here we have used the term *coherent* only to indicate a temporal periodic evolution of the lattice distortion with non-null mean position and momentum. This does not imply that the pump excited phonon is in a coherent state of the quantum harmonic oscillator.

evolves as a free harmonic oscillator with frequency Ω. The temporal evolution up to the probing time Δt is ruled by the unitary operator:

$$\widehat{U}_{free}(\Delta t) = e^{-i\Omega \widehat{b}_\Omega^\dagger \widehat{b}_\Omega \Delta t} \tag{2.62}$$

The optical probing effects are consequently determined by the phononic state at time Δt, that is the instant at which the probe interaction occurs. The phononic state at the probing time is fully described through its density operator $\widehat{\rho}^{phon}(\Delta t)$ which is determined by the ISRS pump excitation and by the subsequent free evolution up to Δt:

$$\widehat{\rho}^{phon}(\Delta t) = \widehat{U}_{free}(\Delta t)\, \widehat{U}_{Raman}(\tau)\, \widehat{\rho}_0^{phon}\, \widehat{U}_{Raman}^\dagger(\tau)\, \widehat{U}_{free}^\dagger(\Delta t) \tag{2.63}$$

Therefore, up to first order in the phonon-photon coupling parameter $\tau\boldsymbol{\chi}^{(1)}$ the average of the phononic operator $\widehat{b}_\Omega$ at time Δt reads:

$$\langle \widehat{b}_\Omega(\Delta t) \rangle = Tr\left[\widehat{\rho}_0^{phon}\left(e^{-i\Omega\Delta t}\left(\widehat{b}_\Omega + i\tau\frac{\sqrt{V_s}\gamma^{pump}}{2V\sqrt{2m\Omega}}\right)\right)\right] = i\tau\frac{\sqrt{V_s}\gamma^{pump}}{V\sqrt{2m\Omega}}e^{-i\Omega\Delta t} \tag{2.64}$$

where we recall:

$$\gamma^{pump} = \sum_{\lambda\lambda',j} \omega_j \chi^{(1)}_{\lambda\lambda'} |\alpha^{pump}_{\lambda,j}||\alpha^{pump}_{\lambda',j+\frac{\Omega}{\delta}}| \tag{2.65}$$

The probe hence acts on a phonon excited state whose mean value position and momentum evolve as:

$$\begin{aligned} \langle \widehat{q}_\Omega(\Delta t) \rangle &= \frac{\tau\gamma^{pump}}{2Vm\Omega}\sin(\Omega\Delta t) \equiv \frac{R}{m\Omega}\sin(\Omega\Delta t) \\ \langle \widehat{p}_\Omega(\Delta t) \rangle &= \frac{\tau\gamma^{pump}}{2V}\cos(\Omega\Delta t) \equiv R\cos(\Omega\Delta t) \end{aligned} \tag{2.66}$$

In the previous equations we have expressed the mean momentum and position of the coherent phonon in terms of the radius R of its trajectory in phase space. The latter corresponds to the phonon momentum shift imparted by the pump:

$$\begin{aligned} R &\equiv \gamma^{pump}\frac{\tau}{2V} \\ &= \frac{\tau}{2V}\sum_{\lambda\lambda',j} \omega_j \chi^{(1)}_{\lambda\lambda'} |\alpha^{pump}_{\lambda,j}||\alpha^{pump}_{\lambda',j+\frac{\Omega}{\delta}}| \end{aligned} \tag{2.67}$$

and it is a crucial parameter, since it describes the symmetry properties of the excited phonon.

Having in mind these preliminary concepts, let us now move to the fully description of the processes undergone by the the probe pulse.

Linear refractive modulation (LRM)

The modification of the probe photonic operator $\widehat{a}_{\mu j}$ due to LRM interaction with the pumped sample is ruled by the unitary operator $\widehat{U}_{ref}(\tau) = e^{-i\widehat{H}_{ref}\tau}$. Up to first order in $\tau\boldsymbol{\chi}^{(1)}$ its evolution therefore reads:

$$\begin{aligned} \widehat{a}_{\mu j}(\tau) &\simeq \widehat{a}_{\mu j} + i\tau\left[\widehat{H}_{ref}, \widehat{a}_{\mu j}\right] = \\ &= \widehat{a}_{\mu j} + \frac{V_s}{V}\sum_{\lambda j}\omega_j\left(\chi^{(0)}_{\mu\lambda} + \widehat{q}_\Omega\chi^{(1)}_{\mu\lambda}\right)\widehat{a}_{\lambda j} \end{aligned} \tag{2.68}$$

In our experiment, the perturbation of the photonic degrees of freedom of the probe pulse is mapped in the **phase** and **amplitude** dynamics of the mean homodyne current. If we single out only the LRM probing effect, the latter reads:

$$\langle \widehat{I}^{Ref}_{\mu_j,\phi_j}(\Delta t)\rangle = |z_{\mu j}||\alpha_{\mu j}|\cos(\phi_j)+|z_{\mu_j}|\frac{2\tau V_s\omega_j}{V}\sin(\phi_j)\sum_{\lambda}|\alpha_{\lambda j}|\left(\chi^{(0)}_{\mu\lambda}+\chi^{(1)}_{\mu\lambda}\langle\widehat{q}_\Omega(\Delta t)\rangle\right) \tag{2.69}$$

If we now separate the equilibrium and the phonon-dependent contribution, we note that the refractive modulation affect both the pumped and the unpumped response.

$$\begin{aligned}\langle \widehat{I}^{Ref}_{\mu_j,\phi_j}(\Delta t)\rangle_{eq} &= |z_{\mu j}||\alpha_{\mu j}|\cos(\phi_j)+|z_{\mu_j}|\frac{2\tau V_s\omega_j}{V}\sin(\phi_j)\sum_{\lambda}|\alpha_{\lambda j}|\chi^{(0)}_{\mu\lambda}\\ \langle \widehat{I}^{Ref}_{\mu_j,\phi_j}(\Delta t)\rangle_{pump} &= |z_{\mu_j}|\frac{2\tau V_s\omega_j}{V}\sin(\phi_j)\sum_{\lambda}|\alpha_{\lambda j}|\chi^{(1)}_{\mu\lambda}\frac{R}{m\Omega}\sin(\Omega\Delta t)\end{aligned} \tag{2.70}$$

As a matter of fact, the static homodyne current is influenced by the phonon-independent susceptibility $\boldsymbol{\chi}^{(0)}$, while the pumped response is sensitive to the phonon modulated refractive properties modelled through $\boldsymbol{\chi}^{(1)}$.

We stress that we dub this effect as *Linear* only because it is linear in the photonic degrees of freedom of the probe, i.e. it does not cause any spectral weight shift. The non-linearity of the process resides in the ISRS-driven pumping excitation which is mapped into a non-linear probe response ruled by a phonon-dependent susceptibility $\tilde{\chi}^{(1)}_{\mu\lambda}$ of the form:

$$\begin{aligned}\tilde{\chi}^{(1)}_{\mu\lambda} = \frac{R}{m\Omega}\chi^{(1)}_{\mu\lambda} &= \frac{\tau}{2Vm\Omega}\sum_j\sum_{mn}\chi^{(1)}_{\mu\lambda}\chi^{(1)}_{mn}|\alpha^{pump}_{mj}||\alpha^{pump}_{nj+\frac{\Omega}{\delta}}|\omega_j\\ &\equiv \frac{\tau}{2Vm\Omega}\sum_j\sum_{mn}\chi^{(3)}_{\mu\lambda mn}|\alpha^{pump}_{mj}||\alpha^{pump}_{nj+\frac{\Omega}{\delta}}|\omega_j\end{aligned} \tag{2.71}$$

In the previous equation we have pointed out the non-linearity of the probing process by making explicit the four rank susceptibility tensor $\chi^{(3)}_{\mu\lambda mn}$. Moreover, we note that the cross-section of the probe-phonon interaction $\tilde{\chi}^{(1)}_{\mu\lambda}$ is enhanced through the pumping process, since it is proportional to the phonon-coupled pump modes. By looking at the structure of Equation 2.69, we note that the refractive effect results both in a phase and in an amplitude shift of the homodyne current. Indeed, LRM introduces both in the equilibrium and in the pumped current, a response proportional to $\sin(\phi_j)$ which is $\pi/2$-shifted with respect to the sample-independent one ($\propto\cos(\phi_j)$).

The LRM-driven phase and amplitude dynamics are shown in Figure 2.5. The presented plots have been obtained by separately fitting the pumped and the equilibrium response (Equation 2.70) with a sinusoidal function and by taking the difference between the pumped and equilibrium parameters (phase and amplitude). In this way we are able to single out the phonon-dependent shifts. Moreover, in this preliminary simulation we have taken $\boldsymbol{\chi}^{(0)}$ as a real tensor, thus supposing that at equilibrium the sample does not exhibit birefringence[7].

[7] In Chapter 5, where the mean value measurements on α-quartz are presented, we will also take into account static birefringence.

The simulated dynamics confirms what has been predicted with the classical model. As a matter of fact, phase and amplitude shifts resulting from the modulation of the refractive properties follows the temporal evolution of the coherent phonon oscillations $\langle \widehat{q}_\Omega(\Delta t) \rangle$, confirming the classical predictions.

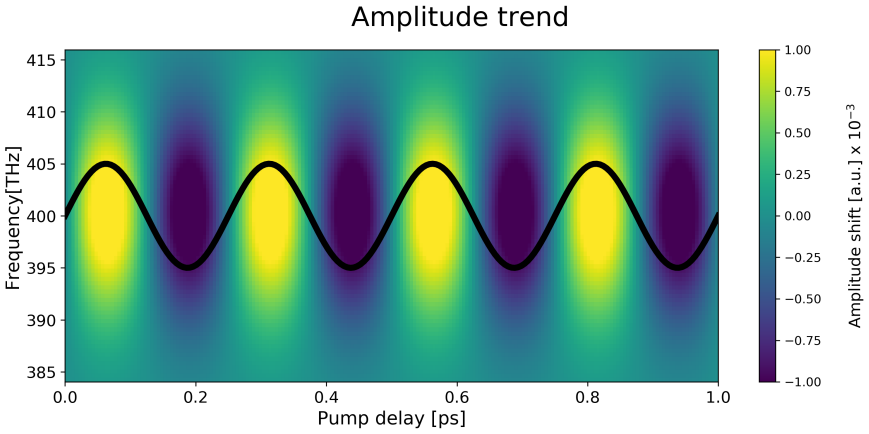

(a) Amplitude dynamics (refractive contribution)

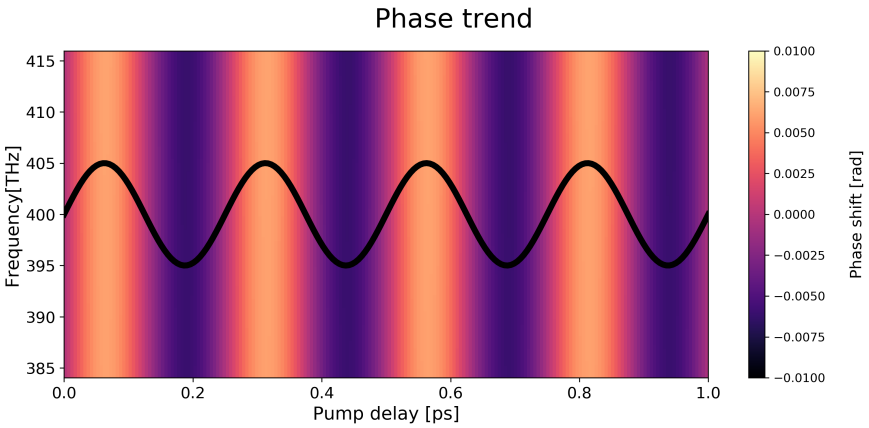

(b) Phase dynamics (refractive contribution)

Figure 2.5: Simulated amplitude and phase dynamics of each probe mode in case of LRM probe-phonon interaction. The trends have been obtained by separately fitting $\langle \widehat{I}^{Ref}_{\mu_j,\phi_j}(\Delta t) \rangle_{eq}$ and the full response $\langle \widehat{I}^{Ref}_{\mu_j,\phi_j}(\Delta t) \rangle_{pump} + \langle \widehat{I}^{Ref}_{\mu_j,\phi_j}(\Delta t) \rangle_{eq}$ with a sinusoidal function and by taking the difference between the pumped and unpumped parameters. In the present simulation: $|z_j| = 10|\alpha_j|$; $|\alpha_j^{pump}| = 10^3|\alpha_j|$; $\tau = 50$ fs; $\tilde{\chi}^{(1)}_{\mu\lambda} \simeq 10^{-4}$ (Chapter 5); $\chi^{(0)}_{\lambda\lambda'} \sim 0.1$ [14]. Phase and amplitude shifts follow the nuclear displacement dynamics (black line). We note that LRM causes no spectral weight shifts among probe modes.

Impulsive Stimulated Raman Scattering (ISRS)

Let us now study the energy exchange between the probing pulse and the excited phonon. In non-absorbing media this is dominated by ISRS. Since the effect of the Raman process is a shift of phonon momentum, we expect that by probing the sample at different times from the excitation (i.e. at different points in the phase space trajectory of the free evolving phonon) we can dynamically dump or force the phonon oscillations (Figure 2.6). This means that by controlling the pump-probe delay we can induce a Stokes or an Anti-Stokes process among the modes of the probe pulse.

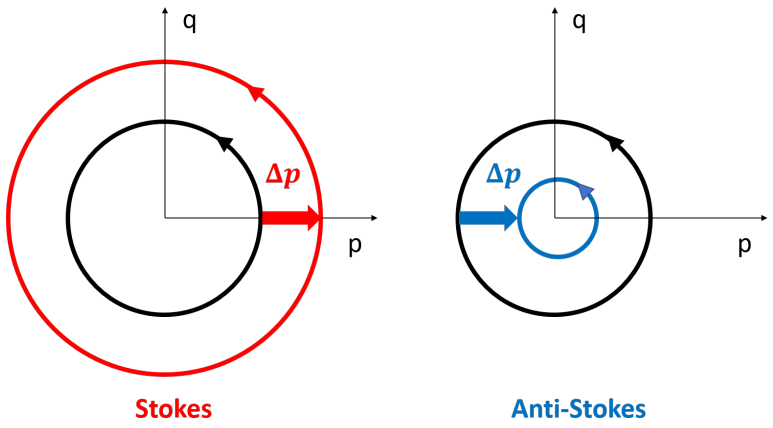

Figure 2.6: Effects of the ISRS interaction between the probe pulse and the coherent phonon. The probe imparts to the phonon a positive momentum shift (arrow). The momentum shift, depending on the phonon phase space coordinate, can force (Stokes process) or dump (Anti-Stokes process) the phonon oscillations, thus modifying the radius of its trajectory.

In this case, the probe-phonon interaction is ruled by the action of $\widehat{H}_{Raman}$ and the frequency-resolved homodyne current therefore reads (cfr Equation 2.61):

$$\begin{aligned}\langle \widehat{I}^{Raman}_{\mu_j,\phi_j}(\Delta t)\rangle =& |z_{\mu_j}||\alpha_{\mu_j}|\cos(\phi_j)+ \\ &+|z_{\mu_j}|\frac{\tau V_s \omega_j}{2V}\sum_\lambda \chi^{(1)}_{\mu\lambda}\Big(\cos(\phi_j)\left(|\alpha_{\lambda j+\frac{\Omega}{\delta}}|-|\alpha_{\lambda j-\frac{\Omega}{\delta}}|\right)\frac{\langle\widehat{p}_\Omega(\Delta t)\rangle}{m\Omega}+ \\ &+\sin(\phi_j)\left(|\alpha_{\lambda j+\frac{\Omega}{\delta}}|+|\alpha_{\lambda j-\frac{\Omega}{\delta}}|\right)\langle\widehat{q_\Omega}(\Delta t)\rangle\Big)\end{aligned} \tag{2.72}$$

In order to retrieve the ISRS-driven modifications of the probe field, let us split the homodyne current equation in its equilibrium and a pumped contribution:

$$\begin{aligned}\langle \widehat{I}^{Raman}_{\mu_j,\phi_j}(\Delta t)\rangle_{eq} &= |z_{\mu j}||\alpha_{\mu j}|\cos(\phi_j) \\ \langle \widehat{I}^{Raman}_{\mu_j,\phi_j}(\Delta t)\rangle_{pump} &= |z_{\mu_j}|\frac{\tau V_s \omega_j}{2V}\sum_\lambda \chi^{(1)}_{\mu\lambda}\Big(\cos(\phi_j)\left(|\alpha_{\lambda j+\frac{\Omega}{\delta}}|-|\alpha_{\lambda j-\frac{\Omega}{\delta}}|\right)\frac{R\cos(\Delta t)}{m\Omega}+ \\ &\quad+\sin(\phi_j)\left(|\alpha_{\lambda j+\frac{\Omega}{\delta}}|+|\alpha_{\lambda j-\frac{\Omega}{\delta}}|\right)\frac{R\sin(\Omega\Delta t)}{m\Omega}\Big)\end{aligned} \tag{2.73}$$

The previous equation shows that ISRS induces a pumped optical response having two contributions.

The first one is in phase with the equilibrium response ($\propto \cos(\phi_j)$) and it is therefore mainly responsible for the phonon-induced amplitude shifts. The temporal dependence of this contribution is ruled by the phonon momentum.

Conversely, the second term in Equation 2.73 is $\pi/2$-shifted with respect to the unpumped response and follows the instantaneous atomic displacement $\langle \widehat{q}(\Delta t) \rangle$. This contribution rules the phase dynamics and its origin resides in the fact that the homodyne response resulting from ISRS interaction is a map of the quadrature of the excited phonon field, and hence of the linear combination of phonon momentum and position (Equation 2.59). Therefore, the phase modulation ruled by the instantaneous lattice displacement is present also in the case of Raman probe-phonon interaction.

Let us focus on the ISRS-driven amplitude shifts (Figure 2.7) and retrieve their peculiar dynamics. As previously stated, the leading contributions to phonon-dependent amplitude shifts originate from the pumped term proportional to $\cos(\phi_j)$ and hence in phase with the equilibrium one. The pumped response proportional to $\sin(\phi_j)$ is indeed null when the equilibrium one is maximum, and therefore causes negligible amplitude shifts. The ISRS-driven amplitude dynamics has been obtained by fitting with a sinusoidal function the pumped response and the equilibrium one and by subsequently subtracting the pumped fitted amplitude to the unpumped one. Figure 2.7 shows that the amplitude exhibits the Raman behaviour. Indeed, the ISRS-driven photon-phonon interaction induces a spectral weight shift among the probe modes which follows the phonon momentum (cfr classical model).

In Figure 2.8 we compare the ISRS-driven amplitude dynamics with the LRM-driven phase trend. They are $\pi/2$-shifted for any probe frequency, since respectively ruled by phonon momentum and phonon position.

The extent of phonon-driven amplitude shifts are ruled by the **cross-section** of the Raman process $\tilde{\chi}^{(1)}_{\mu\lambda}$. In this quantum model, the latter reads[8]

$$\begin{aligned} \tilde{\chi}^{(1)}_{\mu\lambda} = \frac{R}{m\Omega}\chi^{(1)}_{\mu\lambda} &= \frac{\tau}{2Vm\Omega}\sum_j \sum_{mn} \chi^{(1)}_{\mu\lambda}\chi^{(1)}_{mn}|\alpha^{pump}_{mj}||\alpha^{pump}_{nj+\frac{\Omega}{\delta}}|\omega_j \\ &\equiv \frac{\tau}{2Vm\Omega}\sum_j \sum_{mn} \chi^{(3)}_{\mu\lambda mn}|\alpha^{pump}_{mj}||\alpha^{pump}_{nj+\frac{\Omega}{\delta}}|\omega_j \end{aligned} \tag{2.74}$$

The previous equation clearly shows that ISRS results from a non-linear response in the susceptibility ruled by the four rank tensor $\chi^{(3)}_{\mu\lambda mn}$.

We stress that since the probe interacts with an excited coherent phonon, the cross-section of the interaction ($\tilde{\chi}^{(1)}_{\mu\lambda}$) is sensitive to the intensity of the pulse that has induced the vibrational excitation (i.e. the pump). In particular, Equation 2.74 shows that the Raman cross-section $\tilde{\chi}^{(1)}_{\mu\lambda}$ scales as the product of the phonon-coupled pump modes. Therefore, if the pump intensity is constant, we can exploit the measure of the Raman cross-section to retrieve the coupling strength between electronic and vibrational degrees of freedom.

[8]By using this definition, the cross-section of the non-linear probing process $\tilde{\chi}^{(1)}_{\mu\lambda}$ is adimensional. Indeed, $\frac{R}{m\Omega}$ represents the spatial extent of nuclear oscillations, while $\chi^{(1)}_{\mu\lambda}$ has the dimension of the inverse of a length (Equation 2.36).

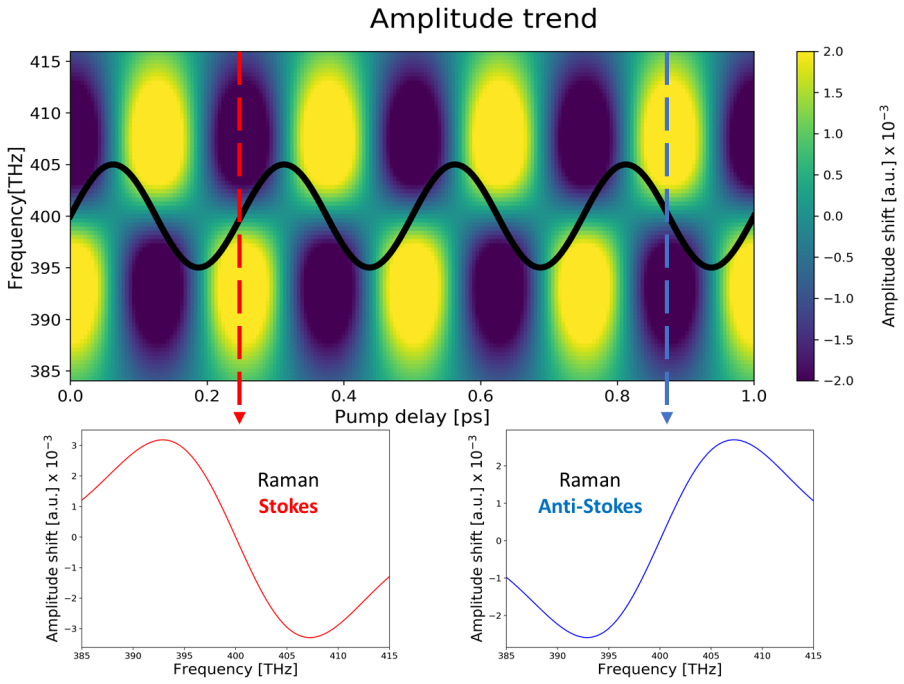

(a) Amplitude dynamics (ISRS contribution)

Figure 2.7: Simulated amplitude dynamics of each probe mode in case of ISRS probe-phonon interaction. The trends have been obtained by separately fitting $\langle \hat{I}^{Raman}_{\mu_j,\phi_j}(\Delta t)\rangle_{eq}$ and the full response $\langle \hat{I}^{Raman}_{\mu_j,\phi_j}(\Delta t)\rangle_{pump} + \langle \hat{I}^{Raman}_{\mu_j,\phi_j}(\Delta t)\rangle_{eq}$ with a sinusoidal function and by taking the difference between the pumped and unpumped parameters. In the present simulation: $|z_j| = 10|\alpha_j|$; $|\alpha_j^{pump}| = 10^3|\alpha_j|$; $\tau = 50$ fs; $\tilde{\chi}^{(1)}_{\mu\lambda} \sim 10^{-4}$ (Chapter 5). ISRS causes a dynamical spectral weight shift inside the probe in phase with the momentum phonon oscillations (black line). This results in a π-shift of the differential amplitude of modes at opposite sides of the gaussian pulse.

In Figure 2.9 we summarize the quantum model of the pump-probe experiment with the description of the observable effects.

We stress that in this chapter we have separated the LRM and the ISRS response only to distinguish their peculiar features. In the real experiment, the two effects occur together in the probing process. However, since we expect to be LRM the only probing effect responsible to polarization rotation, we can isolate it by controlling the polarization of the incident and emitted probe field. Consequently, in order to completely describe the experimental homodyne response we will need to introduce a further Hamiltonian modelling the polarization selection of the outgoing probe. We will examine in detail this issue in Chapter 5, where we will apply the model to the employed α-quartz and $CuGeO_3$ samples and discuss the symmetry properties of their Raman phonons.

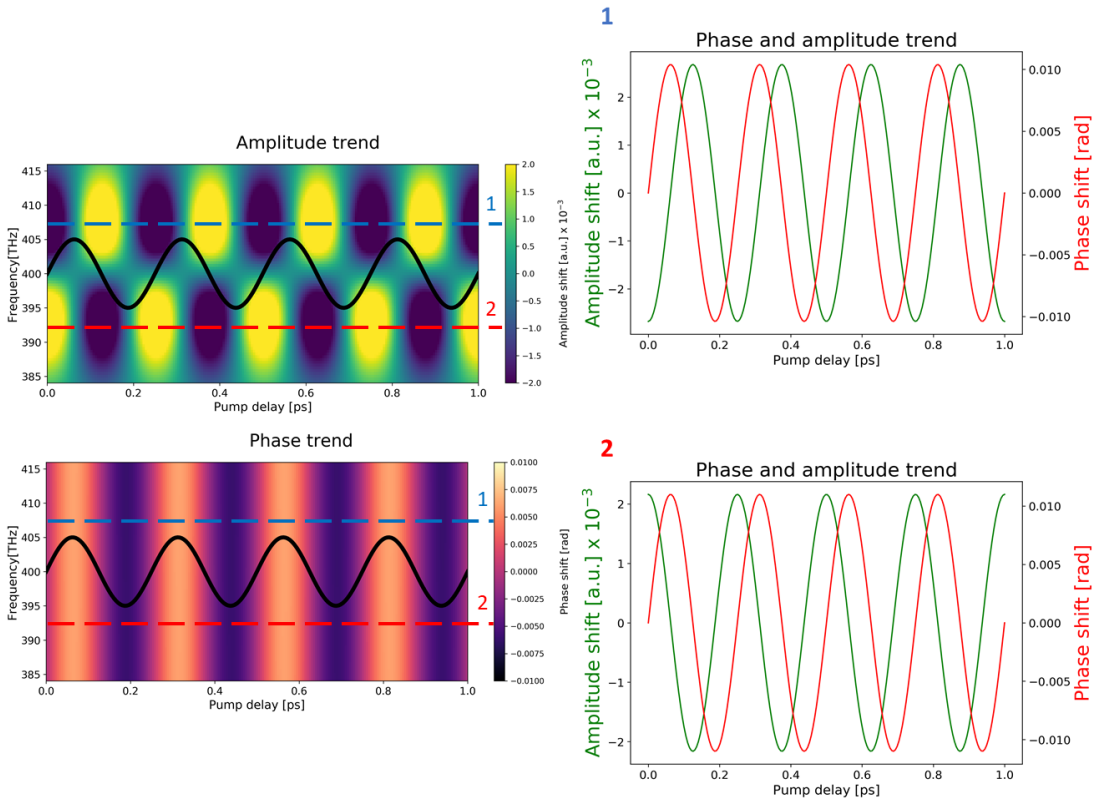

Figure 2.8: Comparison between ISRS-driven amplitude dynamics and LRM-driven phase dynamics. The amplitude shift imprinted on the probe resulting from the Raman interaction follows the phonon momentum. Conversely, the phase is ruled by the mean phonon position (black line) and it is therefore $\pi/2$-shifted with respect to the amplitude.

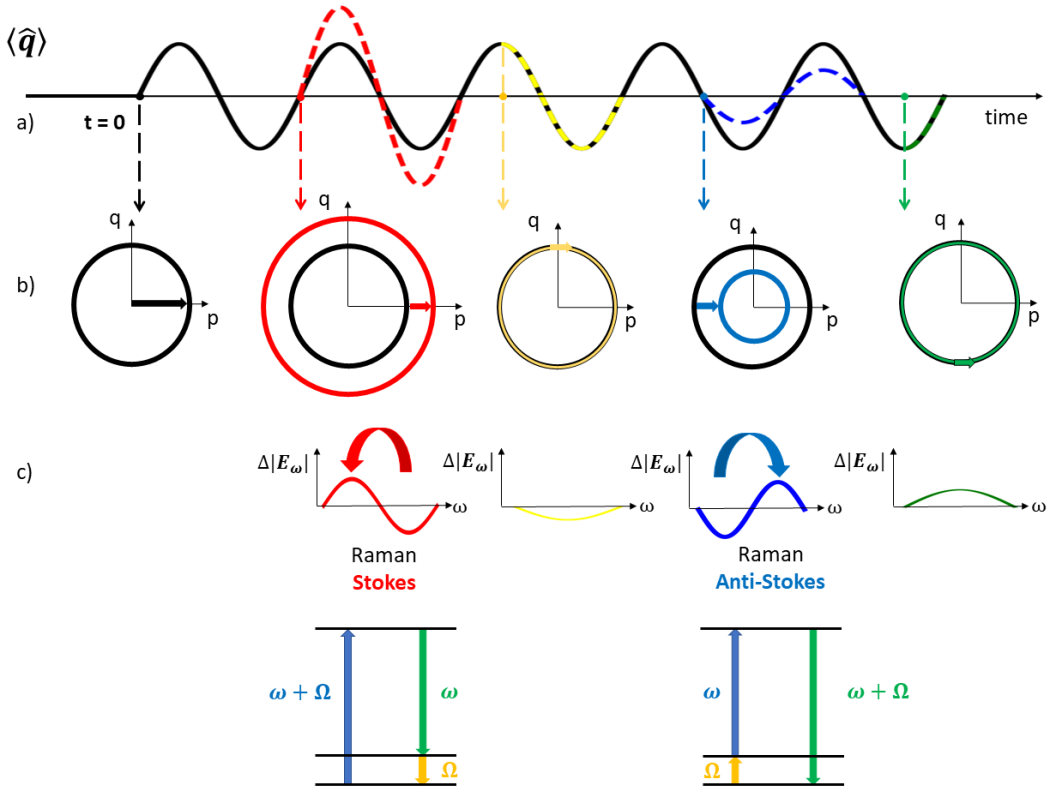

Figure 2.9: Description of the pump-probe experiment by mean of the quantum model. In a) we depict the mean phonon oscillations induced trough ISRS by the pump at $t = 0$ and ruled at positive times by a quantum oscillator Hamiltonian. In (b) we illustrate the modification of the phonon phase space trajectory due to the probe-target interaction. The ISRS probing effect is maximum when the phonon carries the maximum momentum modulus. ISRS results indeed in a positive shift of the phonon trajectory along the p axis. Depending on the probing time, ISRS can either force (Stokes process) or dump (Anti-Stokes process) the phonon. The first occurs when the probe interacts at the positive maximum phonon momentum, while the latter when the phonon exhibits at the interaction time the minimum negative momentum. As depicted in (c) Stokes and Anti-Stokes probing processes result respectively in a red shift or blue shift of the probe pulse. Conversely, at the extremes of the phonon oscillations the ISRS-driven amplitude shift is negligible and no change of the spectral weight occurs. In this case the dominating probing effect is the Linear Refractive Modulation.

Chapter 3

Experimental apparatus

In Chapter 2 we have theoretically described how we can exploit multimode homodyne detection to address the coherent motion of atoms in solids in both its amplitude and phase dynamics. In this chapter we provide the experimental description of this innovative spectroscopic technique. After having outlined which are the experimental requirements needed for the realization of the technique, we will focus on the pulse-shaper, that is a crucial component on which the success of multimode homodyne relies. Eventually, we will describe the potentiality of our detection system of performing measurements in shot-noise conditions. This possibility, together with the frequency resolution of our technique, can open the perspective of unveiling multimode quantum correlation imprinted on an optical pulse trough its non-linear interactions with a phononic system (Chapter 6).

3.1 Time-resolved multimode homodyne set-up

As anticipated in Chapter 2, the scope of this work is to build a set-up suitable to combine two different spectroscopic techniques: pump-probe spectroscopy and multimode homodyne detection. By combining these two approaches we are able to overcome the intensity detection limitation of standard pump-probe spectroscopy and have access to phase and amplitude dynamics of each probe mode. A simplified scheme of this experimental combination is depicted in Figure 3.1.

The experiment can be divided into three consecutive parts:

- The sample under investigation is driven out of equilibrium by an intense ultrashort pulse. At a precise delay Δt after the sudden excitation a second laser pulse, the probe, interacts with the material and it is scattered carrying information about the photo-excited system (Figure 3.1(a)).

- Each transmitted probe pulse, called *signal* in the homodyne framework (Figure 3.1(b)), is made interfere through a 50:50 beam splitter with a local oscillator (LO) shaped in its frequency content. The local oscillator shaping is the innovative part of the approach and determines the frequency resolution of the technique. Indeed, by modulating the LO spectral content, we are able to drive the interference to select the frequencies of the emitted probe field. Experimentally, this purpose is accomplished trough an ultrafast pulse-shaper that permits to modulate amplitude and phase of each spectral component of a pulse. As illustrated in Figure 3.1, we have

decided to send to the pulse-shaper also the probe (signal), even if no frequency modulation has been applied to it. This choise ensures to increase the noise stability of the interferometer, since signal and local oscillator share most of the same optics. Moreover, exploiting the capability of the pulse-shaper to modulate the phase of each spectral component, we can correct the probe temporal compression (Section 3.2), without changing its spectral content.

- Finally the two outputs of the 50:50 beam splitter are acquired with two photodiodes and the difference between the two generated photo-voltages (homodyne current) is measured. This observable maps the phase-resolved quadrature of the probe field (Equation 1.18). The differential current can be acquired by changing three different degrees of freedom: the local oscillator frequency, its relative phase with respect to the signal and the pump-probe delay Δt. In particular, as presented in Figure 3.2, we are able to reconstruct each probe mode for every pump-probe delay and eventually retrieve its full statistics. We will exploit the latter possibility of our detection system in Section 3.3.

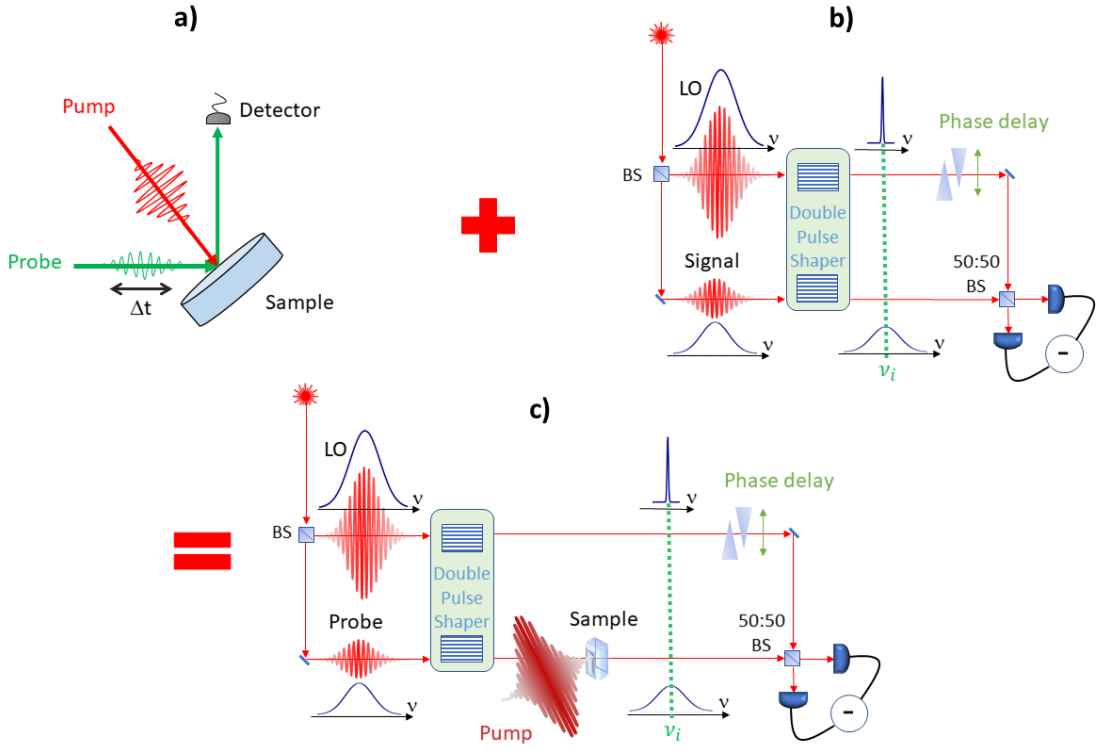

Figure 3.1: Pump-probe multimode homodyne detection set-up. The combination between standard pump-probe approach (a) and multimode homodyne balanced detection (b) gives rise to the set-up adopted in this thesis (c).

In Figure 3.3 we present a more detailed representation of the employed set-up. The ultrashort pulses are produced by a Kerr-Lens-Mode-Locked Nd-YAG oscillator (*Pharos Light Conversion*) followed by a Chirped Pulse Amplifier. The pulses, produced at a repetition rate of 200 kHz, are subsequently sent to a two-stage Optical Parametric Amplifier (*Orpheus-F* OPA) seeded with supercontinuum white light. The signal in output of the OPA is sent to interferometer

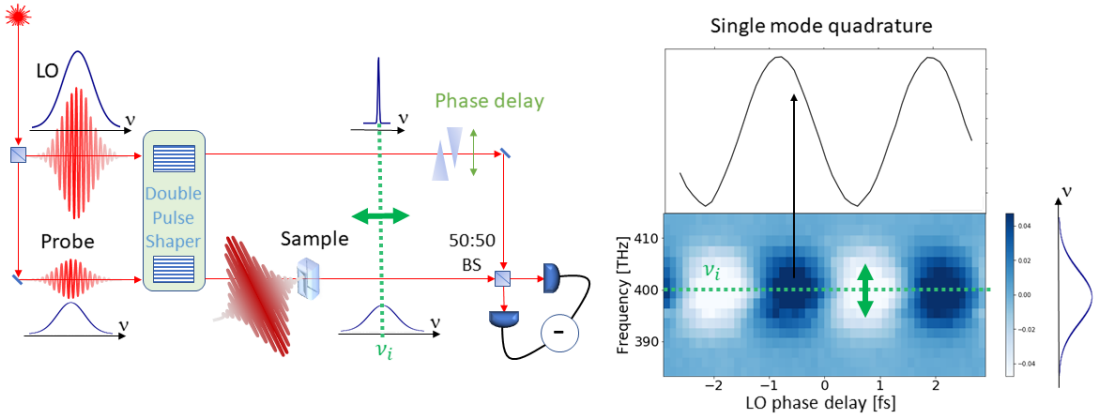

Figure 3.2: Frequency-resolved homodyne map obtained at a fixed pump-probe delay. The selection of the local oscillator frequency (green arrow) allows to reconstruct the quadrature of each probe mode. This is achieved by scanning the LO phase at a fixed frequency ν_i.

and has a duration of 50 fs and a tunable wavelength. The wavelengths used for our experiment are 760 nm and 745 nm. Conversely, the idler in output of the parametric amplification stage is employed as pump. The latter has a duration of 100 fs and a wavelength in the Near-Infrared-Range (1656 nm).

The signal is divided by mean of a beam splitter into two beams: one acts as local oscillator, while the other is employed as probe. Both the probe and the local oscillator are sent to the pulse-shaper which allows the frequency resolution of the experiment, enabling the modulation of the spectral content of the LO. The phase-mismatch between the probe and the local oscillator is controlled by mean of a wedge mounted on a piezoelectric translator.

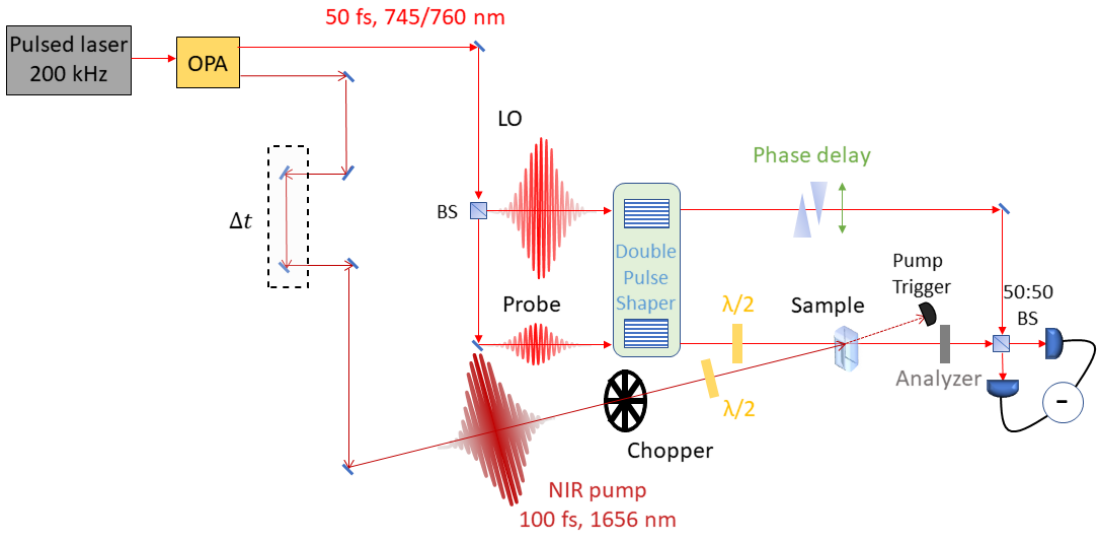

Figure 3.3: Experimental set-up adopted for performing multimode homodyne detection in time domain.

The delay Δt between the pump and the probe is controlled by mean of a mechanical translation stage inserted on the pump line. Since we want to isolate from the homodyne current purely dynamical features imprinted on the

equilibrium response (i.e. without the pump), we have inserted a chopper along the pump beam. Indeed, by chopping the pump beam at a frequency (400 Hz) much slower than the laser repetition rate and by triggering the pump arrival by mean of a diode, both the pumped and the equilibrium quadrature can be measured at each delay. The difference between the previous two will encode the pump-dependent dynamics of the probe quadrature. Moreover, by chopping the pump, we can eliminate from the homodyne current noises slower than the chopping rate (400 Hz).

Polarization selectivity In the set-up we have also implemented the possibility of performing polarization dependent measurements. This is crucial to map the phonon symmetry properties and to discriminate the two leading probing effects resulting from photon-phonon interaction: LRM and ISRS (Chapter 2). The polarization selectivity has been implemented by controlling the pump-probe polarization angle and by selecting the polarization of the transmitted probe field. To accomplish this requirement an half-wave-plate ($\lambda/2$) has been introduced before the sample on both pump and probe beam and a polarizer (analyzer) has been placed on the probe line after the sample. The relative orientation between the two $\lambda/2$ rules the pump-probe polarization angle. Conversely, the orientation of the analyzer with respect to the $\lambda/2$ on the probe line, enables to select the polarization of the emitted field.

3.1.1 Multimode homodyne with multiple-shaped local oscillator

Our set-up is also feasible to perform homodyne detection with a multiple-shaped local oscillator. By working with a multiple-shaped local oscillator we can have access to the jointly statistics of the corresponding probe modes. The latter encodes multimode correlations (Figure 1.6) which, thanks to the possibility of the detector of working in shot-noise regime, are of quantum origin. In Figure 3.4 we show the set-up employed for the preliminary measurement of two mode correlation presented in Chapter 6. In this configuration, the local oscillator is shaped into a two-mode state and the statistics of the differential current is measured as a function of the frequency difference of the two LO modes.

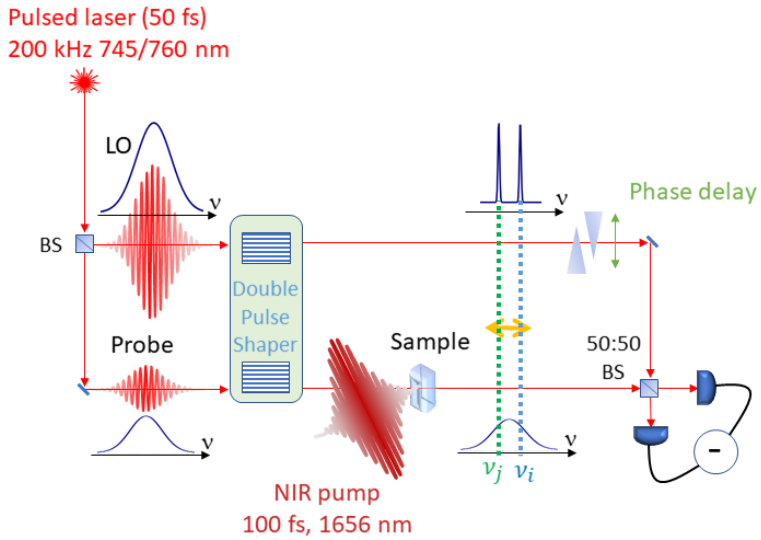

Figure 3.4: Set-up adopted for measuring two-modes correlations among the probe modes selected by the local oscillator shaping.

3.2 Ultrafast pulse-shaping

In the previous section we have pointed out the necessity of controlling the spectral content of the local oscillator in order to reconstruct in a frequency-resolved scheme the probe field. We have accomplished this requirement by mean of an ultrafast pulse-shaper, whose main features will be highlighted in this section.

Before going trough the description of how our pulse-shaper works, let us give a general outlook on pulse-shaping techniques.

With the expression *ultafast pulse-shaping* we refer to all the techniques able to manipulate femtosecond pulses in both its frequency and phase content. Even if there are many ways to achieve this purpose [24], here we will only focus in the shaping techniques involving the spatial masking of the spatially dispersed pulse frequency spectrum. With this widely employed approach, an arbitrary shaping of the ultrashort pulse can be achieved by independently controlling the phase and the amplitude of each dispersed spectral component.

The most basic pulse-shaper adopting spatial masking shaping is depicted in Figure 3.5 and it is commonly called $4f$*-line*. It consists of a pair of diffraction gratings and cylindrical lenses, arranged so that they are equally spaced by a distance f, corresponding to the focal length of the lenses. The frequency components within the incoming pulse are angularly dispersed by the first grating and are then focused by the first lens at its Fourier plane. By placing a spatial mask $M(x) = |A(x)|e^{i\phi(x)}$ in the Fourier plane we are able to selectively act on the dispersed frequency components and thus transfer a precise amplitude and phase pattern from the mask to the pulse spectrum. After the spatial shaping, a second pair lens-grating recombines the dispersed light, so that the final output is a shaped collimated beam.

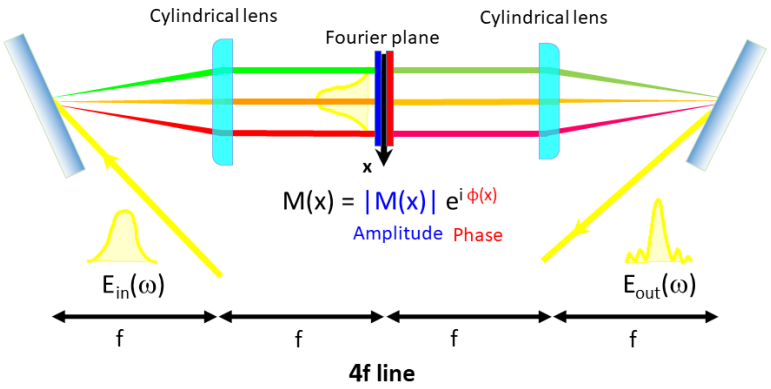

Figure 3.5: Simplified scheme of a spatial masking pulse-shaper, working in a $4f$ geometry.

The masks previously described are static, in the sense that they need to be replaced if one wants to change the features of the pulse more then ones. In our experiment a scan in the local oscillator frequency content is required (Figure 3.3). Therefore, static masks are not suitable for our purpose. We have overcome this limitation by using a 2D Liquid Crystal Spatial Light Modulator (LC-SLM) which enables to dynamical control the shaping mask.

3.2.1 Two-dimensional Liquid Crystal Spatial Light Modulator (LC-SLM)

A Liquid Crystal Spatial Light Modulator (LC-SLM) is a pulse shaper that exploits the birefringent properties of liquid crystals to dynamically control the optical path (and hence the phase) on light impinging on it. It consists of a pair of electrodes with a thin layer of nematic[1] liquid crystals placed between them, in such a way that their director is parallel to the substrates when no voltage in applied between them [32]. As shown in Figure 3.6, if the incoming beam is linearly polarized along the direction parallel to the director of the liquid crystals, it experiences two distinct situations according to whether or not a voltage is applied between the electrodes. When no voltage is applied, the beam experiences the maximum difference between the extraordinary (n_e) and the ordinary (n_o) refractive index. On the contrary, when a voltage is applied, the molecules of the liquid crystal realign along the electric field that has been established. In this configuration, the impinging pulse experiences no difference between the two refractive indices along the two directions (Figure 3.6). Therefore, the LC-SLM acts as a waveplate which is responsible for a voltage-dependent phase delay ϕ equal to:

$$\phi(V,\omega) = \frac{\omega \Delta n(V,\omega) d}{c} \tag{3.1}$$

where V is the applied voltage, ω the frequency of the impinging light, $\Delta n(V,\omega)$ the differential refractive index between the ordinary and the extraordinary axis and d the thickness of the liquid crystal layer [24]. Consequently to Equation

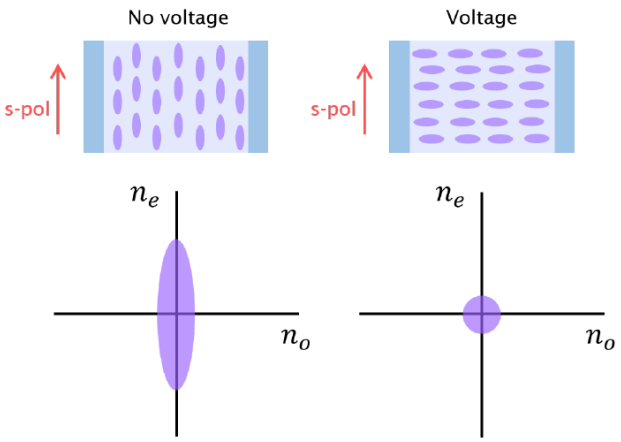

Figure 3.6: Birefringence of the nematic liquid crystals placed between the two electrodes of the LC-SLM. A light beam linearly polarized along the extraordinary axis of the liquid crystals experiences different refractive indices (and hence different phase shifts) according to whether or not a voltage is applied between the electrodes [32].

3.1, the first outcoming beam in Figure 3.6 is phase-shifted with respect to the second one.

[1]Liquid crystals are named *nematic* when their molecules have no positional order but tend to point towards the same direction, indentified by the name *director*.

In a more general framework, by independently varying the voltages applied in distinct sections of the layer, we can imprint a specific phase delay for a light beam impinging on that specific section. This possibility is shown is Figure 3.7, where we present a side view of the LC-SLM. The crucial difference between this

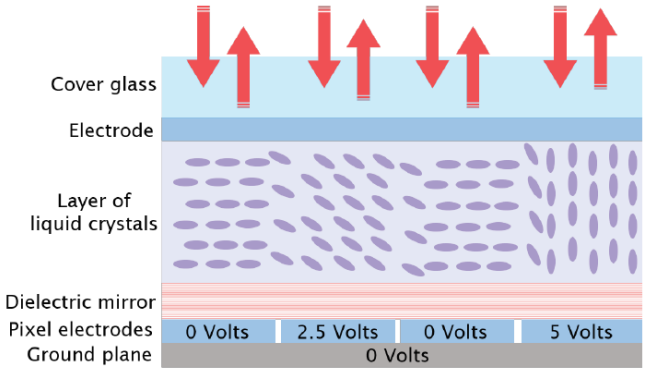

Figure 3.7: Side view of Liquid Crystal Spatial Modulator (LC-SLM) working in reflection geometry [32]. The phase shift between the incoming and the outcoming light (red arrows) depends on the applied voltage.

general configuration and the simplified scheme presented in Figure 3.6 resides in the pixelation of the bottom electrode. Therefore, we can think the simple representation of Figure 3.6 as just one single pixel of the more general structure of Figure 3.7. Moreover, the presence of a dielectric mirror (Figure 3.7) suggests that a reflection geometry rather than a transmission one can be also employed [32]. Recalling the $4f$ scheme of Figure 3.5, a reflection geometry (typically called *folded 4f scheme*) can be set up by using only the first grating-lens pair, which act both as dispersive and collimating element.

Therefore, a simple LC-SLM consists of a pixelated array on which the pulse spectrum is dispersed along the direction of pixelation (i.e. in the horizontal direction of Figure 3.7). By controlling the voltage applied at each pixel it is possible to control the phase of each dispersed spectral component impinging on it.

Until now, we have only explored the capability of the LC-SLM of manipulating the phase of each pulse component. However, more complex tools based on a similar scheme (Figure 3.7) can be used to achieve a simultaneous shaping of both phase and amplitude of the femtosecond pulse. We stress that having access to frequency-resolved amplitude shaping is crucial in our experiment since we need to control the spectral content of the local oscillator. To achieve this experimental purpose we have exploited the method presented in [23], which is the basis of the pulse-shaper arrangement employed in our experiment (Figure 3.3).

The method relies on the use of a 2D LC-SLM instead of a linear one. The LC-SLM employed in our set-up consists of a pixelated matrix of 1050 x 1440 pixels, which is placed at the focal plane of a *folded 4f scheme*. The fundamental advantage of using a 2D matrix relies in the fact that in this case we have access to an additional degree of freedom, that is the choise of the voltages to be applied along the vertical direction. The method proposed in [23] consists in choosing a proper combination of voltages, whose final effect results in the application, to

each spectral component, of a sawtooth phase function along the vertical direction of the matrix. The overall result of this method is that every frequency component impinging on the LC-SLM sees a blazed phase grating (Figure 3.8), by which it will be diffracted according to well known grating equation:

$$d[\sin(\theta_m) - \sin(\theta_i)] = m\lambda \tag{3.2}$$

In the previous equation, d is grating period, m the diffraction order, Θ_m the angle at which the m-order beam is diffracted, Θ_i the incidence angle and λ the wavelength of the impinging spectral component.

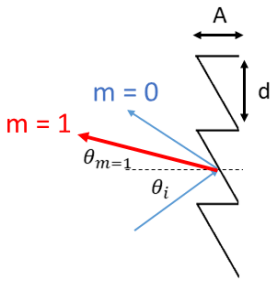

Figure 3.8: Diffraction of a monochromatic beam by a blazed grating with period d and amplitude A.

By aligning the pulse-shaper, it is possible to make the first order diffracted beam (Figure 3.8) go back to the cylindrical lens, in order to eventually get a collimated beam out of the pulse-shaper (Figure 3.9).

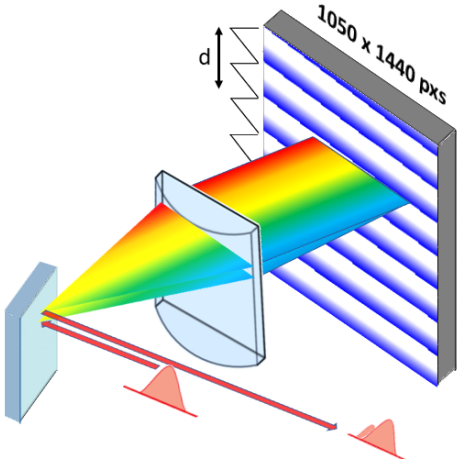

Figure 3.9: LC-SLM $4f$-folded geometry employed in our experiment.

In the experimental adopted framework (Figure 3.9) the LC-SLM mask can be hence regarded as a set of several blazed gratings, as many as the pixels along the horizontal direction. Therefore, a complete control on the first-order diffracted light can be achieved by modifying the parameters of each blazed grating. More precisely, the vertical position and the depth of each grating (A) can be modified in order to modulate respectively the spectral phase and the amplitude of the first-order diffracted beam. Experimentally, these phase and amplitude manipulations related to the sawtooth grating parameters are obtained by applying a proper combination (a *pattern*) of voltages at each pixel within the 2D matrix.

In order to illustrate how the pattern selection is mapped onto the amplitude and phase spectral features of the pulse, in Figure 3.10 we present four simple patterns that can be sent to the 2D LC-SLM and discuss the corresponding effects on the outcoming pulse.

- Figure 3.10(a): The same blazed grating is chosen throughout all the matrix. Therefore, each spectral component dispersed along the horizontal direction will see the same blazed grating. All the outcoming pulse modes will hence preserve their relative amplitude and phase relation. However, the absolute pulse amplitude will change, since only the first-order diffracted beam is analyzed.

- Figure 3.10(b): A blazed pattern is applied only in correspondence with certain pixels along the the dispersion direction (x). Only the dispersed frequency components impinging on the blazed grating will experience first-order diffraction and subsequently be refocused out of the $4f$-folded line. Therefore, applying this pattern is suitable to independently select the frequency content of the pulse without changing the phase relation among the selected spectral components. We will exploit such a pattern to modulate the local oscillator spectral content. We note once again that, since we are analyzing only the first-order of diffraction, the absolute amplitude of each modulated spectral component will be reduced.

- Figure 3.10(c): This pattern is similar to the one depicted in Figure 3.10(c) with the difference that a discontinuity has been introduced along the horizontal axis, affecting the phase properties of the pulse. Indeed, the grating of the second half of the matrix has been shifted by half of a period with respect to the first one. This implies that spectral components in the same portion keep their initial phase relation, but spectral components impinging on different halves of the matrix gain a relative phase shift of π. Conversely, the relative amplitudes are conserved along the whole horizontal axis.

- Figure 3.10(d): In this case both the amplitude and the vertical position of the grating have been modified along the LC-SLM horizontal axis. Indeed, the depth of the sawtooth grating increases going from the left to the right (and so does the diffraction efficiency), while the vertical position of the grating follows a quadratic trend along the horizontal axis. By applying this pattern we get a chirped [2] pulse with a linearly decreasing intensity. Applying a quadratic phase pattern (i.e. introducing a quadratic displacement of the blazed gratings along the vertical direction) is therefore suitable to control the temporal broadening of the pulse. In our experiment (Figure 3.3), we exploit this possibility of the LC-SLM to accurate control the probe temporal compression and to eventually ensure a short duration of the pump-probe overlap (approximatively 150 fs).

Until now we have only taken into account the situation in which a single beam impinges the shaping matrix. However, our pulse-shaper can be easily adapted to

[2]The pulse is chirped since we are introducing a quadratic frequency dependence of the spectral components phase. Therefore, the pulse phase velocity will scale linearly with the frequency, thus introducing a temporal chirp.

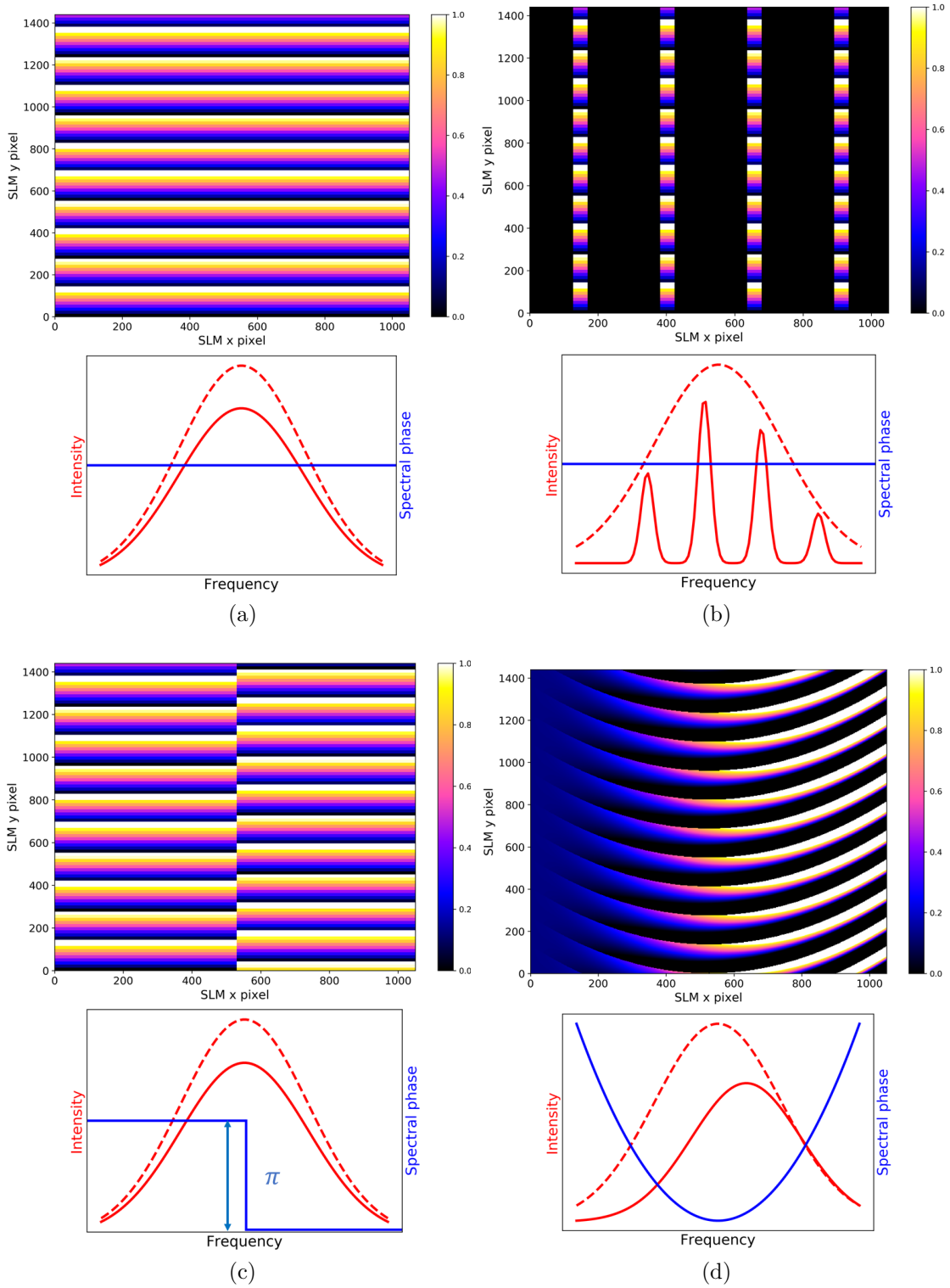

Figure 3.10: Representative example of 2D LC-SLM patterns. Below them the corresponding amplitude and phase features imprinted by the SLM pattern on an incoming gaussian pulse (dotted line).

perform multiple-beam shaping, that is a needed requirement to independently shape the signal and the local oscillator in our multimode homodyne set-up. The multiple-beam shaping can be accomplished by applying a different pattern in

distinct vertical portions of the SLM matrix. In Figure 3.11 we illustrate the double shaping configuration adopted in our set-up (Figure 3.3). The incoming local oscillator sees a grating pattern that enables its frequency selection. Conversely, the signal (probe) experiences a uniform pattern along the dispersion axis which does not modulate its spectral content. For the measurements presented in Chapter 5 and 6 we will adopt this double shaping configuration[3]. In Appendix B we instead present a case in which also the signal is shaped in its frequency content.

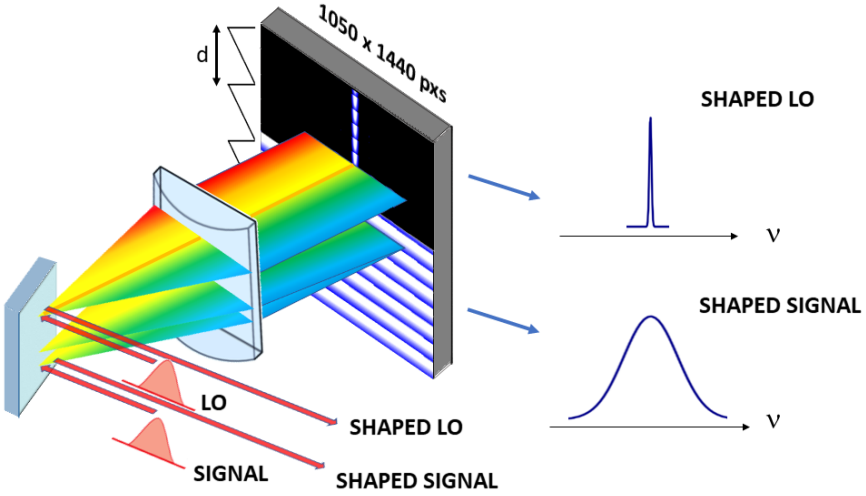

Figure 3.11: Double shaping configuration of both signal and local oscillator adopted in our LC-SLM.

Pulse-shaper calibration

In order to introduce these spectral features in a controlled manner, a calibration of the pulse-shaper is required. In particular, the following calibration tests are needed [32]:

- *Frequency calibration*, in order to retrieve which frequency component of the incoming pulse impinges on which pixel along the dispersion axis of the LC-SLM. In our experiment, this calibration is required to determine the selected frequency components of the shaped local oscillator.

- *Calibration of liquid crystals phase*, in order to know which voltage has to be applied in order to get the desired phase shift from the liquid crystal (Equation 3.1)

- *Amplitude calibration*, to obtain a relation between the blazed grating depth and the first-order diffracted amplitude.

- *Grating period calibration*: We note that, according to Equation 3.2, different frequencies would be diffracted in different directions by a grating

[3]Actually, the signal (probe) pattern has been modified in order to introduce a frequency dependence of the spectral phase (cfr Figure 3.10(d)). Through this modulation the probe temporal compression can be controlled.

having a fixed period. Since our purpose is to collimated the shaped beam in output of the $4f$-folded-line, we linearly increase the period of the gratings on which higher frequency spectral components impinge.

The fully characterization of the LC-SLM adopted in our set-up can be found in [34]. In the following, we illustrate only the frequency calibration of the shaped pulses. This is particularly crucial in our experiment (Figure 3.3), since it is the selection of the local oscillator frequencies that drives the selection of the correspondent modes in the probe field, thus allowing the frequency resolution of the homodyne detection.

The aim of the frequency calibration is to match each SLM horizontal pixel with the central frequency of its corresponding range and determine the spectral resolution of the pulse shaper. The latter consequently determines the frequency resolution of our multimode homodyne scheme. To achieve this purpose, we send to the LC-SLM a single mode pattern like the one depicted in Figure 3.12(a), in which a one-pixel-diffraction grating is applied at a specific horizontal position within the illuminate area of the LC-SLM. The result of the application of this pattern is that the first-order diffracted beam contains only the narrow band components which have impinged on the one-pixel grating. The outgoing beam from the pulse-shaper is detected by mean of a fiber spectrometer which allows to acquire the shaped spectrum (green line of Figure 3.12(b)). To determine the frequency position of the peak, we subtract the detected spectrum from its background and we eventually perform a gaussian fit on the rescaled peak. By repeating the previous procedure by changing the horizontal position of the one-pixel grating (Figure 3.12(a)) we can construct the graph presented in Figure 3.12(c). In this plot the central frequencies of the peaks estimated through the fit are plotted as a function of their corresponding SLM horizontal pixels at which the narrow gratings are centred. By fitting the red points of Figure 3.12(c) with a linear function, we get the whole frequency scale (black line) which assigns a specific frequency to each of the 1050 pixels.

The frequency difference between two neighbouring pixels determines the maximum spectral resolution $\Delta\omega$ of the pulse-shaper and hence of our frequency-resolved interferometer. For our pulse-shaper we have estimated $\Delta\omega \sim 0.1$ THz. In the homodyne framework, this implies that interference patterns originating by probe modes (Figure 3.3) that differ less then 0.1 THz can not be isolated. Consequently, supposing the shaped local oscillator to be a gaussian with standard deviation σ, in the frequency-resolved measurements presented in Chapter 5 and 6 we have always set $\sigma \geq 0.1$ THz.

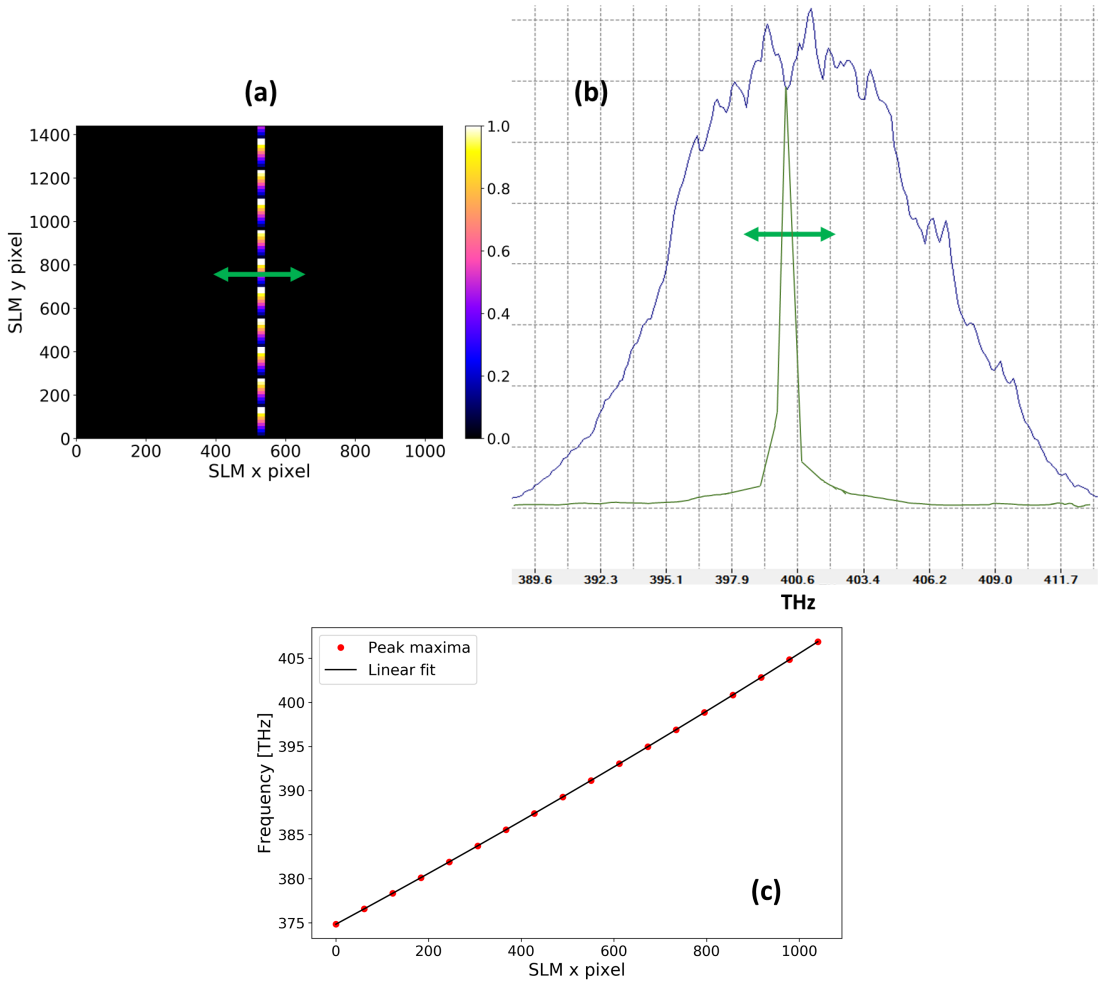

Figure 3.12: Frequency calibration of the LC-SLM pulse-shaper. In (a) the SLM pattern used for the frequency calibration procedure and in (b) the corresponding shaped spectrum (green line). For the frequency calibration, the single grating pattern is gradually shifted (green arrow) along the whole horizontal direction of the SLM matrix. In (c) the central frequencies (red dots) of the shaped single mode spectra for different horizontal position of the grating. In (c) the whole frequency scale (black line) is obtained through a linear fit.

3.3 Detection system

In this section we present the fundamental characteristic of the detection system employed in our set-up. Since we want to design an apparatus in which quantum noise sensitivity is contemplated, the following requirements has to be accomplished:

- In order to have access to statistical property of light, the detector electronic should be fast enough to separate the signals coming from different laser pulses. The laser produces pulses at a repetition rate of 200 kHz, that is a pulse every $\Delta\tau = 5$ μs. In order to acquire single pulses, the detector temporal response should hence be shorter than 5 μs.;

- The detector must operate a precise subtraction of the two photocurrents (Figure 3.3) in order to ensure a prefect balanced detection and eventually filter out the classical noise of the local oscillator (Section 1.2.1);

- The detector should be able to work in shot-noise conditions. This means that it has to be sensitive to fluctuations pertaining to the intrinsic quantum nature of light. To accomplish this requirement the detector should provide low noise to the differential current. The noise contribution given by the detector to the differential current is quantified by the efficiency parameter η_{eq} which describes the ratio between the shot-noise and the total noise at a certain intensity of the local oscillator. A complete characterization of the shot-noise sensitivity will be provided in Chapter 4.

In the following we describe how we have experimentally achieved the previously stated requirements.

3.3.1 Balanced detector and fast digitizer

The **detector** consists of two *Hamamatsu S3883* Silicon PIN photodiodes with quantum efficiency $\eta_{pd} = 0.94$ at 800 nm [7]. This means that the number of electrons produced by the diode is the 94% of the total number of photons impinging on it. The two photodiodes are connected in reverse bias and followed by a low noise charge amplifier. The reverse bias configuration allows to physically subtract the two photocurrents produced by the diodes, while the amplification takes place only at the final stage (i.e. after the subtraction). Performing the amplification after the physical subtraction permits not to increase the value of the noise produced by the electronic system. The charge amplifier sensitivity is 5.2 mV/fC, i.e. a detector response of 1 mV corresponds to approximatively 1.15×10^3 electrons [19]. In Figure 3.13 we present how the amplifier output voltage scales as a function of the number of photons impinging on a single diode. Up to 4 V (i.e. 3.0×10^6 ph/pulse) the relation is linear for either the positive and the negative diode.

The amplifier output voltage is digitized by a high speed **digitizer** ADC card (*Spectrum M2i*) with a dynamical range of 16 bit. The voltage digitalization is performed by exploiting the *Multiple Recording* option of the card, which allows to trig the acquisition to acquire only for a limited time-range each trigger. In fact, the repetition rate of the pulses is 200 kHz, which means that there is a 5

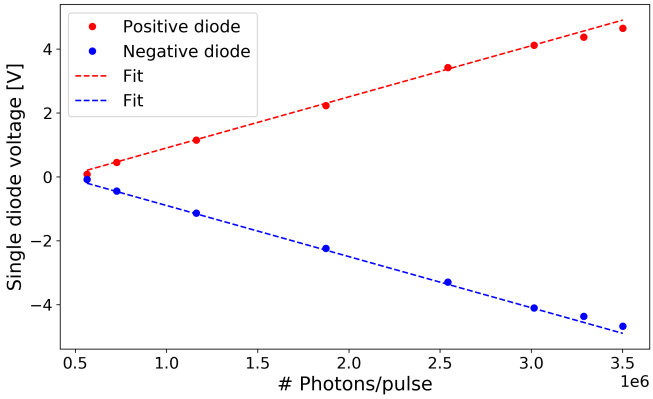

Figure 3.13: Linearity test of each diode of the balanced detector. The amplifier output voltage is measured on a single diode at an increasing photon fluence. The relation is linear up to 4 V (i.e. 3.0×10^6 ph/pulse).

μs interval between two successive pulses. Since the response of the diodes to a single pulse lasts for about 80 ns (Figure 3.15), a continuous acquisition of the output of the charge amplifier would contain mostly irrelevant data. Conversely, by using the *Multiple Recording* option and triggering the acquisition with copies of the pulse themselves, the acquisition is limited to the "duration" of the pulses[4], eliminating the dead times in between (Figure 3.14).

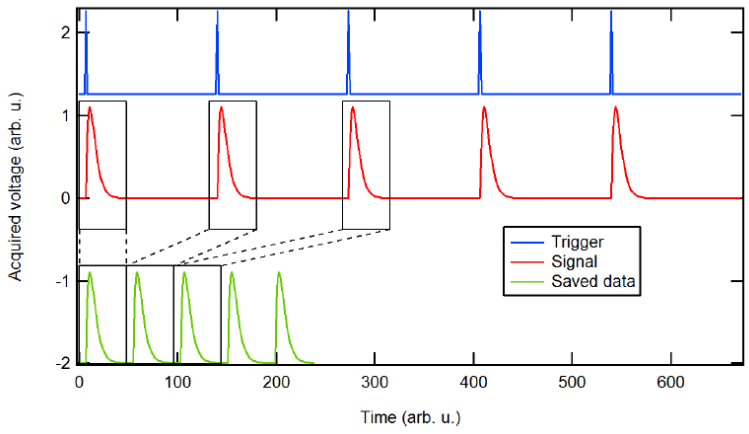

Figure 3.14: Working principle of the *Multiple recording* mode used in our digitizer [29].

Differential current integration

Once the detector response has been digitized, we need a systematic way to convert the acquired signal (Figure 3.14) to a number representative of the pulse intensity.

This single number has been obtained by performing the **scalar product** between the digitized pulse and the detector response and by subsequently integrating the so obtained pulse. The detector response has been measured by digitizing the output voltage of a single diode and by normalizing its response.

[4]Here, we refer as the actual "duration" of the pulse the temporal response of the diode which is approximatively 80 ns

The scalar product enables to apply different weights to different noise contribution. In particular, the negative time current fluctuations (i.e. before the pulse arrival), related to electronic noise, can be strongly reduced. With this integration process we can hence enhance the detection efficiency η_{eq}. In Figure 3.15 we illustrate an example of digitized pulses: the positive, negative and differential response are plotted. They are all multiplied by the normalized detector response measured on the positive channel. If the two channels are balanced, the differential current fluctuations (black line) map the intrinsic quantum noise (Section 1.2.1).

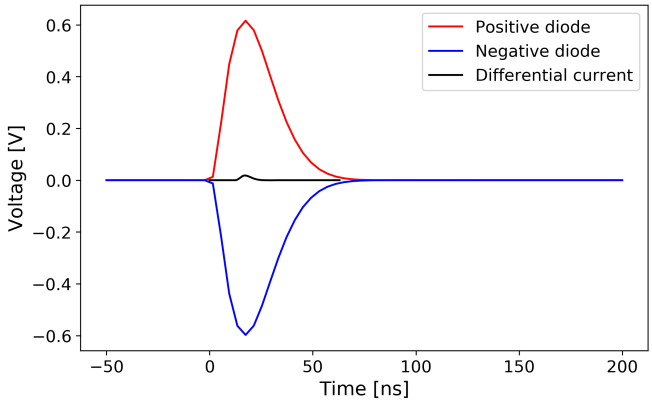

Figure 3.15: Positive, negative and differential current response multiplied by the normalized detector response. The latter has been obtained on the positive diode.

Chapter 4

Measuring quantum fluctuations: set-up noise calibration

Since the final purpose of the project is to retrieve intrinsic quantum fluctuations imprinted on an optical pulse by its non-linear interaction with matter, a systematic characterization of our set-up noise is essential. In Chapter 1 we have proved that through Balanced Homodyne Detection we are sensitive to intrinsic quantum fluctuations of an optical field that can be unveiled exploiting the potentiality of our set-up of performing single pulse acquisition (Section 3.3). These fluctuations are directly linked to the electromagnetic field quantization and correspond to the minimum detectable noise: the *shot-noise*.

The optical element required to reach the shot-noise limit is the 50:50 beam splitter (Section 1.2.1). Indeed, measuring the variance of the differential intensity between the outgoing beams of a 50:50 BS enables to eliminate the classical contribution to the total noise and keep only the partition one pertaining to the intrinsic quantum nature of light (Equation 1.32).

However, it is experimentally very hard to find an ideal 50:50 beam splitter. We have hence to introduce dissipative optical elements in the two output channels of the BS in order to work in balanced conditions. In this chapter we focus on the description of how the presence of these dissipative elements affects the noise detection. Unveiling this link is crucial in order to discriminate from the measured noise dynamics only the sample-dependent one. For the characterization of the quantum noise sensitivity of our set-up we will make use of the quantum model presented in [19]. This model is based on the assumption that any optical dissipative element can be described as an ideal beam splitter which splits the incoming beam in two.

Noise conditions have been tested by taking the signal in its vacuum state (Figure 4.1) and by performing two different tests:

- **Classical noise characterization**: The test is performed by measuring the differential intensity of BS outputs (homodyne current) for different unbalance conditions between the two channels. In this way, we can study how local oscillator classical fluctuations enter in the homodyne current noise.

- **Shot-noise test**: The test is performed by changing the local oscillator intensity in balanced conditions. With this experiment the shot-noise lin-

earity (Equation 1.32) can be tested and confronted with the theoretical prediction of the model [19].

Both the tests have been performed either in the low and high fluence regime of the local oscillator in order to characterize how detector non-linearities affect the noise detection and eventually select a suitable LO[1] fluence range for the measurements presented in Chapters 5 and 6.

Furthermore, we illustrate how collecting the signal statistics in its vacuum state (Figure 1.4) can be exploited to rescale the quadrature traces and eventually estimate from them the mean number of photons in the signal channel. We conclude the chapter by presenting the analysis of correlation between successive pulses, which is a test useful to check whether we are performing repeated measurements on the same quantum system.

4.1 Noise in unbalanced conditions

In Section 1.2.1 we have stated that measuring the homodyne response in balanced condition is the fundamental requirement of quantum noise sensitivity. In this section we preliminary study how classical fluctuations enter in the homodyne response as a consequence of an unbalance between the detected beams. Let us start with the ideal situation depicted in Figure 4.1 in which no dissipative processes occur. Moreover, we will consider the signal in its vacuum state $|0\rangle$ and study only how classical fluctuations from the local oscillator affect the differential current in unbalanced conditions. To achieve this purpose, let us recall the

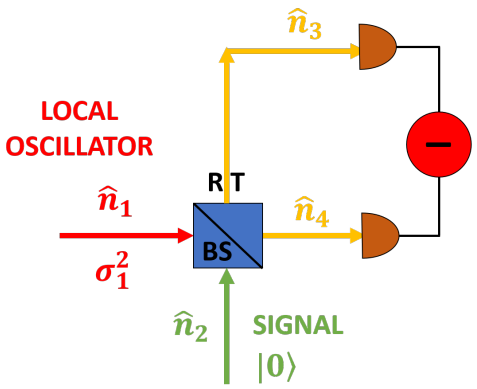

Figure 4.1: Homodyne detection in variable balancing conditions. In this simplified model, the balancing between the two channels is ruled by the BS parameters R and T.

variance of the differential current σ^2_{3-4} (Equation 1.31):

$$\begin{aligned}\sigma^2_{3-4} &= \left\langle (\hat{n}_3 - \hat{n}_4)^2 \right\rangle - \langle (\hat{n}_3 - \hat{n}_4) \rangle^2 \\ &= (|R|^2 - |T|^2)^2 \sigma_1^2 + 4|R|^2|T|^2\langle \hat{n}_1 \rangle\end{aligned} \tag{4.1}$$

[1]Local oscillator

and let us express it as a function of the mean homodyne current $\langle \hat{n}_{3-4} \rangle = (|R|^2 - |T|^2)\langle \hat{n}_1 \rangle$. We therefore get:

$$\sigma^2_{3-4} = \frac{\sigma^2_1 - \langle \hat{n}_1 \rangle}{\langle \hat{n}_1 \rangle^2} \langle \hat{n}_{3-4} \rangle^2 + \langle \hat{n}_1 \rangle \tag{4.2}$$

The previous equation shows that classical fluctuations of the local oscillator enter quadratically as a function of the unbalance $\langle \hat{n}_{3-4} \rangle$. Indeed, in the configuration of Figure 4.1 the variance of the homodyne current as a function of the unbalance is a parabola centred at the perfect balancing $\langle \hat{n}_{3-4} \rangle = 0$. In this situation, the local oscillator classical noise (σ^2_{3-4}) is completely filtered out by the subtraction and the detected noise σ^2_{3-4} is the minimum reachable one (*shot-noise*):

$$\sigma^2_{3-4} = \langle \hat{n}_1 \rangle \tag{4.3}$$

By looking at Equation 4.2, we note that if the local oscillator has a poissonian statistics (i.e. no classical field fluctuations σ^2_1 affect its statistics) the shot-noise condition is fulfilled for any detector unbalance $\langle \hat{n}_{3-4} \rangle$.

Conversely, if local oscillator has a statistics affected by classical noise (for example a super-poissonian statistics with $\sigma^2_1 > \langle \hat{n}_1 \rangle$) working in balanced condition is crucial to reach the shot-noise limit.

From the experimental point of view, the beam splitter before the detection system (Figure 3.3) can have a response that is not 50:50. The balanced configuration is therefore experimentally reached by introducing in the output channels of the BS dissipative optical elements whose response has to be taken into account when modelling the homodyne current variance (Section 4.2). The adopted set-up after the last beam splitter is presented in Figure 4.2. The balancing between the two detected beams is reached by changing the relative orientation of the $\lambda/2$ and the polarizer.

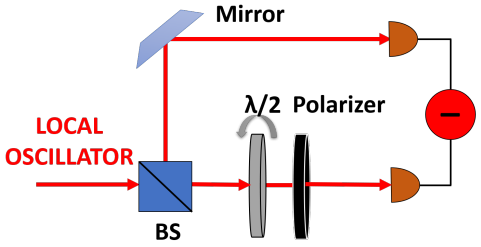

Figure 4.2: Experimental set-up adopted to balance the two outputs of the beam splitter. We balance the two detected beams by blocking the signal input beam and changing the relative orientation of the $\lambda/2$ and the polarizer.

4.2 Characterizing the set-up noise: the "Beam Splitter Model"

In the previous section we have pointed out the experimental necessity of introducing optical dissipative elements in beam splitter outputs in order to compensate the BS unbalance and eventually ensure a balanced detection. We expect

the presence of these optical elements to affect not only the mean value of the homodyne current, but also its variance. Therefore, in order to characterize the detected quadrature noise, we need a theoretical model in which optical dissipation is included. A suitable quantum model for this purpose is the one presented in [19] and goes under the name of "Beam Splitter Model".

The model is based on the hypothesis that any optical dissipative process can be described as a beam splitter which splits with a defined ratio a beam in two. This ratio is represented by the riflectivity/transmittance of the theoretical beam splitter and can be experimentally obtained by measuring the light intensity before and and after the dissipative optical element we want to model. Treating the optical dissipators as beam splitters is useful, since a beam splitter optical response can be easily studied in a quantum framework (Section 1.2.1).

In this theoretical framework, the set-up illustrated in Figure 4.2 can be represented trough the "Beam Splitter Model" as in Figure 4.3. We underline that, since we are working in a quantum framework, the theoretical beam splitters have always two entries, even if there is only one physical beam impinging on the modelled optical element [19]. In this case, the other theoretical BS input beam is represented by the photon vacuum state $|0\rangle$. Exploiting the BS formalism pre-

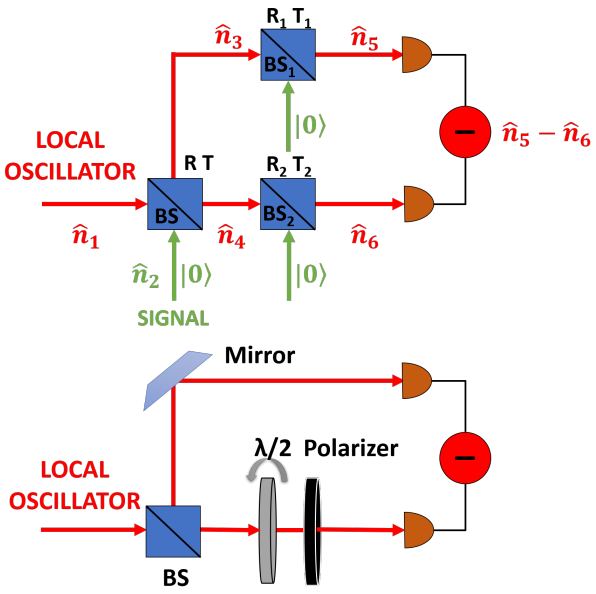

Figure 4.3: Modelization of our set-up (upper panel) by mean of the "Beam splitter model" (lower panel). In the upper panel the first beam-splitter (BS) correspond to the real beam-splitter, while BS_1 and BS_2 model two dissipative optical elements present in our set-up. BS_1 models the mirror, while BS_2 the couple $\lambda/2$-polarizer used to balance the two channels of the interferometer. The signal ($\hat{n}_2$) is supposed to be in its vacuum state $|0\rangle$.

sented in Section 1.2.1, we can evaluate for the set-up of Figure 4.3 the detected quantities in the homodyne measurement: the mean homodyne current $\langle \hat{n}_{5-6} \rangle$ and its variance σ^2_{5-6}. The first turns out to be:

$$\langle \hat{n}_{5-6} \rangle = |T_2|^2 |R|^2 \langle \hat{n}_1 \rangle - |T_1|^2 |T|^2 \langle \hat{n}_1 \rangle \tag{4.4}$$

while the latter reads:

$$\begin{aligned}\sigma^2_{5-6} &= \left\langle (\hat{n}_5 - \hat{n}_6)^2 \right\rangle - \langle (\hat{n}_5 - \hat{n}_6) \rangle^2 \\ &= \Big(|T_2|^2|R|^2 - |T_1|^2|T|^2)^2 \sigma_1^2 + \\ &+ (|T_2|^4|R|^4|T|^2 + |T_2|^2|R_2|^2|R|^2 + |T_1|^4|T|^2|R|^2 \\ &+ |T_1|^4|R_1|^2|T|^2 + 2|T_1|^2|T_2|^2|R|^2|T|^2 \Big) \langle \hat{n}_1 \rangle\end{aligned} \tag{4.5}$$

The previous equations clarify the necessity of working in balanced conditions in order to eliminate the local oscillator classical fluctuations. Indeed, we notice that by setting $\langle \hat{n}_{5-6} \rangle = 0$ the contribution to homodyne current noise proportional to σ_1^2 is cancelled.

Before going trough the detailed characterization of the homodyne current noise of our set-up, let us underline some peculiar features that the presence of optical dissipators introduces in the homodyne noise response. We will do it by mean of the "Beam splitter model" presented in Figure 4.3.

Classical noise characterization Let us exploit the model to preliminary predict how the variance of the differential current changes as a function of the unbalance $\langle \hat{n}_{5-6} \rangle$ (Figure 4.4). In the absence of optical dissipations (Figure 4.1), we have seen that the minimum noise level is reached at perfect balancing between the two channels (Equation 4.2).

Conversely, if optical dissipators are inserted in order to compensate the first BS unbalance, Figure 4.4 suggests that this is not true anymore. Indeed, the vari-

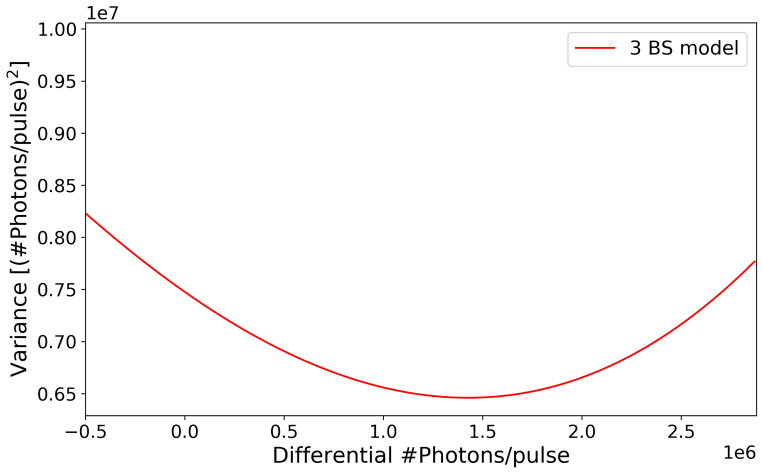

Figure 4.4: Variance of the differential current as a function of the unbalance predicted with the ideal set-up presented in Figure 4.3 ("3 Beam splitter model"). In the present plot the local oscillator has an intensity of 7.8×10^6 ph/pulse. For this example, the BS parameters inside the simulation are the same of Figure 4.8.

ance of the differential current exhibits a quasi-quadratic trend whose minimum noise level is not reached at perfect balancing (i.e. at $\langle \hat{n}_{5-6} \rangle = 0$). We will denote with $\langle \hat{n}_{5-6} \rangle_{min}$ the mean homodyne current corresponding to the minimum detected noise.

Moreover, the "Beam splitter model" (Figure 4.3) predicts that, in presence of optical dissipators, the minimum noise position is sensitive to classical fluctuations of the local oscillator σ_1^2 (Figure 4.5). In particular, if the local oscillator classical noise increases, $\langle \widehat{n}_{5-6} \rangle_{min}$ decreases, although it does not change sign (Figure 4.5). This effect is related to the presence of dissipators in the two

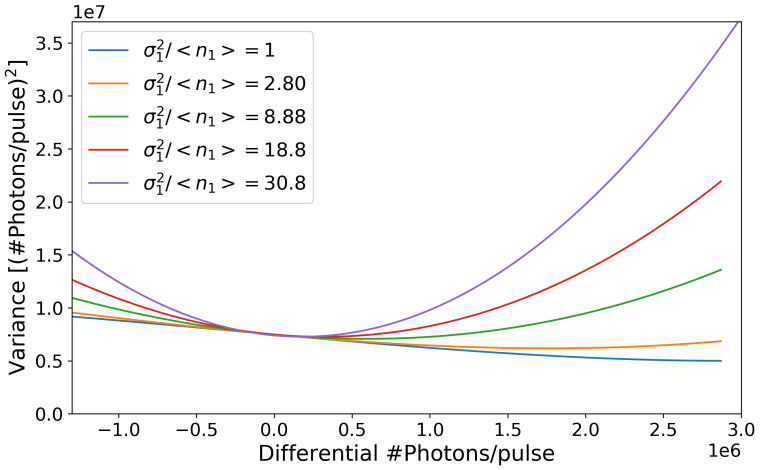

Figure 4.5: Variance of the differential current σ_{5-6}^2 as a function of the photon number unbalance $\langle \widehat{n}_{5-6} \rangle$ for different noise conditions of the local oscillator. The LO input noise is expressed as its variance-to-mean ratio ($\sigma_1^2/\langle \widehat{n}_1 \rangle$), where $\langle \widehat{n}_1 \rangle$ is hold constant to 7.8×10^6 ph/pulse. The BS parameters inside the simulation are the same of Figure 4.8.

channels, since in the ideal single beam splitter case (Figure 4.1) the minimum noise level is reached at perfect balancing for any local oscillator noise condition (Equation 4.2).

Shot-noise Let us now predict through the "Beam Splitter Model" how the presence of the dissipators is mapped into the shot-noise test. Combining Equations 4.4 and 4.5, we see that if the detected beams are perfectly balanced ($\langle \widehat{n}_{5-6} \rangle = 0$) the variance of the homodyne current (σ_{5-6}^2) scales linearly with the local oscillator intensity. More important, its contributions proportional to local oscillator classical noise (σ_1^2) are null. Indeed, by setting $\langle \widehat{n}_{5-6} \rangle = 0$, we get:

$$\begin{aligned} \sigma_{5-6}^2 =& (|T_1|^4|R|^4|T|^2 + |T_1|^2|R_1|^2|R|^2 + |T_2|^4|T|^2|R|^2 \\ &+ |T_2|^4|R_2|^2|T|^2 + 2|T_2|^2|T_1|^2|R|^2|T|^2\Big)\langle \widehat{n}_1 \rangle \end{aligned} \tag{4.6}$$

which is independent on σ_1^2.

In Figure 4.6 we exploit the "3 Beam splitter model" (Figure 4.3) to illustrate how the shot-noise trend is influenced by the presence of optical dissipators. Figure 4.6 shows that the variance of the homodyne current is linear with the local oscillator intensity, but its slope is less than the one corresponding to the case in which no optical dissipations are present (grey line of Figure 4.6). This singular feature predicted by the model is a consequence of the photon number loss caused by the optical dissipators. In shot-noise conditions, a photon loss is indeed mapped into a decrease of the homodyne current variance proportional

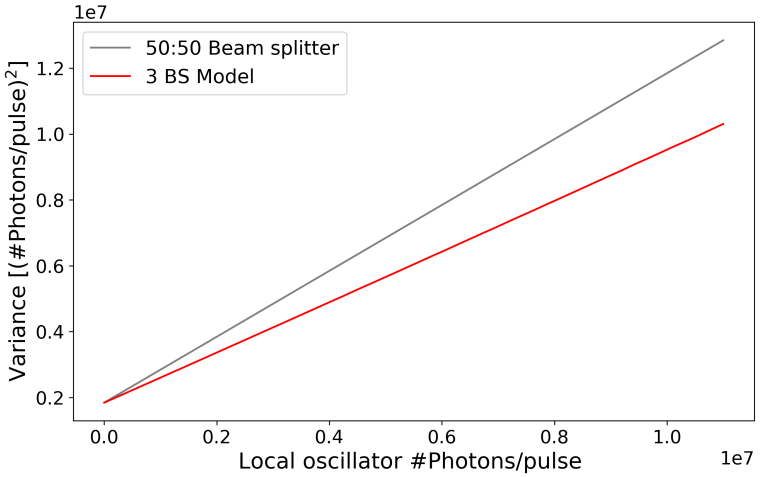

Figure 4.6: Shot-noise test: Variance of the homodyne current as a function of the LO intensity predicted in the case of the ideal set-up presented in Figure 4.3 ("3 Beam splitter model"). For this example, the employed BS parameters are the same of Figure 4.9. In grey, the noise trend predicted in the absence of optical dissipators (i.e. only with a single 50:50 balanced beam splitter as in Figure 4.10). In the presented plot the variance of the homodyne current is not null when the local oscillator is in a vacuum state only because there is the electronic noise contribution of the detection system (Section 4.2.1).

to the loss itself (cfr Equation 4.6). In the "3 Beam splitter" framework we can exploit Equation 4.6 to quantify it:

$$\begin{aligned} r = \frac{\sigma^2_{5-6}}{\langle \widehat{n}_1 \rangle} =& (|T_1|^4|R|^4|T|^2 + |T_1|^2|R_1|^2|R|^2 + |T_2|^4|T|^2|R|^2 \\ &+ |T_2|^4|R_2|^2|T|^2 + 2|T_2|^2|T_1|^2|R|^2|T|^2\big) \end{aligned} \tag{4.7}$$

In the previous equation, r represents the poissonian noise loss of the local oscillator due to optical inefficiencies.

After these preliminary considerations, we will exploit the "Beam splitter model" for quantitative prediction of the homodyne current noise detected in our set-up. We will do it either in the low ($\sim 10^6$ ph/pulse) and in the high ($\sim 10^8$ ph/pulse) fluence regime of the local oscillator. This is crucial to study how detector non-linear response affects the detected noise and to consequently select a suitable local oscillator intensity regime. For both the LO fluences regime we measure either the variance of the differential current as a function of the unbalance and the shot-noise test in the balanced configuration. In both the situations the signal is blocked and therefore it is in its vacuum state.

4.2.1 Local oscillator low fluence regime

In this section the quantitative noise characterization in the low fluence regime of the local oscillator (i.e. up to 8.2×10^6 ph/pulse) is presented. The detected differential variance is compared with the theoretical response (Equation 4.6) obtained with the "3 Beam splitter model" in the configuration of Figure 4.3. For the quantitative comparison we need to know the transmittances parameters of

the model beam splitters. The latter can be experimentally retrieved by measuring the ratio between the intensity of the outgoing and incoming beam from the optical element we want to represent as a BS (i.e. the initial BS, the mirror and the couple $\lambda/2$-polarizer (Figure 4.3)).

Moreover, by looking at Equation 4.6, a parameter required for the theoretical estimation of the differential current noise is the variance σ_1^2 of the incoming local oscillator. The latter can be evaluated by measuring the variance of the integrals of a pulse train (typically 800 pulses) on a single diode of the detector. In order to filter out classical slow noises, the variance has not been calculated over the full train pulse. We have decided indeed to evaluate it by averaging the variances calculated over smaller pulse subsets of 10 pulses each. In this way, noises slower then the duration of a train of 10 pulses (50 μs at 200 kHz) can be filtered. All the experimental variances presented in the following paragraphs have been obtained through this filtering procedure. At a local oscillator fluence of 7.8×10^6 ph/pulse we have measured:

$$\sigma_1^2 = 3.0 \times 10^7 (ph/pulse)^2 \tag{4.8}$$

Therefore, at this intensity the local oscillator variance-to-mean ratio reads:

$$\frac{\sigma_1^2}{\langle \widehat{n_1} \rangle} = 3.8 \tag{4.9}$$

unveiling the super-poissonian nature of its statistics.

Electronic noise We stress that until now we have not taken into account the contribution to the homodyne current variance due to the electronic noise of the detection system. This noise is independent on local oscillator intensity and is due to any non-desirable ambient noise, dark current noise from the diodes and to the intrinsic noise of the charge amplifier. Electronic noise can be estimated by measuring the variance of the differential current with the two channels blocked, which corresponds to the detected noise before the arrival of each pulse (Figure 4.7). The effect of electronic noise is to add a random quantity δ to each homodyne

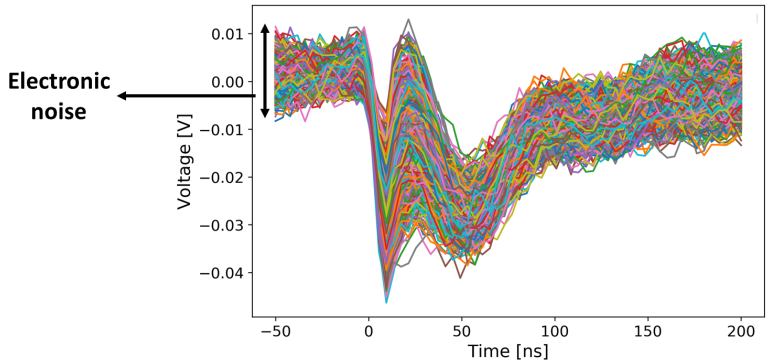

Figure 4.7: Digitized differential current of a train of 800 pulses with indicated the electronic noise background at negative times (i.e. before the pulse arrival). The presented pulses are digitized with a dynamical range of 500 mV.

current measure [30]:

$$I_{\phi_j}^{meas} = I_{\phi_j} + \delta \tag{4.10}$$

Since the electronic noise is independent on fluctuations of the local oscillator, we can take δ as a stochastic gaussian variable [35] whose statistics is independent on the local oscillator one. For this reason, photon-dependent fluctuations and electronic ones can be added. Therefore, electronic fluctuations enter as a costant background noise in the homodyne current statistics. They can hence be added to the variance predicted by the "3 Beam Splitter model" (Equation 4.5) in order to compare it with the experimental results.

In the following we present the noise characterizations of the homodyne photocurrent in the low intensity regime of the local oscillator.

Classical noise characterization In Figure 4.8 we present the measured variance as a function of the unbalance for a local oscillator of 7.8×10^6 ph/pulse and the comparison with the "3 Beam splitter model" (Equation 4.5) with the experimental transmittances of the ideal beam splitters of Figure 4.8(c). The unbalance between the two channels is achieved by changing the relative orientation of the $\lambda/2$ and the polarizer. In the theoretical "3 Beam splitter model" this correspond to change the transmittance $|T_2|^2$ of BS_2 (Figure 4.8(c)). As previuosly anticipated, we notice that the minimum noise level is not reached at perfect balancing.

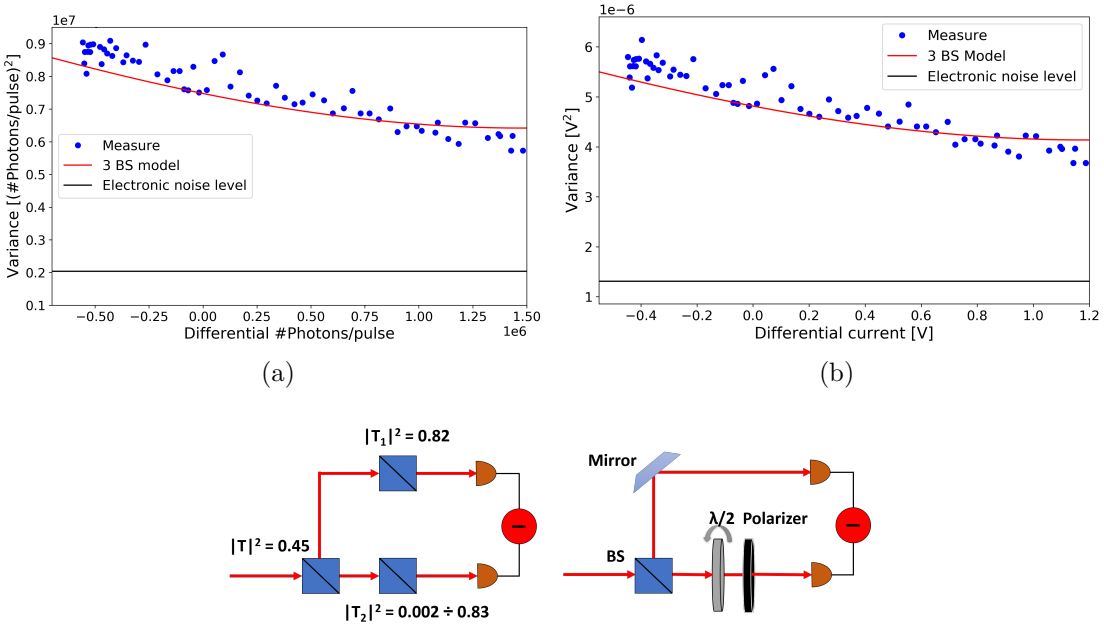

Figure 4.8: Variance of the homodyne current as a function of the unbalance in the LO low fluence regime (7.8×10^6 ph/pulse). In (a) the unbalance is measured as the differential number of photons/pulse, while in (b) as the differential current. In red the "3 BS model" prediction shifted by the electronic noise background (black line) and evaluated with the ideal beam splitter parameters measured from the set-up (c)

Shot-noise test In Figure 4.9 we present the shot-noise test performed on our set-up in balanced conditions and the comparison with the "3 Beam splitter model" (Equation 4.6). We have adopted the balanced configuration, since the model predicts that this is the only situation in which the homodyne current variance has no contribution from the local oscillator classical fluctuations (Equation 4.6). The increase of the local oscillator intensity ($\langle \hat{n}_1 \rangle$) has been performed by tuning the efficiency of the LC-Spatial Light Modulator (Section 3.2.1). Figure

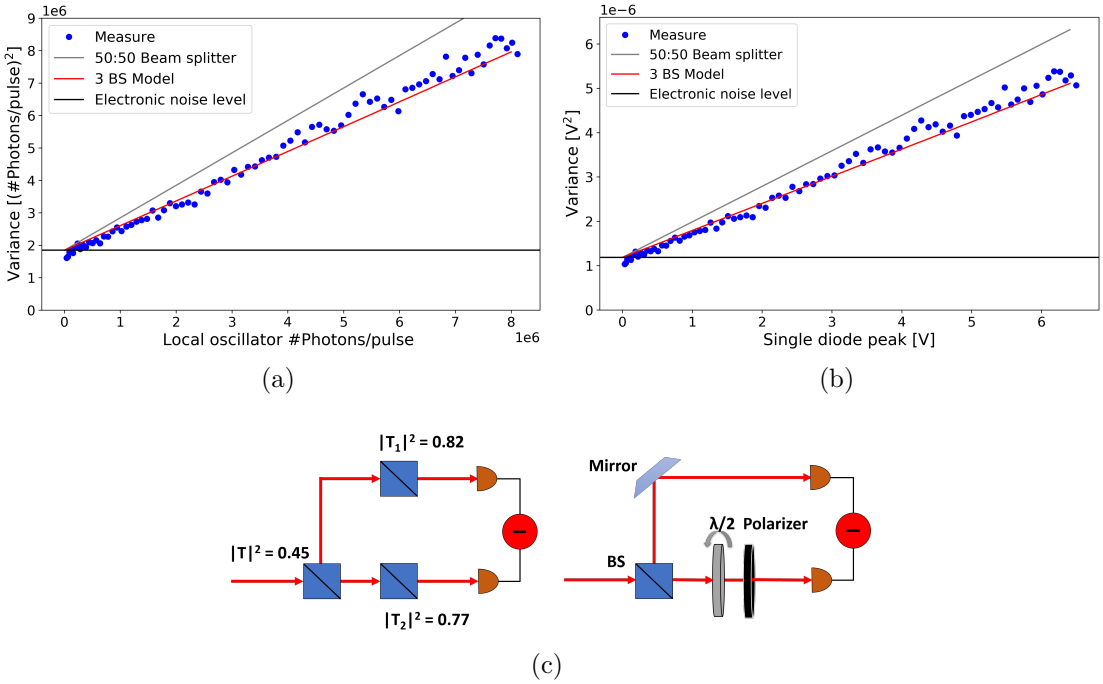

Figure 4.9: Shot-noise test for our homodyne set-up in the LO low fluence regime ($3.9\times 10^4 - 8.2\times 10^6$ ph/pulse) and comparison with the "3 BS model" trend (red) shifted by the electronic noise level (black). In (a) the variance measured as function of LO number of photons per pulse, in (b) as a function of the voltage peak as measured by a single diode. In (c) the 3 BS transmittances measured in our set-up. In (a) and (b) the grey line represents the shot-noise trend in the ideal case ($|T|^2 = 0.5$, $|T_1|^2 = |T_2|^2 = 1$) in which no optical dissipations occur (configuration of Figure 4.10).

4.9 shows that the measured variance trend increases linearly with the LO intensity, but with a slower rate with respect to the case of a single 50:50 balanced BS (grey line) (Figure 4.10). The "3 Beam splitter model" confirms the experimental trend, proving the fact that the lower experimental slope is related to the presence of optical dissipators (i.e. BS_1 and BS_2 of Figure 4.9). These dissipators cause a decrease of the shot-to-noise ratio at any local oscillator intensity.

4.2.2 Local oscillator high fluence regime

In the ideal homodyne measurement (Figure 4.10) we can work in the local oscillator shot-noise regime whatever is its intensity. This is true because in the ideal framework we are neglecting any photon-dependent noise contribution introduced by the detection system.

In this section we characterize this additional detector noise contribution. We perform this analysis with the aim of selecting an operative local oscillator intensity that minimize this detection noise and simultaneously maximize the shot-to-electronic-noise ratio. We will consider as high fluence regime, local oscillator

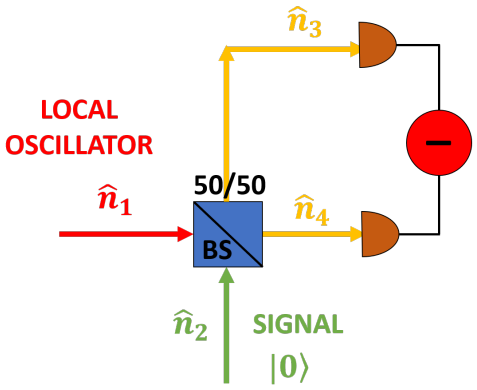

Figure 4.10: Ideal homodyne experiment with a signal in vacuum state.

intensities up to 7.9×10^8 ph/pulse. In Figure 4.11 we present the characterization of the detected differential variance for the set-up in Figure 4.3 in the case of a local oscillator with an intensity of 7.9×10^8 ph/pulse. Furthermore, we compare it with the "3 Beam splitter model" with the measured BS transmittances of Figure4.11(c), supposing that also in this fluence regime the variance-to-mean ratio of the incoming local oscillator is the same of the low fluence case (i.e. $\sigma_1^2/\langle\hat{n}_1\rangle = 3.8$).

We note that the experimental variance trend as a function of the unbalance is flat in the non-saturating range of the detector[2] and it is positive-shifted with respect to the "3 Beam splitter model" prevision[3]. We underline that the extra noise is intrinsic of the detection apparatus and not due to an increase of the variance-to-mean ratio of the incoming local oscillator ($\sigma_1/\langle\hat{n}_1\rangle$) caused by a non-linear increment of the LO classical fluctuations. Indeed, as shown in Figure 4.5, the leading effect of an increase of the classical fluctuations of the local oscillator is a change of the concavity of the variance trend and not its rigid shift. The presence of this photon-dependent detector noise also affects the shot-noise measurement (Figure 4.12). Indeed, it causes a non-linear deviation from the theoretical variance trend predicted by the "3 Beam splitter model".

We want now to retrieve in the "3 Beam splitter model" framework (Figure 4.3) the experimental variances trends shown in Figure 4.11 and 4.12. The lat-

[2]The variance has a flat trend only because the high LO intensity allows to work only in a limited range of the unbalancing parameter $|T_2|^2$ without saturating the detector. The sudden variance decrease is to be attributed to detector saturation.

[3]The theoretical variance prevision has been shifted by the photon-independent electronic noise background. However, since the latter is 1000 times smaller than the detected variance, its level is not visible in Figure 4.11

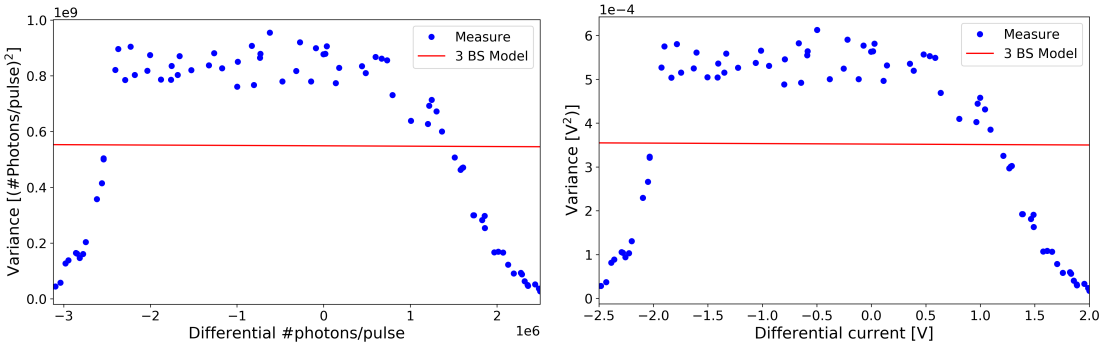

(a) (b)

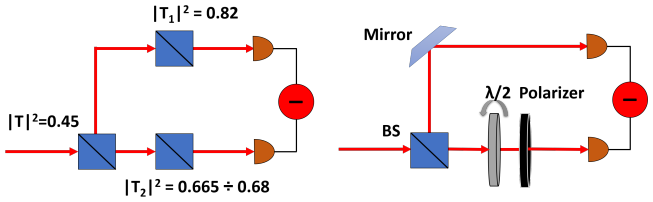

(c)

Figure 4.11: Variance of the homodyne current as a function of the unbalance in the LO high fluence regime (7.9×10^8 ph/pulse). In red the noise trend predicted by the ideal "3 BS model" with the measured transmittances presented in (c). For the comparison, the variance-to-mean ratio of the incoming local oscillator is supposed to be the same of the low fluence case ($\sigma_1^2/\langle\hat{n}_1\rangle = 3.8$).

ter are both affected by the photon-dependent detection noise that we will add numerically. With reference to the ideal "3 BS" set-up of Figure 4.3 we model the number of photons inside the i^{th} pulse of the incoming LO as a stochastic variable of the form:

$$n_1^i = n_{Poisson}^i + g\langle n_1\rangle x_{Gauss}^i \tag{4.11}$$

In the previous expression $n_{Poisson}^i$ is a poissonian variable whit expectation value $\langle\hat{n}_1\rangle$, while x_{Gauss}^i is a random variable with a normal gaussian distribution. The parameter g is tuned in order to have a variance-to-mean ratio of the LO comparable with that obtained from the single channel measure (Equation 4.9). Moreover, we simulate each ideal beam splitter (Figure 4.3) as a random divider object that splits the incoming n^i photons in two parts. The random division follows a poissonian statistics ruled by the transmission ($|T|^2$) and reflection ($|R|^2 = 1 - |T|^2$) beam splitter probabilities. We numerically introduce the detector noise inside the statistics of the two detected beams (n_5 and n_6 of Figure 4.3) in the following way:

$$\begin{aligned} n_{5,\,det}^i &= n_5^i + k\langle n_5\rangle x_{Gauss}^i \\ n_{6,\,det}^i &= n_6^i + k\langle n_6\rangle x_{Gauss}^i \end{aligned} \tag{4.12}$$

where x_{Gauss}^i is a stochastic variable with a normal gaussian distribution. We therefore suppose that the effect of the detector noise is to add a random response of each diode proportional to the mean number of photons impinging on

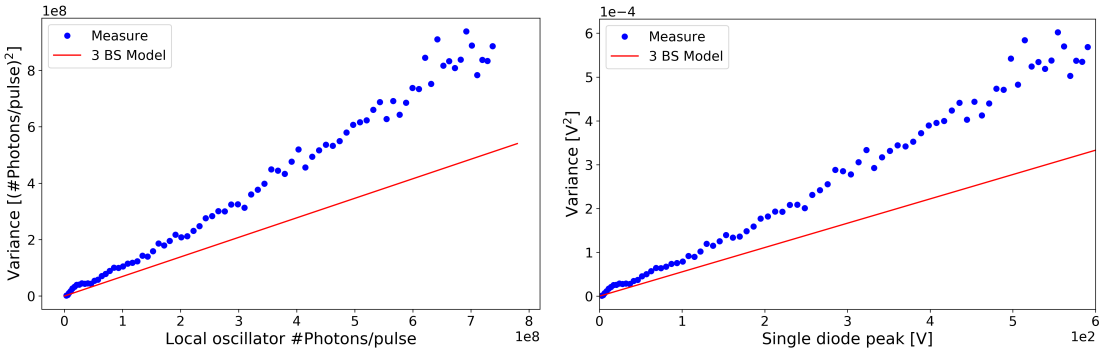

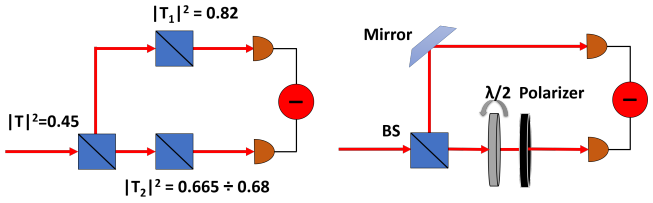

Figure 4.12: Shot-noise test in the LO high fluence regime (up to 7.9×10^8 ph/pulse). In red the noise trend predicted by the ideal "3 BS model" with the measured transmittances presented in (c). For the comparison, the variance-to-mean ratio of the incoming local oscillator is supposed to be the same of the low fluence case ($\sigma_1^2/\langle\hat{n}_1\rangle = 3.8$).

it. The parameter k inside the simulated response of each channel (n_5 and n_6) represents the strength of this multiplicative noise. By setting $k = 5 \times 10^{-5}$ we can qualitatively retrieve either the variance dynamics in function of the unbalance (Figure 4.13) and the shot-noise test trend (Figure 4.14) in the high fluence regime of the local oscillator.
For the measurements presented in Chapter 5 and 6 we adopt a local oscillator intensity of approximatively 1.0×10^7 ph/pulse. For this fluence we are still in the linear variance range with a shot-to-electronic-noise ratio of 7 dB.

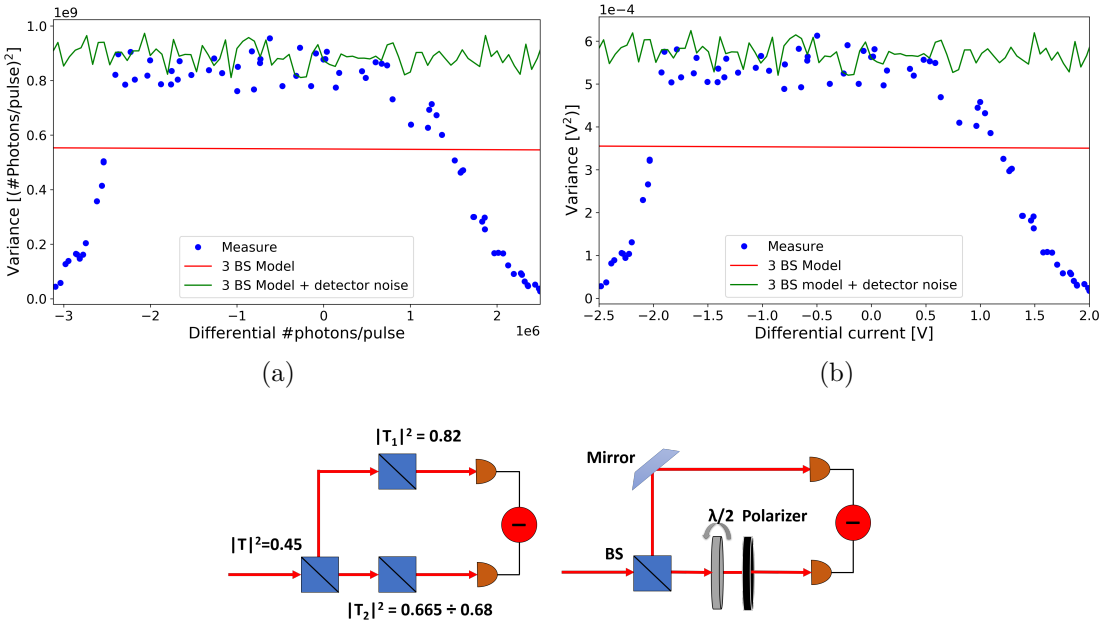

Figure 4.13: Noise trend as a function of the unbalance in the LO high fluence regime (7.9×10^8 ph/pulse). In red the noise trend predicted by the "3 BS model". In green the simulated noise trend, supposing the presence of a multiplicative noise introduced by both the diodes (Equation 4.12).

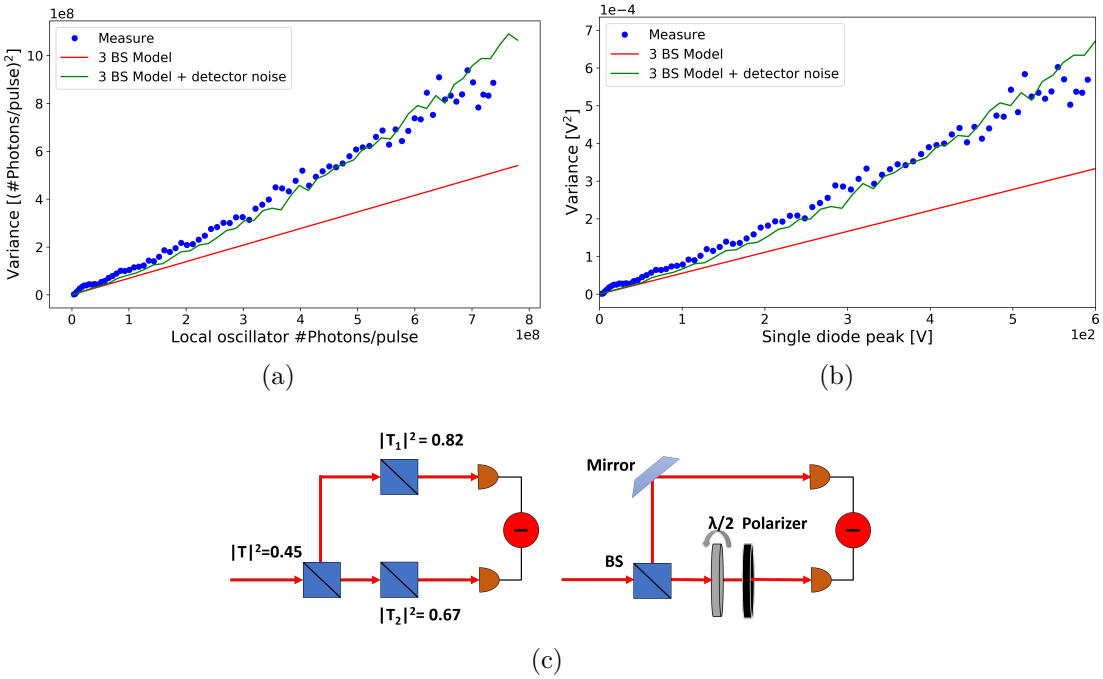

Figure 4.14: Shot-noise test for our homodyne set-up in the LO low fluence regime ($3.5 \times 10^6 - 7.4 \times 10^8$ ph/pulse) and comparison with the "3 BS model" trend (red). In green the simulated noise trend, supposing the presence of a multiplicative noise introduced by both the diodes (Equation 4.12).

4.3 Defining quadrature units: vacuum noise calibration

In the present section we see how we can exploit the measurement of the statistics of the signal vacuum state to calibrate the homodyne current and eventually retrieve from it the signal quadrature X_{ϕ_j}. This is crucial since the measured quadrature encodes amplitude and phase statistics of the signal electric field (Equation 1.10). We have already proved (Equation 1.18) that the measured differential current[4] $I_{\phi_j}^{meas}$ at a fixed LO phase ϕ_j is proportional to the signal quadrature field. We can express this proportionality as:

$$I_{\phi_j}^{meas} = \gamma X_{\phi_j} \tag{4.13}$$

Since our purpose is to retrieve the proportionality factor γ, we need a reference data whose quadrature statistics is known *a priori*. This is the case of the signal quadrature vacuum state whose variance σ_0^2 is phase-independent and equal to 1/2:

$$\sigma_0^2 \equiv \sigma^2[\widehat{X}_{\phi_j}]_{|0\rangle} = \langle \widehat{X}_{\phi_j}^2 \rangle_{|0\rangle} - \langle \widehat{X}_{\phi_j} \rangle_{|0\rangle}^2 = Tr[\widehat{X}_{\phi_j}^2 |0\rangle\langle 0|] = \langle 0| \frac{\widehat{a}_j^\dagger \widehat{a}_j}{2} |0\rangle = \frac{1}{2} \tag{4.14}$$

The latter is proportional to the observable homodyne current variance $(\sigma_0^{meas})^2$ which, exploiting Equation 4.13, reads:

$$(\sigma_0^{meas})^2 = \gamma^2 \sigma_0^2 = \frac{\gamma^2}{2} \tag{4.15}$$

$(\sigma_0^{meas})^2$ can be experimentally retrieved by measuring the variance of the differential current with the signal channel blocked. Indeed, through homodyne we are able to map the vacuum fluctuations of the signal field onto the partition noise of the local oscillator (Figure 1.4). Once measured $(\sigma_0^{meas})^2$, we can subsequently evaluate the homodyne trace scaling factor γ (Equation 4.13):

$$\gamma = \sqrt{2(\sigma_0^{meas})^2} \tag{4.16}$$

In the previous treatment we have not taken into account the electronic noise contribution to homodyne photocurrent variance (Figure 4.7). Following [3], the latter can be treated as an optical loss channel with an equivalent transmission efficiency given by:

$$\eta = \frac{A}{A+B} = \left(\frac{\gamma^2}{\gamma'^2} \right) \tag{4.17}$$

In the previous equation A and B represent respectively the shot and electronic noise contribution to homodyne photocurrent variance (Figure 4.15), while γ' is the rescaling quadrature factor which includes the electronic noise loss. Actually, inside η we have also to consider photodiodes inefficiencies. The latter are quantified by their nominal quantum efficiency: $\eta_{pd} = 0.94$ [7]. Contempleting also this loss channel, we get:

$$\eta_{eq} = \eta \eta_{pd} \tag{4.18}$$

[4]Only the j^{th} mode of the local oscillator is considered.

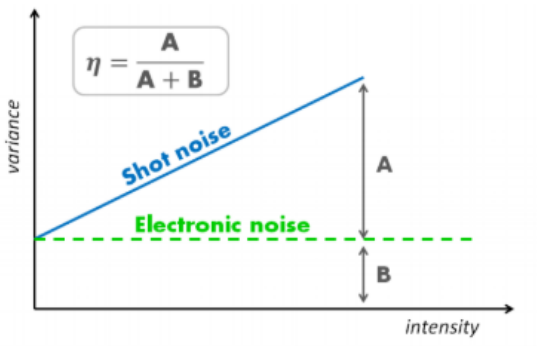

Figure 4.15: Shot-noise and electronic noise contribution to homodyne current variance.

For a local oscillator in low intensity regime (7.8×10^6 ph/pulse), we have measured $\eta_{eq} = 0.68$. Consequently, the rescaled signal quadrature trace in terms of the observable differential current $I_{\phi_j}^{meas}$ reads:

$$X_{\phi_j} = \frac{I_{\phi_j}^{meas}}{\gamma'} = \sqrt{\eta_{eq}} \frac{I_{\phi_j}^{meas}}{\gamma} = \sqrt{\eta_{eq}} \frac{I_{\phi_j}^{meas}}{\sqrt{2(\sigma_0^{meas})^2}} \tag{4.19}$$

In Figure 4.16 we present the rescaled homodyne traces in the case of a signal in vacuum state (a) and in a coherent state (b). In both the cases the local oscillator is frequency-shaped (Figure 3.3) and therefore the homodyne traces are representative of a single mode of the signal electric field. We stress that, by mean of the rescaling procedure, both the vacuum and that coherent signal state have a variance 1/2, as theoretically expected [30]. Indeed, any classical noise fluctuations is filtered out through the homodyne acquisition. Conversely, the unavoidable electronic noise will entry as a loss channel, thus reducing the amplitude of the quadrature oscillations (Equation 4.19). The rescaled homodyne

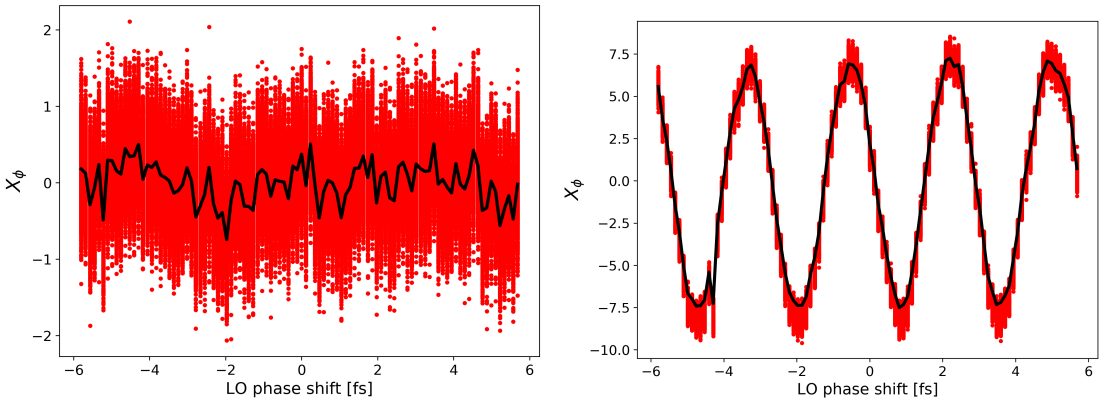

(a) (b)

Figure 4.16: Rescaled quadrature traces. In (a) the quadrature corresponding to the signal vacuum state. In (b) the rescaled quadrature of a signal in a coherent state. In black the mean value quadratures, while in red their statistical distribution, resulting from the independent integration of 800 pulses at each local oscillator phase.

traces can be exploited to evaluate the mean number of photons of the signal field

($\langle\widehat{n}\rangle$). Supposing the signal to be in a coherent state $|\alpha\rangle$, the quadrature of its j^{th} mode reads (Equation 1.22):

$$\langle\widehat{X}_{\phi_j}\rangle = Tr[\widehat{X}_{\phi_j}|\alpha\rangle\langle\alpha|] = \langle\alpha|\frac{\widehat{a}_j e^{-i\phi_j} + \widehat{a}_j^{\dagger} e^{i\phi_j}}{\sqrt{2}}|\alpha\rangle = \sqrt{2}|\alpha|\cos(\phi_j) \tag{4.20}$$

Therefore, if we now fit the rescaled quadrature (Equation 4.19) with a sinusoidal function of the form:

$$f(t) = A_0 + A'\cos(\omega_j t + \phi_0) \tag{4.21}$$

and we compare the amplitude parameter A' with the coherent state quadrature (Equation 4.20) we can estimate $\langle\widehat{n}\rangle$ as follows:

$$\langle\widehat{n}\rangle = |\alpha|^2 = \frac{A'^2}{2} = \sqrt{\eta_{eq}}\frac{|I_{\phi_j}^{meas}|^{max}}{2\gamma} = \sqrt{\eta_{eq}}\frac{|I_{\phi_j}^{meas}|^{max}}{2\sqrt{2(\sigma_0^{meas})^2}} \tag{4.22}$$

In the previous equation we have denoted with $|I_{\phi_j}^{meas}|^{max}$ the maximum extent of the homodyne current oscillations experimentally measured. In Table 4.1 we report the estimations of the number of photons in the signal channel ($\langle\widehat{n}\rangle$) for different local oscillators intensity. In the table, the estimation of $\langle\widehat{n}\rangle$ from the homodyne trace is compared with that obtained by measuring the photocurrent on a single diode of the detector. In the absence of any electronic noise, we expect the two photon estimations to coincide. However, from Table 4.1 we note that the ratio between the number of photons estimated from the single diode ($\langle\widehat{n}\rangle$(Diode)) and the one evaluated from the homodyne trace ($\langle\widehat{n}\rangle$(Homodyne)) increases at higher local oscillator intensities. This trend is due to the presence of the photon-dependent detection noise pointed out in Section 4.2.2 which enters as an inefficiency in the rescaled homodyne trace X_{ϕ_j} (Equation 4.19). Indeed, by looking at Equation 4.19, an extra detection noise causes an increment of $(\sigma_0^{meas})^2$ and hence a decrease of the rescaled signal quadrature amplitude X_{ϕ_j}.

Local oscillator ph/pulse	$\langle\widehat{n}\rangle$ (Single diode)	$\langle\widehat{n}\rangle$ (Homodyne trace)	($\langle\widehat{n}\rangle$ (Diode))/ ($\langle\widehat{n}\rangle$ (Homodyne))
$\mathbf{1.3 \times 10^8}$	1.6×10^4	6.8×10^2	23
	6.6×10^3	2.8×10^2	24
	1.7×10^3	6.6×10^1	26
$\mathbf{5.5 \times 10^7}$	6.5×10^3	3.2×10^2	20
	6.6×10^3	2.8×10^2	24
	7.0×10^2	3.2×10^2	20
$\mathbf{3.4 \times 10^6}$	4.0×10^2	6.6×10^1	6.0
	1.7×10^2	2.7×10^1	6.3
	4.4×10^1	5.9×10^0	6.7

Table 4.1: Comparison between the number of photons estimated from the rescaled homodyne traces and the one measured on a single channel of the detector. The estimation has been performed at three different local oscillator intensities.

4.4 Correlation between successive pulses

We conclude the noise characterization of the set-up by presenting the study of the correlation between successive laser pulses at a repetition rate of 200 kHz. This test is useful to verify whether we are measuring independent copies of the same state, so that each pulse yields only one quadrature value. In Figure 4.17(a) we present a correlation 2D plot in which the integral of the $n+1^{th}$ pulse is plotted against the integral of the n^{th} for a total number of 2000 pulses. The lack of correlation is qualitatively proved, since the n^{th} and the $n+1^{th}$ have a radial distribution. This means that there is no significant impact on the measured integral of the $n+1^{th}$ pulse from that of the n^{th} pulse. This analysis can be made quantitatively by evaluating the Pearson correlation coefficient between pulse integrals as a function of their distance. Between the i^{th} and the j^{th} integral pulse the latter reads:

$$\rho(I_i I_j) = \frac{\langle I_i I_j \rangle - \langle I_i \rangle \langle I_j \rangle}{\sigma(I_i)\sigma(I_j)} \tag{4.23}$$

and it is ± 1 in the case of perfect correlation/anti-correlation between I_i and I_j, while it is 0 if the measures of the integral of the two pulses is completely uncorrelated. The Pearson correlator as a function of the pulse distance is presented in Figure 4.17(b). The correlator between the pulses at a fixed distance has been calculated on a subset of 100 pulses from the full 2000 pulses train. The correlator $\rho(I_i I_j)$ oscillates around 0 as a function of the pulse distance, thus confirming the potentiality of our set-up to measure equally prepared copies of the same quantum light system produced at the laser repetition rate (200 kHz).

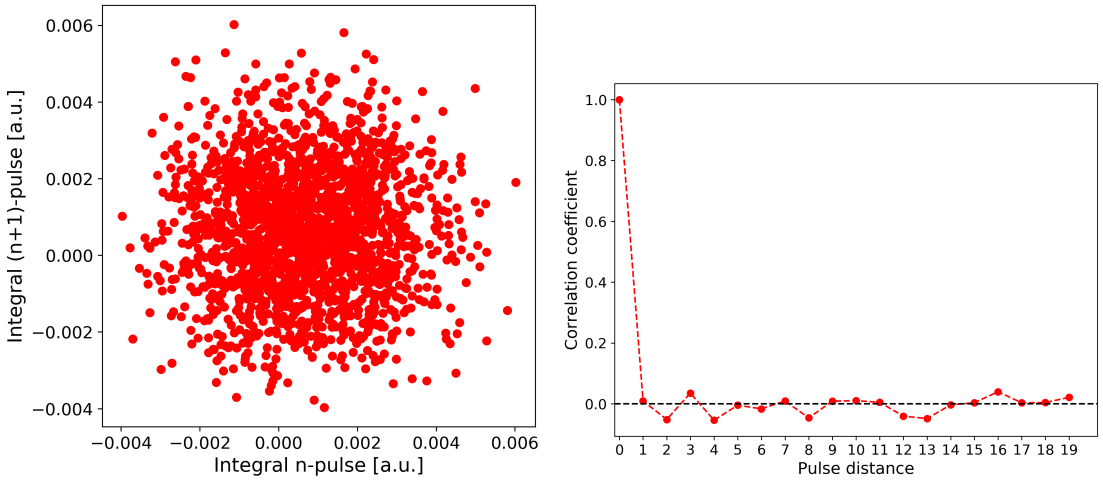

(a) (b)

Figure 4.17: Test of the correlation between successive pulses. In (a) the plot of the integral of a pulse with respect to the integral of the successive one for a local oscillator with 5.3×10^7 ph/pulse and for 2000 total pulses. In (b) the Pearson correlator as a function of the pulse distance.

Chapter 5

Mean value time-resolved measurements

In Chapter 3 we have shown the potentiality of our set-up to retrieve in a frequency-resolved scheme the full structure of an optical pulse, in both its phase and amplitude features.

In this chapter we want to exploit this peculiar feature to address the coherent evolution of lattice vibrations in solid state systems. The typical approach in this sense is the *pump-probe* one that consists in injecting in the system a large number of vibrational excitations within a femtosecond time window and subsequently monitor the system optical response by mean of a second ultrafast pulse (*probe*) at a variable delay. The modification of the probe spectral features as function of the delay from the sudden excitation will carry information on the evolution dynamics of the excited mode. Since the time resolution of the pump-probe experiment is shorter than the intrinsic phonon period, such a technique is phase-resolved for what concerns atomic coherent oscillations.

While in standard pump-probe spectroscopy the optical observable is the probe intensity, with our innovative set-up we are able to selectively address each probe mode response in both its phase and amplitude and therefore reconstruct the full emitted field resulting from photon-phonon interaction.

In Chapter 1 and 4 we have proved that, thanks to the possibility of performing single pulse integration, we can even go deeper and have access to the full statistics of the emitted field. However, in this chapter we will only focus on probe phase and amplitude mean value dynamics. The latter are obtained by averaging the variation of our optical observable (the homodyne current) resulting from the interaction of many subsequent pulses on an equally prepared phononic system. By mean of this mean value approach, we will experimentally prove through Fourier analysis that the emitted probe field encodes the structure of the phonon field. Therefore, our approach enables to simultaneously track amplitude and phase of coherent phonons.

After having presented the general features of a time-resolved multimode homodyne measurement, we will present the results on quartz and Copper Germanate ($CuGeO_3$) obtained with the set-up described in Figure 3.3. In particular we will simultaneously make use of amplitude and phase dynamics of the detected probe to unveil the photon-phonon interaction processes presented in Chapter 2: Impulsive Stimulated Raman Scattering (ISRS) and Linear Refractive Modula-

tion (LRM).

Moreover, we will quantitatively exploit the quantum model presented in Chapter 2 to retrieve from amplitude and phase trends the Raman cross-sections of the detected phonons.

5.1 Time-resolved experimental response

In this section we present the general features of a pump-probe multimode homodyne measurement, which are common to all the configurations we will examine. In particular, we will show how the raw data are generally treated and how we obtain from them the phonon-dependent features encoded inside the detected probe.

The basic datasets are shown in Figure 5.1(a)(b) and consist of two dimensional maps representing the dynamical evolution of the probe quadrature. Indeed, a vertical cut in those maps represents the mean probe quadrature calculated at a fixed pump-probe delay. The latter, for each pump-probe delay, is measured by varying the relative phase between the probe and the local oscillator. Each quadrature value (i.e. a point in the map) results from the average of 2000 pulses at a repetition rate of 200 kHz. In these maps the resolution along the x-axis is determined by the pump translation stage step (approximatively 10 fs), while that on the y-axis by the piezo step (1.2×10^{-4} fs). Since the pump pulse is chopped at a frequency of 400 Hz, for each delay both the pumped and the equilibrium quadrature can be measured. By subtracting the pumped response to the unpumped (Figure 5.1) we are able to single out the purely dynamical features imprinted on the equilibrium quadrature at each delay, i.e. its amplitude and phase shifts (Figure 5.1(c)). The latter are obtained by separately fitting for each delay the pumped and equilibrium quadrature and by subsequently subtracting the pumped amplitude and phase fitted parameters to the unpumped ones (Figure 5.1(c)). The acquisition of the equilibrium quadrature at each pump-probe delay is also crucial to filter out the piezo phase-drift. The piezo drift correction is performed by fitting with a sinusoidal function all pumped and equilibrium quadratures and by subsequently rescaling their phase to that of an arbitrarily selected unpumped quadrature.

In integrated pump-probe homodyne [7] the time-resolved quadrature maps (Figure 5.1) are integrated in frequency, since a short local oscillator broad in its frequency content is employed. In this case, the quadrature does not map the electric field of a single mode, but instead the coherent superposition of all the probe modes within the local oscillator bandwidth. With our set-up we can overcome this limitation, since a frequency-shaped local oscillator is employed (Chapter 3). Indeed, by tuning the local oscillator frequency we are able to independently monitor the pump-probe evolution of each probe mode quadrature and experimentally get the 2D maps of Figure 5.1 for each probe frequency.

Therefore, by controlling the spectral content and the phase of the local oscillator, we are able to monitor phase and amplitude quadrature shifts not only for each delay, but also for each probe frequency. By performing a fit of the amplitude and phase of each spectral component we can obtain the maps presented in Figure 5.2 representing the time evolution of amplitude and phase of each spectral component of the probe pulses. An horizontal cut in these maps represents

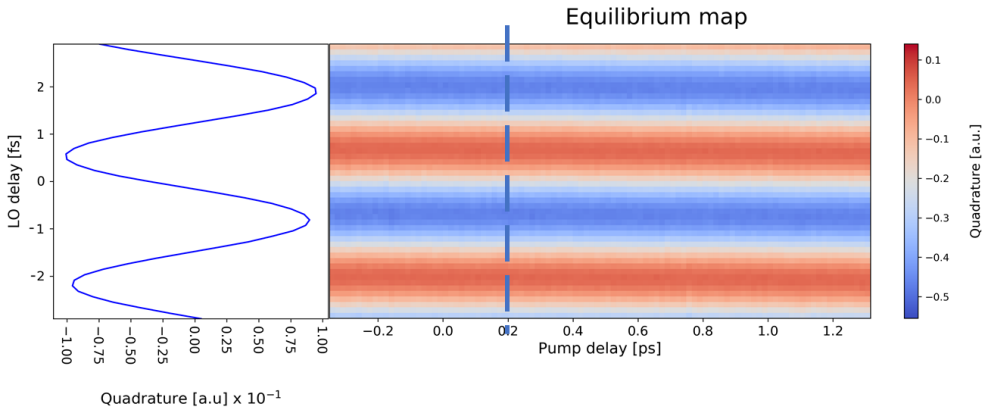

(a)

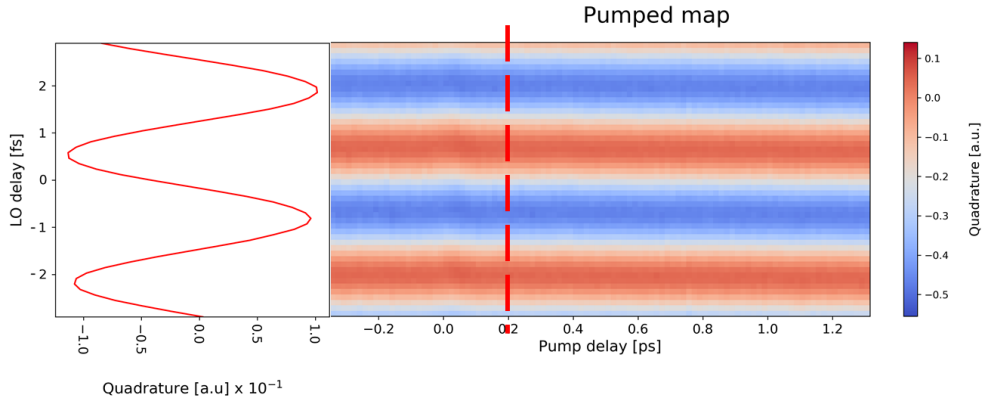

(b)

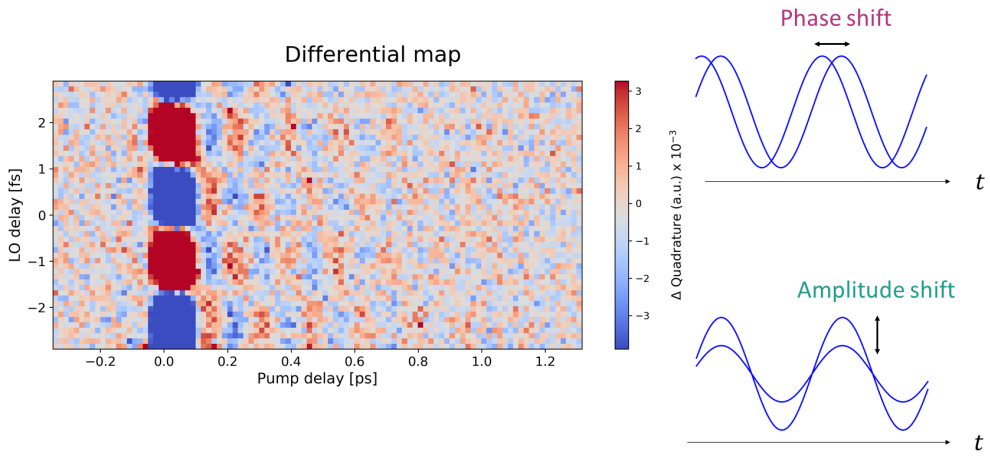

(c)

Figure 5.1: Time-resolved multimode homodyne measurement for a fixed local oscillator frequency. In (a) the equilibrium quadrature. In (b) the pumped one. In (c) the differential map between the previous two, mapping pump-dependent dynamics, i.e. phase and amplitude quadrature shifts.

the amplitude/phase evolution of a single probe mode. Conversely, a vertical cut describes the spectral dependence of amplitude/phase at a fixed delay.

Amplitude and phase shifts pump-probe dynamics encode the phonon-dependent contribution to the pumped quadrature. This can be shown by performing the

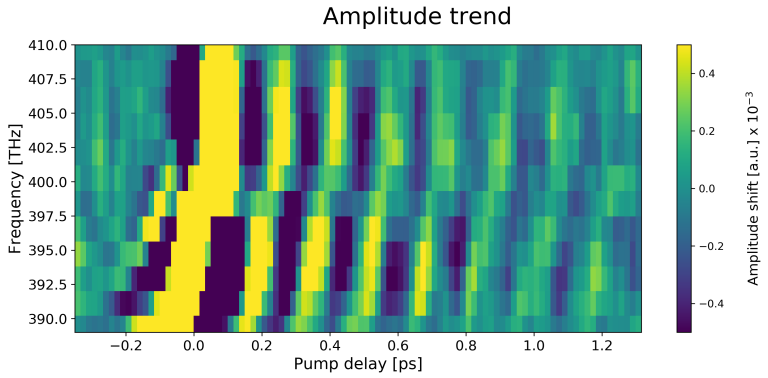

(a)

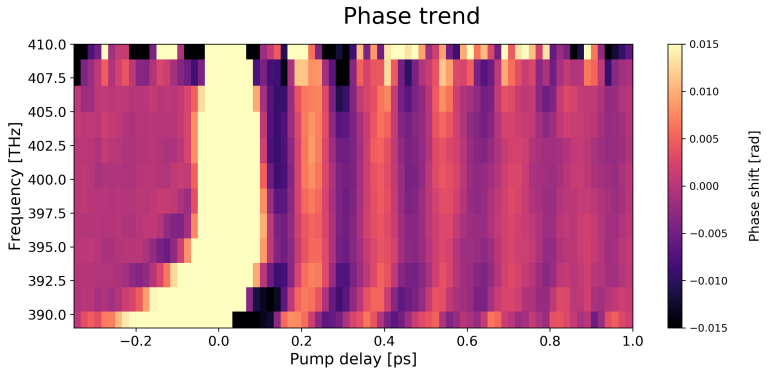

(b)

Figure 5.2: Frequency-resolved amplitude (a) and phase (b) shifts of the emitted field quadrature measured in our experiment.

Fourier transform along the delay axis of Figure 5.2(a)(b). The resulting FT maps are presented in Figure 5.3, where the vertical lines represent the detected phonon frequencies. Since we are considering only the modulus of the Fourier transform, every probe frequency carries the same information to the Fourier spectra and so, in order to retrieve it, we can safely average along probe frequency axis. These frequency spectra are illustrated in Figure 5.3(c) and Figure 5.3(d) for phase and amplitude respectively with indicated the detected phonon frequencies.

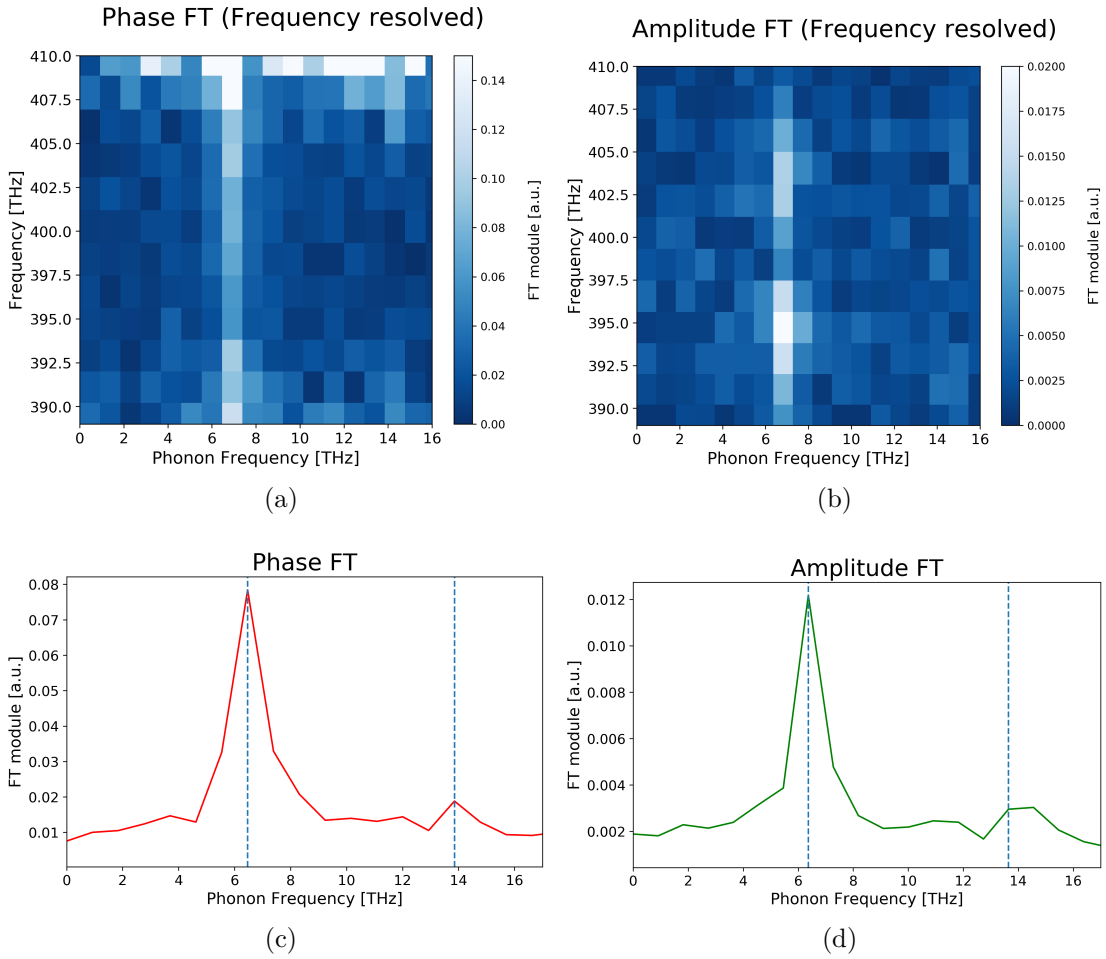

Figure 5.3: In (a) and (b) the frequency-resolved Fourier transforms of the amplitude and phase dynamical shifts obtained performing the FT along the delay axis of Figure 5.2. In (c) and (d) the Fourier spectra of phase and amplitude obtained averaging (a) and (b) along the probe frequency axis (y-axis).

5.2 Time-resolved measurements on α-quartz

In this section the time-resolved measurement on α-quartz are presented. This material represents a benchmark system to test multimode homodyne detection for tracking phase and amplitude mean dynamics of coherent phonons in solids. Quartz is indeed characterize by an high transparency within the probe spectral range ($\sim$ 400 THz) and exhibits strong Raman lines [14].

We will investigate the low temperature phase of quartz which is dubbed α-*quartz*. The latter has a trigonal crystalline structure with a D_3 symmetry and $N = 9$ atoms per unit cell (Figure 5.4(a)). Group theory calculations [17] show that the $3 \times N = 3 \times 9 = 27$ vibrational degrees of freedom are divided into 2 acoustic vibrations of A_2+E symmetry and 16 optical vibrations of $4A_1+4A_2+8E$ symmetry. Among them, the Raman active modes are 4 totally symmetric of species A_1 and 8 doubly degenerate of species E.

In our experiment we employ a 0.2 mm tick α-quartz sample oriented in order to have the principal symmetry axis (c-axis) parallel to the probe propagation direction. In this configuration, the accessible vibrational modes are only those

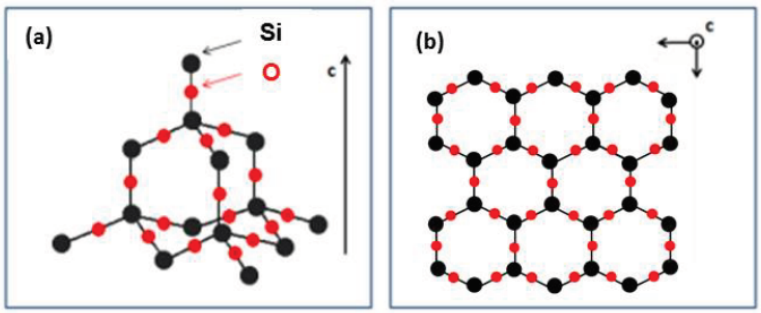

Figure 5.4: Arrangement of Si an O atoms in α-quartz. In (a) the 3D structure, while in (b) its projection on a plane perpendicular to the c-axis [27].

with C_3 rotational symmetry around the c-axis. These modes correspond to that of a triatomic molecule with the atoms collocated at the corners of an equilateral triangle and consist of an A total symmetric mode and two degenerate E-symmetry modes (Figure 5.5). Assuming that also the pump propagates along

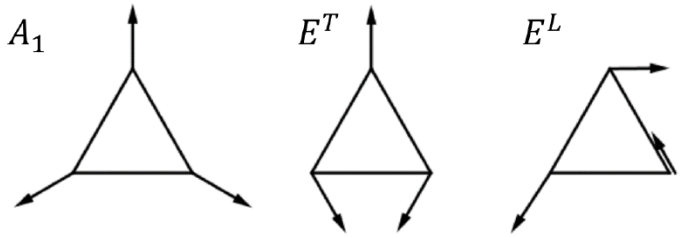

Figure 5.5: Normal vibrational modes for a system with C_3 symmetry. A total symmetric A-mode and a doubly-degenerate E-mode are allowed [20]. These modes corresponds to the ones allowed for α-quartz excited along the c-axis.

c-axis (Figure 5.6) we can limit our analysis in the xy plane. In this configuration the Raman tensors $\chi^{(1)}_{\mu\lambda} = (\delta\chi/\delta q)_{\mu\lambda}|_{q=0}$ for the three allowed modes read [22]:

$$A = \begin{pmatrix} a & 0 \\ 0 & a \end{pmatrix} \qquad E^L = \begin{pmatrix} c_L & 0 \\ 0 & -c_L \end{pmatrix} \qquad E^T = \begin{pmatrix} 0 & -c_T \\ -c_T & 0 \end{pmatrix} \tag{5.1}$$

From the previous ones we can subsequently calculate the four rank non-linear susceptibility tensor $\chi^{(3)}_{\mu\lambda mn}$. The latter encodes the information about the symmetry of the excited phonon-modes and rules the probe optical response after the ISRS-driven pump excitation. For our C_3-symmetric system it turns out to be:

$$\chi^{(3)}_{\mu\lambda mn} = A_{\mu\lambda}A_{mn} + E^L_{\mu\lambda}E^L_{mn} + E^T_{\mu\lambda}E^T_{mn} =$$

$$= \begin{pmatrix} \begin{pmatrix} a^2 + c_L^2 & 0 \\ 0 & a^2 - c_L^2 \end{pmatrix} & \begin{pmatrix} 0 & c_T^2 \\ c_T^2 & 0 \end{pmatrix} \\ \begin{pmatrix} 0 & c_T^2 \\ c_T^2 & 0 \end{pmatrix} & \begin{pmatrix} a^2 - c_L^2 & 0 \\ 0 & a^2 + c_L^2 \end{pmatrix} \end{pmatrix} \tag{5.2}$$

The four rank susceptibility tensor encodes both the pump-phonon and probe-phonon coupling. Indeed, its inner indices ($\mu\,\lambda$) are relative to the probe polar-

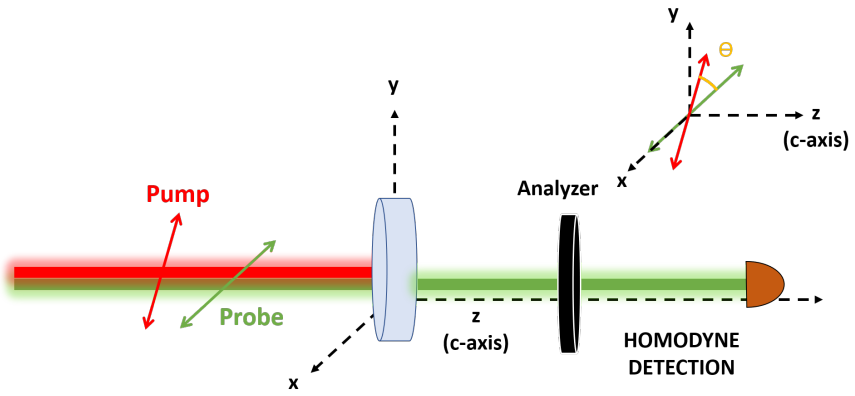

Figure 5.6: Geometry adopted for the pump-probe experiment on α-quartz. Pump and probe propagate collinearly along the c-axis of the crystal. The x direction is the one corresponding to the probe polarization. The relative polarization between the two fields is denoted with Θ. The analyzer is a polarizer allowing the selection of the emitted probe field polarization component.

Probe-analyzer angle	Pump-probe polarization angle (Θ)	Detected phonons	Tensor element
90°	0	X	0
90°	±45°	E^T	c_T^2
90°	±90°	X	0
0°	0°	$A + E^L$	$a^2 + c_L^2$
0°	±45°	A	a^2
0°	±90°	$A + E^L$	$a^2 - c_L^2$

Table 5.1: Summary of the α-quartz detected phonons as a function of the probe-analyzer and the relative pump-probe polarization angle Θ. The phonon selection is ruled by the symmetry of the non-linear susceptibility tensor $\chi^{(3)}_{\mu\lambda mn}$ (Equation 5.2).

ization components, while the external $(m\,n)$ account for the pump ones with respect to the reference system depicted in Figure 5.6.

We will see in the following that by varying the pump-probe polarization angle and by properly choosing the polarization of the emitted probe field we are able to select the optical response of specific elements of $\chi^{(3)}_{\mu\lambda mn}$ and eventually discriminate phonons with different symmetry. On the base of $\chi^{(3)}_{\mu\lambda mn}$ symmetries, we summarize the detected phonons in different exciting and probing geometries in Table 5.1.

Furthermore, the polarization selection opens the possibility to single out the two main probing effects described in Chapter 2: *Linear Refractive Modulation* (LRM) and *Impulsive Stimulated Raman Scattering* (ISRS). Indeed, we expect the refractive modulation to be the only responsible for the photon exchange between the different polarizations. This opportunity will allow us to monitor phase and amplitude dynamics of each probe mode in the two cases and subsequently

distinguish the different phonon field temporal structure encoded in the probe pulse.

Since we have stated that polarization selection of the emitted field plays a crucial role in determining the probing features, let us start by exploring this possibility and see what the experimental evidence suggest. In particular, we will report the results in two different probe-analyzer configurations:

- The **parallel** configuration, in which the analyzer selects the same polarization of the probe;
- The **cross** (**extinction**) configuration, in which the detected emitted field polarization is perpendicular to the probe one.

5.2.1 Parallel configuration

In this paragraph the measures in parallel geometry are presented. In particular, we are interested in exploiting phase and amplitude dynamical trends to unveil the probing processes in this configuration. We report the experimental results in this geometry in Figure 5.7. In the presented measurements the pump-probe polarization angle Θ is set to $+45°$.

The measured trends show that the emitted field in parallel polarization encodes two different effects. The amplitude exhibits a frequency-dependent response, while the phase does not show any spectral-dependent feature. This implies that the amplitude maps a multimode probe-phonon interaction, while the phase a probe-phonon interaction in which no frequency mixing occurs. In our framework, the first is the Impulsive Stimulated Raman scattering, while the latter the Linear Refractive Modulation.

Moreover, as shown in Figure 5.8, the frequency mixing is time-dependent. This is due to the fact that through ISRS we can, depending on the probing time, force (Stokes process) or dump (Anti-Stokes) the phonon oscillations. Figure 5.7(c) clarify the different nature of the two processes. As a matter of fact, amplitude and phase evolve both at the frequency of the excited phonon (Figure 5.9), but with a phase-difference which is $\pi/2$, independently of the probe frequency. Phase follows the instantaneous atomic displacement, while amplitude the phonon velocity, thus proving the stimulated nature of ISRS.

To sum up, the experimental evidence shows that the emitted field in parallel geometry encodes both the two probing effects. Its amplitude modification encodes the multimode interaction with the phonon, while its phase shifts the linear modulation of the refractive properties due to the atomic periodic displacement.

We will now move to the cross geometry and see if, through polarization, we can isolate the two probing processes.

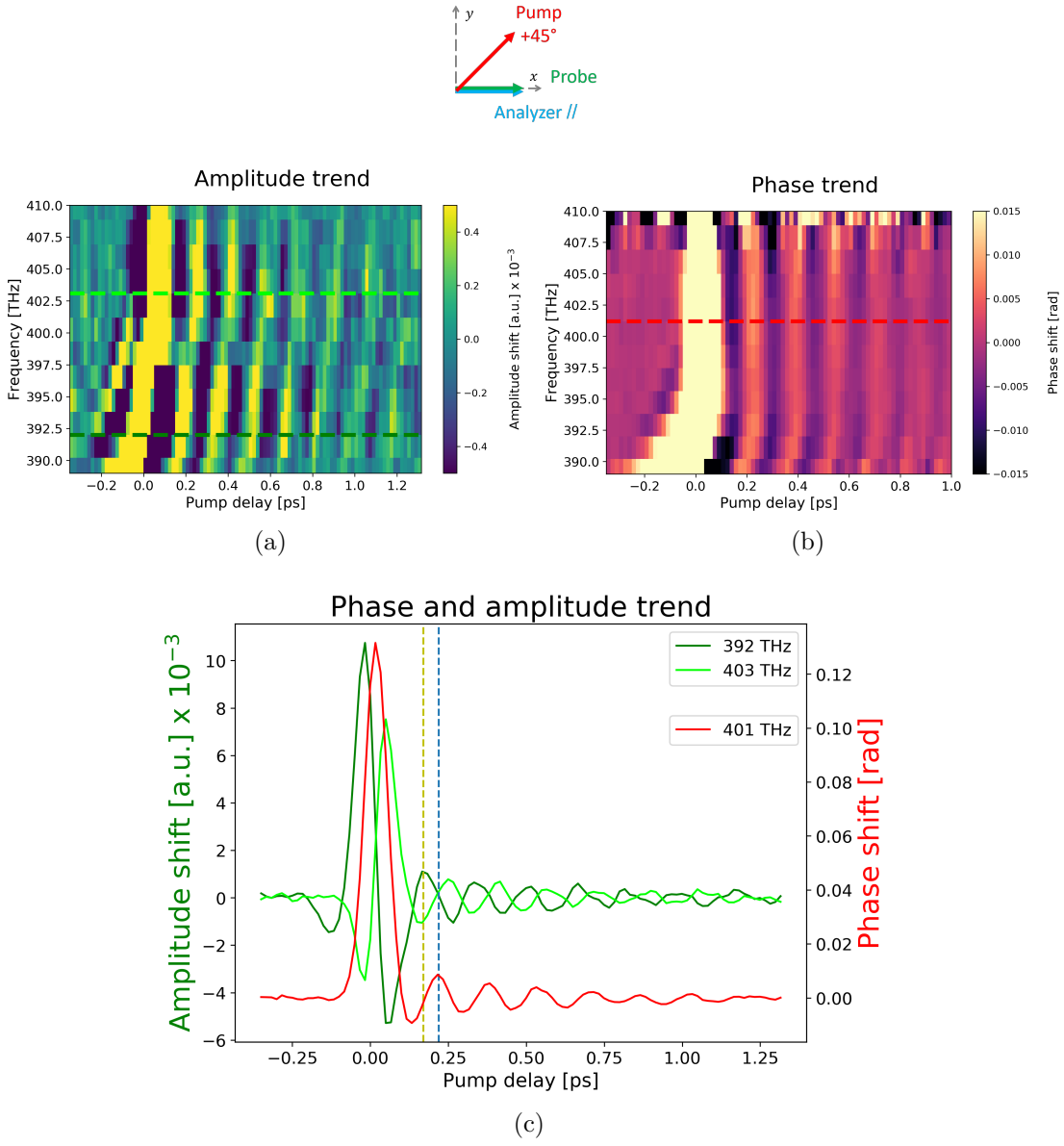

Figure 5.7: Parallel geometry: amplitude (a) and phase (b) temporal dynamics of each mode of the emitted probe field. Phase and amplitude are $\pi/2$-shifted (c) since they are ruled by two separate probing effects. Amplitude modulation is driven by ISRS and follows the phonon momentum (yellow line). Phase modulation is instead determined by the phonon-dependent refractive properties and follows the instantaneous atomic oscillations whose maxima are in correspondence of the blue line. The maximum spectral weight shift occurs when phonon exhibits its maximum momentum (yellow line). Probe power $= 3.8 \times 10^6$ ph/pulse; Pump power $=4.8 \times 10^{12}$ ph/pulse; LO power (single mode with $\sigma = 0.1$ THz) $= 1.0 \times 10^7$ ph/pulse.

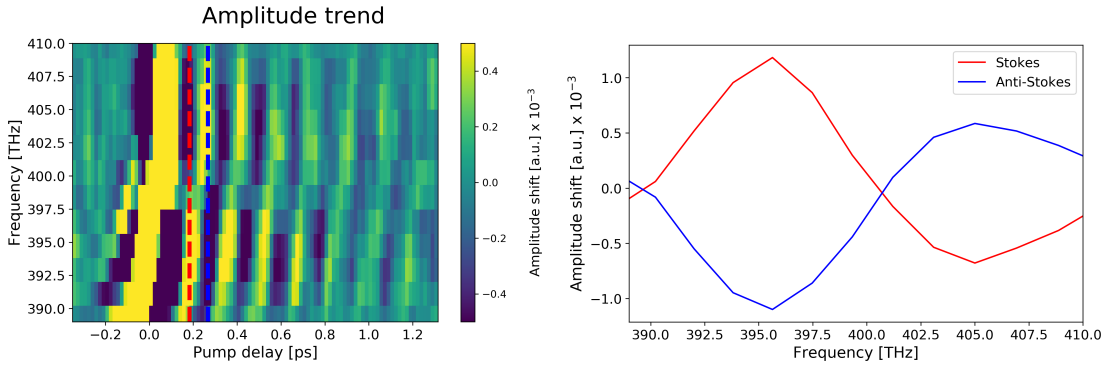

(a) (b)

Figure 5.8: Parallel geometry. Probe spectral weight shifts at two different delays (a) resulting from Stokes and Anti-Stokes probe-phonon interaction (b).

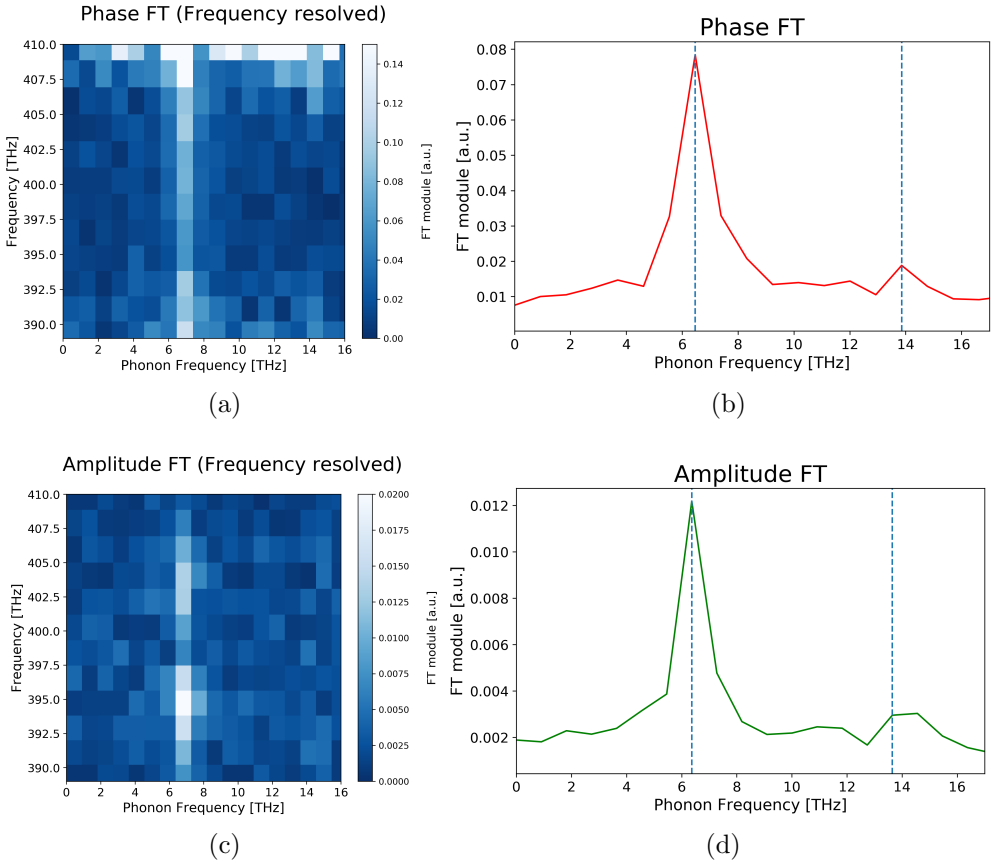

(a) (b)

(c) (d)

Figure 5.9: Parallel geometry: Fourier analysis. In (a) and (c) phase and amplitude frequency-resolved FT maps calculated from each probe mode amplitude and phase temporal dynamics. In (b) and (d) the mean FT obtained averaging over the frequency axis of maps (a) and (c) in a spectral window of 10 THz around the probe central mode. Since the pump-probe polarization angle Θ is set to 45°, 6.2 THz and 14 THz A-modes are detected (Table 5.1).

5.2.2 Cross configuration

In this paragraph the multimode homodyne measurements in cross geometry are presented. The evolution of phase and amplitude parameters in this configuration is shown in Figure 5.10. The pump-probe polarization angle Θ adopted for the presented measures is 45°. Indeed, in this configuration the phonon-dependent dynamics can be retrieved in the optical response with the maximum efficiency, since the photon-phonon cross-section is maximized (Table 5.1).

The pump-dependent amplitude and phase shifts evolve at the frequency of the detected phonon (the E^T-one at 4 THz), but they do not exhibit any spectral-dependent feature. We indeed interpret the phase response at high frequency of Figure 5.10(b) as originating from a non-extinguished probe component with parallel polarization. This consideration is supported by the fact that, as shown in Figure 5.11, its phonon-dependent modulation is 10 times higher than the low frequency one.

In this case, no multimode probe-photon processes are mapped into amplitude and phase dynamics of the probe pulse. Therefore, the emitted photons in cross-polarization have not experienced ISRS interaction with the excited phonon. This experimental evidence is supported by the stimulated nature the of Raman interaction. Photons emitted in a stimulated process are indeed likely to be created in a mode state which is already occupied. The cross-polarization geometry hence allows to filter out ISRS signatures. This statement is strongly confirmed by the comparison between the temporal evolution of phase and amplitude of each probe mode. As a matter of fact, in this configuration both amplitude and phase evolve in phase with the phonon periodic displacement (Figure 5.10(c)), thus mapping a refractive modulation. Also for this comparison only the low frequency phase response has been considered, as a consequence of a residual parallel component on the high frequency side (Figure 5.11).

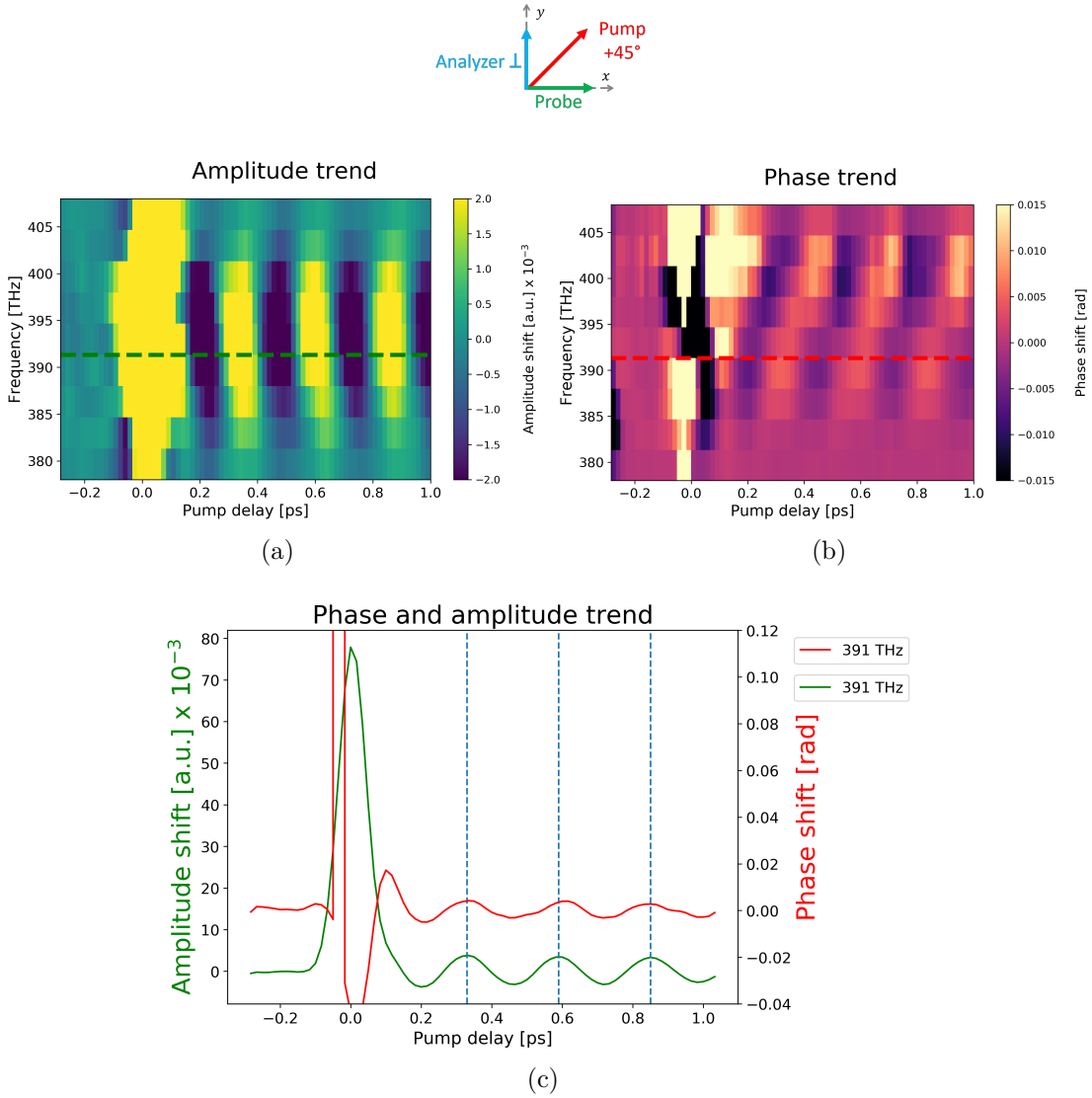

Figure 5.10: Cross geometry: amplitude (a) and phase (b) temporal dynamics of each mode of the emitted probe field. Setting the analyzer in probe extinction regime allows to filter out the ISRS features. Indeed, no spectral weight shift occurs among probe modes (a) and amplitude and phase oscillate with the same phase (c). We have considered only the phase response of the lower part of the pulse, since that of the upper one originates from a non-extinguished parallel polarization component (Figure 5.11.) Probe power $= 3.8 \times 10^6$ ph/pulse; Pump power $= 4.8 \times 10^{12}$ ph/pulse; LO power (single mode with $\sigma = 0.5$ THz) $= 1.6 \times 10^7$ ph/pulse.

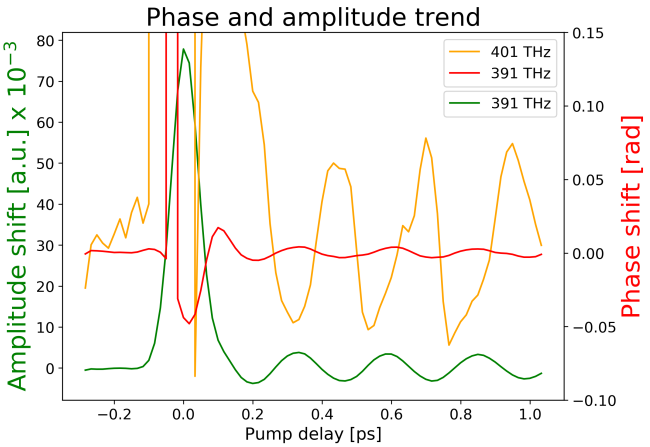

Figure 5.11: Comparison between the phase trend of the lower (391 THz) and upper (401 THz) part of the emitted probe pulse in the case of cross geometry. The phase response at higher frequency is dominated by a non-extinguished emitted field whose polarization is parallel to the that of the incoming probe.

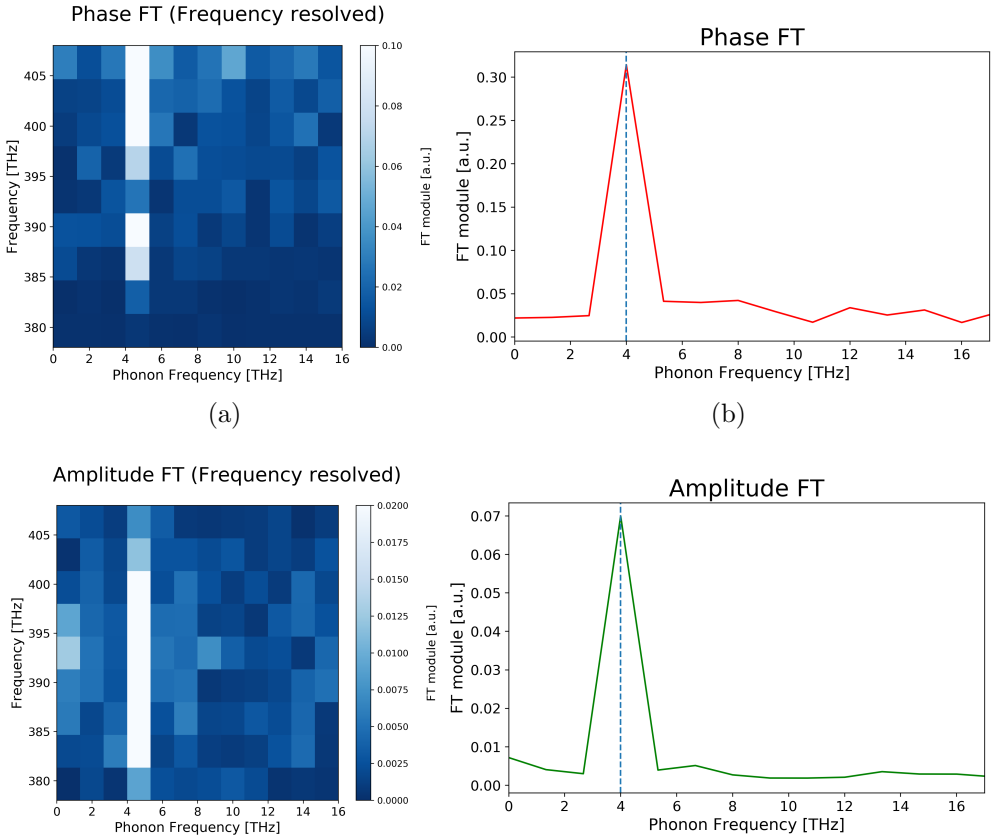

Figure 5.12: Cross geometry: Fourier analysis. In (a) and (c) phase and amplitude frequency-resolved FT maps calculated from each probe mode amplitude and phase temporal dynamics. In (b) and (d) the mean FT obtained averaging over the frequency axis of maps (a) and (c) in a spectral window of 10 THz around the probe central mode. For a pump-probe polarization angle $\Theta = 45°$, 4 THz E^T-mode is detected in extinction geometry.

5.2.3 Pump-probe polarization angle dependence

In the previous section we have considered how the selection of the polarization of the emitted probe field enables to single out the two probing effects. The results indeed show that the multimode photon-phonon interaction (ISRS) is only encoded inside the emitted field with the same polarization of the incident one. Until now we have not explored how the excitation geometry (i.e. the pump-probe polarization angle Θ) affects phonon evolution.

In this section we will focus on this issue and exploit multimode homodyne detection to track A-phonon and E-phonon evolution as a function of the pump-probe polarization angle. By looking at the selection rules presented in Table 5.1, we point out that a suitable angle to perform this comparison is $|\Theta| = 45°$. Indeed, if $|\Theta| = 45°$, A and E-phonons responses can be singled out by switching the probe-analyzer configuration from the parallel to the cross one. Since our purpose is to independently study the A and E-phonon response as function of pump polarization, the cases $\Theta = \pm 45°$ have been studied.

Let us start with the E-symmetry phonon. As previously stated, the latter can be isolated in cross-polarization geometry. Phase and amplitude trends for $\Theta = \pm 45°$ resulting from the probe interaction with the E-phonon are presented in Figure 5.13. The experimental results show that by exciting the E-mode with a pump polarization at 45° with respect to the probe or at $-45°$, a π-shift in both amplitude and phase temporal trends occurs (Figure 5.14).

The same π-shift does not occur when the probe interacts with the A-mode (Figures 5.15, 5.16). This is evident in Figure 5.16 where we compare the A-phonon amplitude and phase response in the two excitation geometries ($\Theta = \pm 45°$). Since the A-phonon is detected in parallel geometry, amplitude exhibit the Raman behaviour (Figure 5.15). For this reason, we have compared the amplitude trends in the two pump configurations ($\Theta = \pm 45°$) for either the upper and lower part of the pulse (Figure 5.16(a)(b)).

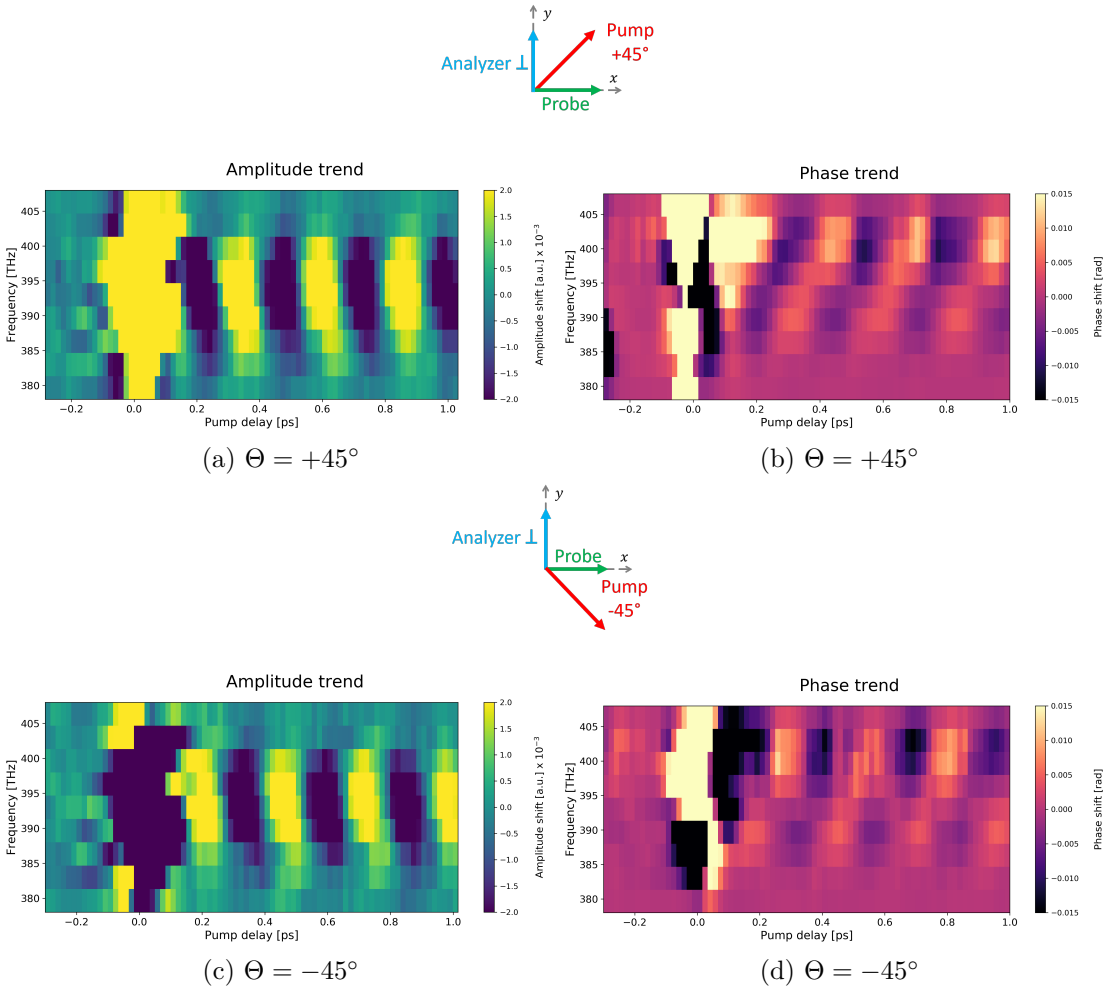

(a) $\Theta = +45°$ (b) $\Theta = +45°$

(c) $\Theta = -45°$ (d) $\Theta = -45°$

Figure 5.13: Cross geometry (E^T-phonon response): pump-probe polarization angle dependence ($\Theta = \pm 45°$) of phase and amplitude frequency-resolved dynamics. Probe power $= 3.8 \times 10^6$ ph/pulse; Pump power $= 4.8 \times 10^{12}$ ph/pulse; LO power (single mode with $\sigma = 0.5$ THz) $= 1.6 \times 10^7$ ph/pulse.

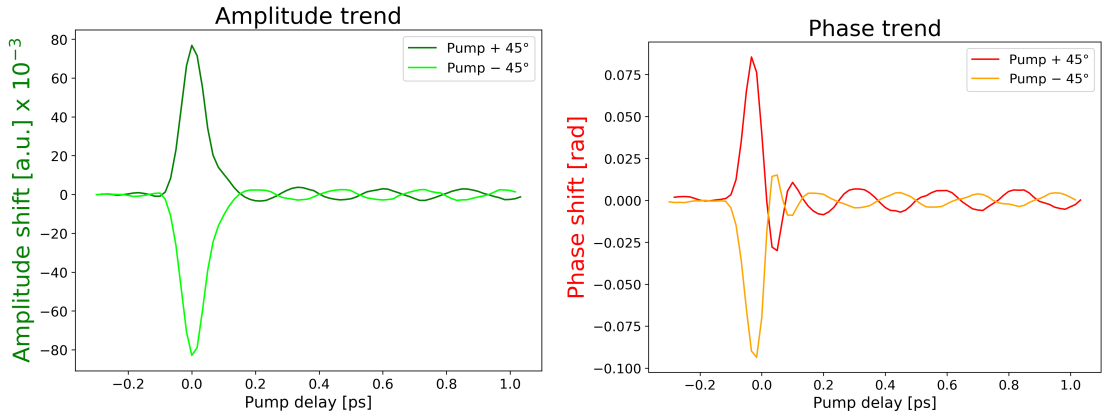

(a) (b)

Figure 5.14: Cross geometry (E^T-phonon response): pump-probe polarization angle dependence ($\Theta = \pm 45°$) for a representative probe mode at 391 THz (Figure 5.10). Phase and amplitude of the emitted probe field are both π-shifted in the two excitation configurations.

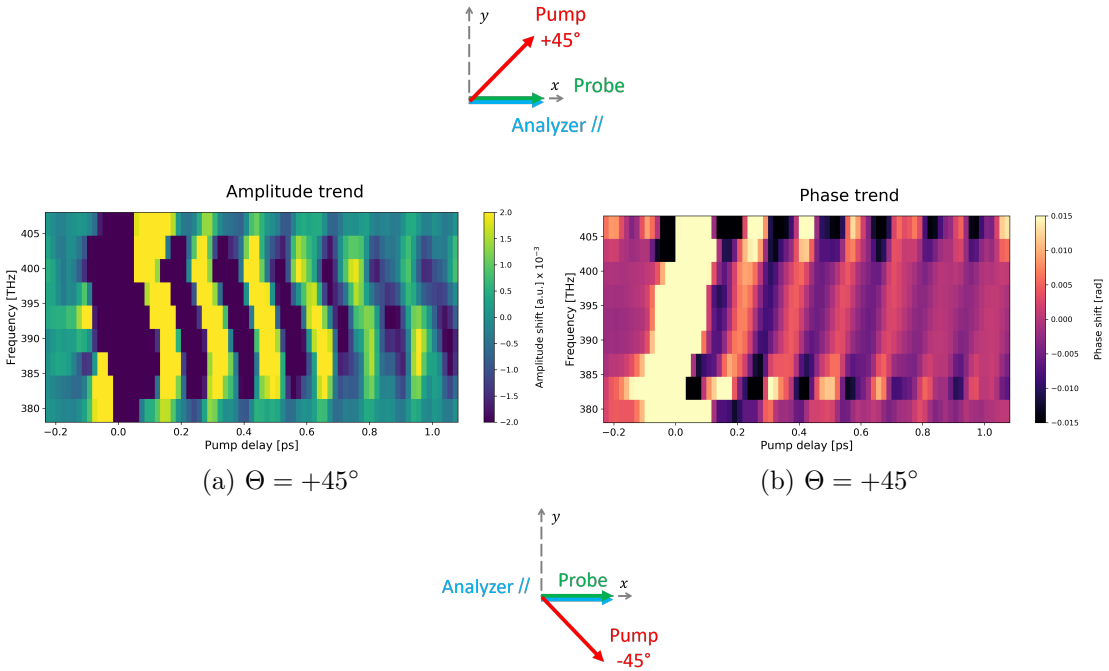

(a) $\Theta = +45°$ (b) $\Theta = +45°$

(c) $\Theta = -45°$ (d) $\Theta = -45°$

Figure 5.15: Parallel geometry (A-phonon response): pump-probe polarization angle dependence ($\Theta = \pm 45°$) of phase and amplitude frequency-resolved dynamics. Probe power $= 5.7 \times 10^6$ ph/pulse; Pump power $= 4.8 \times 10^{12}$ ph/pulse; LO power (single mode) $= 1.6 \times 10^7$ ph/pulse.

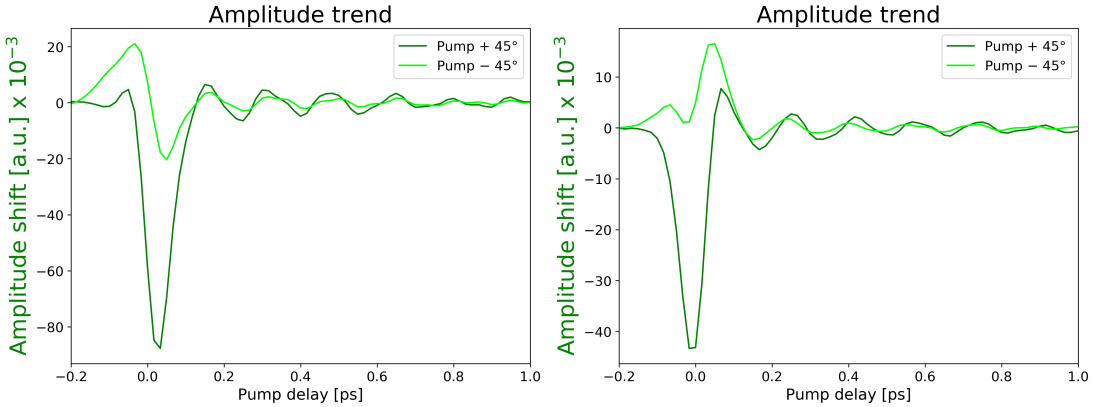

(a) 384 THz

(b) 398 THz

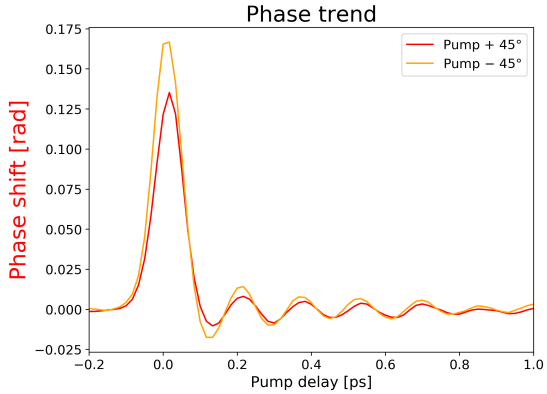

(c) 394 THz

Figure 5.16: Parallel geometry (A-phonon response): pump-probe polarization angle dependence ($\Theta = \pm 45°$). In (a) and (b) amplitude dynamics in both geometries for modes at opposite side of the central one (384 e 398 THz) (Figure 5.15). In (c) phase temporal evolution in the two excitation geometries for a representative mode at 394 THz (Figure 5.15). Amplitude and phase oscillations are no sensitive to the excitation geometry (i.e. they do not change their phase).

5.2.4 Comparison with the model

In the previous section we have presented the time-resolved measurements on α-quartz and shown that the selection of the emitted probe field allows to distinguish the two main probing effects resulting from probe-phonon interaction: LRM and ISRS. Moreover, by changing the pump polarization we have exploited homodyne detection to retrieve the symmetry properties of the detected phonons.

In this section we want to interpret the mean value phase and amplitude dynamics in the adopted configurations on the basis of the model presented in Chapter 2. Moreover, we will quantitatively make use of amplitude and phase shifts in both parallel and extinction geometry to estimate the Raman cross-section of the probing interaction.

Since in our set-up the two main probing effects are mapped onto amplitude and phase dynamics of the frequency-resolved homodyne current, let us starting by recalling its expression (Chapter 2) in the case of refractive and ISRS probe-phonon interaction. The latter has a pumped and an equilibrium contribution and in the two cases reads:

$$\begin{aligned}
\langle \widehat{I}^{Ref}_{\mu_j,\phi_j}(\Delta t)\rangle_{eq} &= |z_{\mu j}||\alpha_{\mu j}|\cos(\phi_j) + |z_{\mu_j}|\frac{2\tau V_s \omega_j}{V}\sin(\phi_j)\sum_{\lambda}|\alpha_{\lambda j}|\chi^{(0)}_{\mu\lambda} \\
\langle \widehat{I}^{Ref}_{\mu_j,\phi_j}(\Delta t)\rangle_{pump} &= |z_{\mu_j}|\frac{2\tau V_s \omega_j}{V}\sin(\phi_j)\sum_{\lambda}|\alpha_{\lambda j}|\chi^{(1)}_{\mu\lambda}\frac{R}{m\Omega}\sin(\Omega\Delta t)
\end{aligned} \tag{5.3}$$

$$\begin{aligned}
\langle \widehat{I}^{Raman}_{\mu_j,\phi_j}(\Delta t)\rangle_{eq} &= |z_{\mu j}||\alpha_{\mu j}|\cos(\phi_j) \\
\langle \widehat{I}^{Raman}_{\mu_j,\phi_j}(\Delta t)\rangle_{pump} &= |z_{\mu_j}|\frac{\tau V_s \omega_j}{2V}\sum_{\lambda}\chi^{(1)}_{\mu\lambda}\Big(\cos(\phi_j)\left(|\alpha_{\lambda j+\frac{\Omega}{\delta}}| - |\alpha_{\lambda j-\frac{\Omega}{\delta}}|\right)\frac{R\cos(\Delta t)}{m\Omega} + \\
&\quad + \sin(\phi_j)\left(|\alpha_{\lambda j+\frac{\Omega}{\delta}}| + |\alpha_{\lambda j-\frac{\Omega}{\delta}}|\right)\frac{R\sin(\Omega\Delta t)}{m\Omega}\Big)
\end{aligned} \tag{5.4}$$

In the previous expression the dependence of the pumped current on phonon momentum and position is hidden inside the time-dependent terms. We can make it explicit by recalling Equation 2.66:

$$\begin{aligned}
\langle \widehat{q}_{\Omega}(\Delta t)\rangle &= \frac{R}{m\Omega}\sin(\Omega\Delta t) \\
\langle \widehat{p}_{\Omega}(\Delta t)\rangle &= R\cos(\Omega\Delta t)
\end{aligned} \tag{5.5}$$

R represents the momentum shift imparted by the pump to the phonon initially at rest. This will be a crucial parameter in the following analysis, since it determines the entity of photon-phonon coupling and its dependence on the excitation geometry (i.e. on pump-probe polarization angle Θ). By looking at the structure of the previous equations, we can point out that phase and amplitude shifts resulting from probing interaction are both ruled by the non-linear susceptibility $\tilde{\chi}^{(1)}_{\mu\lambda}$ defined in Equation 2.74:

$$\tilde{\chi}^{(1)}_{\mu\lambda} = \frac{R}{m\Omega}\chi^{(1)}_{\mu\lambda} = \frac{\tau}{2Vm\Omega}\sum_j\sum_{mn}\chi^{(3)}_{\mu\lambda mn}|\alpha^{pump}_{mj}||\alpha^{pump}_{nj+\frac{\Omega}{\delta}}|\omega_j \tag{5.6}$$

The latter represents the phonon-dependent correction to the linear susceptibility $\boldsymbol{\chi}^{(0)}$ and we will dub it as the Raman cross-section of probe-phonon interaction.

In order to clarify its definition we recall Equation 2.36 in the case of a single vibrational mode and subsequently write the susceptibility expansion as:

$$\chi_{\mu\lambda} = \chi^{(0)}_{\mu\lambda} + \chi^{(1)}_{\mu\lambda} q \equiv \chi^{(0)}_{\mu\lambda} + \tilde{\chi}^{(1)}_{\mu\lambda} \tag{5.7}$$

Therefore, as stated in Chapter 2, the phonon-dependent probe response in both its amplitude and phase features is determined by the symmetry properties of the excited phonon through the four-rank susceptibility $\chi^{(3)}_{\mu\lambda mn}$ and by the amplitude of the phonon-coupled pump modes.

Conversely, the phonon-independent optical response is ruled by $\boldsymbol{\chi}^{(0)}$. $\boldsymbol{\chi}^{(0)}$ is the equilibrium susceptibility describing static refractive effects like polarization rotation and birefringence and we model it as an hermitian tensor [4] of the form:[1]

$$\chi^{(0)}_{\mu\lambda} = \begin{pmatrix} 1 & |w|e^{i\alpha} \\ |w|e^{-i\alpha} & 1 \end{pmatrix} \tag{5.8}$$

In the previous tensor $|w|$ and α model two different static refractive effects induced on a linearly polarized state. $|w|$ accounts for the *polarization rotation*, while α for the *static birefringence*, modelling the ellipticity of the outgoing polarization state. We stress that for quartz is crucial taking $\alpha \neq 0$ since it is experimentally proved that out of the c-axis the polarization state is elliptical. Indeed, by increasing the thickness of the sample and by orienting the analyzer in cross configuration, the degree of non-extinguished light increases. Therefore, referring to the geometry of Figure 5.6, birefringence will cause a de-phasing between the emitted fields in x and y directions, i.e. the directions perpendicular to the propagation direction.

After these preliminary considerations, let us now exploit the model to reproduced the effects of the detected phonons on amplitude and phase probing responses. We will work under the hypothesis of no coupling among phonons of different frequencies and hence we will add their relative homodyne response independently [4]. As previously pointed out, the symmetry of the excited phonon in our model is encoded inside the radial parameter R which represents the pump-driven phonon momentum shift and contains all the information about the excitation geometry. For the three quartz Raman modes allowed in our geometry (i.e. pump and probe collinear along c-axis), the latter read:

$$\begin{aligned} R_A &= a\eta^{pump}_{\Omega_A} \\ R_{E^L} &= c_L \cos(2\Theta)\eta^{pump}_{\Omega_E} \\ R_{E^T} &= -c_T \sin(2\Theta)\eta^{pump}_{\Omega_E} \end{aligned} \tag{5.9}$$

In the previous expression we have denoted with η^{pump}_{Ω} the contribution to the momentum shift R depending on the amplitude of the phonon-coupled pump modes:

$$\eta^{pump}_{\Omega} = \frac{\tau}{2V} \sum_j \omega_j |\alpha^{pump}_j||\alpha^{pump}_{j+\frac{\Omega}{\delta}}| \tag{5.10}$$

From Equation 5.9 we can immediately recognize a peculiar difference between A and E-modes. Indeed, while the momentum imparted by the pump at the first is

[1] We set to 1 the diagonal terms since, unless we record the response without the sample, we are not sensitive to them.

no sensitive to the polarization Θ, the momentum shift of E-modes can change in different pump excitation geometries.

In our model, this different phonon dynamics is linked to the optical one by the Raman cross-section $\tilde{\chi}^{(1)}_{\mu\lambda}$ which rules both amplitude and phase response. Its non-null elements for the three phonon symmetry-classes read[2]:

$$\begin{aligned}
\tilde{a} &= \frac{R_A}{m\Omega_A} a = \frac{\eta^{pump}_{\Omega_A}}{m\Omega_A} a^2 \\
\tilde{c_L}\cos(2\Theta) &= \frac{R_{E_L}}{m\Omega_A} c_L = \frac{\eta^{pump}_{\Omega_E}}{m\Omega_E} c_L^2 \cos(2\Theta) \\
\tilde{c_T}\sin(2\Theta) &= \frac{R_{E_T}}{m\Omega_E} c_T = \frac{\eta^{pump}_{\Omega_E}}{m\Omega_E} c_T^2 \sin(2\Theta)
\end{aligned} \tag{5.11}$$

These cross-sections clearly depend on pump intensity but, if we set it constant, their measure can be exploited to unveil the relative coupling strength between electronic and nuclear displacement of different phonon modes, i.e. $\chi^{(1)}_{\mu\lambda} = (\delta\chi/\delta q)_{\mu\lambda}|_{q=0}$. We will achieve this purpose by looking at the extent of phase and amplitude shifts of the frequency-resolved homodyne current, which encode that of each probe mode.

Until now we have treated ISRS and the refractive modulation as separated processes. Actually, in the real experiment the two effects occur simultaneously in the probing process. In the model we treat the combined action of ISRS and LRM at first order. In our quantum language, this means that the action of the overall Hamiltonian ($\widehat{H}_{probe}$) describing the probe-phonon interaction is simply the action of the sum of the two Hamiltonians ruling the two separate effects:

$$\widehat{H}_{probe} = \widehat{H}_{Ref} + \widehat{H}_{Raman} \tag{5.12}$$

Therefore the overall frequency resolved homodyne current reads:

$$\langle \widehat{I}_{\mu_j,\phi_j}(\Delta t)\rangle = \langle \widehat{I}^{Ref}_{\mu_j,\phi_j}(\Delta t)\rangle + \langle \widehat{I}^{Raman}_{\mu_j,\phi_j}(\Delta t)\rangle \tag{5.13}$$

We clarify that some probing effects are hidden through this first order approximation. For istance, we are neglecting the modification of the phonon selection rules due to the static polarization rotation of the sample.

Although ISRS and LRM occur simultaneously, measurements suggest (Figure 5.7 and Figure 5.10) that through polarization selection of the emitted field we are able to wash out ISRS features. Let us therefore go through the modelization of the homodyne response in parallel and cross geometry.

Parallel configuration Referring to coordinate system of Figure 5.6, in parallel configuration the analyzer selects the polarization along the x-component ($\mu = x$). In this case the leading contribution to the optical response are zero-order in the polarization rotation. This implies that the equilibrium response does not depend on $\boldsymbol{\chi}^{(0)}$. Moreover, by selecting $\mu = x$ the symmetry of the $\chi^{(1)}_{\mu\lambda}$ Raman tensors (Equation 5.1) implies that the only contribution to the pumped

[2]Since for each phonon $\frac{R}{m\Omega}$ represents the pump-driven atomic displacement and the Raman tensor elements $\chi^{(1)}_{\mu\lambda}$ have the dimension of the inverse of a length, the so defined cross-sections are adimensional.

response originates from the A and E^L-phonons. In parallel geometry we therefore get:

$$\begin{aligned}
\langle \widehat{I}_{x_j,\phi_j}(\Delta t)\rangle_{eq} &= |z_{x_j}||\alpha_{x_j}|\cos(\phi_j) \\
\langle \widehat{I}_{x_j,\phi_j}(\Delta t)\rangle_{pump} &= \tilde{a}\frac{|z_{xj}|\tau V_s\omega_j}{2V}\Bigg(\cos(\phi_j)\left(|\alpha_{xj+\frac{\Omega_A}{\delta}}| - |\alpha_{xj-\frac{\Omega_A}{\delta}}|\right)\cos(\Omega_A\Delta t)+ \\
&\qquad + \sin(\phi_j)\left(|\alpha_{xj+\frac{\Omega_A}{\delta}}| + |\alpha_{xj-\frac{\Omega_A}{\delta}}| + 4|\alpha_{xj}|\right)\sin(\Omega_A\Delta t)\Bigg)+ \\
&+\tilde{c_L}\cos(2\theta)\frac{|z_{xj}|\tau V_s\omega_j}{2V}\Bigg(\cos(\phi_j)\left(|\alpha_{xj+\frac{\Omega_E}{\delta}}| - |\alpha_{xj-\frac{\Omega_E}{\delta}}|\right)\cos(\Omega_E\Delta t)+ \\
&\qquad + \sin(\phi_j)\left(|\alpha_{xj+\frac{\Omega_E}{\delta}}| + |\alpha_{xj-\frac{\Omega_E}{\delta}}| + 4|\alpha_{xj}|\right)\sin(\Omega_E\Delta t)\Bigg)
\end{aligned} \tag{5.14}$$

The previous equation qualitatively clarifies the phase and amplitude observed features (Figure 5.7).

Amplitude is dominated by the only term inside the pumped response in phase with the equilibrium one (i.e. $\propto \cos(\phi_j)$). This is proportional to the phonon momentum ($\cos(\Omega\Delta t)$) and exhibits the predicted Raman shifts (Figure 2.7). It is indeed proportional to the difference of the amplitude of the phonon-coupled probe modes. Even if refractive contribution is included inside the parallel response, it does not influence the amplitude dynamics. As a matter of fact, it is proportional to $\sin(\phi_j)$ and hence null when the Raman response is maximum. Therefore, even if the refractive modulation is always present, its amplitude-driven modulation are hidden by the Raman-driven ones.

Conversely, the LRM contributions originate from the term proportional to $\sin(\phi_j)$. This term is $\pi/2$-shifted with respect to the unpumped current and drives phase modulation with a periodicity that follows the atomic oscillations ($\sin(\Omega\Delta t)$). A qualitatively plot of phase and amplitude trends of the homodyne response in parallel geometry is presented in Figure 5.17.

Cross configuration Let us now move to the qualitatively description of the extinction case (Figure 5.10). Since ISRS is a stimulated process we expect that the photons produced in a Raman process are likely to be created in mode states initially occupied [21]. For this reason we expect the photons emitted in the orthogonal polarization to have not undergone the Raman process. Consequently, as suggested by the experimental evidences (Figure 5.10), the extinction geometry is suitable to filter out the ISRS signatures.

In this case, both static polarization and birefringence have to be taken into account. Moreover we have to introduce in the model a further Hamiltonian describing polarization selection. The latter has the features of a static refractive Hamiltonian but with the off-diagonal terms which are real and have the opposite sign of that of $\boldsymbol{\chi}^{(0)}$ (Equation 5.8) in order to model polarization rotation. We take an analyzer Hamiltonian $\widehat{H}_{an}$ of the form:

$$\widehat{H}_{an} = -\frac{V_s}{2V}\sum_{\lambda\lambda',j}\omega_j\chi^{(0)\,an}_{\lambda\lambda'}\left(\hat{a}^\dagger_{\lambda j}\hat{a}_{\lambda' j} + \hat{a}_{\lambda j}\hat{a}^\dagger_{\lambda' j}\right) \tag{5.15}$$

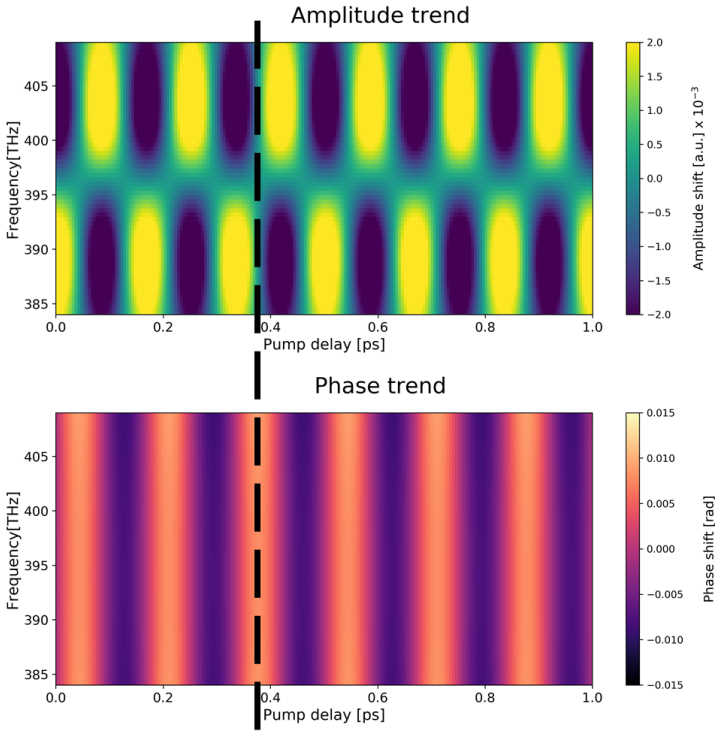

Figure 5.17: Parallel configuration: qualitative phase and amplitude temporal features. ISRS and LRM jointly contribute to the optical response of each probe mode. ISRS dominates amplitude dynamics, while LRM the phase one.

Here $\boldsymbol{\chi}^{(0)\ an}$ is a real tensor whose off-diagonal terms rule the polarization selection of the emitted field:

$$\chi^{(0)\ an}_{\lambda\lambda'} = \begin{pmatrix} 1 & -|w| \\ -|w| & 1 \end{pmatrix} \tag{5.16}$$

Therefore, the frequency-resolved homodyne current in this case results from the action of the combined Hamiltonian:

$$\widehat{H}_{probe} = \widehat{H}_{Ref} + \widehat{H}_{an} \tag{5.17}$$

on the initial probe state polarized along x. We stress once again that at first order no modification of Raman selection rules due to static probe polarization rotation occurs. Therefore we can set the y-direction as the analyzer direction (i.e. $\mu = y$). In this configuration the only phonon-dependent response is the LRM one and originates from the E^T-mode. The frequency-resolved homodyne current therefore reads:

$$\begin{aligned} \langle \widehat{I}_{y_j,\phi_j}(\Delta t)\rangle_{eq} &= |z_{y_j}||\alpha_{x_j}|\cos(\phi_j) + |w|(\cos(\alpha)-1)\frac{2\tau|z_{yj}|V_s\omega_j}{V}|\alpha_{yj}|\sin(\phi_j) \\ \langle \widehat{I}_{y_j,\phi_j}(\Delta t)\rangle_{pump} &= \tilde{c_T}\sin(2\theta)\frac{|z_{yj}|\tau V_s\omega_j}{2V}4|\alpha_{yj}|\sin(\Omega_E\Delta t)\sin(\phi_j) \end{aligned} \tag{5.18}$$

A qualitative plot of phase and amplitude shifts resulting from the extinction response is presented in Figure 5.18. The trends qualitatively confirm the experimental response (Figure 5.10). Indeed, amplitude exhibits no ISRS-driven

spectral weight shifts and it is instead ruled, as well as as the phase, by the periodic atomic displacement ($\propto \sin(\Omega \Delta t)$).

We underline that in the simulation it is crucial to take into account the static birefringence of the sample α in order to retrieve the measured amplitude trend. Indeed, if $\alpha = 0$ Equation 5.18 shows that the pumped response will be $\pi/2$-shifted with respect to the equilibrium one. Therefore no significant amplitude modulation will occur and this is in contrast with what we experimentally observe (Figure 5.10).

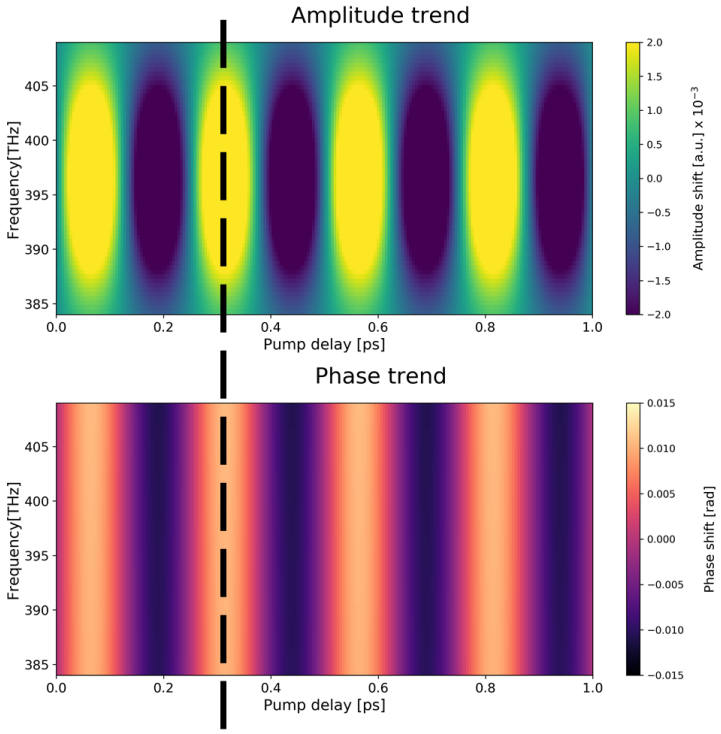

Figure 5.18: Cross configuration: qualitative phase and amplitude temporal features. ISRS features are filtered through polarization selection. LRM determines both amplitude and phase dynamics.

In Table 5.2 we summarize the predictions of the model for α-quartz. In particular, we present the detected phonons in parallel and extinction geometry for specific pump-probe polarization angles and the corresponding leading probing interaction.

Phonon cross-sections estimation Until now we have just conducted a qualitative analysis of amplitude and phase trends. We want now to go deeper and exploit the model to estimate the Raman cross-sections $\tilde{\chi}^{(1)}_{\mu\lambda}$ of probe-phonons interaction. The latter are indeed encoded inside the experimental quadrature shifts.

We observe that in parallel geometry no dependence of the homodyne current on static susceptibility occurs at first order (Equation 5.14). We can therefore exploit this configuration to retrieve the Raman cross-sections of the phonons detected in this geometry. Since phase shifts, unlike amplitude ones, do not depend on the probe intensity, we decide to employ them for the estimation. They are clearly sensitive to pump intensity but this has been taken constant

Probe-analyzer angle	Pump-probe angle (Θ)	Detected phonons	Probing process
90°	0	X	LRM^{eq}
90°	±45°	E^T	LRM^{phon} + LRM^{eq}
90°	±90°	X	LRM^{eq}
0°	0°	$A + E^L$	ISRS + LRM^{phon} + LRM^{eq}
0°	±45°	A	ISRS + LRM^{phon} + LRM^{eq}
0°	±90°	$A + E^L$	ISRS + LRM^{phon} + LRM^{eq}

Table 5.2: Summary of the α-quartz detected phonons as a function of the probe-analyzer and pump-probe polarization angle. For each configuration, we report the leading probing processes predicted by the quantum model. LRM^{phon} represents the phonon-dependent modulation of the sample refractive properties modelled through $\boldsymbol{\chi}^{(1)}$, while LRM^{eq} the equilibrium response ruled by $\boldsymbol{\chi}^{(0)}$.

among all the measurements. An experimental prove of this issue is presented in Figure 5.19 where we compare phase and amplitude trends in two fluence regimes of the probe (10^4 ph/pulse and 10^6 ph/pulse) at constant pump fluence (10^{12} ph/pulse).

In parallel geometry and with a pump polarized at $\Theta = 45°$, Fourier analysis (Figure 5.9) shows that the leading contributions to phase and amplitude shifts originate from the 6.2 THz total symmetric A-phonon[3]. The parallel measure (Figure 5.7) is therefore suitable for evaluating its Raman cross-section. Since this estimation passes through the determination of the phase shifts, we need a systematic way to evaluate them from the measurements. In particular, we note that in the real experiment there is a dissipative dynamics that causes an exponential decay of phonon oscillations and eventually of the phase shifts. Phase shifts scale indeed as $R/m\Omega$ which is the extent of the atomic displacement whose dumping is due to the phonon finite lifetime. However, the model does not include any dissipation dynamics of the excited phonon. For this reason, in order to compare the experimental phase shifts with the simulated one we have to normalize the phase dynamics to an exponential decay function which is characteristic of each phonon. The latter has been obtained by fitting the phase decay maxima in order to extract the coherent phonon lifetime (Figure 5.20(a)). The experimental phase trend has been subsequently rescaled with this exponential decay. Once rescaled, the phase trend has been fitted with a sinusoidal function to extract the amplitude of the oscillations. Once estimated the extent of phase oscillations, we have tuned the value of the Raman cross-section of the 6.2 THz A-phonon:

$$\tilde{a} = \frac{R_A}{m\Omega_A} a = \frac{\eta_{\Omega_A}^{pump}}{m\Omega_A} a^2 \tag{5.19}$$

in order to numerically obtain from the pumped contribution of Equation 5.14[4] a phase shift comparable with the experimental one within a 10% error band.

[3]Phase shifts contribution due to the 14 THz A-phonon are neglected.

[4]The pumped response of Equation 5.14 contains also the response from the E^L-phonon but

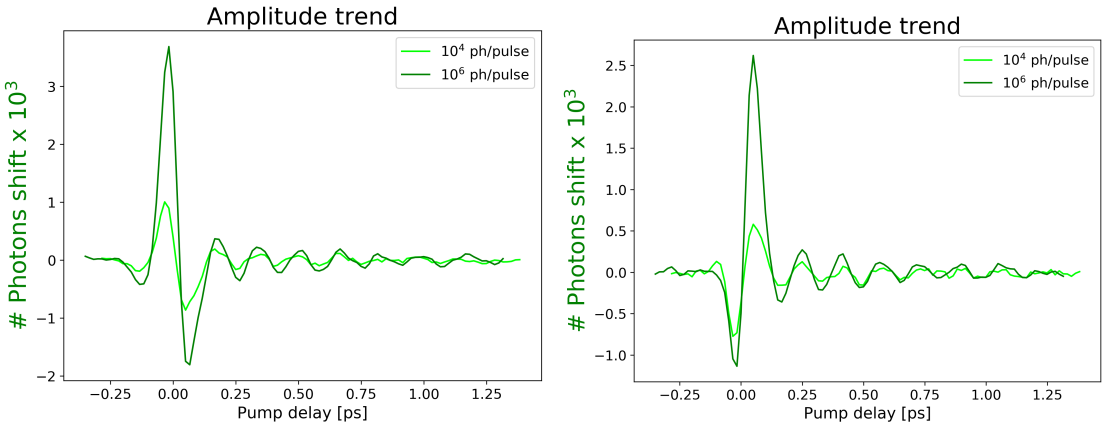

(a) 392 THz

(b) 403 THz

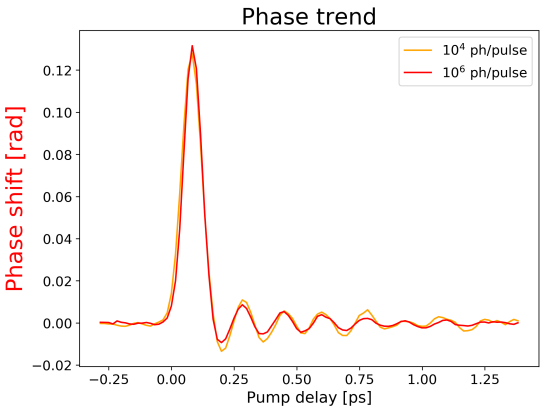

(c) 401 THz

Figure 5.19: Dependence of the amplitude and phase shifts on the intensity on the incident probe. In (a) and (b) the amplitude dynamics for two opposite side of the pulse (392 THz and 403 THz (Figure (5.7)) in the case of an incoming probe with 10^4 photons/pulse and 10^6 photons/pulse. In (c) the phase dynamics at the two previous fluences for the probe mode at 401 THz (Figure 5.7). In all the previous measurements the pump intensity is constant and equal to 10^{12} photons/pulse. LO power (single mode with $\sigma = 0.1$ THz) $= 1.0 \times 10^7$. The detected intensity is the same in both fluence regimes and equal to 2.0×10^4 ph/pulse.

The incoming probe has been simulated as a broad normalized gaussian pulse with $\sigma = 10$ THz and the local oscillator intensity scaled with respect to the probe one. Moreover we have set the photon-phonon interaction time τ as the probe duration (50 fs) and approximate $V_s/V \simeq 1$ (Equation 5.14). In this way, the only unknown parameter ruling phonon-dependent dynamics is indeed the A-phonon cross-section $\tilde{a}$ (Equation 5.14). The plot of the comparison between the experimental phase trend in parallel geometry and the simulated one is presented in Figure 5.20(b). The obtained cross-section of the 6.2 THz A-phonon reads:

$$\tilde{a} = \frac{R_A}{m\Omega_A} a = (1.45 \pm 0.09) \times 10^{-4} \tag{5.20}$$

we have neglect it since the pump-probe polarization angle in the presented parallel configuration is 45°. This is confirmed by the Fourier analysis of Figure 5.9.

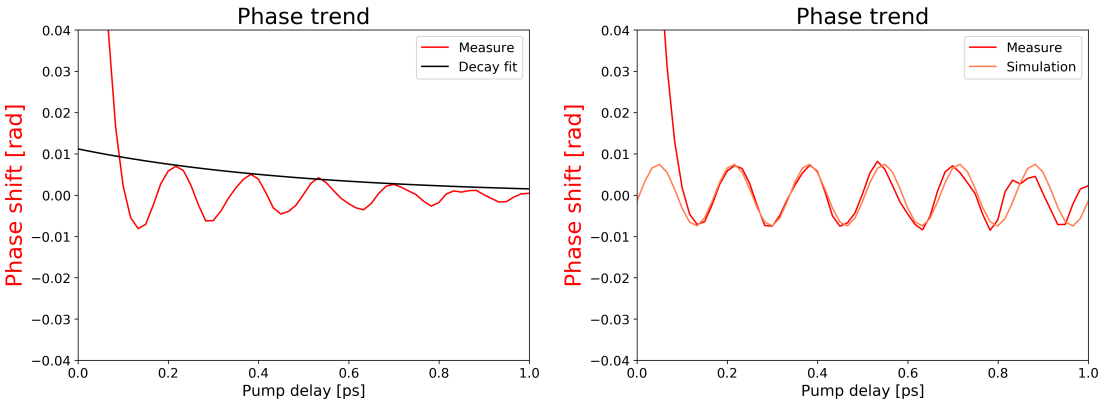

(a) (b)

Figure 5.20: Parallel geometry: phase dynamics ruled by the 6.2 THz A-mode. In (a) the experimental trend with the fit of the exponential dissipative decay (τ_A (6.2 THz) = 0.5 ps). Since the phase evolution exhibits no spectral dependence, the presented trend has been obtained by averaging the phase response of probe modes in a frequency window of 10 THz around the pulse center (Figure 5.7(b)). In (b) the experimental phase trend normalized with the decay function and the simulated phase dynamics used to estimate the Raman cross-section for A-phonon ($\tilde{a}$).

Therefore, the correction to the linear susceptibility resulting from the non-linear interaction with the A-phonon is approximatively 10^{-4} (Equation 5.7).

In Figure 5.21 we compare the experimental and simulated phase and amplitude trends for the parallel case (Figure 5.7) with the A-phonon cross-section estimated as before and the with local oscillator and probe intensity as in Figure 5.7. In the presented plots simulated trends have been rescaled by the lifetime decay of the 6.2 THz A-phonon (0.5 ps).

We can now exploit the estimation of the A-mode cross-section to retrieve the cross-section of the doubly degenerate E-modes. Selection rules (Table 5.2) imply that when pump, probe and detected field are all co-polarized, A and E-phonons [5] can be simultaneously detected with the maximum cross-section. Since phase shifts scale linearly with the photon-phonon cross-section, the cross-section of the E-mode can be unveiled by looking at ratio between the Fourier components at 4 THz and 6.2 THz of phase trend in co-polarized geometry (Figure 5.22). In this way we can retrieve the Raman cross-section of the E^L-mode which reads:

$$\tilde{c_L} = \frac{R_{E^L}}{m\Omega_E} c_L = (1.13 \pm 0.09) \times 10^{-4} \tag{5.21}$$

This cross-section is the same of that of the degenerate E^T-phonon detected in the extinction geometry:

$$\tilde{c_T} = \frac{R^{max}_{E^T}}{m\Omega_E} c_T = (1.13 \pm 0.09) \times 10^{-4} \tag{5.22}$$

In Table 5.3 we summarize the Raman cross-sections of the detected phonons in α-quartz. Since these cross-sections have been all evaluated at constant pump

[5] Actually, in the co-polarized geometry the detected phonon is the E^L which has a different symmetry with respect to the E^L one. However, they share the same Raman cross-section.

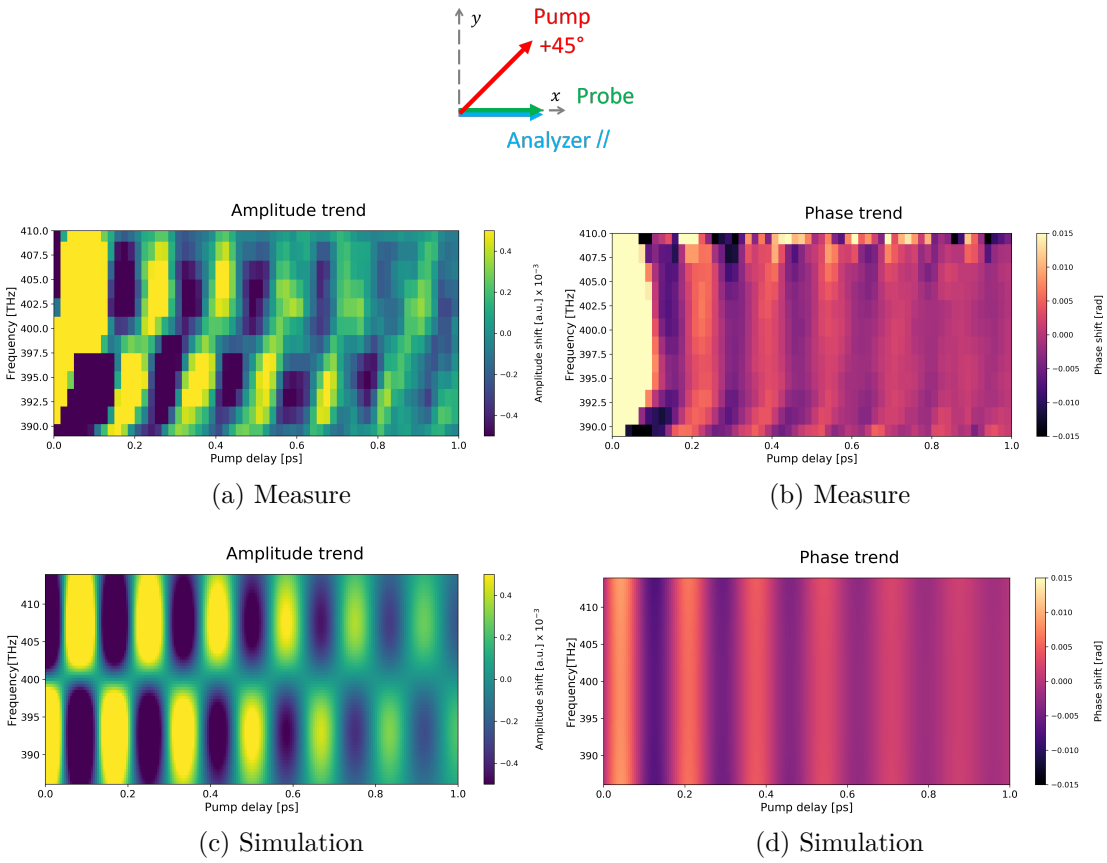

(a) Measure (b) Measure

(c) Simulation (d) Simulation

Figure 5.21: Parallel geometry: quantitative comparison between experimental and simulated amplitude and phase trends. Phase and amplitude shifts are ruled by the 6.2 THz A-phonon cross-section estimated to be $\tilde{a} = (1.45 \pm 0.09) \times 10^{-4}$. This is the only phonon detected with the pump polarization at $\Theta = 45°$ (Figure 5.12). In simulated trends the finite lifetime of 6.2 THz A-mode (0.5 ps) is included.

fluence ($4.8{\times}10^{12}$ ph/pulse) their relative values are representative of their relative photon coupling strength.

Detected phonon	Frequency	Cross-section
A	6.2 THz	$(1.45 \pm 0.09) \times 10^{-4}$
E^L	4.0 THz	$(1.13 \pm 0.09) \times 10^{-4}$
E^T	4.0 THz	$(1.13 \pm 0.09) \times 10^{-4}$

Table 5.3: Raman cross-sections of the α-quartz phonons at a constant pump intensity of 4.8×10^{12} ph/pulse.

Static birefringence estimation Until now we have shown how we can quantitatively exploit phonon-dependent phase shifts for the estimation of Raman cross-sections. In the following, we will exploit the time-resolved measurement to retrieve an equilibrium property of quartz: the static birefringence.

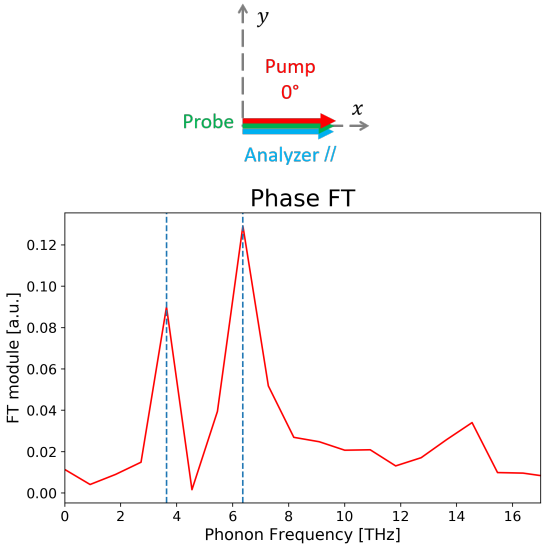

Figure 5.22: Phase dynamics FT spectrum in the of co-polarized probe, pump and detected field. In this configuration the Raman cross-section of the 4 THz E^L-mode is maximum.

The model suggests that the suitable geometry to do this is the extinction one. Indeed, at first order, static birefringence (α) comes out only in the optical response of the emitted field component whose polarization is normal to the incident one (Equation 5.18). The information due to static birefringence encoded in amplitude and phase shifts are not redundant. Equation 5.18 indeed shows that we can get phase shifts even in the absence of amplitude shifts (i.e. when $\alpha = 0$). Since in this formalism we are encoding a static property into dynamical ones, to retrieve the static birefringence from the time-dependent amplitude and phase shifts is essential to know the Raman cross-section of the detected phonon. In this geometry and with a pump-probe polarization angle $\Theta = 45°$, the only detected phonon is the E^T-symmetry one (Figure 5.12) whose cross-section has been estimated in the previous paragraph and reads:

$$\tilde{c_T} = \frac{R_{E^T}^{max}}{m\Omega_E} c_T = (1.13 \pm 0.09) \times 10^{-4} \tag{5.23}$$

Once retrieved the cross-section of the phonon detected in cross-polarization (E^T), we can now exploit Equation 5.18 to estimate the static birefringence α. The equilibrium response (Equation 5.18) depends not only on α, but also on the static polarization rotation whose value is required to estimate birefringence. Since our 0.2 mm-tick sample rotates the incoming x-polarization of about $\beta = 4°$ we set:

$$|w| = \frac{|\alpha_{yj}|}{|\alpha_{xj}|} = \tan(\beta) = 0.07 \tag{5.24}$$

Therefore, once known $\tilde{c_T}$ and the polarization rotation $|w|$, the only free parameter in Equation 5.18 is α. We can hence tune it in order to numerically obtain a homodyne response whose amplitude and phase dynamics simultaneously fit the experimental ones within a 15% error window (Figure 5.23). The representative probe mode used for the estimation is the same of Figure 5.10 (391 THz). Since the model does not predict any amplitude and phase decay due to phonon finite

lifetime, the representative trends have been normalized to the decay trend of 4 THz E^T-phonon whose lifetime has been estimated to be τ_{E^T} (4 THz) = 3.0 ps. Moreover, for the comparison with theoretical model predictions the amplitude dynamics has been normalized to the unpumped amplitude response in order to let it to be independent on probe incident intensity. Within an error of 15% in

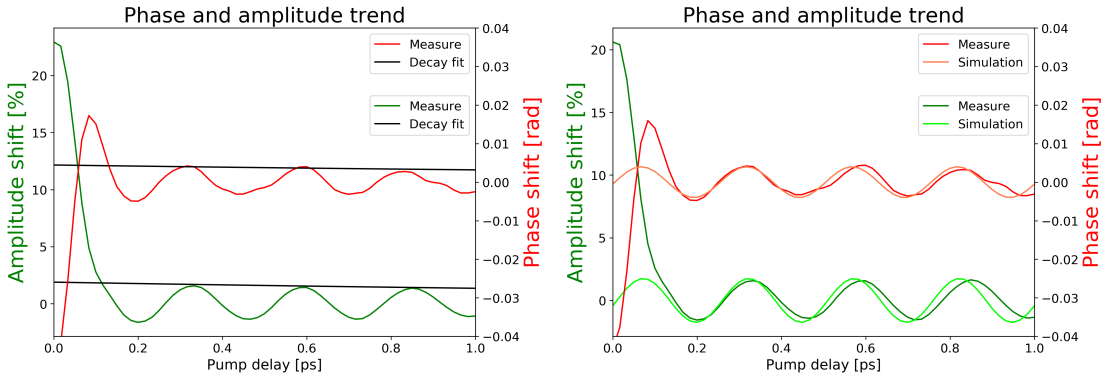

(a) (b)

Figure 5.23: Cross geometry: phase and amplitude dynamics of a representative emitted probe mode at 391 THz (Figure 5.10). In (a) the experimental trends with the fit of the exponential dissipative decay of E^T-phonon ($\tau_{E^T} = 3.0$ ps). In (b) the experimental amplitude and phase trends normalized with the decay function and simulated dynamics used to estimate quartz birefringence.

both phase and amplitude estimations, the static birefringence for our 0.2 mm tick α-quartz sample reads:

$$\alpha = (24.8 \pm 0.6)^\circ \tag{5.25}$$

This is the phase-mismatch between the two orthogonal polarization components of the incident probe. This de-phasing is responsible for the elliptical polarization of the outgoing probe (Figure 5.24).

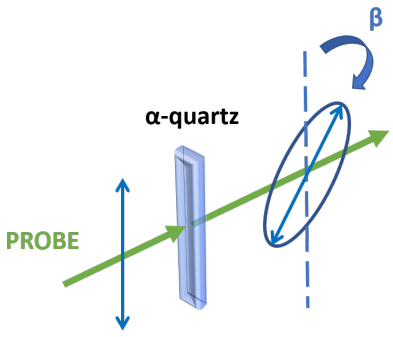

Figure 5.24: Static probing effects resulting from equilibrium refractive properties of α-quartz. Due to the combined action of polarization rotation and birefringence the outgoing probe polarization state is elliptical.

We stress that this is a static effect and hence ruled by $\boldsymbol{\chi}^{(0)}$. The phonon-dependent contribution will entry as a modulation of amplitude and phase of

the two orthogonal polarization components. However, the model predicts that phonon-induced phase modulations of the two orthogonal components are both in phase with the nuclear oscillations. This implies that at first order no de-phasing due to phonon contribution occurs. Hence, phonon-dependent birefringence will be an higher order effect.

In Figure 5.25 we summarize the theoretical predictions in extinction geometry obtained from the previously derived Raman cross-section $\tilde{c_T}$ and static birefringence α. We note that the simulated phase trend in this geometry reproduces only the low-frequency response. As pointed out in Figure 5.11 the strongest phase shifts at higher frequencies are likely to derive from a non-extinguished emitted field whose polarization is parallel to the incoming one.

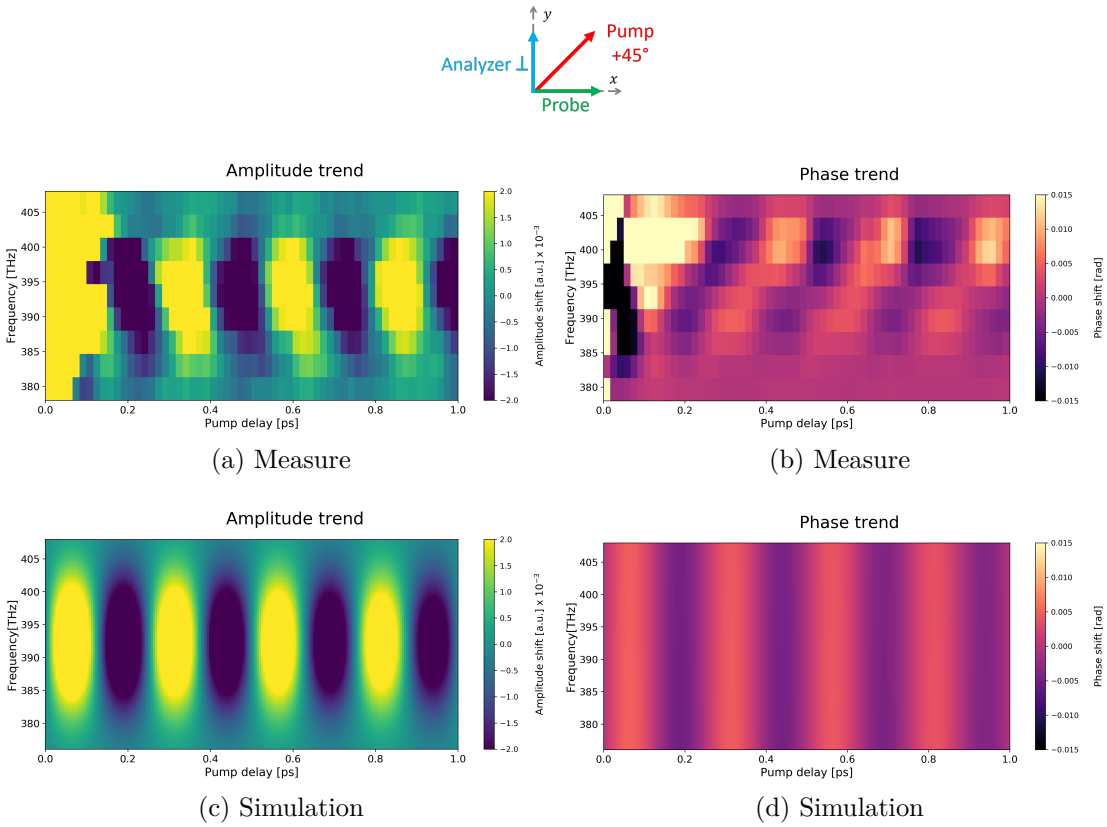

(a) Measure (b) Measure

(c) Simulation (d) Simulation

Figure 5.25: Cross geometry: quantitative comparison between experimental and simulated amplitude and phase trends. Phase and amplitude shifts are ruled by the 4 THz E^T-phonon cross-section estimated to be $\tilde{a} = (1.13 \pm 0.09) \times 10^{-4}$, by static polarization rotation ($\beta = 4°$) and birefringence ($\alpha = (24.8 \pm 0.6)°$). In simulated trends the finite lifetime of 4 THz E^T-mode (3.0 ps) is included. Simulated phase trends reproduce only the low frequency phase response, since the upper is supposed to derive from a non-extinguished parallel polarized emitted field (Figure 5.11.

Pump-probe polarization angle dependence Finally, we move to the analysis of the dependence of amplitude and phase trends on the pump-probe polarization angle (Θ). In particular, we will compare with the model the predictions of the measurements at $\Theta = \pm 45°$ in extinction and parallel geometry. As shown

in Table 5.1, this is a suitable geometry to separately address the coherent dynamics of phonons belonging to different symmetry groups. Indeed, if the pump is polarized at 45° with respect to the probe we can isolate the response of A-mode and E-mode by selecting the polarization of the emitted field. As presented in Figures 5.14 5.16 we expect the symmetry of the detected phonon to be mapped onto phase and amplitude temporal structure of the probe. In particular, the experimental evidence shows that by probing the E-mode after an excitation at $\Theta = +45°$ or at $\Theta = -45°$ a π-shift of amplitude and phase temporal dynamics occurs (Figure 5.14).

This effect can be retrieved from the model exploiting the expression of the mean homodyne current in extinction geometry (Equation 5.18). This is indeed the only configuration in which the optical response of an E-mode can be isolated (i.e. the E^T one). The crucial issue for the explanation of this π-shift is noting that the pumped homodyne current is proportional to the momentum R imparted by the pump to the phonon initially at rest. For the E-symmetry mode this momentum shift is sensitive to pump polarization Θ and reads (Equation 5.9):

$$R_{E^T} = -c_T \sin(2\Theta) \tag{5.26}$$

The previous expression clarifies the observed amplitude and phase dynamics. By switching the pump polarization angle from $-45°$ to $45°$, the pump imparts to the E-phonon a momentum which has opposite sign. Consequently, the atomic oscillations induced by the pump are in anti-phase in the two excitation geometries (Figure 5.26).

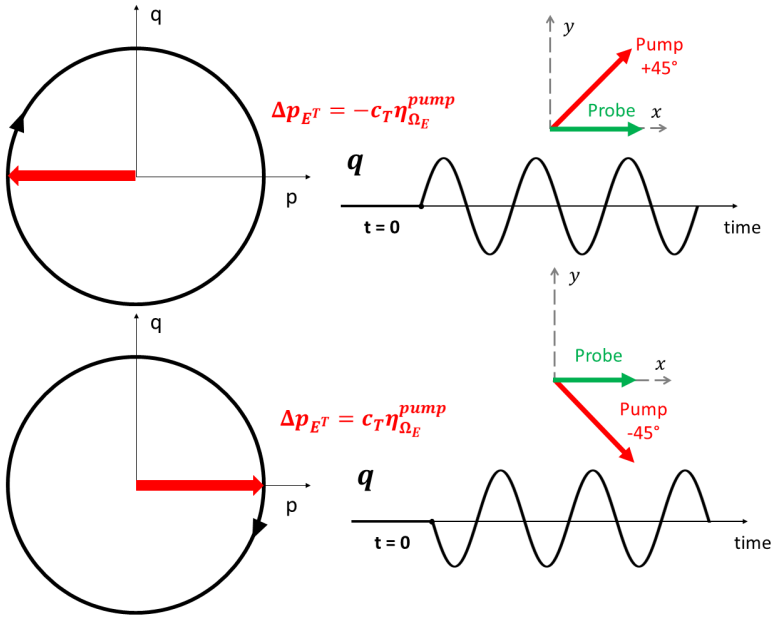

Figure 5.26: Effect of pump angle on E^T-phonon phase oscillation. At the top the case $\Theta = +45°$, at the bottom the case $\Theta = -45°$. Coherent oscillations are π-shifted in the two cases.

Now, since the excited phonon is probed in extinction geometry, the leading probing effect is LRM which encodes the instantaneous atomic displacement into both phase and amplitude dynamics of the outgoing probe. Since E-phonon oscillations are π-shifted in the two excitation geometries, amplitude and phase of

each emitted field mode will be likewise in anti-phase. This theoretical evidences are presented in Figure 5.27 where we compare the simulated amplitude and phase dynamics resulting from the detected E^T-mode.

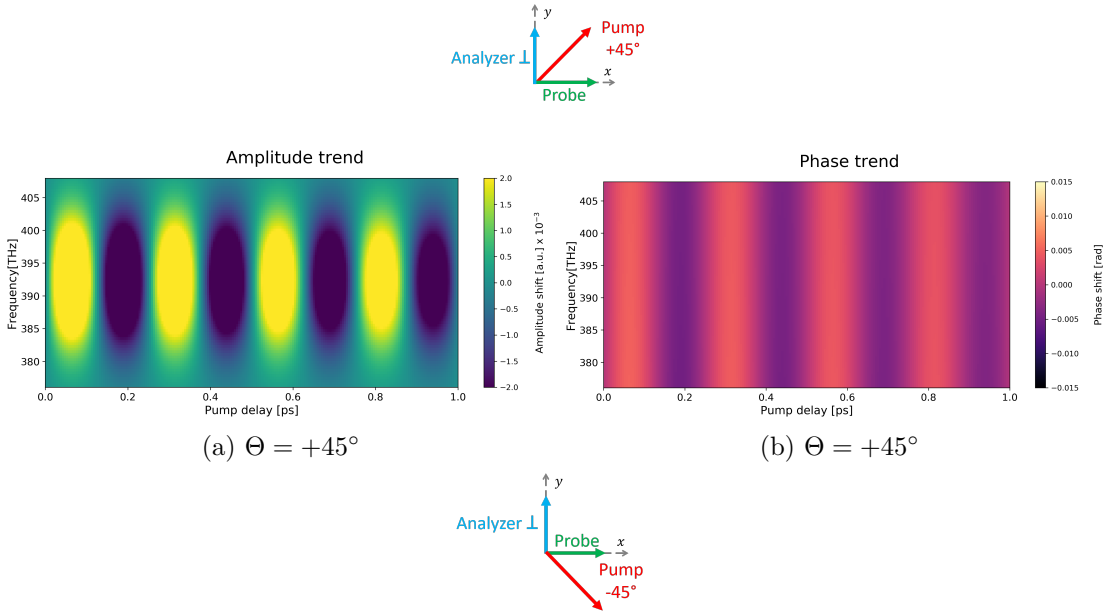

(a) $\Theta = +45°$ (b) $\Theta = +45°$

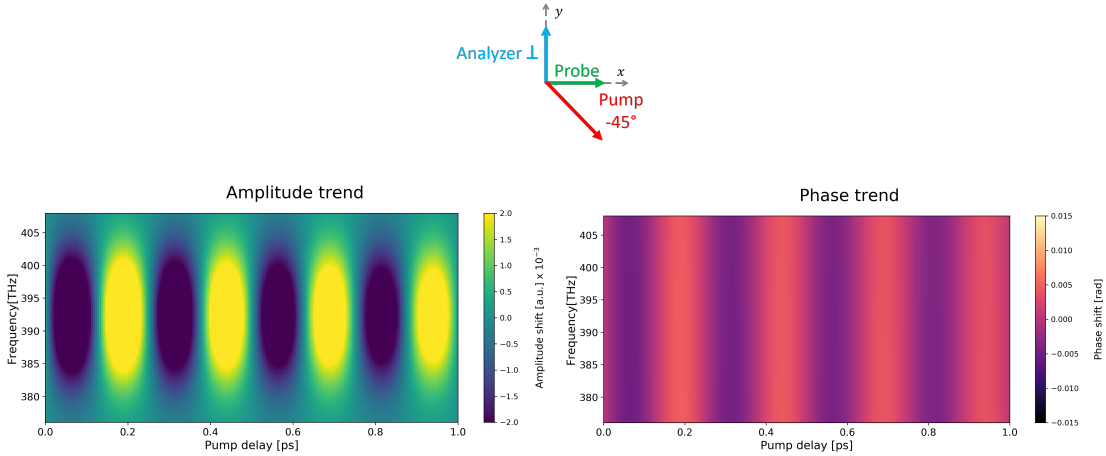

(c) $\Theta = -45°$ (d) $\Theta = -45°$

Figure 5.27: Cross geometry: simulated dependence on pump-probe polarization angle ($\Theta = \pm 45°$) for the detected E^T-phonon. Model confirms experimental trends (Figure 5.13): phase and amplitude response are π-shifted when the detected E^T-phonon is excited at $\Theta = +45°$ and at $\Theta = -45°$.

The simulation agrees with the experimental results: phase and amplitude response of each mode are in anti-phase when the E^T-phonon is excited with a pump polarized at $\Theta = +45°$ or $\Theta = -45°$.

On the other hand, this pump angle dependence does not subsist in parallel geometry. In this case ($\Theta = \pm 45°$), the only detected phonon is indeed the total symmetric one whose pump-induced momentum shift is not sensitive to pump polarization. Consequently, no dependence on Θ is present in the pumped contribution to frequency-resolved homodyne current. This explain the experimental evidence presented in Figure 5.16: amplitude and phase response of the emitted field resulting from the interaction of the probe with A-phonon is not sensitive to pump polarization.

5.3 Beyond non-absorbing materials: time-resolved homodyne on $CuGeO_3$

In the previous section we have exploited the feasibility of our technique to track the mean phononic field evolution in transparent materials, such as quartz. In those materials no electronic transitions are permitted within probe bandwidth and light-matter interaction is dominated by ISRS. We want now to apply multi-mode homodyne detection to more complex systems and address coherent phonon dynamics in resonance with electronic transitions. This is particularly interesting in systems where low energy modes are able to drive orbital excitations, such as Copper-Germanate ($CuGeO_3$).

Copper Germanate is an insulating crystal belonging to the family of cuprates. Its room temperature structure is schematized in Figure 5.28 and takes the name of "normal" or "undistorted" phase, in order to distinguish it from the distorted phase present below 14 K. Phase transition between the undistorted and distorted crystal structure is a spin-Peierls transition, in which the lattice distortion is accompanied by the formation of a spin-singlet ground state and the creation of a energy gap in the spectrum of magnetic excitations [28]. The room temperature structure is orthorombic: the Cu ions are at the center of edge-sharing octahedra CuO_6 whereas the Ge ions are at the centre of corner-sharing tetrahedra GeO_4. $CuGeO_3$ represents a playground system for the study of the interplay between

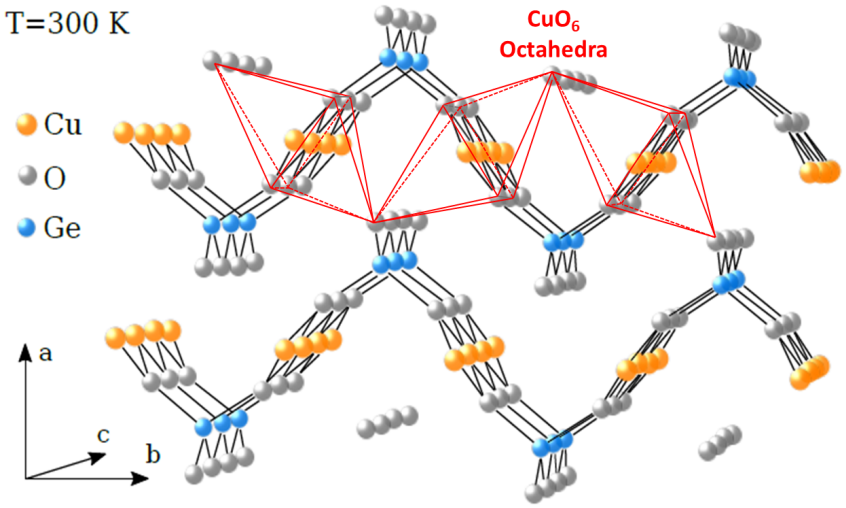

Figure 5.28: Room temperature $CuGeO_3$ structure with indicated the chain of edge-sharing CuO_6 octahedra (Adapted from [28]).

orbital excitations and phonon modes in Cu-O planes. This interplay plays a crucial role in the physics of cuprates, where various evidences [31] point towards a preferential channel for mapping the low energy physics of Cu-O vibrational modes to high energy electronic responses, such as *d-d* transitions. This coupling between vibrational and orbital excitations is easier to understand in $CuGeO_3$ since *d-d* and charge transfer transition are clearly separated in energy (Figure 5.29).

In our experiment we excite through ISRS a coherent lattice oscillation and probe the so excited system at 1.6 eV in resonance with *d-d* electronic transitions.

The objective of this kind of experiment is to see whether signatures of an ISRS probing process can be retrieved also in resonance with an orbital excitation and eventually retrieve the coupling strength between electronic and vibrational degrees of freedom.

Homodyne detection is well suited to study weak transmitted beams out of an absorptive material. Its low intensity sensitivity originates from the fact that the emitted field amplification is driven by an external local oscillator. Standard non-linear spectroscopies employ indeed self-heterodyne detection which is intrinsically limitated by equilibrium absorption. In the self-heterodyne scheme the local oscillator is not an external field, but is instead one of the transmitted probe which drives the emitted field amplification[6]. Clearly, if the transmitted intensity is attenuated due to static absorption the amplification effect is strongly reduced. With our set-up this limitation is overcome.

In our experiment we employ a geometry in which pump and probe are collinear

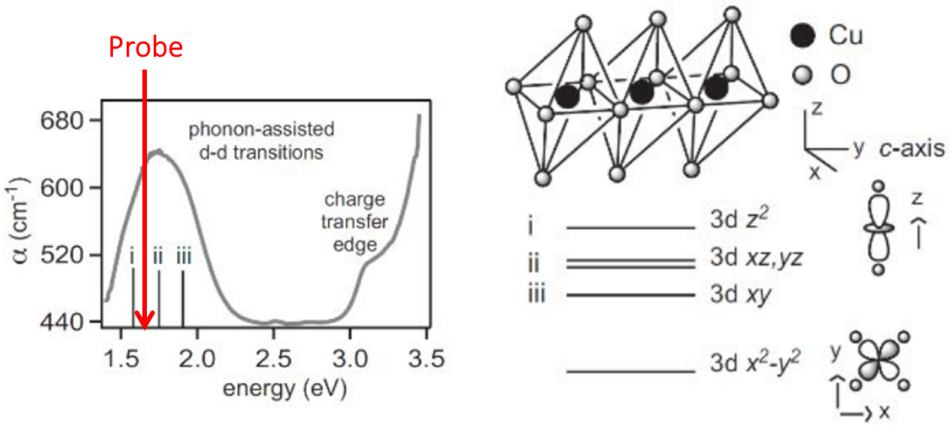

Figure 5.29: Left: absorption spectra of $CuGeO_3$ at 300 K. In our experiment the system is probed in the region of the *d-d* phonon-assisted transitions. Right: Cu-O octahedra and representation of the energy levels of the *d-d* transitions that are splitted by the effect of crystal field (Adapted from [28]).

along c-axis and only the parallel polarization component of the emitted field is detected. In this configuration we are able to detect only a total symmetric mode of A_g symmetry at 5.6 THz. This mode originates from in-phase vibration of Ge and O atoms of GeO_3 chains along the c-axis (Figure 5.30). Using the same

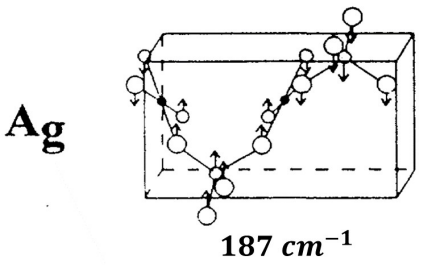

Figure 5.30: Total symmetric A_g-mode detected in our configuration.

[6]Also in our configuration the emitted field is self-heterodyned by the probe. However, the leading amplification process is driven by the external local oscillator, whose intensity is typically 100 times greater than the transmitted probe one.

notation adopted for quartz, its Raman tensor reads:

$$A_g = \begin{pmatrix} a & 0 \\ 0 & a \end{pmatrix} \tag{5.27}$$

and its pump-dependent cross-section ruling the probing process is:

$$\tilde{a} = \frac{R_A}{m\Omega_A} a = \frac{\eta_{\Omega_A}^{pump}}{m\Omega_A} a^2 \tag{5.28}$$

Multimode homodyne response (Figure 5.31) shows that also in resonance with an electronic transition we are able to encode inside the high energy probe field the low energy vibrational excitation. In particular, the amplitude shifts of each probe mode map the energy transfer between the high energy field components and the vibrational ones, while the amplitude shifts map the periodic lattice displacement. The first are ruled by ISRS, while the latter originate from the refractive modulation.

Let us now apply the quantum model presented in Chapter 2 to reproduce amplitude and phase dynamics and eventually estimate the A_g-mode Raman cross-section. The latter will give information about the coupling strength between the d electrons and the low energy mode. Since we are detecting the emitted field whose polarization is parallel to the probe one, the contributions to frequency-resolved homodyne response originate from both ISRS and LRM. By using the same notation adopted for α-quartz, the latter reads:

$$\begin{aligned} \langle \widehat{I}_{x_j,\phi_j}(\Delta t)\rangle_{eq} &= \mu |z_{x_j}||\alpha_{x_j}| \cos(\phi_j) \\ \langle \widehat{I}_{x_j,\phi_j}(\Delta t)\rangle_{pump} &= \mu\tilde{a}\frac{|z_{xj}|\tau V_s \omega_j}{2V}\Bigg(\cos(\phi_j)\left(|\alpha_{xj+\frac{\Omega_A}{\delta}}| - |\alpha_{xj-\frac{\Omega_A}{\delta}}|\right)\cos(\Omega_A \Delta t) + \\ &\quad + \sin(\phi_j)\left(|\alpha_{xj+\frac{\Omega_A}{\delta}}| + |\alpha_{xj-\frac{\Omega_A}{\delta}}| + 4|\alpha_{xj}|\right)\sin(\Omega_A \Delta t)\Bigg) \end{aligned} \tag{5.29}$$

where we have denoted with μ the static field absorption. For our sample we have measured $\mu = 0.12$. As for quartz, we can exploit the measured phase shift to obtain the Raman cross-section of the detected A_g phonon. We make use of them, rather then the amplitude ones, since they are independent on probe absorption. By following the same procedure (Figure 5.32) adopted for quartz phonons we get, within an error of 10% between simulated and experimental phase oscillations, a cross-section equal to:

$$\tilde{a} = \frac{R_{A_g}}{m\Omega_{A_g}} a = (8.3 \pm 0.6) \times 10^{-5} \tag{5.30}$$

The latter quantifies the pump-driven cross-section between the A_g mode and the d electrons at a pump intensity equal to that of the experiment on quartz (4.8×10^{12} ph/pulse). For this reason we can directly compare them. In Table 5.4 we summarize the cross-sections calculated for the detected phonons in quartz and $CuGeO_3$. Finally, we stress that in our set-up the vibrational mode excitation has been induced through ISRS by a near-infrared (NIR) pump. As a future

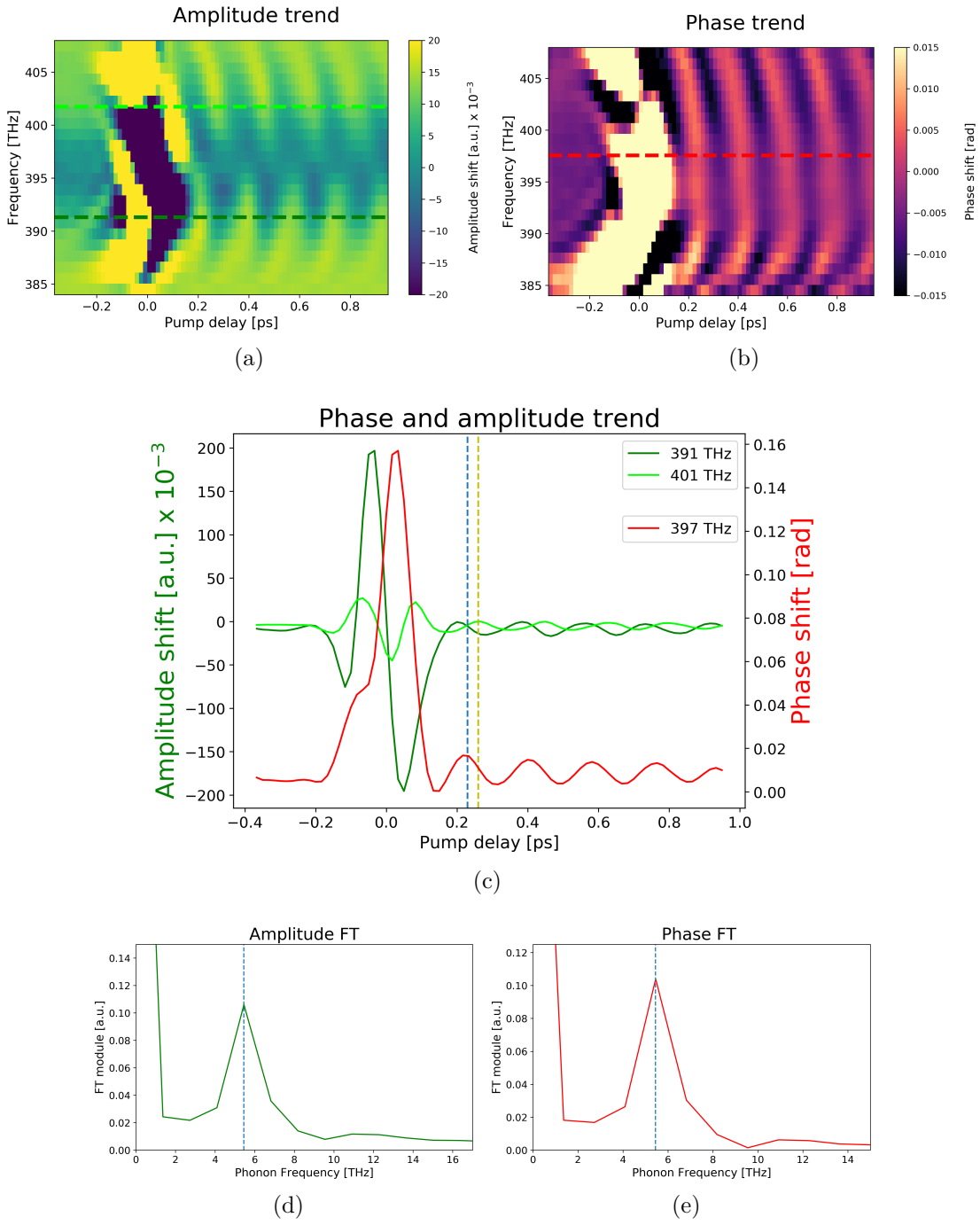

Figure 5.31: $CuGeO_3$ excited along c-axis: amplitude (a) and phase (b) temporal dynamics of each mode of the emitted probe field. ISRS features are visible in amplitude dynamics also with a probe at 1.6 eV in resonance with *d-d* transitions. Conversely, phase trend encodes LRM effects and is therefore $\pi/2$-shifted with respect to amplitude (c). Amplitude (d) and phase (e) FT unveil the detected mode: 5.6 THz A_g-mode. Probe power $= 1.3 \times 10^7$ ph/pulse; Pump power $= 4.8 \times 10^{12}$ ph/pulse; LO power (single mode with $\sigma = 0.2$ THz) $= 1.2 \times 10^7$ ph/pulse.

perspective, we will explore the possibility of pumping the phonon resonantly to its characteristic energy and map also in this case the high energy response. This

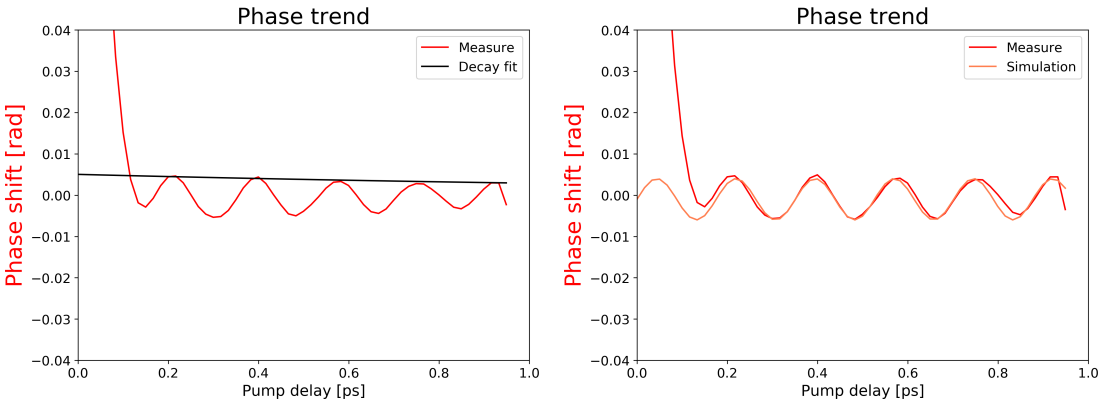

(a) (b)

Figure 5.32: Phase dynamics ruled by the detected A_g-mode. In (a) the experimental trend with the fit of the exponential dissipative decay ($\tau_{A_g} = 1.8$ ps). Since the phase evolution exhibits no spectral dependence, the presented trend has been obtained by averaging the phase response of probe modes in a frequency window of 10 THz around the pulse center (Figure 5.7(b)) Moreover the trend has been shifted by the constant phase response at negative times (Figure 5.31). In (b) the experimental phase trend normalized with the decay function and the simulated phase dynamics used to estimate the Raman cross-section of the A_g-phonon ($\tilde{a}$).

	Detected phonon	Frequency	Cross-section
α-quartz	A	6.2 THz	$(1.45 \pm 0.09) \times 10^{-4}$
α-quartz	E^L	4.0 THz	$(1.13 \pm 0.09) \times 10^{-4}$
α-quartz	E^T	4.0 THz	$(1.13 \pm 0.09) \times 10^{-4}$
$CuGeO_3$	A_g	5.6 THz	$(8.30 \pm 0.60) \times 10^{-5}$

Table 5.4: Raman cross-sections of the detected phonons in α-quartz and $CuGeO_3$ at a constant pump intensity of 4.8×10^{12} ph/pulse.

idea is driven by the fact that in this case an excess of thermal incoherent induced by the NIR-pump excitation will be avoided.

Chapter 6

Towards statistical analysis

Time-resolved techniques monitor the modification of the optical properties of a sample after a sudden excitation. In the standard pump-probe approach this purpose is reached by measuring the variation of the mean number of photons transmitted or reflected by the sample at a variable time from the pump-induced excitation. With this detection system we are able to obtain clean optical responses in which the noise is considerably reduced through the average of many pulses. The strong limit of this approach resides in the fact that the many pulses integration cuts off not only the environmental noise, but also the intrinsic quantum fluctuations of the detected signal which can be unveiled with our set-up (Chapter 4).

With our innovative approach (Figure 3.3) we are sensitive not only to intensity fluctuations of quantum origin. Indeed, our optical observable (frequency-resolved homodyne photocurrent) maps both the amplitude and the phase of each detected field mode. The time-resolved multimode homodyne approach allows therefore to track phase-dependent modifications of each probe statistics and to study how these quantum noise modifications evolve after the pump excitation.

Furthermore, the possibility of isolating through local oscillator shaping the homodyne response of only a subsets of the full probe modes (for example two mode response) and retrieve their statistics (Figure 1.6) opens the perspective of unveiling multimode quantum correlations imprinted on photon modes by their non-linear interaction with the sample. In the systems studied in this thesis (α-quartz and $CuGeO_3$) the leading non linear-interaction is ISRS which couples probe modes whose frequency difference matches the phonon one (Chapter 2). In a more formal language, the single probe modes fluctuations allows to reconstruct the diagonal terms of the covariance matrix of the probe state (cfr Equation 1.37), while the multimode ones permit to retrieve the off-diagonal ones, related to the correlations between different optical modes. The detection of the two previous observables will eventually open the possibility to reconstruct the multimode probe quantum state (through its covariance matrix) and monitor its time-dependent variation.

In this chapter, we present the preliminary single mode and multimode time-resolved fluctuations measurements on the two samples studied in this thesis: α-quartz and $CuGeO_3$. For the multimode case, we will limit our preliminary measurements to the two modes case (Figure 1.6) and hence study multimode quantum correlations imprinted by ISRS only on the two phonon-coupled modes.

6.1 Single mode statistical measurements

In this section we present the results of time-resolved single probe mode fluctuations on $CuGeO_3$ and α-quartz measured by mean of the set-up illustrated in Figure 3.3. We remark that in all the presented measures we will work with a local oscillator intensity suitable to ensure the detection in shot-noise conditions (Chapter 4). In this regime, the detected homodyne current noise, once filtered of photon-independent contributions, maps the quantum fluctuations of the probe electric field.

We will start by illustrating how the measured data are treated in order to filter out these slow noise contributions and then move to a preliminary analysis of the filtered noise trends.

6.1.1 Variance data analysis

In Figure 6.1(a) we show a representative measurement of the probe quadrature variance dynamics detected with our set-up. In the presented plot the response of a single probe mode is isolated, since a single frequency local oscillator is employed (Figure 3.3). A vertical cut in the map represents the phase-resolved quadrature variance obtained by changing the local oscillator phase. Conversely, an horizontal cut describes how quadrature variance at fixed phase evolves after the pump excitation. For each point of the 2D map, the variance is calculated on a pulse train of 2000 pulses at the laser repetition rate (200 kHz).

We note (Figure 6.1) that, by calculating the variance with this method, slow noise contribution are not filtered out. This can be understood by looking at the variance response at negative times, which exhibits a phase-dependent dynamics. In fact, before the phonon excitation, we expect the probe to be in a coherent state whose variance is phase-independent and equal to 1/2. In order to filter out these slow noise contribution, we have decided to evaluate the variance of the full digitized train of pulses by averaging the variances calculated over smaller pulse subsets of 10 pulses each. Through this data treatment, noises slower than the duration of a 10 pulses train (50 μs) are cancelled. In Figure 6.1(b) we present the filtered variance map. The effectiveness of the filtering is proved by the elimination of the slow periodic noise at negative times.

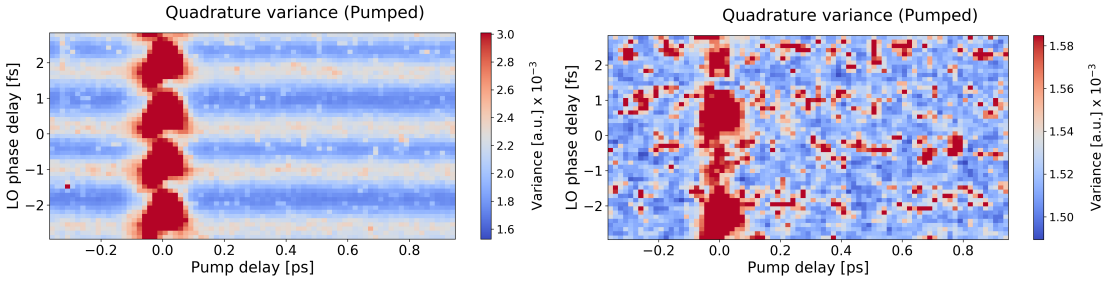

(a) Raw variance

(b) Filtered variance

Figure 6.1: Single mode quadrature variance. In (a) the variance calculated on the full pulses train (2000 pulses). In (b) the variance evaluated by taking the average variance of 200 smaller pulse subsets (10 pulses each) in order to filter classical slow noises.

As for mean value measurements (Chapter 5) pumped and unpumped maps can be acquired at the chopping rate at each delay. The latter are presented in Figure 6.2 together with the differential one resulting from the subtraction of the previous two.

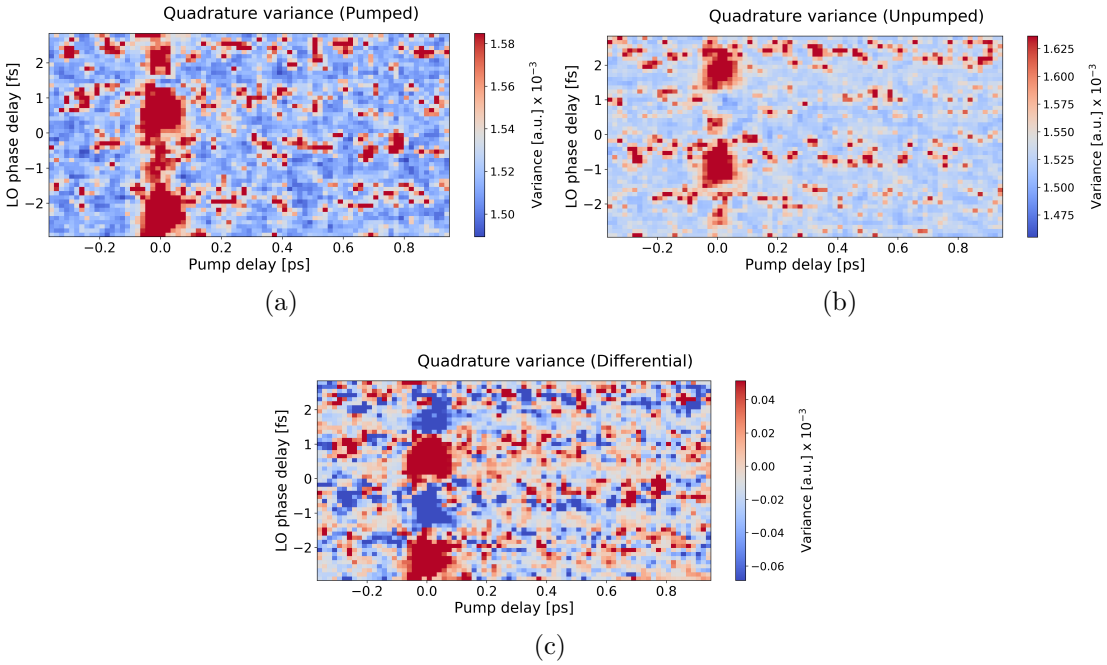

Figure 6.2: Single mode quadrature variance datasets. In (a) and (b) the pumped and the unpumped variance measured at the chopping rate (400 Hz). In (c) the difference between (a) and (b).

6.1.2 Measurements on $CuGeO_3$

In this section the preliminary statistical measures on $CuGeO_3$ are shown. Sample phonons are excited trough ISRS by the pump and the induced optical response is probed in resonance with *d*-*d* transitions. The objective of these measurements is to see whether exists a phase-dependent modification of probe statistics due to an absorptive process. The adopted configuration is the same as the one described in Section 5.3: the sample is excited along the *c*-axis (Figure 5.29) and the detected probe polarization is parallel with respect to the incident one.

In Figure 6.3(a) we present the time-resolved pumped variance response of a single probe mode. We notice that the pump induces at the overlap (time = 0) a phase-dependent modification of the probe statistics. In particular, we notice (Figure 6.3(b)) that this variance modulation evolves at the same frequency of the equilibrium probe quadrature and has its maxima in correspondence with the zeros of the mean probe field (blue curve in Figure 6.3(b)).

As shown in Figure 6.4, the pump excitation induces a phase-dependent modulation also of the unpumped variances measured at the chopper rate. This modulation is in anti-phase with respect to the pumped variance.

Both the modulation of the pumped and the unpumped noise are triggered

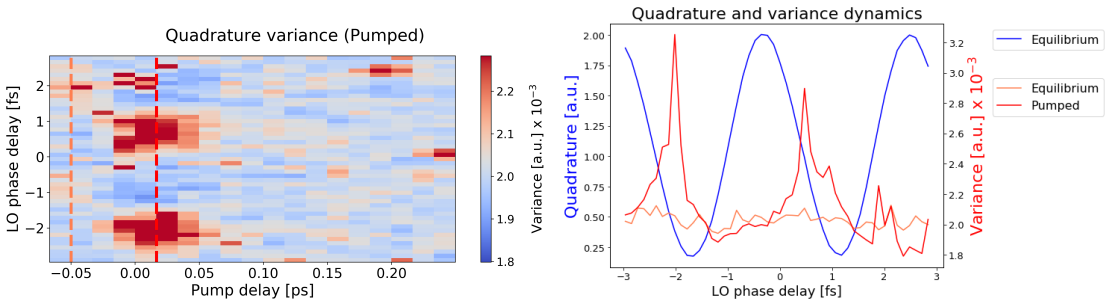

(a) (b)

Figure 6.3: $CuGeO_3$: pump-probe dynamics of a single probe mode quadrature variance (395 THz). In (a) the pumped variance response as a function of the pump-probe delay. In (b) the phase-dependent modulation of the equilibrium variance induced by the pump at the overlap (red line). Probe power $= 1.2 \times 10^7$ ph/pulse; Pump power $= 4.7 \times 10^{12}$ ph/pulse; LO power (single mode with $\sigma = 0.2$ THz) $= 1.2 \times 10^7$ ph/pulse.

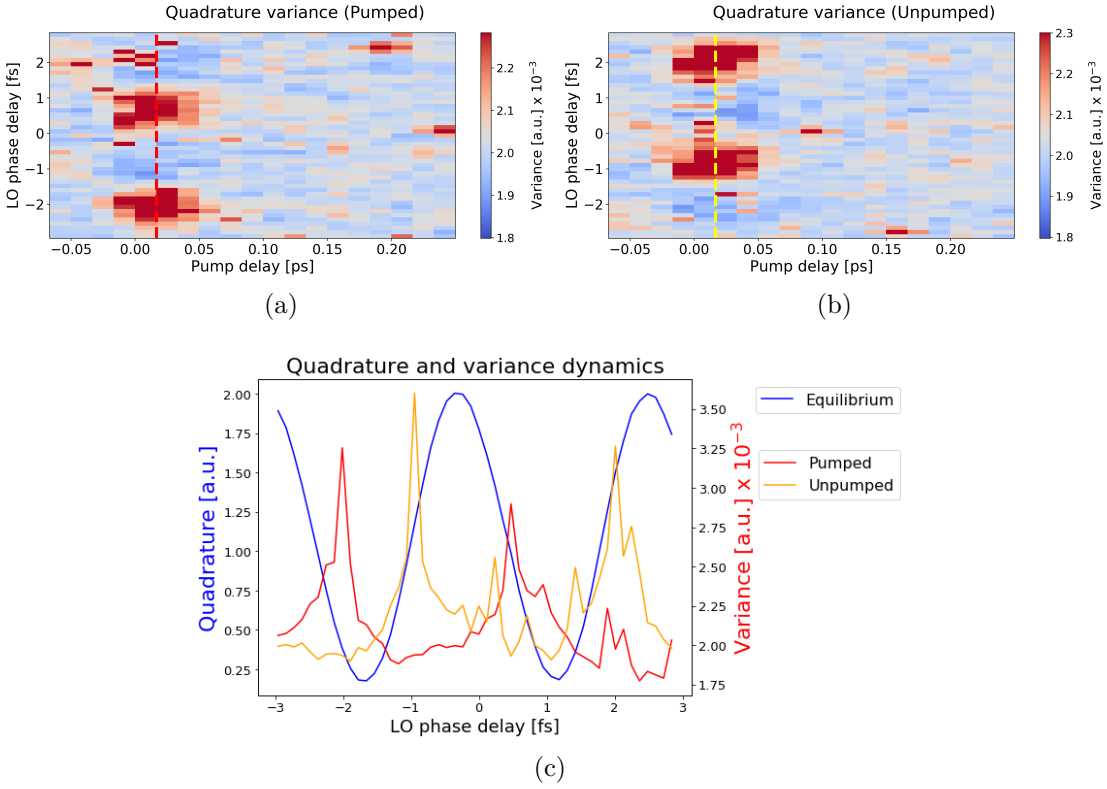

(a) (b)

(c)

Figure 6.4: $CuGeO_3$: pump-probe dynamics of a single probe mode quadrature variance (395 THz). In (a) the dynamical pumped variance response, in (b) the unpumped one measured at the chopping rate (400 Hz). At the overlap, the pump induces a phase-dependent modulation also in the unpumped statistics (c) with an opposite phase.

only at a certain chopper frequency (Figure 6.5). This means that, if the pump beam is not chopped, no modification of probe statistics can be retrieved.

The phase-dependent variance as a function of the chopper rate helps to clarify the origin of the detected noise. Indeed, since no variance modulation occurs

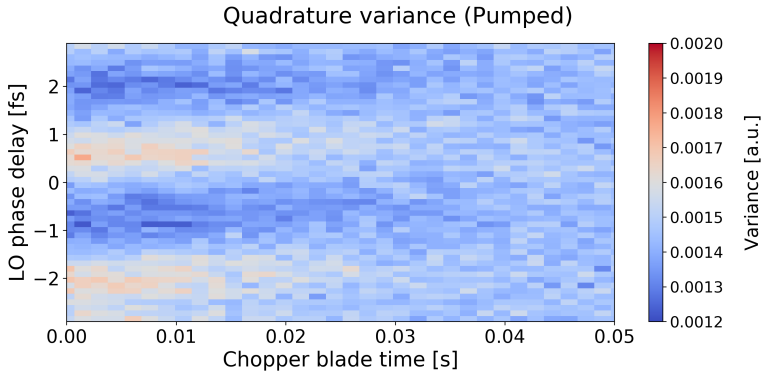

(a)

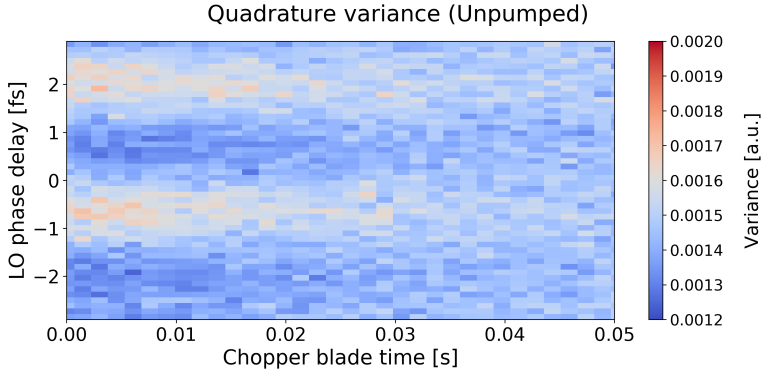

(b)

Figure 6.5: $CuGeO_3$: phase-resolved variance as a function of the chopping time. The variance is evaluated at the pump-probe overlap. In (a) the pumped variance response, while in (b) the unpumped one measured at the chopping rate at positive times. They are both evaluated at an increasing chopping period (x-axis).

when the sample is constantly[1] pumped, the detected noise trend is related to a pump-dependent transition between two states that last more than the temporal separation between two subsequent pulses. These two states can be:

- A thermal ground state in which the system stays in the absence of the pump.
- An excited thermal state in which the system is driven by the pump at the overlap.

Phase-dependent quadrature fluctuations do not occur when the system is in one of the two states. Indeed, by looking at Figure 6.5, in the limit of no chopping (i.e. high chopper blade times) the variance is flat at the overlap. Therefore, these fluctuations originate only from the transitions between these two thermal states triggered by pump chopping (Figure 6.5). In this scenario, phase-dependent quadrature noise of the probe encodes the thermal fluctuation induced by the pump at the overlap.

[1]Without being chopped at a frequency much lower than the laser repetition rate.

6.1.3 Measurements on α-quartz

In this section the preliminary statistical measurements on α-quartz are shown. In particular, we will present the single probe mode variance dynamics both in parallel (Section 5.2.1) and cross (Section 5.2.2) configuration.

Parallel configuration

In this section the statistical measurements in parallel configuration are presented. As shown in Figure 6.6, at the overlap we detect a phase-dependent modulation of the probe statistics whose maxima occur at the zeros of the equilibrium probe quadrature. As in $CuGeO_3$, thermal noise fluctuations induced by the pump at the overlap are mapped both in the pumped and the unpumped variance acquired at the chopping rate. The two phase-resolved fluctuations are π-shifted.

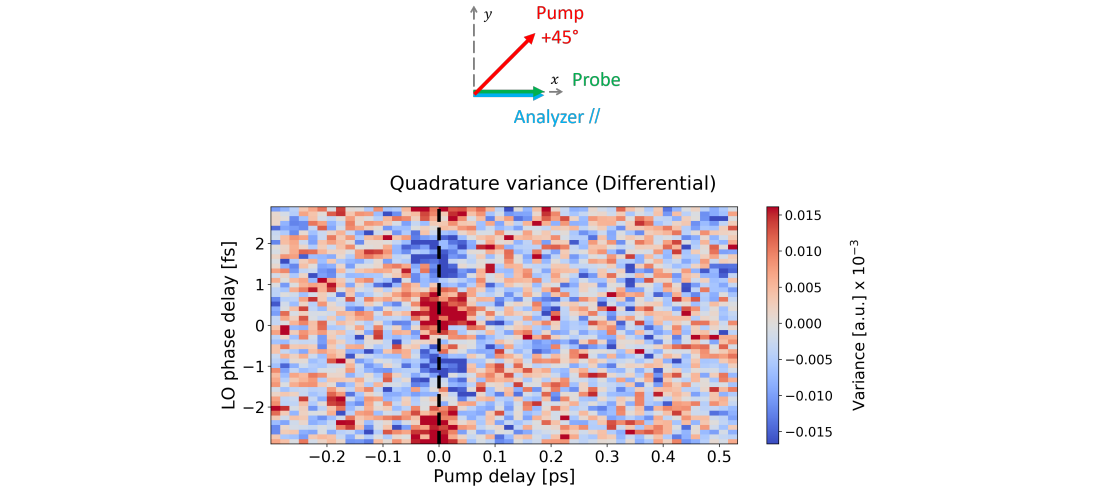

(a)

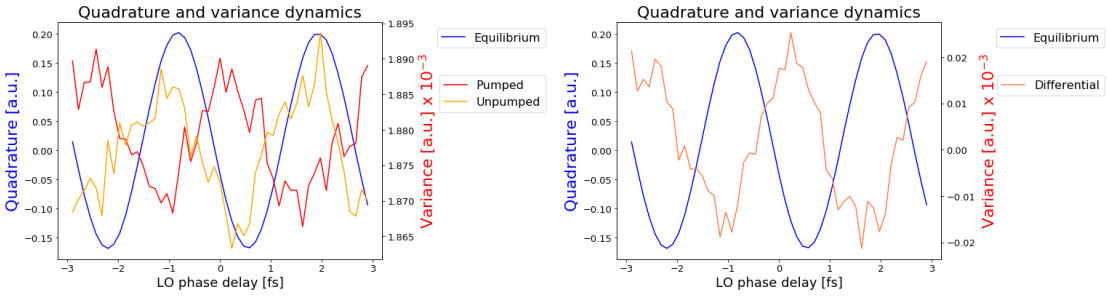

(b) Pumped and unpumped variance at overlap

(c) Differential variance at overlap

Figure 6.6: Quartz, parallel configuration. In (a) the experimental differential variance mapping pump-induced variance modulations. In (b) the phase-resolved variance dynamics of the pumped and unpumped quadrature sets evaluated at the pump-probe overlap (black line of plot (a)). In (c) the differential variance at temporal overlap whose maxima occur in correspondence with the zeros of the equilibrium quadrature (blue line). Probe power = 3.8×10^4 ph/pulse; Pump power = 4.7×10^{12} ph/pulse; LO power (single mode with $\sigma = 0.3$ THz) = 1.2×10^7 ph/pulse.

Cross configuration

In Figure 6.7 we present the pumped variance response of a single emitted probe field in cross polarization. A strong pump-induced variance response is detected at the pump-probe overlap (Figure 6.7). In contrast to the parallel case, the pump modulates equilibrium probe statistics in phase with equilibrium quadrature. Therefore, the modulation of the emitted field in cross polarization follows the fluctuations of the number of photons scattered by the sample in orthogonal polarization.

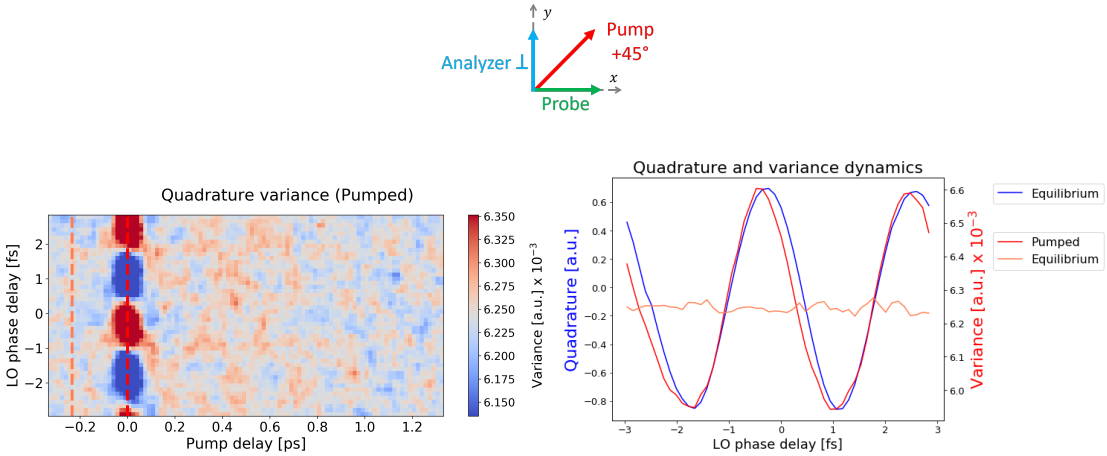

(a) (b)

Figure 6.7: Quartz, extinction configuration: pump-probe dynamics of a single probe mode quadrature variance (392 THz). In (a) the pumped variance response as a function of the pump-probe delay. In (b) the phase-dependent modulation of the equilibrium variance induced by the pump at the overlap (red line). The modulation is in phase with the equilibrium quadrature (blue trend in (b)). Probe power $= 3.8 \times 10^4$ ph/pulse; Pump power $= 4.7 \times 10^{12}$ ph/pulse; LO power (single mode with $\sigma = 0.7$ THz) $= 2.3 \times 10^7$ ph/pulse.

At the overlap, also the unpumped variance acquired at the chopper rate (400 Hz) is influenced by the pump excitation (Figure 6.8). Indeed, it modulates in anti-phase with respect to the pumped one.

In this polarization geometry, the variance modulation induced by the pump is also visible at the maxima of the phonon oscillations[2]. We illustrate this feature in Figure 6.9 where we present the noise dynamics at the first maximum amplitude of the nuclear displacement. Also at this delay (Figure 6.9(b, d)), the phase-dependent noise evolution follows the equilibrium quadrature (Figure 6.9(d)).

[2]The detected phonon in this geometry (analyzer and probe in cross configuration and pump polarized at $\Theta = 45°$) is the 4 THz one with symmetry E^T.

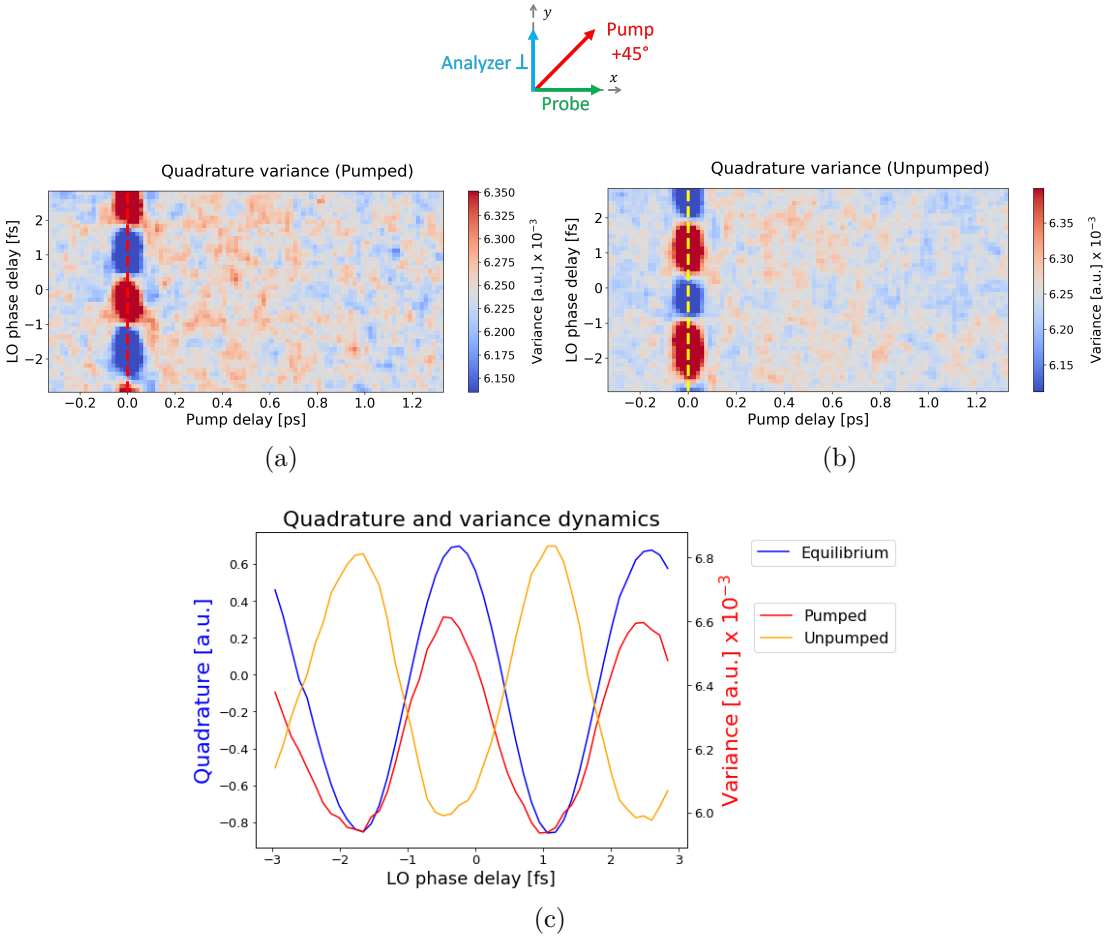

Figure 6.8: Quartz, extinction configuration: pump-probe dynamics of a single probe mode quadrature variance (392 THz). In (a) the dynamical pumped variance response, in (b) the unpumped one. For each pump-probe delay the latter are acquired at the chopping rate (400 Hz). At the overlap the pump induces a phase-dependent modulation also of the unpumped statistics with opposite sign with respect to the pumped one (c).

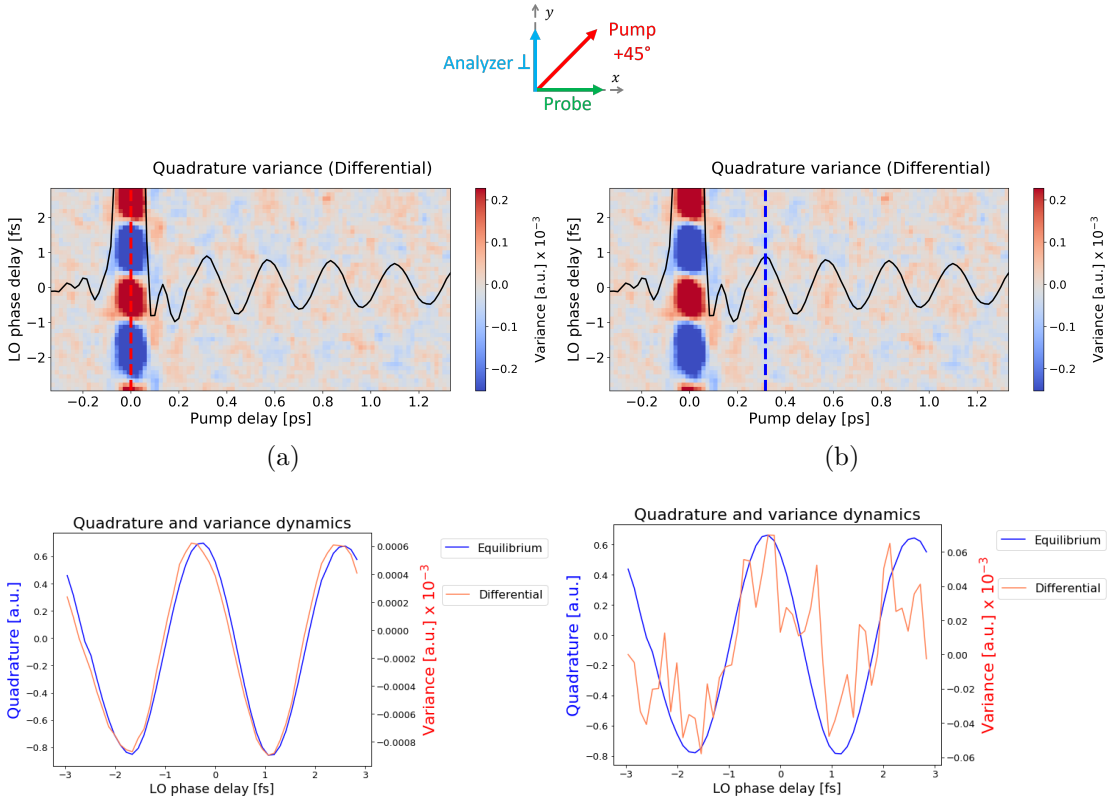

Figure 6.9: Quartz, extinction configuration: differential variance pump-probe dynamics (a, b) ruled by the phonon amplitude oscillations (black line). In (c) and (d) the phase-resolved variance dynamics evaluated at the overlap (c) and at the first phonon oscillation maxima (d). They are both in phase with the equilibrium quadrature (blue trend in (c) and (d)).

6.2 Perspectives: measuring multimode quantum correlations

In the previous section we have focused our attention on single mode variance dynamics. This approach is useful to track the phase-dependent modification of the probe field statistics.

However, every multimode response resulting from non-linear probe-sample interaction is hidden through this approach. With our set-up we are able to overcome this limitation and have access to a multiplicity of quantum correlations structures. These are encoded inside the measure of the statistics of the homodyne current with a multiple-shaped local oscillator (Figure 1.6). By multiple-shaping the local oscillator we are indeed able to tailor the measurement basis of the multimode probe state by reconstructing its covariance matrix. The covariance matrix encodes both single mode statistical predictions and intrinsic multimode quantum correlations [1]. In particular, the latter are related to its off-diagonal terms (Equation 1.39).

Multimode correlations we are looking for in our experiments are introduced among probe modes by their ISRS interaction with the excited phononic state. In order to clarify the origin of these phonon-induced correlations let us examine the following ideal situation. Let us consider a gaussian pulse in which a narrow fluctuation localized at a specific frequency ω has been introduced. The ISRS process will induce similar fluctuations also at frequencies $\omega \pm \Omega$, where Ω is the phonon frequency. If we repeat the measurement many times introducing for each repetition a different unique fluctuation, the Raman process will imprint on the probe pulse correlations among the phonon-coupled modes[3].

Since we are working in shot-noise conditions (Chapter 4), these uncorrelated localized fluctuations introduced at each repetition are caused by the poissonian quantum noise of the probe field. Therefore, we can potentially detect ISRS-driven correlations of purely quantum origin.

In this section we will limit our analysis to two-modes-correlations, thus neglecting higher order correlations introduced by ISRS. In this framework, the phonon-related correlations are encoded inside the off-diagonal terms of the two-modes-covariance matrix. Recalling Equation 1.39, the latter reads[4]

$$C_{ij}(\omega_i,\omega_j)(\phi) = \begin{pmatrix} \sigma^2(\widehat{X}_i(\omega_i))(\phi) & \langle \widehat{X}_i(\omega_i)\widehat{X}_j(\omega_j)\rangle(\phi) \\ \langle \widehat{X}_j(\omega_j)\widehat{x}_i(\omega_i)\rangle(\phi) & \sigma^2(\widehat{X}_j(\omega_j))(\phi) \end{pmatrix} \tag{6.1}$$

Its off-diagonal terms ruling two modes quantum correlations can be conveniently expressed as follows (Equation 1.44):

$$\langle \widehat{X}_i(\omega_i)\widehat{X}_j(\omega_j)\rangle(\phi) = \sigma^2(\widehat{X}_i(\omega_i)+\widehat{X}_j(\omega_j))(\phi) - \sigma^2(\widehat{X}_i(\omega_i))(\phi) - \sigma^2(\widehat{X}_j(\omega_j))(\phi) \tag{6.2}$$

In the previous equation $\sigma^2(\widehat{X}_i(\omega_i)$ and $\sigma^2(\widehat{X}_j(\omega_j)$ represent the phase-dependent single mode quadrature variance obtained through the homodyne measurement

[3]These correlations have been already measured in the classical regime [33], i.e. in the case in which stochastic classical fluctuations are manually introduced at each repetition, thus emulating classical thermal noise.

[4]In the present expression we are neglecting the frequency-dependence of the local oscillator phase shift.

with a single LO frequency (Figure 1.5). Conversely, $\sigma^2(\widehat{X}_i(\omega_i) + \widehat{X}_j(\omega_j))(\phi)$ is the homodyne current variance measured in the case of a two mode-shaped local oscillator (Figure 1.6). In the following, we will make use of the phase-dependent correlator presented in Equation 6.2 as an estimator of the two modes ISRS-driven quantum correlation. In particular, we will see whether correlation features can be retrieved when $\omega_j - \omega_i$ equals the phonon frequency. The adopted system for this study is $CuGeO_3$.

We have studied the ISRS-driven correlations for two different photon-phonon interactions:

- Interaction of the probe photons with a thermal phononic ground state, in which the system lives before the pump arrival.

- Interaction of the probe photons with a displaced phononic state, in which the system is driven by the pump excitation.

We expect the cross-section of the latter process to be resonantly enhanced by the pump excitation (Chapter 2).

In Figure 6.10 we present the phase-resolved correlator $\langle\widehat{X}_i(\omega_i)\widehat{X}_j(\omega_j)\rangle(\phi)$ (Equation 6.2) evaluated at negative pump-probe times (i.e. on a phonon thermal ground state). We notice that no clearly features can be seen in the correlator in correspondence to a frequency difference matching the detected phonon one[5] (5.6 THz).

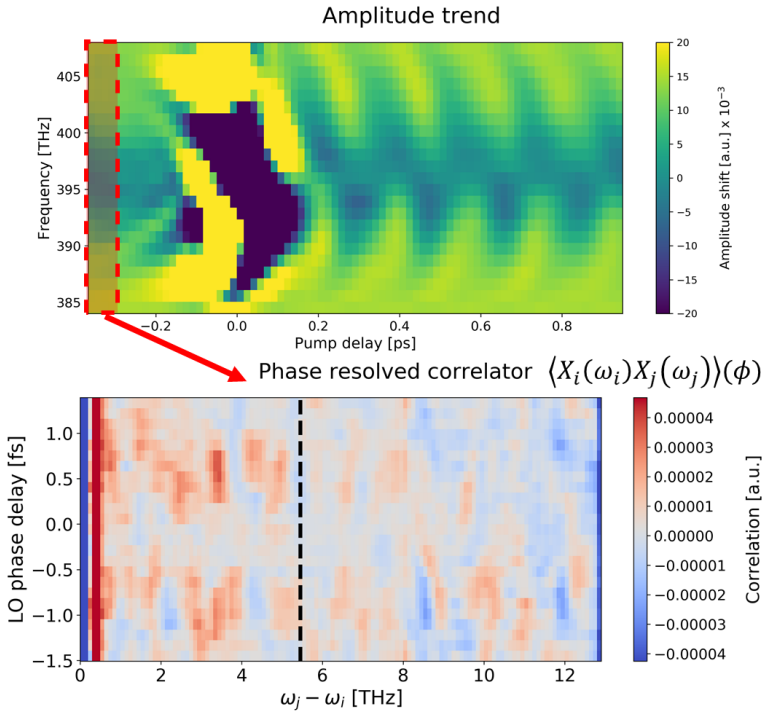

Figure 6.10: $CuGeO_3$: Phase-resolved two-modes-correlator ($\langle\widehat{X}_i(\omega_i)\widehat{X}_j(\omega_j)\rangle(\phi)$) calculated at negative pump-probe times and by scanning the local oscillator phase ϕ. No clearly features can be seen in correspondence to the 5.6 THz phonon (black line).

[5]Total symmetric A_g phonon (Section 5.3)

In Figure 6.11 we present the phase-resolved correlator $\langle \widehat{X}_i(\omega_i)\widehat{X}_j(\omega_j)\rangle(\phi)$ (Equation 6.2) evaluated in correspondence to the first maxima of the phonon oscillations. At this delay, the probe interacts with a displaced phonon. In this situation, we can notice a possible phonon-related correlation peak arising at a frequency difference of 5.6 THz.

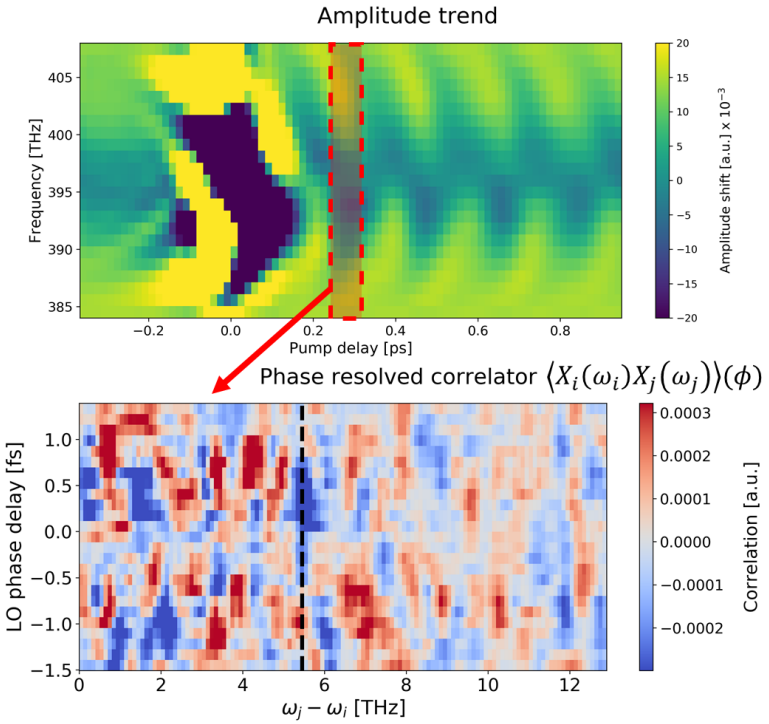

Figure 6.11: $CuGeO_3$: Phase-resolved two-modes-correlator ($\langle \widehat{X}_i(\omega_i)\widehat{X}_j(\omega_j)\rangle(\phi)$) calculated at a pump-probe time corresponding to the first maximum of phonon oscillations. A possible phonon-related peak at 5.6 THz arises.

The comparison between the two previous interactions becomes more clear by integrating the maps presented in Figure 6.10 and Figure 6.11 along the local oscillator phase axis. The phase-integrated correlators are presented in Figure 6.12. As previously anticipated, a possible phonon-related correlation peak is retrieved only when ISRS features are imprinted on the probe pulse through the interaction with a displaced phonon. This is consistent with the increase of the probe-phonon cross section driven by the pump excitation.

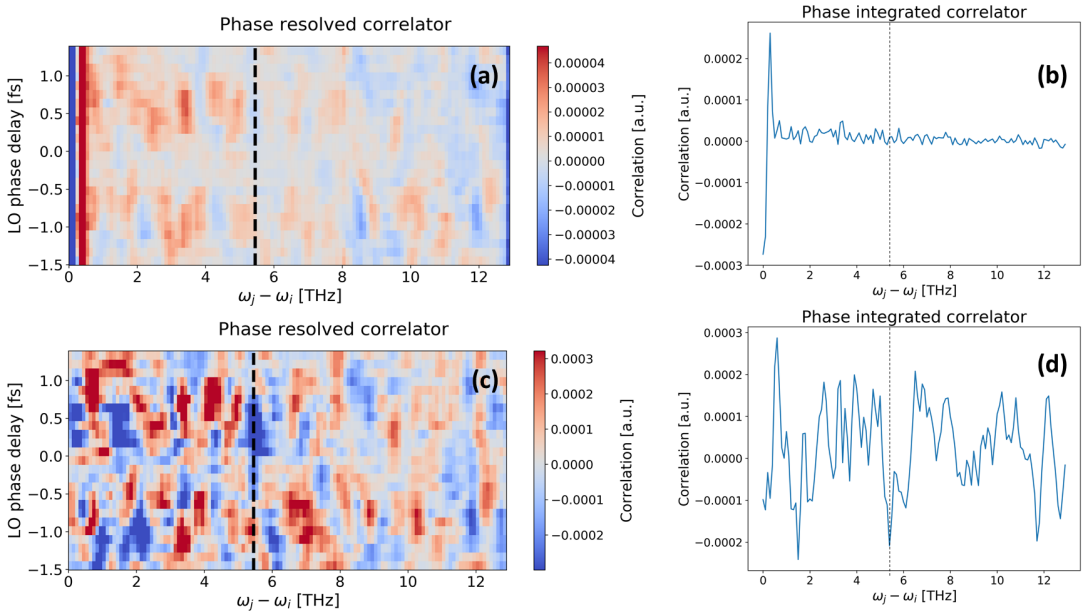

Figure 6.12: In (a) and (b) the phase-resolved and phase-integrated two-modes-correlator calculated at negative times (Figure 6.10). In (b) the same plots evaluated at the first phonon oscillation maxima (Figure 6.11). The phase-integrated correlator in (d) shows a possible phonon-related correlation peak at 5.6 THz.

Conclusions

The coherent motion of atoms in solids is typically addressed by mean of pump-probe spectroscopies. In this widely used approach an intense pump laser pulse drives a collective atomic excitation in the crystal (phonon) and a less intense probe ultrashort pulse interacts with the system out-of-equilibrium. The vast majority of pump-probe techniques measures the intensity of the output probe, providing real-time information about the average of the atomic positions during the collective excitation. However, in this kind of experiments one is discarding all the information present in higher order statistical degrees of freedom of probe photons distribution. The latter encode quantum fluctuations of the atomic positions around their average. Moreover, an integrated detection approach does not permit to track how the photon-phonon interaction is mapped into the phase response of the probe.

In this thesis we have overcome the limitations of the integrated approach by mean of an interferometric technique named *Balanced Homodyne Detection* (BHD) which has been coupled to the standard pump-probe set-up. *Balanced Homodyne Detection* is a powerful method to measure phase-sensitive properties of an optical field and to retrieve its amplitude and phase statistics. In a BHD scheme, the optical field under investigation (*signal*) is mixed in a 50:50 beam splitter (whence the attribute *balanced*) with a strong classical field (*local oscillator*) whose phase is tunable. Mean value and statistical properties of the signal are retrieved by studying how the differential intensity of the two BS outputs (homodyne current) evolve by tuning the local oscillator phase. The phase-dependent homodyne current is indeed a representative observable of the signal field at all orders. The differential acquisition in balanced conditions permits to work in shot-noise conditions. For this reason, the detected signal fluctuations pertain to the intrinsic quantum nature of light.

The novelty implemented during this thesis project resides in the fact that BHD has been performed in a **multimode** scheme. With this innovative approach, we can selectively have access to amplitude and phase statistics of each probe mode and monitor their dynamical evolution after the phonon excitation. This possibility has been accomplished by modulating the frequency content of the local oscillator through an ultrafast pulse-shaper. Performing energy resolved measurements is crucial for characterizing non-linear responses, where probe-matter interaction is accompanied by an energy redistribution within the probe bandwidth. In photon-phonon framework, the leading non-linear interaction is Impulsive Stimulated Raman Scattering (ISRS) which couples all the probe modes differing by the excited phonon frequency.

In this thesis we have exploited multimode homodyne detection to study how photon-phonon coupling is mapped on mean values and fluctuations of amplitude

and phase of each probe mode. The experimental results have been compared with the theoretical previsions of the quantum model presented in [4], which has been tailored to describe also phase dynamics. Exploiting phonon-induced amplitude and phase modulations, we have eventually estimated the probe-phonon cross sections.

Multimode homodyne approach has been firstly apply to α-quartz, which represents a model system for the study of ISRS in non absorbing materials. Amplitude and phase exhibit two different frequency-dependent responses as a function of the pump-probe time.

- The phase of all the probe modes oscillates at the frequency of the excited phonon. This phase trend is due to a linear modulation of the refractive index ruled by the phonon oscillations.

- The amplitude oscillations exhibit a frequency-dependent phase, that results in a time-dependent spectral shift. These spectral shifts are imprinted on the probe spectrum by ISRS and can be filtered out trough the polarization selection of the emitted field. This evidence proves the stimulated nature of ISRS.

Similar amplitude and phase features have been detected also in more complex systems, where phonon excitations are supposed to drive electronic transitions. This evidence proves the feasibility of the technique of tracking low intensity fields out of absorptive materials. We have adopted $CuGeO_3$ probed in resonance with *d-d* transitions for this study.

In the last part of the thesis, we have exploited the unique potentiality of our system to track single mode and multimode statistics under shot-noise conditions. This possibility is guaranteed by the differential acquisition of the BHD scheme. The quantum sensitivity of our detection system has been tested and confirmed by mean of a theoretical model [19]. In particular, we have proved that the inevitable presence of optical dissipators preserves quantum noise sensitivity.

The aim of the statistical analysis was to see whether exists an out-of equilibrium modification of the probe quantum statistics. With our innovative set-up, this statistical modulation can be addressed in a frequency-resolved scheme. In this sense, we have explored the statistics variation of a single probe mode and the modification of the jointly statistics of phonon-coupled modes. We expect the latter to encode the information about the noise correlations imprinted on the probe pulse trough ISRS. These multimode correlations are of purely quantum nature, since detected in shot-noise-limited conditions. Possible signatures of two-modes correlations induced by ISRS have been measured on $CuGeO_3$ only when the photon interacts with a displaced phonon (i.e. not in its thermal ground state).

The innovative approach presented in this thesis can be in principle generalized to the study of any collective excitation in complex systems. In particular, it can be exploited to unveil transient complex dynamics linked to the quantum fluctuations of the atoms around their mean positions. In this perspective, the addition of a second pump pulse will be implemented in the set-up. The idea is to configure the second pump in order to drive a collective atomic excitation in anti-phase with respect to the first pump-excitation. This will in principle suppress the

average atomic oscillations, enabling the study of the intrinsic atomic fluctuations without the contribution of the average displacement.

Appendices

Appendix A

Multimode homodyne current

In Section 1.3 we have stated that the homodyne current resulting from a multimode signal and a multimode local oscillator can be written as the sum of single mode homodyne currents (Equation 1.40). This means that the interference occurs only between modes of the same frequency within signal and local oscillator bandwidth. In this appendix, we will prove this statement in a classical framework, i.e. considering the signal and the local oscillator as classical coherent fields.

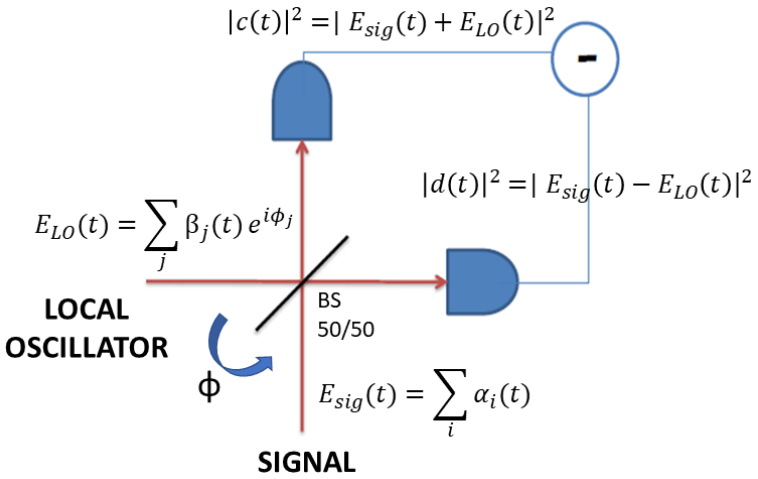

Figure A.1: Classical homodyne with signal and local oscillator in multimode states. The observable quantity is the differential photocurrent between the two outputs of the BS.

With reference to Figure A.1, let us take the *signal* as a classical phase-matched field of the form[1]:

$$E_{sig}(t) = \sum_i |\alpha_i| e^{i\omega_i t} \equiv \sum_i \alpha_i(t) \tag{A.1}$$

As well as the signal, the *local oscillator* is a classical multimode field. Since the phase of the local oscillator can be tuned, its field expression reads:

$$E_{LO}(t) = \sum_j |\beta_j| e^{i\omega_j t} e^{i\phi_j} \equiv \sum_j \beta_j(t) e^{i\phi_j} \tag{A.2}$$

[1]Since the pulse is phase-matched, we have set to 0 the phase of each frequency.

Exploiting now the 50:50 BS action ruled by the unitary matrix described in Equation 1.12, we can get the instantaneous current measured on each diode at time t:

$$\begin{aligned} c^*(t)c(t) &= \sum_i \left(\alpha_i^*(t) + \beta_i^*(t))e^{-i\phi_i}\right) \times \sum_i \left(\alpha_j(t) + \beta_j(t))e^{i\phi_j}\right) \\ d^*(t)d(t) &= \sum_i \left(\alpha_i^*(t) - \beta_i^*(t)e^{-i\phi_i})\right) \times \sum_i \left(\alpha_j(t) - \beta_j(t)e^{i\phi_j})\right) \end{aligned} \tag{A.3}$$

The two instantaneous photocurrents are then integrated over a time $T \sim 100$ ns and the difference between the two integrals (homodyne current) is measured:

$$\begin{aligned} I &= \frac{1}{T}\int_0^T dt\ \left(c^*(t)c(t) - d^*(t)d(t)\right) \\ &= \frac{1}{T}\int_0^T dt \sum_{i,j} \left(\alpha_j^*(t)\beta_i(t)e^{i\phi_i} + \beta_j(t)\alpha_i(t)e^{-i\phi_j}\right) \end{aligned} \tag{A.4}$$

We want now to prove that the relevant contributions to the multimode current derive from the frequency-matched modes. For this purpose, let us write Equation A.4 in the case $i \neq j$:

$$\begin{aligned} I_{ij(i\neq j)} &= \frac{1}{T}\int_0^T dt\Big(\beta_i(t)\alpha_j^*(t)e^{i\phi_i} + \alpha_j(t)\beta_i^*(t)e^{-i\phi_i}\Big) \\ &= |\alpha_j||\beta_i|\frac{1}{T}\int_0^T dt \cos\Big((\omega_j - \omega_i)t + \phi_i\Big) \end{aligned} \tag{A.5}$$

Since the integration time $T \sim 100$ ns is much more longer than the oscillation period of the integral $2\pi/\Delta\omega_{ij} \sim 1$ ps, I_{ij} tends to 0 if $i \neq j$. Therefore, no interference can be detected between signal and LO modes with different frequency. This result confirms the fact (Equation 1.40) that the multimode homodyne response can be expressed as the sum of single mode contributions. Indeed, no interference occurs between modes with different frequencies.

Appendix B

Potentiality of the set-up: multimode homodyne with shaped signal

In the measurements presented in Chapter 5 and 6 we have only explored the possibility of shaping the frequency content of the local oscillator to address the corresponding probe amplitude and phase dynamics. In all those cases the probe was in a multimode state.

Here we present the mean value measurements performed by frequency-shaping also the probe. This approach is potentially suitable to study whether exist some side-bands dynamics in the phase and the amplitude of the homodyne current when the probe-LO differential frequency matches a phonon mode. The employed set-up for this study is presented in Figure B.1. The differential current dynamics is monitored at each pump-probe delay as a function of the frequency mismatch ($\Delta\omega$) between the probe and the local oscillator.

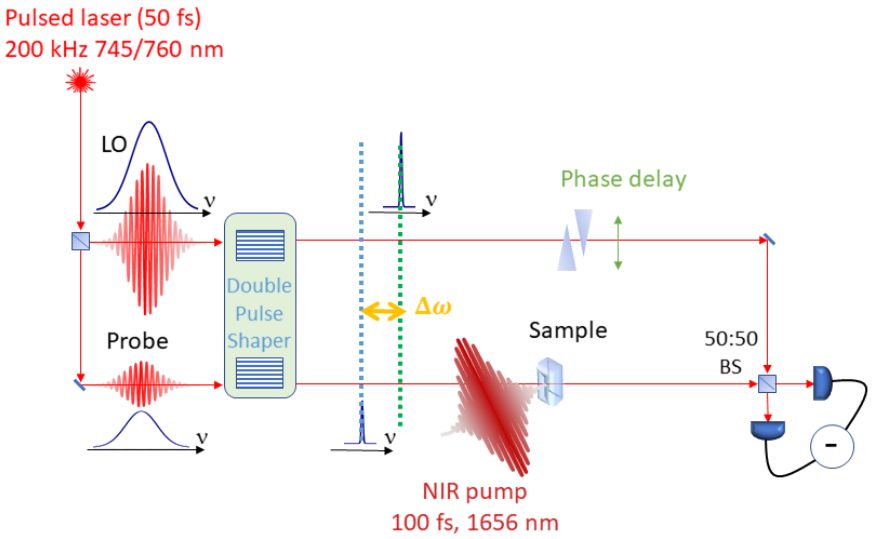

Figure B.1: Set-up employed for time-resolved homodyne with signal (probe) and local oscillator shaped.

The present study has been performed on α-quartz excited along the c-axis and probed in parallel geometry. Amplitude and phase pump-probe dynamics of

the differential current as a function of $\Delta\omega$ are presented in Figure B.2(a),(b). In this configuration, amplitude and phase of the homodyne current evolve in time with a frequency that depends on $\Delta\omega$. In particular, when the local oscillator and the probe are frequency-matched (i.e. $\Delta\omega = 0$) their pump-probe frequency evolution tends to zero (Figure B.2(c),(d)).

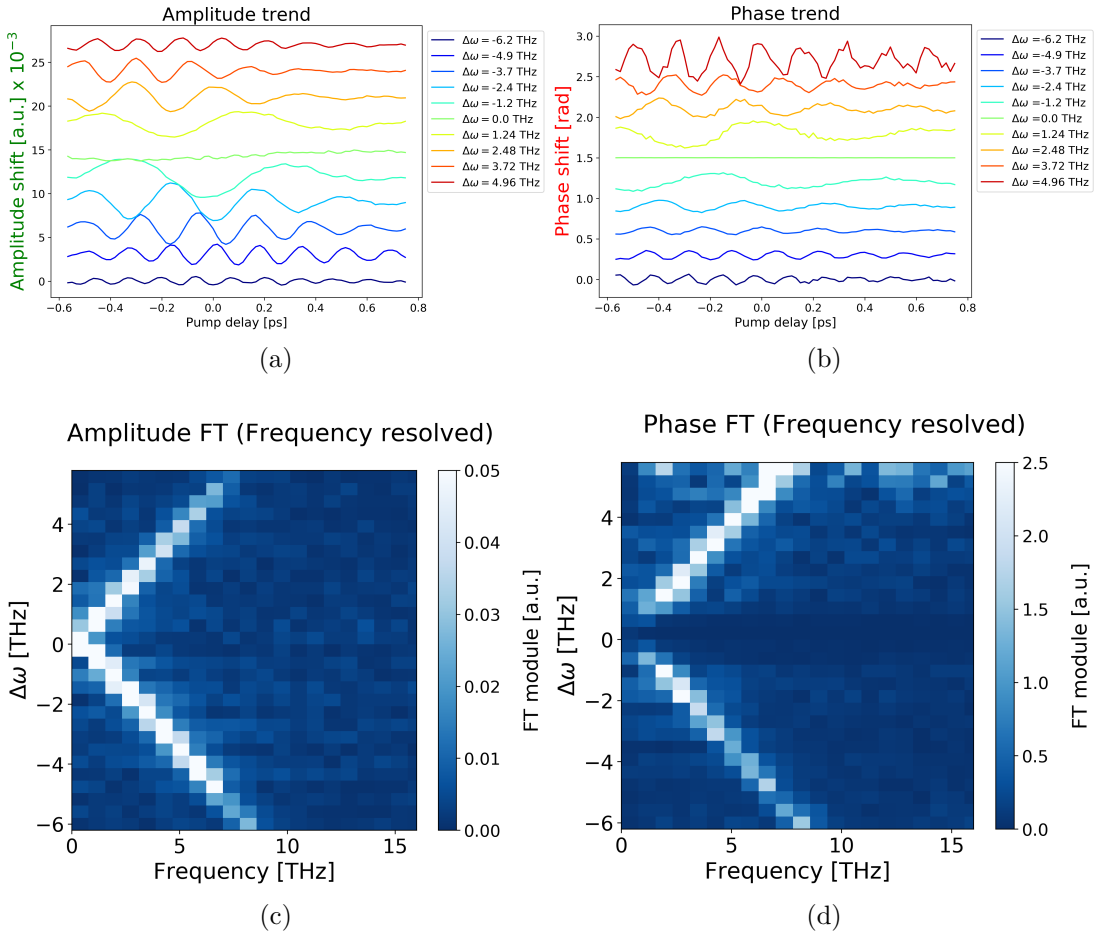

Figure B.2: Quartz, parallel geometry: time-resolved homodyne with probe and local oscillator shaped (Figure B.1). In (a) and (b) the amplitude and phase quadrature pump-probe trends as a function of the frequency difference between signal and local oscillator ($\Delta\omega$). In (c) and (d) the Fourier transforms of the homodyne current as a function of LO-probe frequency difference ($\Delta\omega$).

Riassunto

Lo sviluppo di tecnologie laser ultraveloci ha permesso di ampliare le prospettive delle spettroscopie vibrazionali, permettendo di monitorare le dinamiche coerenti degli atomi su scale temporali che sono minori dei loro periodi di oscillazione. L'approccio sperimentale tipico per questo scopo è la spettroscopia *pump-probe*. In questa tecnica, un intenso impulso laser (*pump*) induce un'eccitazione collettiva degli atomi del reticolo (fonone) la cui dinamica viene monitorata per mezzo di un secondo impulso ultracorto (*probe*). La maggior parte delle tecniche *pump-probe* misura l'intensità del *probe* per estrarre le informazioni sulla dinamica transiente dell'eccitazione collettiva. Attraverso una misura di intensità integrata, si possono estrarre informazioni sull'evoluzione delle posizioni medie degli atomi. Tuttavia, in questa tipologia di esperimenti viene eliminata tutta l'informazione presente nei gradi di libertà statisitci della radiazione di *probe*. Questi gradi di libertà mappano le fluttuazioni degli atomi attorno alle loro posizioni reticolari medie. Inoltre, questo approccio integrato non permette di monitorare come l'interazione fotone-fonone influisce sulla risposta di fase del campo di *probe*.

In questa tesi, si è proposto un metodo capace di superare queste limitazioni per mezzo di una tecnica interferometrica denominata *Detezione omodina bilanciata* (BHD) che è stata accoppiata all'approccio *pump-probe* standard. Questa tecnica è particolarmente efficace per studiare dinamiche di fase di un impulso ottico e per ottenere le informazioni statistiche in esso contenute. Nello schema ideale della BHD, l'impulso ottico che si vuole studiare viene fatto interagire in un *beam splitter* bilanciato (50:50) con un campo classico denominato "oscillatore locale", la cui fase è regolabile. Le proprietà medie e statistiche dell'impulso ottico sono monitorate studiando come la differenza di intensità dei due campi uscenti dal *beam-splitter* (corrente omodina) evolve in funzione della fase dell'oscillatore locale. Questo perchè si può dimostrare che la corrente omodina è rappresentativa del campo ottico in indagine a tutti gli ordini. L'acquisizione in condizioni bilanciate (attraverso un *beam splitter* 50:50) permette inoltre di essere sensibili alle fluttuazioni intrinsiche del campo ottico in indagine (*shot-noise*), derivanti dalla sua natura quantisitca.

La novità dell'approccio adottato in questa tesi risiede nel fatto che la detezione omodina del campo di *probe* è stata relaizzata in uno schema **multimodo**. Con questo approccio innovativo, si è in grado di avere accesso in modo selettivo alla statistica di fase e di ampiezza di ogni modo della radiazione di *probe* e di monitorare la loro dinamica a seguito dell'eccitazione vibrazionale. Questa possibilità è stata sperimentalmente implementata modulando il contenuto spettrale dell'oscillatore locale attraverso un modulatore ottico di impulsi ultracorti (*pulse-shaper*). Misure risolte in energia sono fondamentali per caratterizzare risposte non lineari, in cui l'interazione del *probe* con la materia causa una redistribuzione

energetica all'interno della sua banda spettrale. Per ciò che concerne l'interazione fotone-fonone, la principale interazione non lineare è lo "Scattering Raman Impulsato e Stimolato" (ISRS) che accoppia i modi del probe che differiscono della frequenza del fonone eccitato.

In questa tesi, la detezione omodina multimodo è stata applicata per studiare come l'accoppiamento fotone-fonone modifica la dinamica media e la statistica di ampiezza e fase di ogni modo del *probe*. I risultati sperimentali sono stati comparati con le previsioni teoriche del modello presentato in [4], che è stato adattato per descrivere anche dinamiche di fase. Inoltre, sfruttando le modulazioni di ampiezza di fase indotte dal *probe*, si è stimata la sezione d'urto del processo di interazione fotone-fonone.

L'omodina multimodo è stata preliminarmente testata sul quarzo, che rappresenta un sistema modello per lo studio di eccitazioni Raman in materiali trasparenti. Ampiezza e fase mostrano due differenti risposte spettrali durante la dinamica *pump-probe*. La fase di tutti i modi del probe oscilla alla frequenza del fonone eccitato. Al contrario, le oscillazioni di ampiezza evolvono con una fase che dipende dalla frequenza del probe. Quest'ultimo effetto causa uno *shift* spettrale all'interno del probe che dipende dall'istante nel quale questo ha interagito con il fonone. La modulazione di fase è dovuta ad una modulazione lineare dell'indice di rifrazione determinata dalle oscillazioni del fonone. Al contrario, gli *shift* di ampiezza spettrale sono dovuti all'interazione Raman del probe.

Dinamiche di fase e di ampiezza simili a quelle sopra indicate si sono rilevate anche in sistemi più complessi, dove le eccitazioni vibrazionali di bassa energia si accoppiano a transizioni orbitali. Questo accoppiamento è stato studiato nel $CuGeO_3$ regolando la frequenza del *probe* in modo che sia risonante con le eccitazioni orbitali *d-d*. Il fatto che anche in questo caso le carateteristiche derivanti dall'eccitazione fononica di bassa energia sono rilevabili nel campo di *probe*, dimostra l'adattabilità della tecnica allo studio di campi con pochi fotoni derivanti da processi di assorbimento risonante.

Nell'ultima parte della tesi, è stata sfruttata la singolare potenzialità del nostro set-up di monitorare in condizioni di *shot-noise* dinamiche statistiche di singolo modo e multimodo. Questa possibilità è assicurata dall'acquisizione differenziale dello schema della BHD. La sensibilità quantisitca del sistema di rivelazione è stata testata attraverso un modello teorico [19] che permettesse di vedere come effetti ottici dissipativi influenzano la rivelazione del rumore quantisitco. Si è dimostrato che, anche in presenza di dissipatori ottici, la fluttuazioni classiche possono essere eliminate ed il regime di *shot-noise* conseguentemente garantito.

L'obiettivo dell'analisi statistica è stato quello di monitorare modifiche della statistica quantistica del *probe* fuori dall'equilibrio. Tramite il nostro set-up, questa modulazione della statistica può essere risolta in frequenza. In questo senso, si è studiata sia la variazione delle proprietà statistiche di un singolo modo, che la modifica della distribuzione statistica congiunta dei modi del *probe* accoppiati dal fonone. Ci si aspetta di ottenere da quest'ultima le informazioni relative alle correlazioni multimodo derivanti dal processo Raman. Tali correlazioni derivano dal rumore quantisitco, visto che si lavora in condizioni di *shot-noise*. Una possibile evidenza di correlazioni a due modi indotta dal processo Raman è stata rilevata nel $CuGeO_3$.

L'approccio innovativo presentato in questa tesi può essere in principio gen-

eralizzato allo studio di qualsiasi eccitazione collettiva in sistemi complessi. In particolare, può essere sfruttato per rivelare complesse dinamiche transienti correlate alle fluttuazioni quantistiche degli atomi attorno alle loro posizioni. In questa prospettiva, verrà implementata nel set-up la possibilità di lavorare con due implusi di pompa. L'idea è quella di configurare la seconda pompa in modo da indurre un'eccitazione atomica collettiva che sia in antifase rispetto a quella indotta dalla prima pompa. In linea di principio, con questo approccio possiamo eliminare le informazioni contenute nelle oscillazioni medie ed avere accesso unicamente alle fluttuazioni delle posizioni atomiche.

Bibliography

[1] Medeiros de Araùjo, Roslund J., Cai Y., Ferrini G., Fabre C., Treps N. *Full characterization of a highly multimode entangled state embedded in an optical frequency comb using pulse shaping* Phys. Rev. A 89, 053828 (2014).

[2] Opatrny T., Welsh D. *Multimode density matrices of light via amplitude and phase control* Opt. Commun. 134:112 (1996).

[3] Esposito M., Benatti F., Floreanini R., Olivares S., Randi F., Titimbo K., Pividori M., Novelli F., Cilento F., Parmigiani F., Fausti D. *Pulsed homodyne Gaussian quantum tomography with low detection efficiency* New Journal of Physics 16(4) (2014).

[4] Glerean F., Marcantoni S., Sparapassi G., Blason A., Esposito M., Benatti F., Fausti D. *Quantum model for Impulsive Stimulated Raman Scattering* J. Phys. B: At Mol. Opt. Phys. (2019).

[5] Potma E., Mukamel S. *Theory of Coherent Raman Scattering* CRC Press (2012).

[6] Welsh D., Vogel W., Opatrny T. *Homodyne Detection and Quantum State Reconstruction* Progress in Optics, Vol. XXXIX, ed E.Wolf (Elsevier, Amsterdam) p. 63-211 (1999).

[7] Esposito M. *A new spectroscopic approach to collective excitations in solids: pump-probe quantum state tomography* PhD thesis, Università degli Studi di Trieste (2016).

[8] Vogel K. and Risken H. *Determination of quasiprobability distributions in terms of probability distributions for the rotated quadrature phase* Phys. Rev., 40:2847 (1989).

[9] Loudon R. *The Quantum Theory of Light* Third Edition (Oxford Science Publications)

[10] Fano U. *Description of states in quantum mechanics by density matrix and operator techniques* Review of Modern Physics, 29(1):74, Sec. 6 (1957).

[11] Ulf L. *Measuring the Quantum State of Light* Cambridge Studies in Modern Optics (1997).

[12] Olivares S., Ferraro A., Paris M.G.A. *Gaussian states in quantum information* Bibiopolis, Napoli (2005).

[13] Scully and Zubairy *Quantum Optics* Cambridge University Press (1997).

[14] Rundquist A, Broman J., Underwood D., Blanck D. *Polarization-dependent detection of Impulsive Stimulated Raman Scattering in α-quartz* Journal of Modern Optics 52(17)-2501 2510 (2005).

[15] Glerean F. *Noise Correlation Spectroscopy for Impulsive Stimulated Raman Scattering* Master thesis, Università degli Studi di Trieste (2017).

[16] K.G. Nakamura et al. *Spectrally resolved detection in transient-reflectivity measurements of coherent optical phonons in diamond* Phys. Rev. B 94,024303 (2016).

[17] Scott JF, Porto SPS *Longitudinal and transverse optical lattice vibrations in quartz* Physical Review, 161(3): 903 (1967).

[18] Popovich Z.V., Devic S.V. *Phonons in $CuGeO_3$ studied using polarized far-infrared and Raman Scattering Spectroscopies* Physical Review B Volume 52, Number 6 (1995).

[19] Giusti F. *Intensity and fluctuation dynamics in pump-probe experiments in complex materials* PhD thesis, Università degli Studi di Trieste (2019).

[20] Wefers M., Kawashima H., Nelson K.A. *Optical control over two-dimensional lattice vibrational trajectories in crystalline quartz* Journal of Chemical Physics, 108 (1998).

[21] Merlin R. *Generating coherent THz phonons with light pulses* Solid State Communications 102(2-3), 207-220 (1997)

[22] Umari P., Pasquarello A., Dal Corso A. *Raman scattering intensities in α-quartz: A first-principles investigation* Phys. Rev. B, 63:094305 (2001).

[23] Vaughan J. C., Hornung T., Feurer T., Nelson K. A. *Diffraction-based femtosecond pulse shaping with a two-dimensional spatial light modulator* Optics Letters, 30(3): 323-325 (2005).

[24] Weiner A. M. *Femtosecond pulse shaping using spatial light modulators* Review of scientific instruments, 71(5): 1929-1960 (2000).

[25] R.D. Guenther *Modern Optics* John Wiley and sons (1990)

[26] Bassi M., Camagni P., Rolli R., Samoggia G., Parmigiani F., Dhalenne G., Revcolevshi A. *Optical absorption of $CuGeO_3$* Phys. Rev. B 54, R11030(R) (1996).

[27] Jim Clarke. *The structure of silicon dioxide* http://www.chemguide.co.uk/atoms/structures/giantcov.html (2009)

[28] Damascelli A., Van der Marel D., Dhalenne G., Revcolevshi A. *Optical spectroscopy of pure and doped $CuGeO_3$* Phys. Rev. B 61 18, 12063 (2000).

[29] Randi F. *Pulsed homodyne detection for quantum state reconstruction applied to ultrafast non-equilibrium spectroscopy* Master Thesis, Università degli Studi di Trieste (2013).

[30] Esposito M. *Design and experimental realization of a pulsed homodyne detector for optical quantum states characterization* Master Thesis, Università degli Studi di Trieste (2012).

[31] Giusti F., Mariciniak A., Randi F., Sparapassi G., Boschini F., Eisaki H., Greven M., Damascelli A., Avella A., Fausti D. *Signatures of enhanced superconducting phase coherence trough MID-IR excitation in optimally doped Y-Bi2212* Phys. Rev. Lett. 122, 067002 (2019).

[32] Montanaro A. *Noise Correlation Spectroscopy* Master Thesis, Università degli Studi di Trieste (2018).

[33] Tollerud J., Sparapassi G., Montanaro A., Asban S., Glerean F., Giusti F., Marciniak A., Kourousias G., Billè F., Cilento F., Mukamel S., Fausti D. *Femtosecond covariance spectroscopy* PNAS 116(12) 5383-5386 (2019).

[34] Rigoni E. M. *Messa a punto di un modulatore di luce per il controllo di impulsi ultracorti* Bachelor Thesis, Università degli Studi di Trieste (2018).

[35] Appel J., Hoffmann D., Figueroa E., Lvovsky I. *Electronic noise in optical homodyne tomography* Phys. Rev. A 75, 035802 (2007).